Western University Scholarship@Western

Electronic Thesis and Dissertation Repository

12-1-2016 12:00 AM

Modeling, Sensorization and Control of Concentric-Tube Robots

Ran Xu, The University of Western Ontario

Supervisor: Dr. Rajni V. Patel, *The University of Western Ontario* A thesis submitted in partial fulfillment of the requirements for the Doctor of Philosophy degree in Electrical and Computer Engineering © Ran Xu 2016

Follow this and additional works at: https://ir.lib.uwo.ca/etd

Part of the Robotics Commons

Recommended Citation

Xu, Ran, "Modeling, Sensorization and Control of Concentric-Tube Robots" (2016). *Electronic Thesis and Dissertation Repository*. 4311. https://ir.lib.uwo.ca/etd/4311

This Dissertation/Thesis is brought to you for free and open access by Scholarship@Western. It has been accepted for inclusion in Electronic Thesis and Dissertation Repository by an authorized administrator of Scholarship@Western. For more information, please contact wlswadmin@uwo.ca.

Abstract

Since the concept of the Concentric-Tube Robot (CTR) was proposed in 2006, CTRs have been a popular research topic in the field of surgical robotics. The unique mechanical design of this robot allows it to navigate through narrow channels in the human anatomy and operate in highly constrained environments. It is therefore likely to become the next generation of surgical robots to overcome the challenges that cannot be addressed by current technologies. In CSTAR, we have had ongoing work over the past several years aimed at developing novel techniques and technologies for CTRs. This thesis describes the contributions made in this context, focusing primarily on topics such as modeling, sensorization, and control of CTRs. Prior to this work, one of the main challenges in CTRs was to develop a kinematic model that achieves a balance between the numerical accuracy and computational efficiency for surgical applications. In this thesis, a fast kinematic model of CTRs is proposed, which can be solved at a comparatively fast rate (0.2 ms) with minimal loss of accuracy (0.1 mm) for a 3-tube CTR. A Jacobian matrix is derived based on this model, leading to the development of a real-time trajectory tracking controller for CTRs. For tissue-robot interactions, a force-rejection controller is proposed for position control of CTRs under time-varying force disturbances. In contrast to rigid-link robots, instability of position control could be caused by non-unique solutions to the forward kinematics of CTRs. This phenomenon is modeled and analyzed, resulting in design criteria that can ensure kinematic stability of a CTR in its entire workspace. Force sensing is another major difficulty for CTRs. To address this issue, commercial force/torque sensors (Nano43, ATI Industrial Automation, United States) are integrated into one of our CTR prototypes. These force/torque sensors are replaced by Fiber-Bragg Grating (FBG) sensors that are helically-wrapped and embedded in CTRs. A strain-force calculation algorithm is proposed, to convert the reflected wavelength of FBGs into force measurements with 0.1 N force resolution at 100 Hz sampling rate. In addition, this thesis reports on our innovations in prototyping drive units for CTRs. Three designs of CTR prototypes are proposed, the

latest one being significantly more compact and cost efficient in comparison with most designs in the literature. All of these contributions have brought this technology a few steps closer to being used in operating rooms. Some of the techniques and technologies mentioned above are not merely limited to CTRs, but are also suitable for problems arising in other types of surgical robots, for example, for sensorizing da Vinci surgical instruments for force sensing (see Appendix A).

KEYWORDS: Concentric-Tube Robots, Continuum Robotics, Kinematic Modeling, Kinematic Instability, Force and Shape Sensing, Torsion Sensing, Fiber-Bragg Grating Sensors, Helically-Wrapped FBG Sensors, Position Control of Continuum Robots, Force Control of Continuum Robots, Swiss-Type Micro Engraving. Dedicated to: Yang (Paula) Cheng

Statement of Co-Authorship

IEEE copyrighted material in this thesis is used with the permission of the IEEE. The IEEE requires the following statement to be included as part of this permission: The IEEE does not endorse any of Western University's products or services. Internal or personal use of this material is permitted. If interested in reprinting or republishing IEEE copyrighted material for advertising or promotional purposes or for creating new collective works for resale or redistribution, please go to IEEE website to learn how to obtain a License from RightsLink.

Some material in the thesis has been published in peer-reviewed journal and conference papers, or is under preparation for publication. My colleagues, Aaron Yurkewich, Dr. Ali Asadian, Anish Naidu, Abelardo Escoto, Chris Ward and Farokh Atashzar have also served as co-authors in some of these papers.

Chapter 3: A Fast Torsionally Compliant Kinematic Model of Concentric-Tube Robots

- R. Xu and R.V. Patel, A fast torsionally compliant kinematic model of concentrictube robots, in 2012 Annual International Conference of the IEEE Engineering in Medicine and Biology Society. IEEE, 2012, pp. 904-907.
- Ran Xu Proposed this project; derived the kinematic model; designed the experimental setup; evaluated the proposed model in experiments.

Chapter 4: Position Control of Concentric-Tube Continuum Robots using a Modified Jacobian Based Approach.

- R. Xu, A. Asadian, A.S. Naidu, and R.V. Patel, Position control of concentric-tube continuum robots using a modified Jacobian-based approach, in Proc. IEEE Int. Conf. Robot. Autom. IEEE, 2013, pp. 5813-5818.
- Ran Xu Proposed this project; derived the kinematic model and its Jacobian; implemented the model and controller in MATLAB code; designed and heat treated the tubes used in the experiments; helped with the drive unit design; performed experiments and analyzed the results; prepared the majority of the first draft.

- Ali Asadian Developed the real-time control software; helped with running experiments; drafted the introduction section; reviewed and edited the manuscript.
- Anish Naidu Designed the drive unit; machined and assembled the robotic setup; machined the molds for tube shaping.

Chapter 5: Kinematic Instability in Concentric-Tube Robots: Modeling and Analysis

- R. Xu, S.F. Atashzar, and R.V. Patel, Kinematic instability in concentric-tube robots: modeling and analysis, in Proc. IEEE RAS/EMBS Int. Conf. on Biomed. Rob. Biomech. IEEE, 2014, pp. 163-168.
- Ran Xu Proposed this project; modeled the kinematic instability of CTRs; derived the stability conditions and design criteria for CTRs; performed the simulations and analyzed the results; prepared the first draft.
- Farokh Atashzar Contributed ideas in several steps of the mathematical derivation; helped with preparing the manuscript.

Chapter 6: Real-time Trajectory Tracking for Externally Loaded Concentric-tube Robots

- R. Xu, A. Asadian, S.F. Atashzar, and R.V. Patel, Real-time trajectory tracking for externally loaded concentric-tube robots, in Proc. IEEE Int. Conf. Robot. Autom., 2014, pp. 4374-4379.
- Ran Xu Proposed this project; derived the loaded kinematic model; integrated force/torque sensors into the CTRs; performed the sensor calibration; performed the simulations, experiments and analyzed the results; helped with completing the force-rejection controller; helped with preparing the manuscript.
- Ali Asadian Prepared the first draft of the manuscript; helped with running experiments; reviewed and edited the final manuscript.
- Farokh Atashzar developed the first version of the force-rejection controller; helped with sensor calibration and experiments; helped with preparing the manuscript.

Chapter 7: FBG Sensing in Continuum Robots

- R. Xu, A. Yurkewich, and R.V. Patel, Curvature, torsion, and force sensing in continuum robots using helically wrapped fbg sensors, IEEE Robotics and Automation Letters, vol. 1, no. 2, pp. 1052-1059, 2016.
- R. Xu, A. Yurkewich, and R.V. Patel, Shape sensing for torsionally compliant concentric tube robots, in SPIE BiOS. International Society for Optics and Photonics, 2016, pp. 97 020V-97 020V.
- Ran Xu Proposed the design of helically-wrapped FBG sensors; derived the strainforce model; installed the sensors manually; performed experiments and analyzed the results; prepared the first draft; helped with the development of the Swiss-type micro engraver.
- Aaron Yurkewich Developed the Swiss-type micro engraver; installed the sensors manually; helped with building the experimental setup; helped with most of the experiments; helped with preparing the manuscript.

Acknowledgment

First and foremost, I would like to express my sincere gratitude to my supervisor, Dr. Rajni V. Patel, for his support, guidance and encouragement over the past few years. I have been so fortune to pursue my Ph.D. at CSTAR, a one-of-a-kind research lab equipped with state-of-the-art facilities and equipment, which was established by the remarkable efforts of Dr. Patel. Since my first day here, he has treated me with incredible patience to allow me to gradually grow into a strong researcher and engineer. He has provided constant support throughout all of my research. There are countless times that he has sat down to discuss the future directions of my work, brainstormed creative solutions, and even helped me polish the grammar in my writing. He has been great at achieving the perfect balance between giving me freedom and supervision, which has allowed me to pursue my own interests and develop unique strengths, while still providing guidance. I could not have asked for a better supervisor.

It has been a blessing for me to receive support from so many truly kind and talented people during my Ph.D. I am grateful to my previous supervisor, Dr. Max Meng, who introduced me to Dr. Patel and has continuously shared his wisdom and given help whenever I asked. My thanks also go out to the members of our research group in CSTAR: Dr. Mahdi Azizian, Dr. Ali Asadian, Dr. Iman Khalaji, Chris Ward, Abelardo Escoto, Dr. Farokh Atashzar, as well as others who have been associated with work at CSTAR, namely Chris Vandelaar, Anish Naidu, Wesley Johnson, Tom Grainger, Marko Mikic, and Scott Good. It has been a great pleasure to work with them and I really appreciate all the help they have provided. I would like to extend my special thanks to my dear friends, Aaron Yurkewich and Kaspar Shahzada. They helped me move forward and find my path during the most difficult time of my Ph.D., which I will always remember as I proceed in my future career and personal life.

I am deeply indebted to my family for their incredible patience and support. My parents Ying Zhu, and Lijiang Xu, taught me by example, built my confidence, and motivated me to become the best I could be. They never stopped believing in me and have always been there to offer help whenever I needed it. Finally, I want to express my sincere gratitude to my wife, the lovely Yang (Paula) Cheng, the one I have not stopped thinking about since I first saw her. She has been a source of love and caring, keeping me focussed on what is important, yet reminding me of the beautiful things in life. It is impossible to properly acknowledge in words what she means to me and for everything that she has given me. A new chapter has started and I cannot wait to make it the best for us. This thesis is dedicated to her with the utmost gratitude and love.

Sources of Funding

This research was supported in part by the Natural Sciences and Engineering Research Council (NSERC) of Canada under Grant RGPIN1345, in part by an NSERC Collaborative Research and Training Experience (CREATE) program Grant #371322-2009 on Computer-Assisted Medical Interventions (CAMI), and in part by the Canada Research Chairs Program and a Canada Foundation for Innovation grant. All of these grants were awarded to Dr. R.V. Patel. The work of R. Xu was supported by a postgraduate scholarship from the China Scholarship Council (CSC) of the People's Republic of China.

Table of Contents

Al	bstrac	et	ii
St	ateme	ent of Co-Authorship	v
A	cknow	vledgment	viii
So	ources	s of Funding	x
Li	st of [Tables	xvii
Li	st of l	Figures	xix
No	omeno	clature	XXX
1	Intr	oduction	1
	1.1	A Brief Overview of Concentric-Tube Robots	1
	1.2	Modeling, Sensing and Control of CTRs	3
		1.2.1 Modeling	5
		1.2.2 Sensing	10
		1.2.3 Control	13
	1.3	Remarks	17

	1.4	Thesis Outline and Contributions	19
	Bibl	iography	22
2	Cus	tom Built Experimental Setups	30
	2.1	Tube Shaping Setup	31
	2.2	Tube Engraving Setup	33
	2.3	A Custom-built CTR for Needle Insertion Applications	36
	2.4	A Custom-Built CTR for Teleoperated Manipulation	38
	2.5	A Low-Cost and Compact CTR Design	41
	Bibl	iography	44
3	A Fa	ast Torsionally Compliant Kinematic Model of Concentric-Tube Robots	46
	3.1	Introduction	47
	3.2	Kinematic Model	49
		3.2.1 Cosserat Rod	49
		3.2.2 Torsionally Compliant Model	51
		3.2.3 Fast Torsionally Compliant Model	52
	3.3	Experiments	54
	3.4	Conclusion	57
	Bibl	iography	57
4		tion Control of Concentric-Tube Continuum Robots using a Modified bian-Based Approach	60
	4.1	Introduction and Prior Work	61
	4.2	A Modified Jacobian-Based Strategy For Position	64

		4.2.1	A Fast Torsionally Compliant Model	64
		4.2.2	Jacobian Derivation for the Concentric-Tube Robots	66
		4.2.3	The Multi-Step Jacobian Method	69
	4.3	Simula	ation Study	71
	4.4	Experi	mental Validation	75
		4.4.1	Setup Description	75
		4.4.2	Experiments and Results	76
	4.5	Conclu	ision	79
	Bibl	iography	y	79
5	Kin	ematic I	nstability in Concentric-Tube Robots: Modeling and Analysis	82
	5.1	Introdu	action	83
	5.2	Kinem	atic Stability Condition for Two Concentric Tubes	86
		5.2.1	Kinematic Model for Concentric-Tube Robots	87
		5.2.2	Kinematic Stability Condition for Two-Tube Robots without Straight Parts	88
		5.2.3	Kinematic Stability Condition for Two-Tube Robots including Straight Parts	
	5.3	Kinem	atic Stability Condition for Three or More Concentric Tubes	94
		5.3.1	Kinematic Stability Condition for Three-Tube Robots without Straight Parts	94
		5.3.2	Kinematic Stability Condition for Three-Tube Robots including Straight Parts	99
		5.3.3	Extension to Multiple Tubes	01
	5.4	Simula	tion Validation	02
	5.5	Conclu	usions	06

	Bibl	iograph	y
6	Rea	l-time T	rajectory Tracking for Externally-Loaded Concentric-Tube Robots109
	6.1	Introd	uction
	6.2	Forwa	rd Kinematics and Jacobian in the Presence of an External Point Load 113
		6.2.1	Fast Torsionally Compliant Model for the Loaded Robot 113
		6.2.2	A Modified Jacobian for the Loaded Robot
	6.3	The E	ffect of External Loading and a Dual-Layer Control Approach 118
		6.3.1	The Inner Control Loop
		6.3.2	The Outer Control Loop
	6.4	Simula	ation Study: Trajectory Tracking in the Presence of a Tip Load 122
	6.5	Experi	mental Study
		6.5.1	Setup Description
		6.5.2	Experimental Results
	Bibl	iograph	y
7	FBC	5 Sensir	ng in Continuum Robots 132
	7.1	Introd	uction
	7.2	Desig	n of Helically-Wrapped FBG Sensor
		7.2.1	Selection of FBG Sensors
		7.2.2	Curvature-Strain Model for Helical FBG sensors
		7.2.3	FBG Sensors under Uneven Strain Distribution
		7.2.4	Force-Curvature Model of a Single Super-Elastic Tube
		7.2.5	Strain-Force Calculation
	7.3	Engra	ving Helical Grooves on Super-elastic Nitinol Tubes

	7.4	Experim	mental Validation on a Single Tube	
		7.4.1	Validation on Straight Tubes	
		7.4.2	Validation on Curved Continuum Robots	
	7.5	Design	of a Sensorized Concentric-Tube Robot	
		7.5.1	Design and Fabrication of a Sensorized Tube Assembly	
		7.5.2	Experimental Validation on a Concentric-Tube Robot	
		7.5.3	Results and Discussion	
	7.6	3D For	rce Sensing in Pre-curved Continuum Robots	
		7.6.1	An Alternative Method for Strain-Force Calculation	
		7.6.2	Multi-Plane 2D Force Sensing	
		7.6.3	Robot Design for Optimal 3D Force Sensing	
	7.7	Conclu	sions	
	Bibli	ography		
8	Con	clusion	and Future Work 186	
	8.1	Conclu	ding Remarks	
	8.2	Sugges	ted Future Work	
		8.2.1	Modeling and Control	
		8.2.2	Technological Improvements	
		8.2.3	Clinical Applications	
	Bibli	ography		

Appendices

A	Sens	orizatio	on of a Surgical Robotic Instrument for Force Sensing	197
	A.1	Introdu	uction	. 198
	A.2	Design	of the Sensorized Surgical Instrument	. 199
		A.2.1	Two Cross-Section Design	. 200
		A.2.2	Force-Strain Model	. 201
	A.3	Experi	mental Validation of the Sensorized Surgical Instrument	. 203
		A.3.1	Experimental Setup	. 204
		A.3.2	Calibration	. 204
		A.3.3	Evaluation	. 205
	A.4	Experi	mental Evaluation in Surgical Tasks	. 207
		A.4.1	Surgical Task Setup	. 207
		A.4.2	Evaluation	. 208
	A.5	A Met	hod for Installing FBG Sensors inside Surgical Robotic Instruments	. 211
		A.5.1	Materials and Methods	. 213
		A.5.2	Results	. 214
	A.6	Conclu	ision	. 216
	Bibli	iography	y	. 217
В	Mat	hematic	cal Derivations for Chapter 5	222

List of Tables

3.1	Nomenclature
3.2	Parameters of Four Tube Pairs
3.3	Position Errors of Four Tube Pairs (mm)
4.1	Nomenclature
4.2	Parameters of the Tubes for Simulations
5.1	Nomenclature
5.2	Parameters of Concentric-Tube Robots
6.1	Nomenclature I
6.2	Nomenclature II
6.3	Parameters of the Two-Tube Robot
7.1	Nomenclature I
7.2	Nomenclature II
7.3	Parameters of the Helically-Wrapped FBG Sensors
7.4	Errors in Curvature and Torsion Measurements
7.5	Errors in Force Measurements
7.6	Parameters of the Tubes for Simulation Studies

A.1	Calibrated Parameters								•		•							•	•	•		•		•	•				•	20	6
-----	-----------------------	--	--	--	--	--	--	--	---	--	---	--	--	--	--	--	--	---	---	---	--	---	--	---	---	--	--	--	---	----	---

List of Figures

1.1 (a) Demonstration of the concept of a CTR [1] (© 2010 IEEE). (b) A 3-tube CTR [2] (© 2009 IEEE). (c) A CTR with an micro-grasper attached at the tip [5](© 2012 IEEE).

2

3

4

- 1.2 Beating-heart intracardiac steerable needle surgery. (a) Steerable needle enters internal jugular vein in the neck and navigates through the vasculature into the right atrium. (b) Right atrium view of a 5 DOF manipulator portion of a needle. Arrows mark the patent foramen ovale (PFO) channel allowing abnormal blood flow from the right to left atrium. Surgery is to seal this channel. (c) Steerable needle robot consisting of three telescoping sections. (d) Magnified view of a metal-MEMS tissue approximation device delivered through the lumen of the steerable needle. (e) Teleoperated robot control inside the beating heart is guided by 3D ultrasound. (f) Postmortem view of sealed porcine PFO channel [17] (© 2012 IEEE). . . .
- 1.3 Demonstration of a CTR extending the tool channel of a brochoscope. (a, b) A robot that combines bronchoscope, CTR, and bevel steered needle. (c) steps in deployment involve: (1) deploying the bronchoscope (2) deploying the CTR to the bronchial wall, puncturing through it, and entering the parenchyma, and (3) steering the bevel-tip needle to the target under closed-loop control [18] (© 2015 IEEE). (d, e) Simulation of a single concentric tube robot reaching two pre-specified clinical targets in the bronchial tubes of a human lung [5] (© 2012 IEEE).

1.4	Robot-assisted ICH evacuation prototype setup. (a) The robot is positioned and held in place with a passive articulated arm. The aspirator is attached to the aspiration cannula that enters the brain through a trajectory guide attached to the skull. A reference frame is rigidly attached to the robot for optical tracking. (b) The active cannula deployed to the clot and the aspira- tion tube used to debulk the clot. (c) Blood clot is shown prior to beginning the experiment, (d) progress midway through the removal experiment, and (e) the same area after aspiration [13] (© 2013 IEEE)	4
1.5	An illustration of the robotic system for HoLEP. The surgeon is able to po- sition and angle the endoscope while simultaneously controlling two CTRs that extend from its tip. (a, b) The CAD design of the robotic surgical setup. (c) Distal end of the actual CTRs and endoscope [15] (© 2014 IEEE)	5
1.6	Effect of torsional twisting when two curved tubes are combined. Tube coordinate frames are denoted by $F_i(s)$. The relative z-axis twist angle between frames $\alpha(s)$ varies from a maximum $\alpha(0)$ at the base to a minimum $\alpha(L)$ at the tip. The central angles β_i are proportional to the precurvature and to the tube length L [1] (© 2010 IEEE).	7
1.7	Snapping analysis through video tip tracking [32]. Green marks (left) show the traced distal end of an unstable tube pair that snaps at a certain point, and red marks (right) show the traced distal end of a stable tube pair (© 2014 IEEE).	9
1.8	Contour plots of the energy landscape as the angular difference between the tube bases is increased. Angular difference between the base inputs of the two tubes is listed in the upper right corner of each plot. For small angular differences, there is only one global minimum. As the angular difference approaches 180°, two appear. Beyond 180°, the new minimum becomes the global minimum, and eventually the only minimum [2] (© 2009 IEEE).	9
1.9	Continuum robot inserted inside a porcine heart. (a) Experimental set up; (b) 3D ultrasound image showing both the left atrium and the curved robot [39] (© 2012 IEEE).	12
1.10	Schematic of wire braided polymer tube with surface mounted optical fibers [44] (© 2014 IEEE).	

- 1.13 (a) Simulation of a CTR in a neurosurgery environment executing the motion plan that calculated from the proposed sampling-based approach based on the Rapidly-Exploring Roadmap. The robot is inserted through the nostril and guided toward the pituitary gland (highlighted in green) in the skull base while avoiding skin, bone, blood vessels, and healthy brain tissue. (b, c, d, e) Simulation of a CTR in four different spherical obstacle environment [54] (© 2011 IEEE).
- 1.14 (a) Block diagram of the stiffness controller. (b) Continuum robot represented as a space curve (solid line). W is world coordinate frame, while B, P, T, and T are robot body frames. T and T are tip frames without and with the application of tip wrench F, respectively. Coordinate transformations are denoted by g_{bt}, g_{bt}, and g_{tt}. (c) Robot in contact with environment. The stiffness controller implements a virtual linear spring at the robots tip. Desired actuator positions are such that when robot is deflected from unloaded tip configuration T to configuration T, the desired tip spring force is generated, and the desired tip orientation is achieved [23] (© 2011 IEEE). 18

2.2	 (a) A commercially available Swiss-type CNC lathe, Citizen-Cincom K16 (Marubeni Citizen-Cincom Inc., United States). (b) A view of the machine's full size. (c, d) The CAD design of our desktop micro-engraver (e) The actual setup of the developed desktop micro-engraver. The machining process can be monitored using a microscope through the viewing window on the support block. 	34
2.3	(a, b) The CAD design of a 6DOF CTR drive unit using high precision linear and rotary stages. The parts in grey are commercial products and the rest of the parts are custom built. (c) The actual robotic setup using two linear and two rotary stages.	36
2.4	(a) The CAD design of the CTR drive unit for teleoperated operations. The components in grey are commercial products and the ones in purple are custom designed parts. (b) The CAD model except for the linear stages (c, d) Side view and front view of the actual 6 DOF robotic setup controlled by a haptic device (Touch X, Geomagic, United States)	39
2.5	 (a, b) A side-by-side view of the actual and virtual robot, which was programmed using the Virtual Reality Modeling Language (VRML) in Simulink. (c) The developed CTR prototype in a positioning task controlled by a haptic device. (d) The developed CTR prototype in a surface pattern tracking task. 	40
2.6	CAD design of a low-cost and compact CTR drive unit. (a) View of the main components of the proposed drive unit. (b) View of the overall robot	42
2.7	Assembly of the third prototype of CTR drive unit (except for the outer case)	43
3.1	Cosserat rod	49
3.2	Body frames of tube i and the 1st.	50
3.3	Experimental setup for evaluating kinematic model	56
4.1	(a) Cosserat beam (b) cross section of a concentric-tube robot showing co- ordinate frames associated with the 1^{st} and the i^{th} tubes	64
4.2	Links and sub-links of a concentric-tube robot.	67

Function approximation using a multi-step approach
The relationship between boundary conditions: $u_{iz}(L)$ with respect to $u_{iz}(0)$ as a function of the rotation angle in a two-tube robot
Trajectory tracking using (a) two-tube (blue:outer tube, green: inner tube) (b) three-tube concentric-tube robots (blue:outer tube, green: middle tube, red: inner tube)
Trajectory tracking using conventional Jacobian and modified multi-step Jacobian approach in the two-tube robot
Our concentric-tube robot setup
Desired and experimental trajectories in XY, XZ, and YZ planes (linear trajectory, final tip position = $[41.59 \ 37.51 \ -0.31]^T$ mm)
Desired and experimental trajectories in XY, XZ, and YZ planes (sinusoidal motion, final tip position = $[-0.02 \ 18.76 \ -1.12]^T \ \text{mm}$)
Desired and experimental trajectories in 3D (final tip position = $[2.329 \ 47.79 \ 19.65]^T$ mm, final desired position = $[0 \ 50 \ 20]^T$ mm)
Demonstration of the possible multiple solutions for two tubes with a straight section. The blue and red arrows represent the rotational angles of the two tubes at that location
Simulation results for a two-tube robot with straight sections. Note that a large number of different l_1 were tested in the program, only a few of them were plotted here. (a) position of the robot tip in X direction; (b) magnified view of (a) around the snapping area; (c) position of the robot tip in Y direction; (d) magnified view of (c) around the snapping area. X and Y axes are defined in Fig. 5.1
Tip position (in Y direction) of a three-tube robot without straight parts. Note that a large number of different \hat{u}_{123} were tested in program, only a few of them were plotted here

5.4	Tip position (in Y direction) of a three-tube robot with straight parts. Note that a large number of different l_1 were tested in the program, only a few of them were plotted here
6.1	(a) A loaded concentric-tube robot consisting of q links or tubes each of which is composed of p sub-links [3]; (b) the robot's cross section showing coordinate frames associated with the 1 st and the j th tubes [9]
6.2	Control block diagram for the proposed tracking algorithm
6.3	Simulation of the tip position $X = [X_x \ X_y \ X_z]^T$ tracking using four control strategies: (a) unloaded Jacobian, (b) loaded Jacobian J , (c) loaded Jacobian J plus $\dot{\Delta}_{total}$, and (d) the dual-layer approach
6.4	Simulation of the tip deflection: comparison between the total deflection and the Jacobian-related component
6.5	A view of our concentric-tube robotic system
6.6	Model validation: comparison between measured and predicted tip posi- tions using loaded and unloaded schemes
6.7	Regulation using the inverse unloaded Jacobian approach [3]
6.8	Regulation using the proposed dual-layer control approach
6.9	Estimated tip force components during trajectory tracking using the proposed dual-layer control approach $F_{ext} = [F_x \ F_y \ F_z]^T$
6.10	Tip tracking error using the proposed dual-layer control approach 128
7.1	Demonstration of the curvature-strain model for helical-wrapped FBG sen- sors. κ_{xy} is the curvature vector commonly used for representing the bend- ing radius and the direction of bending. u_{xy} is the curvature vector used for deriving the curvature-strain model presented in this work. Note that $ u_{xy} = \kappa_{xy} = R_b138$
7.2	(a) The dashed lines are the strain values calculated from the previous model in subsection 7.2.2; the solid lines are from the new model; (b) the time-varing force that applied at the tip of the robot

7.3	Signal flow digram for Strain-Force Calculation. The boundary conditions in red blocks are the inputs of the model chain. One of the outputs of this calculation is the tip force measurement (the blue block)
7.4	(a) The CAD model of the engraving system. (b) A magnified view of the support block. (c) The 3D-printed support block. (d) The actual customized engraving system
7.5	(a) Experimental setup for straight-tube torsion validation. (b) Magnified view of fiber embedded in grooved tube. (c) Experimental setup for pre- curved tube analyses. The robot base denoted (X_r, Y_r) , and is rotated -45° with respect to the world frame (X_w, Y_w) . (d) Magnified view of the pre- curved tube with helical grooves
7.6	The torsion measurements (blue) when the motorized stage rotates in a clockwise direction (a) and a counter-clockwise direction (b). The red lines are the linear best-fit to the measurement data
7.7	 (a) Demonstration of the effects of increased bending on the distortion of the FBG sensor output signal. (b) An example of a reflected spectrum with peak distortion. (c) Comparison between the noise from a 1 mm FBG (blue line) and a 5 mm FBG (red line).
7.8	The solid lines are the wavelengths reflected from three FBG sensors that are helically-embedded in a curved tube. The wavelength output of each FBG was biased at the beginning of the test. The dashed lines are the corre- sponding values from the force-curvature-strain model using the calibrated parameters listed in Table 7.3
7.9	The solid lines represent the measured curvature and torsion values using helically-wrapped FBG sensors. The dashed lines are the theoretical values calculated from the model described in subsection 7.2.4. (a) plots the measured and theoretical values of $(u_x - \hat{u}_x)$ under a series of loading; (b) and (c) display $(u_y - \hat{u}_y)$ and $(u_z - \hat{u}_z)$, respectively

- 7.11 Demonstration of the resolution in bending curvature and torsion measurements. The pre-curved Nitinol tube was positioned at 45° relative to gravity and weights of 120 g, 130 g, 135 g, 137 g, and 138 g were suspended at the tip in (a), (b) and (c). Weights of 70 g, 100 g, 120 g, and 137 g were used for (d), (e), and (f). The red and blue lines show the measured bending curvatures, u_x , $1/R_b$. The green lines show the measured torsion, τ . The yellow line denotes the mean value at each incremental load over 5 seconds. 159
- 7.13 Two set of weights were put on the tube tip to test the resolution of the proposed force sensing technolgoy. In (a), the weights are 120g, 130g, 135g, 137g, 138g. In (b), the weights are 70g, 80g, 85g, 87g, 88g. The blue lines are the measured forces using FBG sensors and the red lines are the theoretical gravity values.
- 7.14 Demonstration of the design concept of a sensorized concentric-tube robot. 162
- 7.16 Illustration of the sensitivity of the sensorized CTR in force sensing 164

7.20	Comparision of the force values measured using Nano17 (red) and the sensorized CTR (blue).	. 167
7.21	Signal flow diagram for two strain-force calculation methods. (a) Previous strain-force calculation method. (b) Alternative Strain-force calculation method. The red blocks represent the inputs of these calculations and the blue ones are outputs.	. 170
7.22	Demonstration of the performances of the two proposed strain-force calcu- lation methods with and without added noise. (a) The signal flow of the simulations. (b) The strain values of the FBG sensors when the robot is under load. (c) Force measurements using these strain-force calculation methods developed	. 172
7.23	Lateral and axial forces for straight robotic tools (a) and pre-curved robotic tools (b)	. 173
7.24	Three examples of unobservable forces. In these cases, the force vector cannot be decoupled into two elements by using strain sensors on a single cross-section.	. 175
7.25	Simulation studies for 3D force sensing, using curvature measurements of two sensorized cross-sections. (a) Simulation signal flow. (b, c, d) Simulation results when the noise level is zero. (e, f, g) Simulation results when the noise level is around 2% of the curvature signals. (d, g) Condition numbers of J_{CX} in Eq. (7.46), which is the update strategy for the strain-force calculation.	. 177
7.26	Pre-curved continuum robots with multiple sensorized cross-sections for 2D or 3D force sensing. The red marks represent the sensorized cross-sections.	. 178
7.27	Demonstration of the relation between condition number and noise ampli- fication in curvature-force calculations. (a) The condition number is 2.6; (b) the condition number is 5.8	. 179

7.28	Condition number map for designing the shape of a sensorized continuum robot; (a) two sensorized cross-sections for measuring 2D unobservable forces; (b) two sensorized cross-sections for 3D force sensing; (c, d, e) three sensorized cross-sections for measuring 2D unobservable forces 180
8.1	Conceptual design of an electric tube shaping setup
8.2	(a) Full size virtual operating room developed in Unity (purchased from Unity Asset Store).(b) Magnified view of the virtual CTR developed by our group.194
8.3	Needle-tipped catheter for intramyocardial injection
A.1	(a) A 3D view of the sensorized da Vinci instrument (b) A cross-sectional view of the sensorized tool with two FBG sensors located with an angular difference of γ
A.2	A side view of the sensorized da Vinci Instrument
A.3	Illustration of the 3D printed installation guide for FBG alignment 203
A.4	The experimental setup for calibrating and evaluating the sensorized instru- ment
A.5	(a) Force values measured from the FBG and Nano17 sensors in response to a series of weights applied to the sensorized instrument (b) Error histogram of the FBG force measurement
A.6	Demonstration of the performance of the two cross-section FBG sensing under different loading disturbances. (a) F_X values measured from FBG and Nano17 sensors under a varying axial loading (b) F_X values measured from FBG and Nano17 sensors under varying force coupling about the Y axis
A.7	Demonstration of custom made testbeds for three surgical tasks. (a) One- handed suture knot tightening testbed (b) Hem-O-Lok tightening testbed (c) Tumor localization by palpation testbed

A.8	Illustration of the definition of the mean peak force, representing the ap-
	plied tension to the suture. (b) Histogram of the force error measured
	from a group of six subjects performing one-handed suturing tasks with
	and without VFF.
A.9	The force profiles of one novice (a) and one expert surgeon (b) when per-
	forming Hem-O-Lock tightening, measured by the FBG sensors
A.10	Sensorized instrument mounted on a da Vinci robot
A.11	(a) Disassembled da Vinci instrument; (b) paper template; (c) folded paper
	template (d) rear view of the sensorized instrument after reassembly 213
A.12	Experimental setup for evaluating the performane of force sensing 215
A.13	Comparision of the force measurements from the force/torque sensor (dot)
	and the sensorized instrument (solid)
A.14	Comparision of the theoretical force values (red) and the measured values
	from the sensorized instrument (blue)

Nomenclature

2D	2 Dimensional
3D	3 Dimensional
AR	Augmented Reality
ABS	Acrylonitrile Butadiene Styrene
CAD	Computer-Aided Design
CAMI	Computer-Assisted Medical Intervention
CPU	Central Processor Unit
CREATE	Collaborative Research and Training Experience
CSTAR	Canadian Surgical Technologies and Advanced Robotics
CT	Computed Tomography
CTR	Concentric-Tube Robot
CNC	Computer Numerical Control
DOF	Degrees of Freedom
EDM	Electrical Discharge Machining
EM	Electromagnetic
FBG	Fiber-Bragg Grating
FEM	Finite Element Model
HoLEP	Holmium Laser Enucleation of the Prostate
ICH	IntraCerebral Hemorrhage
IPM	Inches Per Minute
IPT	Inches Per Tooth
MRI	Magnetic Resonance Imaging
NSERC	Natural Sciences and Engineering Research Council
OCT	Optical Coherence Tomography

ODE	Ordinary Differential Equations
-----	---------------------------------

RAM Random Access Memory

RF Radio Frequency

- RMS Root Mean Square
- RPM Revolutions Per Minute
- SFM Surface Feet per Minute
- UDP User Datagram Protocol
- VFF Visual Force Feedback
- VR Virtual Reality
- VRML Virtual Reality Modeling Language

Chapter 1

Introduction

1.1 A Brief Overview of Concentric-Tube Robots

Concentric-tube robots (CTRs) consist of a set of pre-curved elastic tubes with incremental differences in diameter, as shown in Fig. 1.1. By translating and rotating one tube with respect to the other(s) the shape of the robot as well as the position and orientation of its tip can be accurately controlled. Because of this unique design, the robot is able to generate complex 3D curvatures to navigate through winding lumens and steer inside soft tissue. This feature makes CTRs suitable for minimally and non-invasive surgery and therapy [1–3]. The concept of extending curved needles from outer shafts has been implemented in several hand-held medical products to enlarge the surgical workspace and provide better directional control (e.g. StarBurst[®] and Osteo-Rx[®]). However, this idea was not extensively studied until a series of modeling and control algorithms were developed from a robotics perspective [1, 2, 4]. Using these techniques the robot is able to provide clinicians with high dexterity in extremely constrained environments, allowing them to accomplish demanding surgical tasks. Compared to the traditional tools used in minimally invasive surgery such as needles and catheters, CTRs can achieve significantly better balance between flexibility and rigidity in certain applications. Through proper robot design

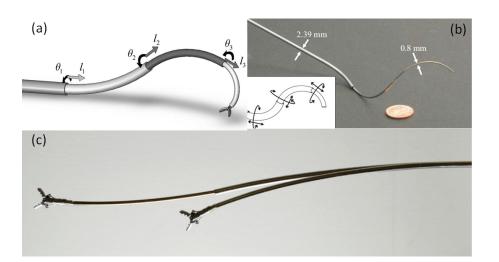


Figure 1.1: (a) Demonstration of the concept of a CTR [1] (\bigcirc 2010 IEEE). (b) A 3-tube CTR [2] (\bigcirc 2009 IEEE). (c) A CTR with an micro-grasper attached at the tip [5](\bigcirc 2012 IEEE).

and control strategies, the robot body could potentially be made compliant while exerting sufficient force at the robot's tip. Further functionality can be offered by installing miniature end-effectors such as graspers and specialized tools at the tip of the robot [6–8], and a wrist can be added close to the distal end to regenerate human-like manipulation [9]. These advantages have motivated researchers to evaluate the effectiveness of CTRs in performing surgical procedures such as cardiac surgery [7, 8, 10–12], brain surgery [6, 13], bronchoscopic interventions [14], and trans-urethral surgery [15, 16].

Fig. 1.2 demonstrates the application of a CTR in beating heart robotic surgery [7, 8, 10– 12]. The robot is inserted into the vascular system through a small incision in the neck and navigated to the right atrium of the heart. A tissue approximation device carried by the CTR is deployed at the foramen ovale channel to maintain a permanent seal. The feasibility and performance of the proposed robotic system was evaluated in trials involving porcine models under 3D ultrasound guidance. In Fig. 1.3, endoscopic-CTR systems are developed to access the peripheral regions in the lung from the inside of bronchi and bronchioles. In these designs, CTRs are extended from the tool channel of the bronchoscope, which reduces the incision size and the risks of lung collapse. A new approach to improve

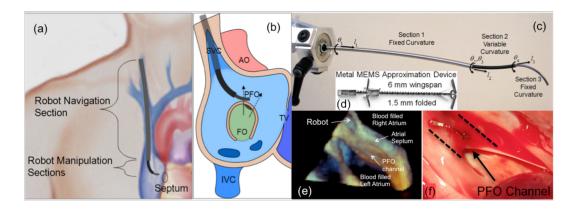


Figure 1.2: Beating-heart intracardiac steerable needle surgery. (a) Steerable needle enters internal jugular vein in the neck and navigates through the vasculature into the right atrium. (b) Right atrium view of a 5 DOF manipulator portion of a needle. Arrows mark the patent foramen ovale (PFO) channel allowing abnormal blood flow from the right to left atrium. Surgery is to seal this channel. (c) Steerable needle robot consisting of three telescoping sections. (d) Magnified view of a metal-MEMS tissue approximation device delivered through the lumen of the steerable needle. (e) Teleoperated robot control inside the beating heart is guided by 3D ultrasound. (f) Postmortem view of sealed porcine PFO channel [17] (© 2012 IEEE).

intracerebral hemorrhage management is proposed by designing and implementing an interchangeable 2-tube CTR. As shown in Fig. 1.4, it is possible to remove around 90% of the hemorrhage through a needle-size incision similar to a standard brain biopsy. A bi-manual robotic system was developed in [15], as shown in Fig. 1.5, to facilitate prostate surgeries, specifically, a procedure called Holmium Laser Enucleation of the prostate (HoLEP). Two CTR arms were used to maximize the dexterity of the endoscopic tools under the constraint of urethral channels.

1.2 Modeling, Sensing and Control of CTRs

This chapter reviews recent developments in concentric-tube robotics by researchers other than our group, focusing on modeling methodologies, sensing modalities and control architectures. The advantages and drawbacks of various methods are discussed in order to guide the selection of application-specific control strategies for current use and the devel-

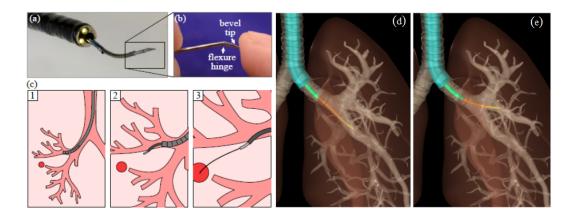


Figure 1.3: Demonstration of a CTR extending the tool channel of a brochoscope. (a, b) A robot that combines bronchoscope, CTR, and bevel steered needle. (c) steps in deployment involve: (1) deploying the bronchoscope (2) deploying the CTR to the bronchial wall, puncturing through it, and entering the parenchyma, and (3) steering the bevel-tip needle to the target under closed-loop control [18] (\car{O} 2015 IEEE). (d, e) Simulation of a single concentric tube robot reaching two pre-specified clinical targets in the bronchial tubes of a human lung [5] (\car{O} 2012 IEEE).

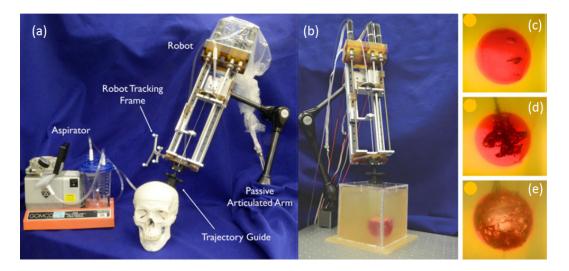


Figure 1.4: Robot-assisted ICH evacuation prototype setup. (a) The robot is positioned and held in place with a passive articulated arm. The aspirator is attached to the aspiration cannula that enters the brain through a trajectory guide attached to the skull. A reference frame is rigidly attached to the robot for optical tracking. (b) The active cannula deployed to the clot and the aspiration tube used to debulk the clot. (c) Blood clot is shown prior to beginning the experiment, (d) progress midway through the removal experiment, and (e) the same area after aspiration [13] (© 2013 IEEE).

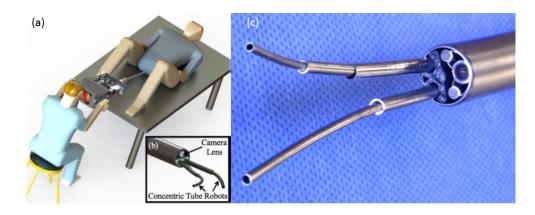


Figure 1.5: An illustration of the robotic system for HoLEP. The surgeon is able to position and angle the endoscope while simultaneously controlling two CTRs that extend from its tip. (a, b) The CAD design of the robotic surgical setup. (c) Distal end of the actual CTRs and endoscope [15] (© 2014 IEEE).

opment of more advanced algorithms to improve the performance of this technology. The contributions by the author are discussed in detail in the rest of this thesis.

1.2.1 Modeling

Understanding the mechanical interaction between pre-curved elastic tubes is essential to designing CTRs and controlling them during surgical interventions. Developing an accurate and practical kinematic model is fundamental to optimizing the robot structure and designing model-based control algorithms.

Simplified Models

In the early days of concentric-tube robotics, several kinematic models were derived by simplifying the mechanical effects of tube interactions. In [19], a kinematic model was derived from purely geometric relations, which constrained tube selection such that the outer tubes could be considered infinitely stiff compared to the inner tubes. A kinematic model was then developed that relaxed this constraint, calculating the resultant bending curvatures of the robot regardless of stiffness ratios between tubes [20]. In both methods,

the position of the distal end was expressed by the multiplication of a series of transformation matrices from the base. This followed the conventional kinematic form of traditional rigid-link robots and resulted in closed-form forward and inverse kinematic models. Through experimentation, it was shown that considering torsion in the kinematic model could increase the model accuracy [2, 21], and a model was proposed that accounted for torsion along the straight portions of the tubes by minimizing an energy function. Although this kinematic model must be evaluated numerically, the differential kinematic model has a closed-form [22]. While more detailed models have been proposed since, these initial models are still used in some applications. As long as the features of the CTR meet certain assumptions these simplified models work effectively with the minimum computational cost and reduce the complexity in designing control schemes. In Intracerebral Hemorrhage Evacuation only one straight and one curved tube is required to access the whole clot [13], and the purely geometric model has been used with sufficient accuracy. In another case, as shown in [23], a model that neglected torsion was used for real-time stiffness control as the bending effect was dominant.

Geometrically Exact Models

Fig. 1.6 demonstrates the torsional twisting along the curved section of a tube pair. It can be seen that the angle difference between the two tube $\alpha(s)$ varies significantly along the shaft of the tubes, which attributes to the final shape of the robot. In order to include this twisting effect into a kinematic model, a geometrically accurate rod theory called Special Cosserat Rod Theory, is used as an optimal tool for modeling the bending, and twisting of concentric-tubes with arbitrary pre-curvatures [1, 4, 24]. Based on this general theory, a torsionally complaint kinematic model was developed and has shown high accuracy in experiments [1, 4, 24]. Considering that CTRs will experience frequent interaction with their environment during surgical interventions, this model was further extended to include the effects of distributed external loading [4, 25]. There are still some assumptions associ-

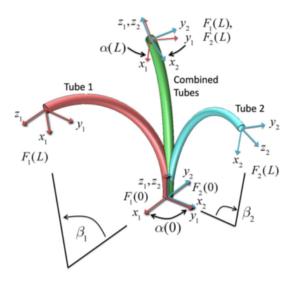


Figure 1.6: Effect of torsional twisting when two curved tubes are combined. Tube coordinate frames are denoted by $F_i(s)$. The relative z-axis twist angle between frames $\alpha(s)$ varies from a maximum $\alpha(0)$ at the base to a minimum $\alpha(L)$ at the tip. The central angles β_i are proportional to the precurvature and to the tube length L [1] (© 2010 IEEE).

ated with this model, such as assumption of shear deformation, elongation, and clearance between the tubes being negligible; however, these assumptions hold in almost all CTR designs. The drawback to this model is its high computational cost, as its kinematic calculations are formulated as a set of differential equations with two-point boundary conditions. Additionally, extra calculations have to be performed since the outputs of this model are tube curvatures, not positions and orientations of the distal tip. To address these challenges, a Fourier series approximation approach was proposed to evaluate the positions and orientations of the robot [1]. This method provides real-time performance but requires pre-computation of a large dataset of position and orientation information over the entire workspace. When the robot is under unknown external loading, it is not practical to precompute all possible kinematic solutions. A framework for calculating the Jacobian and Compliance matrix efficiently was proposed in [26] for general continuum robots allowing a servo rate of 40 Hz for a three-tube CTR. The models mentioned above do not take friction into account, although the amount of friction involved is significant as the tubes move with respect to each other in a telescoping manner. It has been shown through further modelling that including friction into the kinematics will improve the model accuracy [27]. The experimental results presented in this work match the model's output more closely when the friction is assumed to consist of lumped torques concentrated at the robot boundaries as opposed to distributed torques along the body of the robot.

Kinematic Instability

Kinematic instability in CTRs, commonly referred to as the snapping problem [1, 2], is a specific phenomenon that does not exist in conventional rigid-link robots. It occurs when the accumulated torsional energy is too large for the current tube configuration to support. As shown in Fig. 1.7, at the snapping point, the tip of the robot jumps from one equilibrium position (with a higher potential energy) to another (with a lower potential energy). This fast motion of the tip cannot be controlled by the motors connected to the tubes. Therefore, it can be very damaging in a surgical environment, and addressing the issue appropriately is essential. In [2], kinematic instability is described as the bifurcation of the potential energy function. Fig. 1.8 shows an example of analyzing the stability of a 2-tube CTR using energy function, in which, the contours are the potential energy levels of a tube pair, and ψ_i is the tip orientation of the i^{th} tube. It can be seen that for these two tubes under test, in most rotation angles, the energy function only has one local minimum, resulting in an unique tip orientation for the robot. However, when the two tubes are 180° apart, two local minimums exists, which means the tip orientation of the robot becomes non-unique. A stability condition is derived based on this energy method; however, the energy function only considers the torsion in the straight sections of the tubes, which limits this method to tubes with small curvatures. Another way of interpreting the snapping phenomenon is that the solution of the forward kinematic model loses its uniqueness [1]. Following this concept, a stability condition for a tube pair was derived from the analytical solution of the forward kinematics. This condition was extended to a two-tube robot with varying pre-curvatures [28]. A general stability condition for a robot with an arbitrary number of

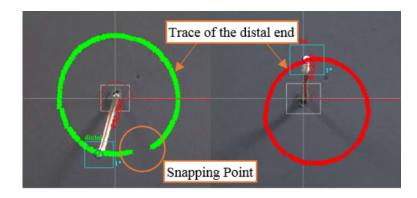


Figure 1.7: Snapping analysis through video tip tracking [32]. Green marks (left) show the traced distal end of an unstable tube pair that snaps at a certain point, and red marks (right) show the traced distal end of a stable tube pair (© 2014 IEEE).

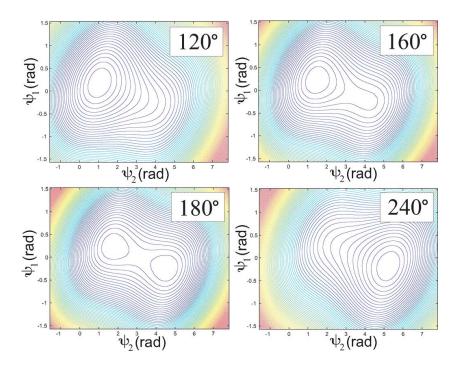


Figure 1.8: Contour plots of the energy landscape as the angular difference between the tube bases is increased. Angular difference between the base inputs of the two tubes is listed in the upper right corner of each plot. For small angular differences, there is only one global minimum. As the angular difference approaches 180° , two appear. Beyond 180° , the new minimum becomes the global minimum, and eventually the only minimum [2] (© 2009 IEEE).

tubes was not discovered yet, but a design test was found in an implicit form [29, 30]. Optimization techniques for designing stable CTRs are developed in [28, 31].

In the cases where the robot has an unstable region in its workspace, stability can be guaranteed by avoiding these regions in path planning or control schemes [30, 31, 33, 34]. The method used in [31, 33] is called a "s-curve" stability test that requires significant precomputation before path planning. To release this constraint, an online stability measure that can be used together with a controller or a motion planner is proposed for the unloaded CTRs in [30]. For CTR under large external loadings, a more general testing method was developed, which consists of a second order sufficient condition, and a separate necessary condition for evaluating the stability of CTRs [34]. Numerical simulation results showed the effectiveness of using this testing method to design stable paths for CTRs. These techniques give more flexibility in designing the tube parameters; for example, highly-curved tubes can be used to navigate and operate in extremely constrained environments. Although various formulations and algorithms have been developed to guide in the design and control of a CTR and ensure stability, the friction effect is still ignored, and how to ensure that the differences between theoretical and experimental results are sufficiently small is an open problem. Another way of improving the kinematic stability of a CTR is by redesigning the structure of the tubes. By manipulating the overall Poisson's ratio the stability condition can be met for tubes with high curvatures. Several feasible solutions were illustrated recently, such as tubes with grooved patterns [32, 35], and multi-layer helical tubes [35]. One concern about this method is that grooved patterns on the surface of the tube will reduce the rigidity at the tip of the robot. Tip rigidity is one of the advantages that concentrictube robots have over other flexible tools such as catheters. The balance between rigidity and kinematic stability should be considered in designing CTRs according to their specific applications.

1.2.2 Sensing

High-frequency, high signal-to-noise ratio feedback is essential for improving the performance of continuum robots due to the nonlinear uncertainties in the kinematic model. For surgical applications, this is especially important since the safety of the robotic system is strongly related to this.

Position and Shape Sensing

Commercially available electromagnetic (EM) tracking has been shown to be a feasible solution for real-time position feedback in CTRs since the small-size tracker can be directly integrated within tubular shafts [6, 23]. In addition, embedding multiple EM trackers or motorizing a single EM tracker along the lumen of a CTR could provide useful information for reconstructing the 3D shape of the robot. The disadvantage of this modality is that the measurement accuracy of the EM tracker can be degraded by other ferro-magnetic components in the surrounding area. In the worst-case scenario, when the accumulated errors are high, the output signal could be discontinuous, which could cause control instability. Imaging feedback is widely used in medical robotic control and navigation, and various shape-sensing and reconstruction techniques have been developed for CTRs based on different imaging modalities such as fluoroscopy [36, 37], and 2D and 3D ultrasound imaging [38–40], as shown in Fig. 1.9. MR compatible CTRs have also been designed in order to use MR imaging for position feedback [41]. Most of these techniques have not been used in closed-loop control; possible reasons include time delay caused by low-sampling rate and high computational cost for image processing. As an alternative, Fiber Bragg Grating (FBG) based sensing seems promising because of its small size and multiplexing capabilities, as well as sterilizability and immunity to EM interference. In recent years, these sensors have been used in various needle-based robotic applications [42, 43], such as a detachable 3D shape sensing tool consisting of a polymer substrate and FBG sensors for continuum robots [44]. Fig. 1.10 demonstrates the design concept of this shape sensing tool. A wide range of surgical instruments can benefit from this technology, because it does not require modifications on the mechanical structures as long as the instruments have a hollow channel. The determination of optimal locations for placing multiple FBG

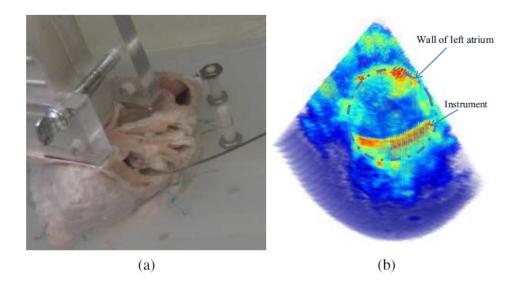


Figure 1.9: Continuum robot inserted inside a porcine heart. (a) Experimental set up; (b) 3D ultrasound image showing both the left atrium and the curved robot [39] (© 2012 IEEE).

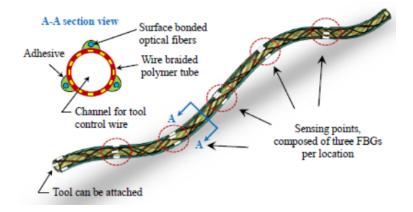


Figure 1.10: Schematic of wire braided polymer tube with surface mounted optical fibers [44] (© 2014 IEEE).

sensors according to the mechanical parameters of CTRs is discussed in [45].

Force Sensing

In order to control robot-tissue interaction, it is important to have force measurements with high speed and precision. Because of the flexibility of CTRs, intrinsic force sensing [46] techniques can be used to convert the deflection of the flexible continuum robot into force measurements through kinematic models [23]. An extended Kalman filter approach was developed to enhance the measurement accuracy in the presence of sensing noise and modeling uncertainties [46]. However, the sampling rate of EM trackers and imaging modalities is not usually sufficient for calculating time-varying interaction forces and quality visual or EM feedback is not always available in a surgical environment. At present, commercially available force sensors are not compact enough to attach to the tip of CTRs as space is extremely limited. In [47], a novel miniature tip force sensor was developed that measured both the magnitude and contact angle; however, this sensor does not allow interventional tools to pass through. Optical strain sensors are another good choice for robots with housing constraints. As in shape sensing, FBG-based strain sensors have revolutionized force sensing technologies for medical robotics [48, 49] and implementations in CTRs are expected in the coming years.

1.2.3 Control

To perform surgical tasks such as tissue manipulation and drug delivery advanced real-time control schemes need to be designed based on comprehensive knowledge in tube modeling and robot control. In contrast to traditional rigid-link robots, the position and force control of CTRs are coupled together in the sense that the deflection of the robot is determined by both actuation and external loading, which increases the difficulty in controller design. The limitations of commercially available sensing technologies for position and force feedback in surgical tools make it even harder to design a reliable controller that can handle time-varying interactions between the robot and the environment.

Control of the Tip

In the literature, the tip of a CTR has been controlled mainly through solving the inverse kinematics or Jacobian and then sending the joint space values to the low-level motor con-

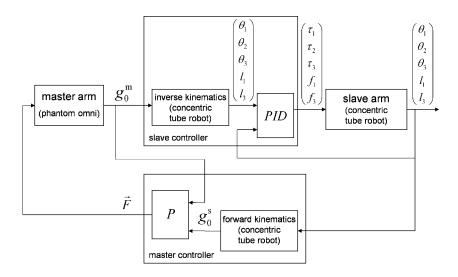


Figure 1.11: The unilateral control block diagram of a teleoperated CTR; θ_i and l_i are the joint space variables of the i^{th} tube [1] (© 2010 IEEE).

troller. To achieve real-time performance, the computationally efficient techniques mentioned in the previous sections are used [1, 26]. In those methods it is assumed that the inverse kinematic model is accurate enough such that the position errors will be compensated for using appropriate feedback. The stability of these control strategies in the presence of modeling errors is not analyzed. In [50], a new control strategy designed at the actuator level is proposed, where the errors in Cartesian space can be reduced using approximate kinematics. In a tele-operation scenario, the position error of the robot's tip can be compensated for by the operator. Bilateral control schemes for CTR have not been studied extensively in the literature; a unilateral architecture is commonly used as shown in Fig. 1.11.

In order to avoid singularities and undesired regions in task space while controlling the position of the robot, Jacobian-based control strategies combined with inequality constraints [51] or a damped least-squares approach [6] have been developed such that the calculated velocities satisfy these constraints. An inverse kinematic control scheme that includes inequality constraints on joint variables ($C(q) \le b$) was proposed, as shown in Fig. 1.12. Experimental results showed that this algorithm can control the movement of the robot's tip while avoiding snapping regions.

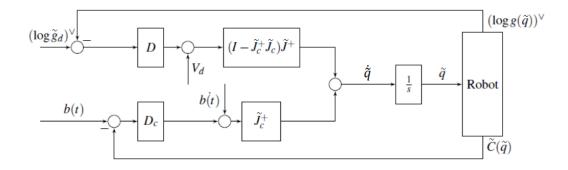


Figure 1.12: The control block diagram of the closed-loop system. The inequality constraints on the joint space variables $C(q) \leq b$ are converted into equal constrains $\tilde{C}(\tilde{q}) = b$, then applied to the inverse kinematic control algorithm. D and D_c are positive definite diagonal matrices, \tilde{J}_c is the augmented constraints Jacobian matrix and $(\log g)^{\vee}$ returns the 6D vector representation of g [51] (© 2014 IEEE).

Control of the Robot's Shape

In clinical applications, the body of the CTR would need to navigate inside organs or through curved lumens of the human body. Therefore, the position of every point along the robots shaft should be precisely controlled to avoid damage to delicate tissue and organs, and several motion planning algorithms have been developed to address this [52–54]. A sampling-based motion planner that employs a torsionally compliant kinematic model was proposed in [54], which leads a CTR to its target with the minimum probability of obstacle collision. Simulation results for this method for spherical objects and a neurosurgery environment are shown in Fig. 1.13. This method was further extended to an online motion planner for systems with teleoperation architectures [55]. In this way, surgeons would only need to direct the tip of the robot during a surgical procedure and the computer program would provide the collision avoidance strategy. A three-stage lung access system [56] uses a motion plan technique similar to the one above to navigate a steerable needle extended from a bronchoscope and a CTR to the peripheral areas in the lung. The previously mentioned motion planners rely on geometric information calculated from preoperative images. Intraoperative updating of the motion plans according to image and sensor feedback is still under investigation.

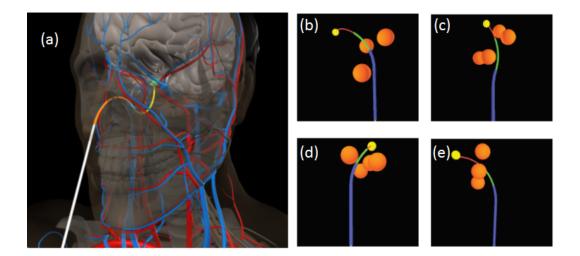


Figure 1.13: (a) Simulation of a CTR in a neurosurgery environment executing the motion plan that calculated from the proposed sampling-based approach based on the Rapidly-Exploring Roadmap. The robot is inserted through the nostril and guided toward the pituitary gland (highlighted in green) in the skull base while avoiding skin, bone, blood vessels, and healthy brain tissue. (b, c, d, e) Simulation of a CTR in four different spherical obstacle environment [54] (© 2011 IEEE).

To reduce tube-tissue forces and avoid collisions with the tube body during tool insertion a follow-the-leader approach has been proposed [1, 31, 57, 58], where the body of the robot is controlled to conform to the path created by the prescribed tool tip trajectory. This deployment manner is automatically achieved when the stiffness of the outer tube dominates all the inner tubes [13, 19]. For CTRs in general, this is not straightforward to achieve since the movement of the tip is usually generated by varying the shape of the robot shaft. To address this issue, conditions have been derived for follow-the-leader deployment [31, 57]. Experimental results showed the feasibility of this method, provided the pre-curvatures and actuation sequences are appropriately designed [31, 58].

Control of Interaction

The control schemes mentioned above are for the situations where the robot moves in free space or with minimal environmental contact. However, in surgical procedures, intensive

tool/tissue interactions may be involved.

A stiffness control algorithm for CTRs is described in [23], and evaluated in an experimental setup. As shown in Fig. 1.14, the robot is controlled to behave as a linear virtual spring with respect to an arbitrary point P_{bt}^r in the environment. The control law starts from calculating the desired tip force ($F_w^d = K^d(P_{bt}^m - P_{bt}^r)$), according to the pre-defined stiffness and real-time tip position and orientation feedback. This force value is then converted to the desired deflection and orientation g_{tt}^d as the input for the inverse kinematics position controller. In the end, the outputs of the position controller drive the actuation unit of the CTR to achieve this deflection and orientation. This algorithm can be generalized to other surgical continuum robots as long as the robot behaves as a single elastic rod. Experimental results with good accuracy and dynamic response were obtained for a two-tube robot. This method can be extended to an impedance control strategy to provide proper damping to the system. For this purpose a velocity-based controller should be considered as an addition to the proposed control scheme in order to stabilize the robot in both the position and velocity domains.

1.3 Remarks

Kinematic modeling provides the fundamental knowledge to facilitate the design and control of CTRs for surgery. The dominant mechanical phenomena (i.e. bending and torsion) have been well modeled with high accuracy but real-time performance still requires improvements. Other mechanical effects may also be significant but the deciding factors for when these effects cannot be neglected have not been addressed in the literature. For example, in some surgical applications, tubes with high curvatures may be necessary, and in these applications nonlinear elasticity and friction may need to be considered. In addition, the kinematic accuracy of specially designed tubes, such as grooved tubes with patterns and multi-layer helical tubes, has not been evaluated experimentally. Based on the pro-

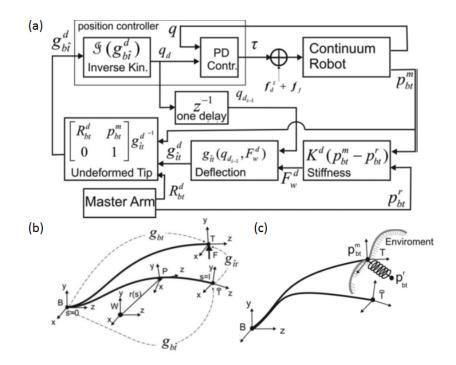


Figure 1.14: (a) Block diagram of the stiffness controller. (b) Continuum robot represented as a space curve (solid line). W is world coordinate frame, while B, P, \hat{T} , and T are robot body frames. \hat{T} and T are tip frames without and with the application of tip wrench F, respectively. Coordinate transformations are denoted by $g_{bt}, g_{b\hat{t}}$, and $g_{\hat{t}t}$. (c) Robot in contact with environment. The stiffness controller implements a virtual linear spring at the robots tip. Desired actuator positions are such that when robot is deflected from unloaded tip configuration \hat{T} to configuration T, the desired tip spring force is generated, and the desired tip orientation is achieved [23] (© 2011 IEEE).

posed kinematic models, a series of control schemes have been developed for performing surgical tasks using CTRs. These methods usually assume that a CTR moves at low speeds and the contact force is minimal. For situations in which the robot and the tissues/organs have complex interactions, algorithms for stiffness control have been proposed but position control under force disturbances is still needed. Other valuable control strategies that are widely used in medical robotics such as force control, impedance control, and haptics in teleoperation have not yet been applied for this type of robot. This could be the result of uncertainties in modeling and limitations in current sensing technologies. With recent and future developments in position, shape and force sensing, the control architecture could be improved to incorporate this additional information, thereby enhancing the performance of

these robots and enabling their use in the next generation of devices for surgical interventions.

1.4 Thesis Outline and Contributions

From the literature review in previous sections, it can been seen that the fundamental theories concerning CTRs are still at an early stage compared to those for conventional rigid manipulators. In addition, specialized sensing technologies for CTRs have not received enough attention. In this thesis, novel techniques and technologies in modeling, sensorization and control of CTRs are proposed and evaluated, and will fill in several of the gaps in the current literature, thereby resulting in significant improvements on the performance and functionality of CTRs for surgical or interventional procedures. The theoretical contributions of the thesis include: (1) the most computationally efficient torsionally compliant kinematic model for CTRs [59, 60]; (2) the first general design criteria that guarantee stability of a CTR in its entire workspace [61]; (3) the first force-rejection control scheme for CTRs [62]; and (4) the first intrinsic force sensing algorithm for CTRs using FBG sensors [63]. The following are the contributions in technological advancements of the work described in the thesis: (1) the first CTR with force sensing capability [62]; (2) the first micro-engraver that can fabricate micro patterns on flexible thin tubes [63]; (3) the first sensorized continuum robot with torsional sensing capability [63, 64]; (4) the first sensorized CTR using embedded FBGs (Chapter 8); and (5) one of the most cost effective, portable and compact CTR drive unit (Chapter 2), which is easy to integrate with other robotic platforms. The details of these contributions are discussed in the following paragraphs and in the rest of the thesis:

• Chapter 2 presents overall descriptions of all the custom-made experimental setups used to complete the work presented in this thesis. Because the nature of this research is to improve a growing technology for future surgical procedures, many components

of the robotic setup had to be custom-made. For shaping the Nitinol tubes, a series of aluminum and steel molds were built for temperature controlled heat treatment. Three robot prototypes were built for the purpose of validating the kinematic models, control techniques, sensorization capabilities of CTRs. In addition, the manufacturing process for embedding FBG sensors into the thin-walled Nitinol tubes was not available. This is an key step to developed sensorized CTRs. Hence, a special microengraving machine was designed and built, in order to machine helical patterns on a flexible hollow tube for embedding FBG sensors.

- Chapter 3 describes a computationally efficient kinematic model developed by applying piecewise linearization on the torsionally compliant kinematic model. Prior to the author's work, the computational efficiency of the torsionally compliant kinematic models of CTRs was too low to be used in real-time trajectory tracking, force control and teleoperation, not to mention online motion planning and redundancy resolution. The fastest calculation speed reported was 40 Hz for a three-tube CTR. For this reason, off-line computation was often used for real-time control problems. To overcome this deficiency, our fast kinematic model was developed. The computation time for solving this kinematics model is generally less than 3 ms in MATLAB scripts and 0.2 ms in C++ programming for a three-tube robot with minimum loss of accuracy. To date, it is still the most efficient algorithm in literature for computing the kinematics of a CTR.
- In Chapter 4, the Jacobian matrix of the computational efficient kinematic model (developed in Chapter 3) is presented along with simulation and experimental results. This augmented Jacobian includes the velocity mapping between joint and Cartesian spaces, as well as the relations between the changes of torques at the proximal and distal ends of the robot. A robot prototype was built from two linear and two rotary stages for testing the Jacobian matrix in several control tasks. A Jacobian-based controller is proposed to command the position of the robot's tip while avoiding the

singularity regions.

- Chapter 5 contains a local disturbance analysis performed on the kinematic model of a CTR. A general stability condition is proposed for CTRs having multiple tubes with and without transmission sections. Prior to this work, there was no general design criteria for a CTR with arbitrary number of tubes, such that the kinematic stability can be guaranteed in the entire workspace. The proposed stability condition overcomes this problem. Simulation studies showed that this condition can evaluate stability of CTRs in the entire workspace without the need for solving the forward kinematics. Although this condition becomes more conservative when the number of tubes increases, its concise form provides an intuitive interpretation of the role of each tube parameter, such as curvature, length, stiffness, and Poisson's ratio, in the stability of a multi-tube robot.
- Chapter 6 discusses the technologies and techniques for controlling a CTR under time-varying tip force disturbances. Although the position controllers mentioned previously were shown to be valid, they did not evaluate the effects of time-varying force disturbances that are typically present in surgical applications. These disturbance could have a negative effect on targeting accuracy and ultimately the effectiveness of the therapy. In order to resolve this problem, the deflection of a CTR under external disturbances is estimated from force sensing and kinematic modeling, in which case the effect of time-varying disturbances can be compensated by reshaping the desired trajectory corresponding to the deflection.
- Chapter 7 presents the first design of a continuum robot that integrates helicallywrapped FBG sensors. The bending curvatures and torsional twisting in the robot's shaft can be accurately measured by these sensors. It is also the first work discussing FBG-based force sensing on pre-curved continuum robots, especially concentrictube robots. A curvature-strain model is proposed to relate the strains in the helicallywrapped sensors to the curvature and twist of the robot shaft. For measuring tip forces

in large deflecting continuum robots, the cosserat rod theory is adapted to develop a force-curvature-strain model. The unsymmetrical nature of the pre-curved structures introduces a non-linearity in the force-strain relationship, which is also included and calibrated in this model. One of the most important problems in designing FBG-based sensing technology is that of fiber protection. In this chapter, a unique design of a sensorized tube assembly is proposed, such that the FBG sensors are protected from the "cutting forces" during the telescopic motions of a CTR. The feasibility of 3D force sensing in continuum robots is studied via simulations.

Bibliography

- [1] P. E. Dupont, J. Lock, B. Itkowitz, and E. Butler, "Design and control of concentrictube robots," *IEEE Trans. Robot.*, vol. 26, no. 2, pp. 209–225, 2010.
- [2] R. J. Webster III, J. M. Romano, and N. J. Cowan, "Mechanics of precurved-tube continuum robots," *IEEE Trans. Robot.*, vol. 25, no. 1, pp. 67–78, 2009.
- [3] H. B. Gilbert, D. C. Rucker, and R. J. Webster III, "Concentric tube robots: The state of the art and future directions," in *Springer Tracts in Advanced Robotics*. Springer International Publishing, 2016, vol. 114, pp. 253–269.
- [4] D. C. Rucker, B. A. Jones, and R. J. Webster III, "A geometrically exact model for externally loaded concentric-tube continuum robots," *IEEE Trans. Robot.*, vol. 26, no. 5, pp. 769–780, 2010.
- [5] L. G. Torres, R. J. Webster, and R. Alterovitz, "Task-oriented design of concentric tube robots using mechanics-based models," in *Proc. IEEE/RSJ Int. Conf. Intell. Robots Syst.* IEEE, 2012, pp. 4449–4455.
- [6] J. Burgner, D. C. Rucker, H. B. Gilbert, P. J. Swaney, P. T. Russell, K. D. Weaver, and R. J. Webster, "A telerobotic system for transnasal surgery," *IEEE/ASME Trans. Mechatronics*, vol. 19, no. 3, pp. 996–1006, 2014.
- [7] N. V. Vasilyev, A. H. Gosline, A. Veeramani, M. T. Wu, G. P. Schmitz, R. T. Chen, V. Arabagi, J. Pedro, and P. E. Dupont, "Tissue removal inside the beating heart using a robotically delivered metal mems tool," *Int. J. Robot. Res.*, vol. 34, no. 2, pp. 236– 247, 2015.
- [8] A. H. Gosline, N. V. Vasilyev, E. J. Butler, C. Folk, A. Cohen, R. Chen, N. Lang, P. J. Del Nido, and P. E. Dupont, "Percutaneous intracardiac beating-heart surgery using metal mems tissue approximation tools," *Int. J. Robot. Res.*, p. 0278364912443718, 2012.

- [9] P. A. York, P. J. Swaney, H. B. Gilbert, and R. J. Webster, "A wrist for needle-sized surgical robots," in *Proc. IEEE Int. Conf. Robot. Autom.* IEEE, 2015, pp. 1776–1781.
- [10] N. V. Vasilyev, P. E. Dupont, and P. J. Del Nido, "Robotics and imaging in congenital heart surgery," *Future cardiology*, vol. 8, no. 2, pp. 285–296, 2012.
- [11] N. V. Vasilyev, A. H. Gosline, E. Butler, N. Lang, P. J. Codd, H. Yamauchi, E. N. Feins, C. R. Folk, A. L. Cohen, R. Chen *et al.*, "Percutaneous steerable robotic tool delivery platform and metal microelectromechanical systems device for tissue manipulation and approximation closure of patent foramen ovale in an animal model," *Circulation: Cardiovascular Interventions*, vol. 6, no. 4, pp. 468–475, 2013.
- [12] A. H. Gosline, N. V. Vasilyev, A. Veeramani, M. Wu, G. Schmitz, R. Chen, V. Arabagi, J. Pedro, and P. E. Dupont, "Metal mems tools for beating-heart tissue removal," in *Proc. IEEE Int. Conf. Robot. Autom.* IEEE, 2012, pp. 1921–1926.
- [13] J. Burgner, P. J. Swaney, R. A. Lathrop, K. D. Weaver, and R. J. Webster, "Debulking from within: a robotic steerable cannula for intracerebral hemorrhage evacuation," *IEEE Trans. Biomed. Eng.*, vol. 60, no. 9, pp. 2567–2575, 2013.
- [14] P. J. Swaney, A. W. Mahoney, A. A. Remirez, E. Lamers, B. I. Hartley, R. H. Feins, R. Alterovitz, and R. J. Webster, "Tendons, concentric tubes, and a bevel tip: Three steerable robots in one transoral lung access system," in *Proc. IEEE Int. Conf. Robot. Autom.* IEEE, 2015, pp. 5378–5383.
- [15] R. J. Hendrick, S. D. Herrell, and R. J. Webster, "A multi-arm hand-held robotic system for transurethral laser prostate surgery," in *Proc. IEEE Int. Conf. Robot. Autom.* IEEE, 2014, pp. 2850–2855.
- [16] R. J. Hendrick, C. R. Mitchell, S. D. Herrell, and R. J. Webster III, "Hand-held transendoscopic robotic manipulators: a transurethral laser prostate surgery case study," *Int. J. Robot. Res.*, vol. 34, no. 15, pp. 1559–1572, 2015.
- [17] P. E. Dupont, "Steerable needles as surgical robots," in *IEEE ICRA 2012 Needle Steer*ing Workshop. IEEE, 2012.
- [18] P. J. Swaney, H. B. Gilbert, R. J. Hendrick, O. Commichau, R. Alterovitz, and R. J. Webster, "Transoral steerable needles in the lung: how non-annular concentric tube robots can improve targeting," in *Hamlyn Symposium on Medical Robotics*, 2015.

- [19] J. Furusho, T. Ono, R. Murai, T. Fujimoto, Y. Chiba, and H. Horio, "Development of a curved multi-tube (cmt) catheter for percutaneous umbilical blood sampling and control methods of cmt catheters for solid organs," in *IEEE Int. Conf. Mecha. Autom.*, vol. 1. IEEE, 2005, pp. 410–415.
- [20] P. Sears and P. Dupont, "A steerable needle technology using curved concentric tubes," in *Proc. IEEE/RSJ Int. Conf. Intell. Robots Syst.*, 2006, pp. 2850–2856.
- [21] R. J. Webster, A. M. Okamura, and N. J. Cowan, "Toward active cannulas: miniature snake-like surgical robots," in *Proc. IEEE/RSJ Int. Conf. Intell. Robots Syst.* IEEE, 2006, pp. 2857–2863.
- [22] R. J. Webster and B. A. Jones, "Design and kinematic modeling of constant curvature continuum robots: A review," *Int. J. Robot. Res.*, 2010.
- [23] M. Mahvash and P. E. Dupont, "Stiffness control of surgical continuum manipulators," *IEEE Trans. Robot.*, vol. 27, no. 2, pp. 334–345, 2011.
- [24] P. E. Dupont, J. Lock, and E. Butler, "Torsional kinematic model for concentric tube robots," in *Proc. IEEE Int. Conf. Robot. Autom.* IEEE, 2009, pp. 3851–3858.
- [25] J. Lock, G. Laing, M. Mahvash, and P. E. Dupont, "Quasistatic modeling of concentric tube robots with external loads," in *Proc. IEEE/RSJ Int. Conf. Intell. Robots Syst.* IEEE, 2010, pp. 2325–2332.
- [26] D. C. Rucker and R. J. Webster, "Computing jacobians and compliance matrices for externally loaded continuum robots," in *Proc. IEEE Int. Conf. Robot. Autom.* IEEE, 2011, pp. 945–950.
- [27] J. Lock and P. E. Dupont, "Friction modeling in concentric tube robots," in *Proc. IEEE Int. Conf. Robot. Autom.* IEEE, 2011, pp. 1139–1146.
- [28] J. Ha, F. C. Park, and P. E. Dupont, "Achieving elastic stability of concentric tube robots through optimization of tube precurvature," in *Proc. IEEE/RSJ Int. Conf. Intell. Robots Syst.* IEEE, 2014, pp. 864–870.
- [29] R. J. Hendrick, H. B. Gilbert, and R. J. Webster, "Designing snap-free concentric tube robots: A local bifurcation approach," in *Proc. IEEE Int. Conf. Robot. Autom.* IEEE, 2015, pp. 2256–2263.

- [30] H. B. Gilbert, R. J. Hendrick, and R. J. Webster III, "Elastic stability of concentric tube robots: A stability measure and design test," *IEEE Trans. Robot.*, vol. 32, no. 1, pp. 20–35, 2016.
- [31] C. Bergeles, A. H. Gosline, N. V. Vasilyev, P. J. Codd, J. Pedro, and P. E. Dupont, "Concentric tube robot design and optimization based on task and anatomical constraints," *IEEE Trans. Robot.*, vol. 31, no. 1, pp. 67–84, 2015.
- [32] J.-S. Kim, D.-Y. Lee, K. Kim, S. Kang, and K.-J. Cho, "Toward a solution to the snapping problem in a concentric-tube continuum robot: Grooved tubes with anisotropy," in *Proc. IEEE Int. Conf. Robot. Autom.* IEEE, 2014, pp. 5871–5876.
- [33] C. Bergeles and P. E. Dupont, "Planning stable paths for concentric tube robots," in *Proc. IEEE/RSJ Int. Conf. Intell. Robots Syst.* IEEE, 2013, pp. 3077–3082.
- [34] J. Ha, F. C. Park, and P. E. Dupont, "Elastic stability of concentric tube robots subject to external loads," *IEEE Trans. Biomed. Eng.*, vol. 63, no. 6, pp. 1116–1128, 2016.
- [35] H. Azimian, P. Francis, T. Looi, and J. Drake, "Structurally-redesigned concentrictube manipulators with improved stability," in *Proc. IEEE/RSJ Int. Conf. Intell. Robots Syst.* IEEE, 2014, pp. 2030–2035.
- [36] J. Burgner, S. D. Herrell, and R. J. Webster, "Toward fluoroscopic shape reconstruction for control of steerable medical devices," in ASME 2011 Dynamic Systems and Control Conference and Bath/ASME Symposium on Fluid Power and Motion Control. American Society of Mechanical Engineers, 2011, pp. 791–794.
- [37] E. J. Lobaton, J. Fu, L. G. Torres, and R. Alterovitz, "Continuous shape estimation of continuum robots using x-ray images," in *Proc. IEEE Int. Conf. Robot. Autom.* IEEE, 2013, pp. 725–732.
- [38] H. Ren and P. E. Dupont, "Tubular structure enhancement for surgical instrument detection in 3d ultrasound," in 2011 Annual International Conference of the IEEE Engineering in Medicine and Biology Society. IEEE, 2011, pp. 7203–7206.
- [39] H. Ren and P. E. Dupont, "Tubular enhanced geodesic active contours for continuum robot detection using 3d ultrasound," in *Proc. IEEE Int. Conf. Robot. Autom.* IEEE, 2012, pp. 2907–2912.
- [40] M. Terayama, J. Furusho, and M. Monden, "Curved multi-tube device for path-error correction in a needle-insertion system," *Int. J Med. Robot. Comp. Assist. Surg.*, vol. 3, no. 2, pp. 125–134, 2007.

- [41] H. Su, D. C. Cardona, W. Shang, A. Camilo, G. A. Cole, D. C. Rucker, R. J. Webster, and G. S. Fischer, "A mri-guided concentric tube continuum robot with piezoelectric actuation: a feasibility study," in *Proc. IEEE Int. Conf. Robot. Autom.* IEEE, 2012, pp. 1939–1945.
- [42] Y.-L. Park, S. Elayaperumal, B. Daniel, S. C. Ryu, M. Shin, J. Savall, R. J. Black, B. Moslehi, and M. R. Cutkosky, "Real-time estimation of 3-d needle shape and deflection for mri-guided interventions," *IEEE/ASME Trans. Mechatronics*, vol. 15, no. 6, pp. 906–915, 2010.
- [43] R. J. Roesthuis, M. Kemp, J. J. van den Dobbelsteen, and S. Misra, "Threedimensional needle shape reconstruction using an array of fiber bragg grating sensors," *IEEE/ASME Trans. Mechatronics*, vol. 19, no. 4, pp. 1115–1126, 2014.
- [44] S. C. Ryu and P. E. Dupont, "Fbg-based shape sensing tubes for continuum robots," in *Proc. IEEE Int. Conf. Robot. Autom.*, 2014, pp. 3531–3537.
- [45] B. Kim, J. Ha, F. C. Park, and P. E. Dupont, "Optimizing curvature sensor placement for fast, accurate shape sensing of continuum robots," in *Proc. IEEE Int. Conf. Robot. Autom.* IEEE, 2014, pp. 5374–5379.
- [46] D. C. Rucker and R. J. Webster III, "Deflection-based force sensing for continuum robots: A probabilistic approach," in *Proc. IEEE/RSJ Int. Conf. Intell. Robots Syst.*, 2011, pp. 3764–3769.
- [47] V. Arabagi, A. Gosline, R. J. Wood, and P. E. Dupont, "Simultaneous soft sensing of tissue contact angle and force for millimeter-scale medical robots," in *Proc. IEEE Int. Conf. Robot. Autom.* IEEE, 2013, pp. 4396–4402.
- [48] I. Iordachita, Z. Sun, M. Balicki, J. U. Kang, S. J. Phee, J. Handa, P. Gehlbach, and R. Taylor, "A sub-millimetric, 0.25 mn resolution fully integrated fiber-optic forcesensing tool for retinal microsurgery," *Int. J. Comput. Assist. Radiol. Surg.*, vol. 4, no. 4, pp. 383–390, 2009.
- [49] X. He, J. Handa, P. Gehlbach, R. Taylor, and I. Iordachita, "A submillimetric 3-dof force sensing instrument with integrated fiber bragg grating for retinal microsurgery," *IEEE Trans. Biomed. Eng.*, vol. 61, no. 2, pp. 522–534, 2014.
- [50] M. N. Boushaki, C. Liu, and P. Poignet, "Task-space position control of concentrictube robot with inaccurate kinematics using approximate jacobian," in *Proc. IEEE Int. Conf. Robot. Autom.* IEEE, 2014, pp. 5877–5882.

- [51] H. Azimian, T. Looi, and J. Drake, "Closed-loop inverse kinematics under inequality constraints: Application to concentric-tube manipulators," in *Proc. IEEE/RSJ Int. Conf. Intell. Robots Syst.* IEEE, 2014, pp. 498–503.
- [52] L. A. Lyons, R. J. Webster III, and R. Alterovitz, "Motion planning for active cannulas." in *Proc. IEEE/RSJ Int. Conf. Intell. Robots Syst.*, 2009, pp. 801–806.
- [53] L. A. Lyons, R. J. Webster, and R. Alterovitz, "Planning active cannula configurations through tubular anatomy," in *Proc. IEEE Int. Conf. Robot. Autom.* IEEE, 2010, pp. 2082–2087.
- [54] L. G. Torres and R. Alterovitz, "Motion planning for concentric tube robots using mechanics-based models," in *Proc. IEEE/RSJ Int. Conf. Intell. Robots Syst.* IEEE, 2011, pp. 5153–5159.
- [55] L. G. Torres, C. Baykal, and R. Alterovitz, "Interactive-rate motion planning for concentric tube robots," in *Proc. IEEE Int. Conf. Robot. Autom.* IEEE, 2014, pp. 1915– 1921.
- [56] A. Kuntz, L. G. Torres, R. H. Feins, R. J. Webster, and R. Alterovitz, "Motion planning for a three-stage multilumen transoral lung access system," in *Proc. IEEE/RSJ Int. Conf. Intell. Robots Syst.* IEEE, 2015, pp. 3255–3261.
- [57] H. B. Gilbert and R. J. Webster, "Can concentric tube robots follow the leader?" in Proc. IEEE Int. Conf. Robot. Autom. IEEE, 2013, pp. 4881–4887.
- [58] H. B. Gilbert, J. Neimat, and R. J. Webster, "Concentric tube robots as steerable needles: achieving follow-the-leader deployment," *IEEE Trans. Robot.*, vol. 31, no. 2, pp. 246–258, 2015.
- [59] R. Xu and R. Patel, "A fast torsionally compliant kinematic model of concentrictube robots," in 2012 Annual International Conference of the IEEE Engineering in Medicine and Biology Society. IEEE, 2012, pp. 904–907.
- [60] R. Xu, A. Asadian, A. S. Naidu, and R. V. Patel, "Position control of concentrictube continuum robots using a modified jacobian-based approach," in *Proc. IEEE Int. Conf. Robot. Autom.* IEEE, 2013, pp. 5813–5818.
- [61] R. Xu, S. F. Atashzar, and R. V. Patel, "Kinematic instability in concentric-tube robots: modeling and analysis," in *Proc. IEEE RAS/EMBS Int. Conf. on Biomed. Rob. Biomech.* IEEE, 2014, pp. 163–168.

- [62] R. Xu, A. Asadian, S. F. Atashzar, and R. V. Patel, "Real-time trajectory tracking for externally loaded concentric-tube robots," in *Proc. IEEE Int. Conf. Robot. Autom.*, 2014, pp. 4374–4379.
- [63] R. Xu, A. Yurkewich, and R. V. Patel, "Curvature, torsion, and force sensing in continuum robots using helically wrapped fbg sensors," *IEEE Robotics and Automation Letters*, vol. 1, no. 2, pp. 1052–1059, 2016.
- [64] R. Xu, A. Yurkewich, and R. V. Patel, "Shape sensing for torsionally compliant concentric-tube robots," in *SPIE BiOS*. International Society for Optics and Photonics, 2016, pp. 97 020V–97 020V.

Chapter 2

Custom Built Experimental Setups

This chapter describes the design and implementation of five experimental setups developed during my research. They were built to validate and demonstrate the proposed techniques and technological advancements in the field of continuum robots. The developed setups are: (1) Tube shaping molds; three different molds were designed and tested to accurately shape Nitinol tubes into desired curvatures; (2) A Swiss-type micro-engraver that can address the challenges in slotting arbitrary 2D or 3D patterns on a thin flexible tubular structure; (3) A CTR prototype for needle insertion applications which consists of four high-precision linear and rotary stages that drive two Nitinol tubes for percutaneous medical applications; (4) A CTR prototype for teleoperated surgical tasks; this robot is an upgraded version of the previous prototype, significant improvements were made on the movement speed and communication rate; (5) A low-cost and compact CTR prototype which features a 6DOF robot with a small cross-section (8 × 15 cm) and light weight (< 5 kg). The total cost is less than \$1200. It is worth mentioning that all of the custom built setups described in this chapter are research prototypes designed to facilitate the experiments in a laboratory environment.



Figure 2.1: Molds used for shaping Nitinol tubes. From left to right, they are made of a half inch aluminum plate, two 1/4 inch low-carbon steel sheets (lid and the bottom pieces), and a half inch low-carbon steel plate. (a) Top view of the three molds (b) Side view of the three molds.

2.1 Tube Shaping Setup

Shape setting of Nitinol is done through a heat treatment process, in which the material is placed in a fixture or on a mandrel, that keeps it firmly constrained into a new shape. The heating method can be an air or vacuum furnace, salt bath, sand bath, heated die, or electrical heating. The temperature should be in the range 500-550°C. In a research lab environment, an air furnace is the most popular choice because it is affordable and does not have a large foot print. The heating method, and the size and material of the fixture. For example, for small parts in a salt bath and heating die, it may take less than a minute, but for massive fixtures in an air furnace, it can take up to an hour. Following the heating process, a rapid cooling such as water quenching is recommended to avoid material aging.

In our experiments, an aluminum plate with curved slots was used as the shaping mold (Fig. 2.1(a)). Nitinol tubes were embedded in this mold and heated up to 540°C for 20 minutes in an air furnace, followed by a rapid water quenching. However, these tubes did not change to the desired shape and lost their superelastic behavior at room temperature. Similar phenomenon is observed by other research groups as well. One solution found by our group was to increase the temperature to 640°C, and heat it for 20 minutes. This method is proven to be effective but not preferable, since 640°C is very close to the melting point of aluminum (660.3°C). It can be seen in Fig. 2.1(b), the aluminum mold was warped during the heat treatment, which reduces the accuracy in shape setting. In addition, higher temperature than 550°C can change the mechanical characteristics of Nitinol tubes, such as reducing their tensile strength. Due to the unsatisfactory performance of the aluminum mold, a low-carbon steel sheet (1/4 inch) was used for the second mold as shown in Fig. 2.1(a). In our experiments, heating this mold at 540° C for 60 minutes can effectively set the new shape of Nitinol tubes. However, the residual stresses generated during the cooling process (uneven cooling speed at two sides of the sheet) caused undesired bending of the steel sheet, as shown in Fig. 2.1(b). This bending increased every time this mold went through the heat treatment. Finally, this problem was addressed by using a 1/2 inch thick steel plate for the third mold shown in Fig. 2.1(a), which has shown better performance than the previous two. It is important to mention that the last two molds are rather heavy for a single person to pick up using a tong. A safe procedure for picking up this red-hot metal should be carefully designed and followed.

For achieving consistent mechanical features along the tubes, it is recommended to embed the full body of the tubes into the mold, even the sections that do not need to be bent. This requirement will result in a prolonged machining time, since many tubes used in CTRs are longer than 300 mm. For example, the second mold mentioned above takes more than 15 hours to engrave by a professional machinist, costing more than one thousand Canadian dollars. It is quite expensive, especially for research, as new molds are required for testing different designs of CTRs.

2.2 Tube Engraving Setup

In this section, a Swiss-type micro-engraver is developed as a general solution to create special designed patterns on a thin flexible Nitinol tubes [1]. In the literature, it has been shown that patterned Nitinol tubes can provide the required features for designing sensorized continuum robots [2, 3] and CTRs with improved stability [4, 5].

There are many challenges in generating precision patterns into the surface of Nitinol tubes including accurate depth of cut, precision profiling and smooth surface finishing. Since the workpiece is superelastic, there should be a special fixation in order to provide constant support in all orientations of the workpiece throughout the machining process. In the literature, non-contact machining methods such as laser cutting and Electrical Discharge Machining (wire-EDM) are commonly used to address the problems in machining flexible tubes. To date, only cutting-through patterns or straight slots can be made into the walls of continuum robots, as shown in [3, 4]. For our work, we are interested in machining helical slots along the surface of the CTRs in order to integrate FBG sensors in a helical layout for real-time shape and force sensing. The depth of these slots needs to be precisely controlled to protect the fiber from the forces and pressures of surrounding structures. In recent years, a Swiss-type CNC lathe that combines the advantages of a CNC mill and a lathe became a popular solution to generate helical cuts in a cylinder structure, as shown in Fig. 2.2(a, b). However, in a normal configuration, there is almost no support on the workpiece except for the clutch. As a result, the machining precision decreases as the rigidity of the workpiece drops. For flexible Nitinol tubes used in CTRs, it is almost impossible to engrave patterns with desired accuracy. Building a custom made jig for this type of machine could be an option, but the cost is quite high.

The promising research potentials in patterned CTRs and deficiencies in current machining processes motivated us to build a desktop micro-engraver, specially for creating various patterns on the surface of flexible tubes. As shown in Fig. 2.2(c, d), a support block was designed to provide constant support in all orientations of the workpiece during the ma-

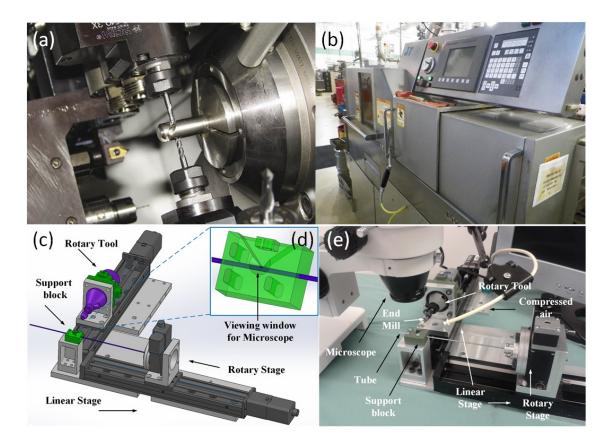


Figure 2.2: (a) A commercially available Swiss-type CNC lathe, Citizen-Cincom K16 (Marubeni Citizen-Cincom Inc., United States). (b) A view of the machine's full size. (c, d) The CAD design of our desktop micro-engraver (e) The actual setup of the developed desktop micro-engraver. The machining process can be monitored using a microscope through the viewing window on the support block.

chining process. The alignment between the end mill and workpiece was maintained by the inner structures of this block, while the workpiece rotates and translates. A new block can be easily custom made for different tube diameters, since it was made out of ABS using a 3D printer. In order to observe the tool-workpiece interface in real-time, a viewing window was designed and a microscope was placed on top of the block. A wide-angle entry from the end mill side was designed for the application of pressurized air. Silicon lubricant was constantly sprayed into the support block to minimize the friction between the block and the Nitinol tube. It also serves as machining coolant to reduce tool wear. To find the required tool offset for machining, a multimeter continuity test was used to probe for contact between the end mill and the workpiece.

Since the hardness of Nitinol is quite high (58-64, Rockwell C scale), an AlTiN-Nano coated carbide mill bit (944215-C6, Harvey Tool, United States) was used in this setup. This mill bit features a ball end and three V-shape helical flutes for maximized chip loading. The diameter of this end mill is 0.015 inch and the cutting length is 0.023 inch. It is special designed for micro-milling exotics & aerospace alloys. The formulas for calculating the machining speed and feed rate are:

$$RPM = (3.82 \times SFM) / D$$
 (2.1)

$$IPM = RPM \times IPT \times T \tag{2.2}$$

where, RPM denotes revolutions per minute; SFM is surface feet per minute; D is the diameter of the end mill; IPT is chip load per tooth; and T is the number of teeth of the end mill. According to the datasheet of the chosen end mill, and the hardness of the Nitinol alloy, these numbers are: SFM = $40 \sim 75$; D = 0.015 inch; IPT = 0.00006; T = 3. As a result, the speed and feed rates for machining Nitinol tubes are: RPM = $10000 \sim 19000$; IPM = 0.9144 m/s; and the depth of cut is 0.1524 mm.

To provide the accuracy and repeatability required for patterning CTRs, high-precision linear stages (T-LSR300B, Zaber Technologies, United States), and rotary stages (T-RS60A, Zaber Technologies, United States) were chosen to generate the cutting profiles. The rotary spindle (200 series rotary tool, Dremel, United States) was mounted on one of the linear stages for accurate depth control. The entire system has a portable size (40 x 40 cm), and weighs less than 7 kg. The performance of this Swiss-type micro-engraver for creating helical patterns on Nitinol tubes will be discussed in detail in Chapter 7. Although this technology was designed for engraving helical patterns, it can be generalized for creating much more complex 3D patterns since all the three axes are computerized. In this case, significant upgrades on the user interface are needed, in order to automatically generate

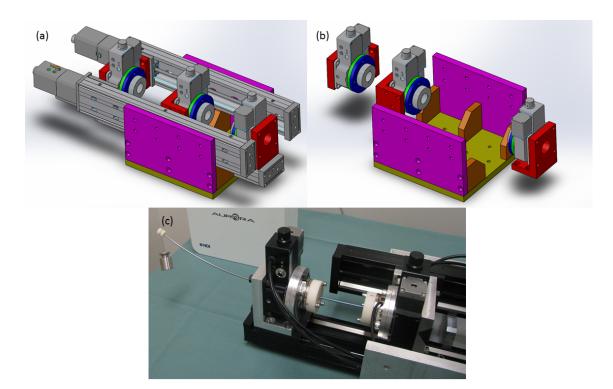


Figure 2.3: (a, b) The CAD design of a 6DOF CTR drive unit using high precision linear and rotary stages. The parts in grey are commercial products and the rest of the parts are custom built. (c) The actual robotic setup using two linear and two rotary stages.

tool paths for machining from standard CAD files.

2.3 A Custom-built CTR for Needle Insertion Applications

Concentric-tube robots can be considered as an extension of steerable needles, since the body of a CTR can generate 3D insertion paths to avoid obstacles. The goal of this section is to develop a robotic setup for the application of CTRs in percutaneous procedures.

In this section, we discuss the design and implementation of a CTR drive unit using commercially available rotary and linear stages (T-RS60A and T-LSR300B, Zaber Technologies, Canada), as shown in Fig. 2.3. In the literature, most CTRs are designed from scratch based on basic mechanical elements such as planar gears, timing belts, ball-screw transmission and guide rods. Compared to this method, our design approach significantly reduces the amount of time and efforts required for developing the first prototype in a research lab. Furthermore, our drive unit has accuracy and reliability similar to commercial products, because all the high-precision mechanical transmissions, such as ball-screw and worm gears, are built into the selected stages by the industrial supplier. In addition, the chances of wiring hazards in this drive unit are also minimized, since the motor controllers are already integrated into the packaging of these stages.

As shown in Fig. 2.3(a, b), the robot frame was designed from several aluminum plates that provided structural support and mounting locations. Three linear and three rotary stages were installed on this frame in a desired alignment, such that the center of each rotary stage (where the tube is attached) was on the same axis. The rotary and linear stages chosen were the same models as the ones in the Swiss-type micro-engravor, because of their high precision and repeatability. Each rotary stage has an opening in the center (30 mm in diameter), which allows the tubes of CTRs to pass through. Two adapter plates (blue and green) were designed to attach Force/Torque sensors (Nano43, ATI Industrial Automation, United States) for force control or haptic feedback. Fig. 2.3(c) shows the actual robotic setup with four motorized stages. Although the stages in this robot use open-loop controlled stepper motors, there should not be any noticeable step missing since the interaction forces between the tubes are much smaller than the load capabilities of these motors. In needle insertion applications, the tip of the robot is not always detectable by imaging feedback. To address this problem, an electromagnetic (EM) tracking system (Aurora, Northern Digital Inc., Canada) was integrated into this setup in order to obtain position feedback. A 5DOF EM sensor was mounted at the tip of the inner tube using a 3D printed adapter (Fig. 2.3(c)). A ring-shaped slot was made in the middle of this adapter to attach calibration weights. The main control program of this robot was developed in MATLAB (Mathworks, United States) and QuaRC toolbox (Quanser Consulting Inc., Canada). This program sent commands to motorized stages through four serial ports at 100 Hz. The tip position and orientation measured by the Aurora system was read by a separate C++ code and sent to the main

program via UDP protocol at 40 Hz. At the beginning of each experiment, two Nitinol tubes rotated together with the same speed for a full revolution to calibrate the registration

matrix between the robot frame and the Aurora frame. Then these tubes moved relative to each other to calibrate the parameters required for force estimation.

2.4 A Custom-Built CTR for Teleoperated Manipulation

The robot described in the previous section has high performance in needle insertion applications because of its precision and reliability. However, for teleoperated manipulations, it has a few shortcomings. First of all, the maximum speed is 2 cm/s for the linear stages, and 13°/s for the rotary stages. From our teleoperation simulation results, the desired speed should be around 10 cm/s for translations, and 360°/s for rotations, in order to follow the operator's hand motion properly. Another problem is that the communication rate between the motor controller and the computer is around 100 Hz, which limits the performance of this robot in force control and haptics-enabled teleoperation. Furthermore, this communication rate drops dramatically when these stages are daisy-chained and connected to the computer through a single port. For the 4DOF robot shown in Fig. 2.3, the communication rate is less than 25 Hz. Multiple serial ports are needed to achieve higher rates, which is not a common configuration of modern computers, and will increase the number of cables in the setup. All of these problems should be addressed in a second prototype.

This section describes the design of our second prototype of the CTR drive unit. Commercial linear and rotary stages were chosen again in order to speed up the design and manufacturing process. A compact hollow-centered rotary stage (FHA-8C-100-US200-E, Harmonic Drive, United States) was chosen for the rotary actuators. It features a harmonic gear box (100:1) with an open center for tubes to pass through (6.2 mm), and a 2000 lines differential encoder, resulting in a theoretical resolution of 0.00045°. The maximum speed of this rotary stage is 360°/s. A 500 mm long linear stage (MXE25P BN08 SM300 LMI

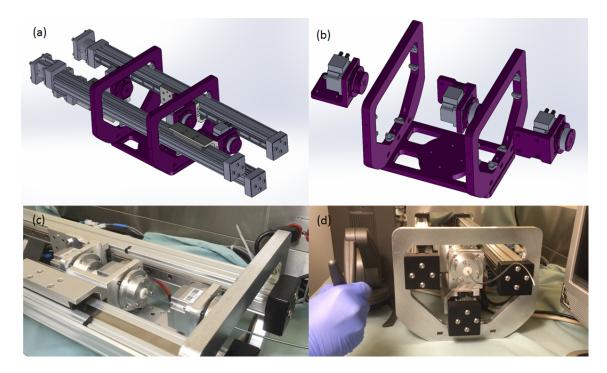


Figure 2.4: (a) The CAD design of the CTR drive unit for teleoperated operations. The components in grey are commercial products and the ones in purple are custom designed parts. (b) The CAD model except for the linear stages (c, d) Side view and front view of the actual 6 DOF robotic setup controlled by a haptic device (Touch X, Geomagic, United States).

YM117004 TC2, Tolomatic Inc., United States) was used to generate translational motions as shown in Fig. 2.4 (a, b). The maximum speed of this linear stage is around 15 cm/s. A Nema 23 servo motor (EXC23-67V60-120-D, ElectroCraft, United States) with a 1000 lines differential encoder was used to motorize this linear stage, resulting in a resolution of 0.00079 mm. Please note that this resolution is calculated from the pitch of the ball-screw and encoder counts, not including the backlash in the linear threaded rod. From our experiments, the backlash of these linear stages can be as high as ± 0.5 mm, which requires software compensations.

In this design, instead of using built-in motion drivers, general purpose motion controllers (DMC-30012, Galil Motion Control, United States) were chosen to achieve high performance position and velocity control. This controller integrates a hardware sinusoidal wave

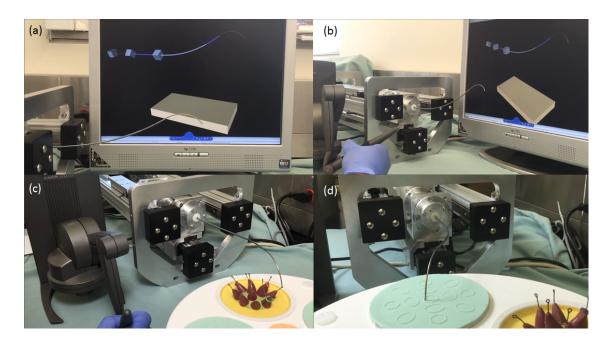


Figure 2.5: (a, b) A side-by-side view of the actual and virtual robot, which was programmed using the Virtual Reality Modeling Language (VRML) in Simulink. (c) The developed CTR prototype in a positioning task controlled by a haptic device. (d) The developed CTR prototype in a surface pattern tracking task.

generator for controlling brushless motors. Each controller is equipped with two Ethernet ports, allowing daisy-chaining multiple controllers to the main computer via a TCP/IP or UDP protocol. The control box of the entire robot consists of six of the above mentioned motion controllers and six panel mount power supplies (PMC-24V050W1AA, DeltaPSU, United States) packaged in an empty computer case.

Beside the mechanical and electrical designs, a simulation environment was developed using the Virtual Reality Modeling Language (VRML) to provide a friendly user interface. This environment is compatible with Simulink and the QuaRC toolbox, which accelerates the programming process. As shown in Fig. 2.5(a, b), the developed software presented a real-time virtual robot in a visualization computer window, which could be useful for evaluating control algorithms before implementing them on the real robot.

The performance of the second robotic prototype was tested in positioning tasks and surface tracking tasks using standard surgical training modules, as shown in Fig. 2.5(c, d). Each

stage was controlled at 10 kHz at the low level, and communicated with the computer at 1 kHz for high-level control. For the second task, the robot can track 2D patterns on a surface while regulating the position of the robot in the gravitational direction. The residual errors in regulation control did not result in applying extensive forces on the tracking pad, due to the inherent compliance of CTRs.

2.5 A Low-Cost and Compact CTR Design

The robot built in the previous section exhibited high performance in teleoperated surgical tasks. However, the cost of this robot was around \$20,000 and the size of it was $25 \times 20 \times 90$ cm (width, height, length), weighing roughly 20 kg. This bulky design does not allow it to be installed on any of the existing surgical robotic platforms; therefore, positioning and orienting this robot during surgical operations will be difficult. In addition, electrical wiring will be challenging, as it has 96 electric conductors between the drive unit and the control box, which must be protected and sealed for medical applications. In this section, a low-cost and compact CTR drive unit is proposed and implemented to address the above mentioned shortcomings. This new design minimizes the complexity in mechanical transmissions and electrical circuits, allowing this prototype to be more affordable and compact than the previous design.

As shown in Fig. 2.6, the actuation module of each tube was made of two stepper motors and an aluminum bracket. A stainless steel linear guide rail (SS_MGN12, RobotDigg, China) with three ball-bearing carriages were used to provide low-friction linear guidance and high-precision alignment between each motorized module. Three hollow-centered stepper motors (HS-Nema17, RobotDigg, China) were used for rotating the tubes. The holding torque of each motor is up to 0.4 Nm, which satisfies the specifications for driving Nitinol tubes in most medical applications. Therefore, the tubes can be directly attached to these rotary motors without the need of gearboxes or timing belts, eliminating the chances

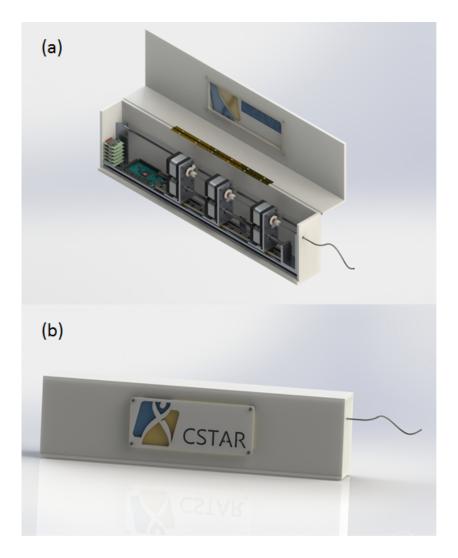


Figure 2.6: CAD design of a low-cost and compact CTR drive unit. (a) View of the main components of the proposed drive unit. (b) View of the overall robot.

of backlash. Three non-captive stepper motors (NC17HS3001-400T84, RobotDigg, China) with a threaded robot passing through their center axis were used for linear actuation. This threaded rod was the only mechanical transmission of the entire robot. Stepper drivers AMIS-30543 (ON Semiconductor, United States) were used to command these motors, which features 1/128 micro stepping, resulting in 0.014° rotary resolution and 0.00031 mm linear resolution. Each of these drivers can output 3.6 A of current without the need of cooling, and 6 A with forced air cooling. A 32-bit ARM core microcontroller board (Arduino Due, Arduino, United States) and an Ethernet shield (V2, Arduino, United States) were



Figure 2.7: Assembly of the third prototype of CTR drive unit (except for the outer case)

used to transmit the position and velocity commands from the main computer to the motor drivers. In this design, for homing the robot, three photo interrupters (OPB930W51Z, Optek Technology, United States) were mounted next to the rotary motors and another three photo interrupters (GP1A51HRJ00F, Sharp Microelectronics, United States) were mounted next to the linear guide rail. These sensors can also be used for detecting the step(s) missing in these motors during robot motion control. Four bumper switches (SS-5GL111-3, Omron Electronic Components, United States) were installed on the aluminum brackets and at one end of the guide rail to avoid collisions between the actuation modules. Based on the experimental results of the previous robotic setup, the errors in the low-level motor control were negligible compared to the total position error, as they mostly came from the inaccuracy in the kinematics of CTRs. Therefore, installing a high resolution encoder for each stepper motor was not necessary. Having said this, the errors of the robot's tip need to be compensated for either by a position sensor or a human operator in teleoperation. Finally, the total cost of the entire robot drive unit was under \$1200.

In order to access the performance of this prototype in an operating room environment, a plastic case (textured ABS) was designed to package and seal all the mechanical and electronic components into one enclosure, as shown in Fig. 2.6. The overall appearance of the robot was designed to be similar to normal-use medical devices to ease the adaption of this

technology by clinicians. The fully assembled robotic setup except for the outer case is shown in Fig. 2.7. One remaining problem is the sterilization process for this robot. After each use in animal trials, in order to detach tubes from the drive unit, these tubes have to pass through the hollow center of the stepper motors. This process could contaminate the motors' shaft with blood or other body fluids. At this stage of development, this contamination is unavoidable, requiring the motors to be cleaned each time. Future work will focus on developing a sterilizable version of this robot.

Bibliography

- [1] http://www.mmsonline.com/articles/understanding-swiss-type-machining.
- [2] Y.-L. Park, S. Elayaperumal, B. Daniel, S. C. Ryu, M. Shin, J. Savall, R. J. Black, B. Moslehi, and M. R. Cutkosky, "Real-time estimation of 3-d needle shape and deflection for mri-guided interventions," *IEEE/ASME Trans. Mechatronics*, vol. 15, no. 6, pp. 906–915, 2010.
- [3] X. He, J. Handa, P. Gehlbach, R. Taylor, and I. Iordachita, "A submillimetric 3-dof force sensing instrument with integrated fiber bragg grating for retinal microsurgery," *IEEE Trans. Biomed. Eng.*, vol. 61, no. 2, pp. 522–534, 2014.
- [4] D.-Y. Lee, J. Kim, J.-S. Kim, C. Baek, G. Noh, D.-N. Kim, K. Kim, S. Kang, and K.-J. Cho, "Anisotropic patterning to reduce instability of concentric-tube robots," *IEEE Transactions on Robotics*, vol. 31, no. 6, pp. 1311–1323, 2015.
- [5] H. Azimian, P. Francis, T. Looi, and J. Drake, "Structurally-redesigned concentric-tube manipulators with improved stability," in *Proc. IEEE/RSJ Int. Conf. Intell. Robots Syst.* IEEE, 2014, pp. 2030–2035.

Chapter 3

A Fast Torsionally Compliant Kinematic Model of Concentric-Tube Robots

Concentric-tube robots have the potential to become an important surgical tool for robotassisted percutaneous interventions. They can provide dexterous operation in a small constrained environment. The kinematic model of a concentric-tube robot has been well developed in terms of accuracy, but the computational cost places limitations on real-time implementation. In this chapter, we propose a new technique that will substantially improve the computational efficiency of evaluating the kinematics of a concentric-tube robot in the context of developing a control strategy without sacrificing the accuracy of the results. The model is validated by comparing the results obtained by computing the kinematic model corresponding to an experimental setup of a concentric-tube robot to which a force/torque sensor has been mounted at its base with those obtained directly from the experimental setup. The results indicate that it is feasible to compute the kinematics of the concentrictube robot fast enough to allow the position/force control loop to be implemented at a rate of 1 kHz.

$\{e_1, e_2, e_3\}$	World frame				
8	Arc length				
i	Tube index				
$\{d_1(s), d_2(s), d_3(s)\}$	Body frame of the cross-section located at s				
$\frac{\{d_1(s), d_2(s), d_3(s)\}}{r(s) = [x(s), y(s), z(s)]^T}$	Position vector of the cross-section located at s				
R(s)	Rotation matrix between a body frame				
	and the world frame				
$n(s) = [n_x(s), n_y(s), n_z(s)]^T$	Stress vector				
$u_i(s) = [u_{ix}(s), u_{iy}(s), u_{iz}(s)]^T$	Bending curvature and torsion of the <i>i</i> th tube				
$\hat{u}_i(s) = [\hat{u}_{ix}(s), \hat{u}_{iy}(s), \hat{u}_{iz}(s)]^T$	Pre-curvature of the <i>i</i> th tube				
$v(s) = [v_x(s), v_y(s), v_z(s)]^T$	Shear strains and elongation				
f(s)	Distributed force vector				
l(s)	Distributed moment vector				
Ki	Stiffness matrix of the i^{th} tube				
k_{ix}, k_{iy}, k_{iz}	Bending and torsional stiffness of the i^{th} tube				
$\alpha_i(s)$	Twist angle difference between the i^{th} and 1^{st} tube				
$R(\alpha_i(s))$	Rotation matrix between the body frames of				
	the i^{th} and 1^{st} tube				
L	Length of the curved section				
l	Length of the straight section				
$\theta_1(s), \theta_2(s), \theta_{i3}(s)$	Euler angles of the rotation matrix $R(s)$				
	of the i^{th} tube				

Table 3.1: Nomenclature

3.1 Introduction

The concentric-tube robots are a new type of continuum robots. A concentric-tube robot consists of several pre-curved elastic tubes inserted one inside another. By translating and rotating two consecutive tubes relative to each other, this kind of robot can achieve to fairly complex 3D shapes. The concentric-tube robot is suitable for surgical environments because it can offer more than 5-DOF (degrees of freedom) with dimensions as small as those of a needle (typically less than 3 mm in diameter). In recent years, various kinematic models of concentric-tube robots have been proposed based on different considerations. The model proposed in [1] is simple but has limited application, since it requires that the

stiffness of the outer tubes is nearly infinite compared to that of the inner tubes. Torsionally rigid models were developed in [2], with the assumption that the tubes only experience bending. The position and orientation of the robot can be obtained analytically regardless of the ratios of stiffness between tubes, and the inverse kinematics also exists in closed form [3]. The importance of introducing torsion effects into the model was shown experimentally in [4]. A kinematic model that contains the torsion of the straight section of robots was proposed in [4]. Although the solution of this model has to be evaluated numerically, the Jacobian kinematics can be obtained in closed form [5]. A torsionally compliant model that includes the torsion effects of both straight and curved sections presents significant improvement with regard to accuracy [6, 7]. However, this model is computationally very expensive, because it involves solving a set of nonlinear differential equations with twopoint boundary conditions. Additional calculations are needed because the solutions do not give the robots position and orientation directly. Other comprehensive models have also been developed by considering the friction effects in the tubes [8] or external loads [9]. The complexity of these models increases as more mechanical effects are included. Efforts have been made to achieve a trade-off between computational efficiency and numerical accuracy. In [10] a function approximation method was developed to implement a torsionally

compliant model in real-time for position control with minimum loss of accuracy. However, the approach requires pre-computation of a large dataset of position and orientation information over the entire workspace. A Fast Jacobian-based inverse kinematic algorithm was presented in [11], and it was shown that the computational time can be reduced to 40 ms for a 3-tube robots. In this chapter, we propose a technique which can significantly decrease the computation time to evaluate a torsionally compliant model in the context of implementing a kinematic control strategy for a concentric-tube robot. This is achieved by improving the model in the following three steps:

- Reformulating the torsionally compliant kinematic model with global variables.
- Piecewise-linearization of the reformulated model.

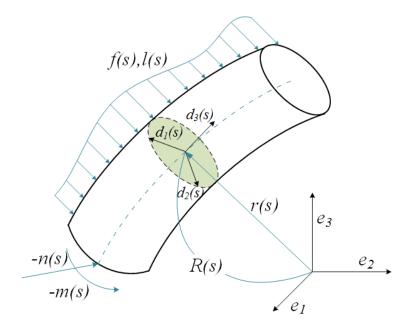


Figure 3.1: Cosserat rod

Measuring all the initial conditions to avoid the two-point boundary problems. These
measurements (which are obtained in real-time during the implementation of a kinematic control strategy) provide inputs for computing the model used in kinematic
control of the robot.

It is shown from the experiments that the computation time is reduced to less than 1 ms using this technique (see Section 3.3). At the same time, the accuracy of this model remains almost equivalent to that of the torsionally compliant models proposed in the literature.

3.2 Kinematic Model

3.2.1 Cosserat Rod

Cosserat rod theory is extensively used in modeling and simulation of slender elastic objects. The elastic tubes used in concentric-tube robots are actually a very good example

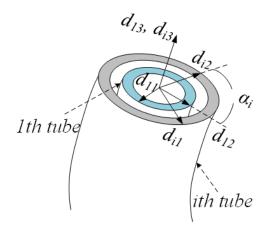


Figure 3.2: Body frames of tube i and the 1st.

of Cosserat rods in 3-D space. The recent kinematic models of concentric-tube robots, including our work, also follow the notation and formulation from the Cosserat model. Therefore, it is necessary to summarize some relevant background concerning Cosserat rod theory. Fig. 3.1 shows a flexible rod in the world-frame $\{e_1, e_2, e_3\}$. A body frame $\{d_1(s), d_2(s), d_3(s)\}$ is attached at an arbitrary cross-section of the rod, where s is the arc length along the center line. The position of this cross-section is represented by the vector r(s), and the orientation is defined by the rotation matrix R(s) between two frames. When the rod experiences a distributed force f(s) and moment l(s), the equations of equilibrium [12] have the following form:

$$\dot{n}(s) + u(s) \times n(s) + f(s) = 0$$
(3.1)

$$\dot{m}(s) + u(s) \times m(s) + v(s) \times n(s) + l(s) = 0$$
(3.2)

where the vector $u(s) = [u_x(s), u_y(s), u_z(s)]^T$ includes the bending curvature $(u_x(s), u_y(s))$, and the torsional curvature $u_z(s)$; and $v(s) = [v_x(s), v_y(s), v_z(s)]^T$ denotes the shear strain $(v_x(s), v_y(s))$ and elongation $v_z(s)$. Both of these vectors are local variables in body frames.

In Cosserat rod theory, curvatures are interpreted as angular rates of change when the body frame slides along the center line. So they have the same expressions as the angular velocity

in rigid-body motion:

$$[u(s)] = R^T(s)\dot{R}(s) \tag{3.3}$$

where [u(s)] is the skew-symmetric matrix corresponding to the vector u(s). Similarly, the shear strain and elongation are analogous to displacements in rigid-body motion and formulated as:

$$[v(s)] = R^T(s)\dot{r}(s) \tag{3.4}$$

But in our application, these phenomena can be ignored which results in v(s) = [0, 0, 1].

3.2.2 Torsionally Compliant Model

Torsionally compliant models show great improvements on accuracy, compared to previous models. The equations from this model also play an important role in our method, so a brief description is exhibited here.

For concentric-tube robots, the following assumptions are made for modeling: 1) At any point along the robot, all the assembled tubes conform to the same curvature; 2) without an external force or moment, the net moment at every cross section of the robot is zero; 3) the bending moment generated by a single tube obeys a linear constitutive equation (arc length s will be omitted for compact expressions):

$$m_i = K_i (u_i - \hat{u}_i) \tag{3.5}$$

in which \hat{u}_i and u_i are the curvatures of the i^{th} tube before and after the conformation, respectively. In the rest of this chapter, the subscript *i* refers to the i^{th} tube. K_i is the stiffness matrix ($K_i = diag[k_{ix}, k_{iy}, k_{iz}]$). Based on these assumptions, the bending curvature of the combined tubes can be formulated as:

$$\begin{bmatrix} u_{ix}(s) \\ u_{iy}(s) \end{bmatrix} = \left(\left(\sum_{j=1}^{n} K_j \right)^{-1} R_Z^T(\alpha_i(s)) \sum_{j=1}^{n} R_Z^T(\alpha_i(s)) K_j \begin{bmatrix} \hat{u}_{jx}(s) \\ \hat{u}_{jy}(s) \end{bmatrix} \right)$$
(3.6)

where $\alpha_i(s)$ represents the angle difference between the body-frames of tube *i* and the 1st and $R(\alpha_i(s))$ represents the rotation matrix between those two, as shown in Fig. 3.2. The formulation of the torsional curvature is achieved by using equations of equilibrium (Eq. (3.2)) from Cosserat rod theory and the constitutive Eq. (3.4):

$$\dot{u}_{iz} = \left(\frac{k_{ix}}{k_{iz}}\right) \left(u_{ix}\hat{u}_{iy} - u_{iy}\hat{u}_{ix}\right) \tag{3.7}$$

By definition of and , we can also conclude:

$$\dot{\alpha}_i = u_{iz} - u_{1z} \tag{3.8}$$

Eqs. (3.6), (3.7) and (3.8) comprise the torsionally compliant model in [6], with boundary conditions $\alpha_i(0)$ (known as input) and $u_{iz}(L) = 0$. More details about this model are given in [6].

3.2.3 Fast Torsionally Compliant Model

As discussed above, the torsionally compliant model is a set of differential equations with two-point boundary conditions. These equations consume a large amount of computational time but only result in a curvature function with respect to the arc length. This function then requires two integrations to calculate the position and orientation of the robot [6]. In our new model, we reformulate the torsionally compliant model with global variables. So the two step calculations can be compressed into one. The bridge between local and global variables lies in Eqs. (3.3) and (3.4) where the rotation matrix R(s) can be parameterized with Euler angles:

$$R(s) = R(\theta_1(s))R(\theta_2(s))R(\theta_3(s))$$
(3.9)

Substituting (3.9) into (3.3), the expressions of curvatures using Euler angles are obtained [13]

(arc length s will be omitted for compact expressions):

$$u_x = \dot{\theta}_1 \cos(\theta_2) \cos(\theta_3) + \dot{\theta}_2 \sin(\theta_3) \tag{3.10}$$

$$u_y = \dot{\theta}_2 \cos(\theta_3) - \dot{\theta}_1 \cos(\theta_2) \sin(\theta_3) \tag{3.11}$$

$$u_z = \dot{\theta}_3 + \dot{\theta}_1 \sin(\theta_2) \tag{3.12}$$

In the same manner, the relationship between positions and Euler angles is obtained by solving (3.4) [13]:

$$\dot{x} = \sin(\theta_2) \tag{3.13}$$

$$\dot{y} = -\sin(\theta_1)\cos(\theta_2) \tag{3.14}$$

$$\dot{z} = \cos(\theta_1)\cos(\theta_2) \tag{3.15}$$

in which x, y, z are position coordinates in world frame. Applying Eqs. (3.10), (3.11) and (3.12) on the torsionally compliant model Eqs. (3.6), (3.7) and (3.8), we get:

$$\dot{\theta}_1 = \frac{u_{ix}\cos(\theta_{i3}) - u_{iy}\sin(\theta_{i3})}{\cos(\theta_2)}$$
(3.16)

$$\dot{\theta}_2 = u_{ix}\sin(\theta_{i3}) + u_{iy}\cos(\theta_{i3}) \tag{3.17}$$

$$\dot{\theta}_{i3} = u_{iz} - \dot{\theta}_1 \sin(\theta_2)$$
 (3.18)

$$\alpha_i(s) = \theta_{i3} - \theta_{13} \tag{3.19}$$

$$\begin{bmatrix} u_{ix} \\ u_{iy} \end{bmatrix} = \left(\left(\sum_{j=1}^{n} K_j \right)^{-1} R_Z^T(\theta_{j3} - \theta_{13}) \sum_{j=1}^{n} R_Z^T(\theta_{j3} - \theta_{13}) K_j \begin{bmatrix} \hat{u}_{jx} \\ \hat{u}_{jy} \end{bmatrix} \right)$$
(3.20)

where θ_{i3} represents the 3^{rd} Euler angle of tube *i*. As shown in Fig. 3.2, all tubes share the same θ_1 and θ_2 . Equations (3.7), (3.13), (3.14), (3.15), (3.16), (3.17), (3.18) and (3.20) form the new torsionally compliant model with Euler angles. Solving these equations directly gives the information of position and orientation. One drawback of this model is that

Eq. (3.16) has a singular point at $\theta_2 = 90^\circ$, but in most applications that angle is not close to 90° . The initial conditions of these equations are directly known from inputs, except one of which need to be calculated:

$$u_{iz}(0) = \frac{Torque}{k_{iz}}$$
(3.21)

m

in which *Torque* is the value measured from Force/Torque sensor attached at the proximal end of the tubes. This model can be simplified (by piecewise linearization) to a set of linear differential equations. Considering the new kinematic model as a vector function $(\bar{f}(u_{iz}, \theta_1, \theta_2, \theta_{i3}, x, y, z))$, and applying the Taylor series expansion, we get:

$$[\dot{u}_{iz}, \dot{\theta}_1, \dot{\theta}_2, \dot{\theta}_{i3}, \dot{x}, \dot{y}, \dot{z}]^T = \begin{bmatrix} a_1, a_2, a_3, a_4, a_5, a_6, a_7\\ b_1, b_2, b_3, b_4, b_5, b_6, b_7 \end{bmatrix}^T \begin{bmatrix} 1\\ s \end{bmatrix}$$
(3.22)

By solving Eq. (3.22), a closed-form kinematic model is obtained for each linear model:

$$[u_{iz}, \theta_1, \theta_2, \theta_{i3}, x, y, z] = \bar{g}(s) + \bar{C}$$
(3.23)

where all entries in $\bar{g}(s)$ are second-order polynomials, and the vector \bar{C} denotes the initial conditions. The accuracy of Eq. (3.23) is very good when s is small. So in the implementation of full model, it is necessary to divide the whole robot into segments and use the linear model consecutively.

3.3 Experiments

For verifying the fast kinematic model, experiments were performed on four pairs of elastic tubes. The material chosen for these tubes was Nitinol, because of its shape setting property and linear elastic behavior. The specifications of all tube pairs are listed in Table 3.2. The setup for the experiments is shown in Fig. 3.3. The outer tube was fixed, and the inner tube was rotated with the motorized stage. The force/torque sensor was installed at the

Tube pair (outer/inner)	1	2	3	4
$l (\mathrm{mm})^a$	0/52.8	0/63.5	0/63.5	0/56.4
$L (\mathrm{mm})^a$	152.6/152.6	157/157	157/157	157/157
$r (\mathrm{mm})^a$	250/250	150/150	150/150	150/150
Stiffness ratio	1/1.79	1/1.30	1/0.76	1/1.79

Table 3.2: Parameters of Four Tube Pairs

^aThe lengths of straight and curved sections of tubes are represented by l and L, respectively. The radius of curvature is denoted as r.

base of the outer tube. An EM (electromagnetic) tracker was installed on the tip of the tube pair using a plastic adaptor. The position of the robots tip can be obtained from the EM tracking system. The effect of gravity as a result of the EM tracker and adaptor was negligible. Since the field generator has the strongest magnetic field in the middle front, the tip of the robot was positioned there to obtain the best accuracy. While this tracking system is accurate to within 1mm, a larger error may occur depending on the accuracy of the method of registration between the tracker and the robot. It should be noted that the angles read from the rotary stage are not the inputs of our model. Actually, because of the torsional effect in the straight part of the tube pair, the inputs need to be calculated as:

$$\theta_{13}(0) = 0 + \frac{Torque}{k_{1z}}, \\ \theta_{23} = Angle - \frac{Torque}{k_{2z}}l_2$$
(3.24)

where *Angle* is the angular position of the rotary stage. The positions measured in the experiments are relative to the starting point of the curved section of the robot. In the experiments, the torque at the proximal end was measured and used as the initial condition for the fast kinematic model. For these tube pairs, the final position was obtained by applying the linear model on 10 mm length segments consecutively (16 segments in total for a robot of 157 mm length). The results showed that the loss of accuracy due to linearization is around 0.1 mm. The difference between the positions predicted by the fast kinematic model and the corresponding values measured during the experiment denotes the errors resulting from the model. As shown in Table 3.3, these errors are similar to those in [8].

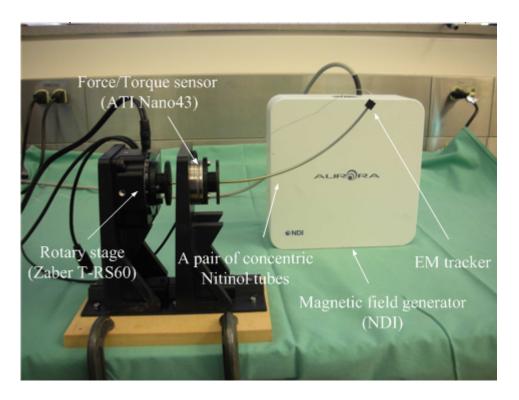


Figure 3.3: Experimental setup for evaluating kinematic model.

Rotary Stage Angle (°)	0	60	120	180	240	300	Average	Max
Pair 1	0.7	1.8	1.0	1.7	1.8	1.7	$1.5 \ (1.0\%)^a$	1.9
Pair 2	1.3	0.7	3.1	8.1	3.1	1.8	3.0 (1.9%)	8.1
Pair 3	1.4	1.8	1.9	10.0	4.0	2.6	3.5 (2.2%)	10.0
Pair 4	1.2	4.9	2.8	9.0	5.7	4.4	4.7 (3.0%)	9.0

Table 3.3: Position Errors of Four Tube Pairs (mm)

^a Values in brackets are normalized errors (the tip errors divide by the length of robot).

Because the main parameters of the tube pair used here (curvature, length of tube, and stiffness ratio) are almost the same as those in [8], we can conclude that our model possesses good accuracy. In terms of the computational time, the fast torsionally compliant kinematic model only takes $0.2 \sim 0.3$ ms to solve. For a 3-tube robot, this time will not exceed 1ms. All the programs were run in MATLAB R2010a, under Windows XP, in a computer with an Intel Xeon 3.2 GHz processor. In a future implementation, we expect to obtain further improvement in computational time by coding the algorithm in C++.

3.4 Conclusion

Concentric-tube robots are a new technology which has excellent potential for applications in minimally invasive surgery and therapy. Several different kinematic models for this robot have been developed. However, most models suffer from the problem of computational cost in evaluation of the models. A new approach has been developed that significantly reduces the computation cost by avoiding two-point boundary problems and piece-wise linearization. Experiments for several tube pairs having comparable parameters (lengths of the tubes, stiffness ratio, etc) as those reported in the literature took a lot less computation time while giving similar accuracy. Our ongoing work is aimed at extending the approach for the Jacobian and also designing a model-based robust control scheme that will allow us to address to some extent the effect of uncertainty due to dynamic changes, sensor noise, etc.

Bibliography

- J. Furusho, "Curved multi-tube systems for fetal blood sampling and treatments of organs like brain and breast," *Int. J. Comput. Assist. Radiol. Surg.*, vol. 1, no. 1, pp. 223–226, 2006.
- [2] P. Sears and P. Dupont, "A steerable needle technology using curved concentric tubes," in *Proc. IEEE/RSJ Int. Conf. Intell. Robots Syst.*, 2006, pp. 2850–2856.
- [3] P. Sears and P. E. Dupont, "Inverse kinematics of concentric tube steerable needles," in *Proc. IEEE Int. Conf. Robot. Autom.* IEEE, 2007, pp. 1887–1892.
- [4] R. J. Webster III, J. M. Romano, and N. J. Cowan, "Mechanics of precurved-tube continuum robots," *IEEE Trans. Robot.*, vol. 25, no. 1, pp. 67–78, 2009.
- [5] R. J. Webster III, J. P. Swensen, J. M. Romano, and N. J. Cowan, "Closed-form differential kinematics for concentric-tube continuum robots with application to visual servoing," in *Experimental Robotics*. Springer, 2009, pp. 485–494.
- [6] P. E. Dupont, J. Lock, B. Itkowitz, and E. Butler, "Design and control of concentrictube robots," *IEEE Trans. Robot.*, vol. 26, no. 2, pp. 209–225, 2010.
- [7] D. C. Rucker and R. J. Webster, "Mechanics-based modeling of bending and torsion in active cannulas," in *Proc. IEEE RAS/EMBS Int. Conf. on Biomed. Rob. Biomech.* IEEE, 2008, pp. 704–709.
- [8] J. Lock and P. E. Dupont, "Friction modeling in concentric tube robots," in *Proc. IEEE Int. Conf. Robot. Autom.* IEEE, 2011, pp. 1139–1146.
- [9] D. C. Rucker, B. A. Jones, and R. J. Webster III, "A geometrically exact model for externally loaded concentric-tube continuum robots," *IEEE Trans. Robot.*, vol. 26, no. 5, pp. 769–780, 2010.

- [10] P. E. Dupont, J. Lock, and B. Itkowitz, "Real-time position control of concentric tube robots," in *Proc. IEEE Int. Conf. Robot. Autom.* IEEE, 2010, pp. 562–568.
- [11] D. C. Rucker and R. J. Webster, "Computing jacobians and compliance matrices for externally loaded continuum robots," in *Proc. IEEE Int. Conf. Robot. Autom.* IEEE, 2011, pp. 945–950.
- [12] S. S. Antman, "Nonlinear problems of elasticity, 1995."
- [13] I. G. Tadjbakhsh and D. C. Lagoudas, "Variational theory of motion of curved, twisted and extensible elastic rods," *International journal of engineering science*, vol. 32, no. 4, pp. 569–577, 1994.

Chapter 4

Position Control of Concentric-Tube Continuum Robots using a Modified Jacobian-Based Approach

Concentric-tube robots can offer dexterous positioning even in a small constrained environment. This technology turns out to be beneficial in many classes of minimally invasive procedures. However, one of the barriers to the practical use of a concentric-tube robot is the design of a real-time control scheme. In previous work by the authors, a computationally efficient torsionally compliant kinematic model of a concentric-tube robot was developed. Using this computationally fast technique and deriving the robot's Jacobian, a new position control approach is proposed in this chapter. This mechanism provides computational efficiency as well as good tracking accuracy. To evaluate the performance, experiments were conducted, and the results obtained demonstrate the feasibility of enabling the robot's tip to perform trajectory tracking in real time.

$\{e_1, e_2, e_3\}$	World frame				
8	Arc length				
i	Tube index				
$\{d_1(s), d_2(s), d_3(s)\}$	Body frame of the cross-section located at s				
$n(s) = [n_x(s), n_y(s), n_z(s)]^T$	Stress vector of the cross-section located at s				
$m(s) = [m_x(s), m_y(s), m_z(s)]^T$	Bending moment vector				
$u_i(s) = [u_{ix}(s), u_{iy}(s), u_{iz}(s)]^T$	Bending curvature and torsion of the i^{th} tube				
$\hat{u}_i(s) = [\hat{u}_{ix}(s), \hat{u}_{iy}(s), \hat{u}_{iz}(s)]^T$	Pre-curvature of the i^{th} tube				
$v(s) = [v_x(s), v_y(s), v_z(s)]^T$	Shear strains and elongation				
f(s)	Distributed force vector				
l(s)	Distributed moment vector				
K_i	Stiffness matrix of the i^{th} tube				
$\frac{k_{ix}, k_{iy}, k_{iz}}{L}$	Bending and torsional stiffness of the i^{th} tube				
	Length of the curved section				
$\Theta(s) = \theta_1(s), \theta_2(s), \theta_{i3}(s)$	Euler angles of the rotation matrix $R(s)$				
	of the i^{th} tube				
$X(s) = [x(s), y(s), z(s)]^T$ R_Z	Position vector of the cross-section located at s				
R_Z	Rotation matrix between the body frames of				
	the i^{th} and 1^{st} tube				
F^n	Forward kinematics of the n^{th} sub-link				
\widetilde{F}^m	Forward kinematics of the m^{th} link				
$ ilde{F}$	Forward kinematics of the entire robot				
p_k	Position of the proximal end of the k^{th} tube				
J_G^i	Jacobian matrix of a sub-link with varying length				
J_M^i	Jacobian matrix of a sub-link with fixed length				
$\begin{array}{c c} & p_k \\ \hline & J_G^i \\ \hline & J_M^i \\ \hline & J_L^i \\ \hline & \tilde{J}_M^m \end{array}$	Jacobian matrix of the last sub-link of the robot				
\widetilde{J}^m	Jacobian matrix of the m^{th} link				
\widetilde{J}	Jacobian matrix of the entire robot				
$\chi(s) = [u_{iz}(s), \Theta(s), X(s)]$	Vector of kinematic variables				

Table 4.1: Nomenclature

4.1 Introduction and Prior Work

To minimize collateral damage to live tissue and access confined areas in minimally invasive procedures, surgical interventions are required that follow complex curved paths inside soft tissue. To this end, flexible needles have been widely used [1] as primary tools while erroneous guidance reduces the effectiveness of the planned therapy or diagnosis.

As an alternative, a concentric-tube robot as a subset of continuum robots is a new technology which provides more dexterity compared to a standard bevel-tip flexible needle or a catheter while having almost the same size [2-10]. This category of instruments has the potential to facilitate targeting in applications in which a complex 3D curvature is required. Another advantage of this developing family of tools is safety enhancement due to its inherent compliance compared with the traditional rigid surgical tools; so they can offer a suitable compromise between stiffness and curvature control. Furthermore, the shaft of the tubes can accommodate cables for controlling articulated tools mounted at the tip. For more details on design and analysis, please see [2, 5].

Note that compared with traditional robotic arms, this family of robots lacks rigid links and discrete joints. Thus, their kinematics cannot be represented solely in terms of constrained motion between rigid bodies, and it must include the deformation of the individual tubes as well. This fact adds more complexity to the modeling and therefore to the real-time control problem for this kind of robotic structures. In this regard, various modeling schemes for concentric-tube robots have been developed over the last few years; however, a variety of mechanical phenomena, e.g., torsion, nonlinear elasticity, and friction, have been ignored in order to simplify the modeling steps or accelerate the process time.

Under certain assumptions on the geometry of the tubes, closed-form forward kinematics can be represented by means of algebraic expressions. Finding the inverse kinematics is also not straightforward in general due to the nonlinear mapping between relative tube displacements and tip configuration as well as due to the multiplicity of solutions. In [9], the tubes were approximated as rigid in torsion and frictionless with piecewise constant curvatures, and forward and inverse kinematic equations were derived. Sears and Dupont presented a generalized inverse Jacobian method for solving the inverse kinematics disregarding the torsion [3].

The importance of including torsional effects was shown in [2, 5–7]. Dupont et al. [2]

developed a torsion model that was applicable to any number of tubes whose stiffness and initial curvature could be arbitrary functions of arc length. In [5], a kinematic model containing only the torsion component of the straight segments was introduced. However, the authors hypothesized that torsion in the curved sections was the most significant unmodeled effect. Webster et al. [7], derived the differential kinematics of a general n-tube active cannula while accounting for torsional compliance in order to improve tip pose prediction. A compliant model including the torsional effects in both straight and curved sections significantly improved accuracy in [6]; however, this model was computationally very expensive.

Deformation of a concentric-tube robot in response to the external contact forces is another important issue. Lock et al. [4] showed that compared with the unloaded model, tip loading could increase the mean tip error by almost 50%. Hence, they developed a quasistatic model relating the externally applied loads to the robot's shape and tip configuration. Rucker et al. [8] applied Cosserat-rod theory to model forward kinematics to describe large deflections as a result of external point or distributed wrench loads.

Towards position control as the main motivation of our study, Dupont et al. [2] developed a functional approximation method to include torsional compliance and achieve computational efficiency for position control. However, this approach required pre-computation of the forward kinematics over the entire workspace and then its approximation using a truncated Fourier series. The research described in this chapter is in line with our previous work [10] and focuses on developing a feasible control strategy for concentric-tube robots without sacrificing accuracy. As is well known, computational cost places limitations on real-time implementations. To overcome this problem, we introduced a fast torsionally compliant kinematic model for a concentric-tube robot using Cosserat theory [10]. In the current study, we exploit this model to control the position of the robot's tip using the robot's Jacobian while the torsional effects for both straight and curved sections are incorporated.

The rest of this chapter is organized as follows. Section 4.2 reviews our Cosserat-rod-

4.2. A MODIFIED JACOBIAN-BASED STRATEGY FOR POSITION CONTROL

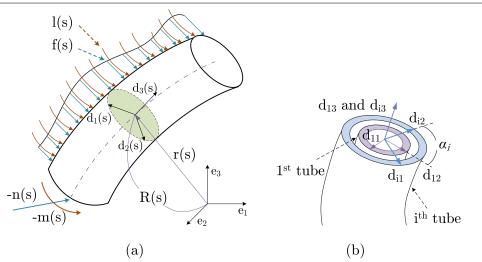


Figure 4.1: (a) Cosserat beam (b) cross section of a concentric-tube robot showing coordinate frames associated with the 1^{st} and the i^{th} tubes.

based model, and introduces the resultant Jacobian. The mechanism utilized for position control is also described in this section. Section 4.3 presents a simulation study and this is followed by an experimental evaluation in Section 4.4. Finally, Section 4.5 concludes the chapter with suggestions for future work.

4.2 A Modified Jacobian-Based Strategy For Position Control

4.2.1 A Fast Torsionally Compliant Model

Following the procedure outlined in [10], we developed a fast model which included torsional effects along the entire robotic arm. This framework is summarized here to provide the basis for the rest of the study.

Concentric-tube robots can be considered as a set of elastic rods undergoing distributed force and torque generated by mechanical interactions. According to the Cosserat theory,

each single elastic rod satisfies the equilibrium equations

$$\dot{n}(s) + u(s) \times n(s) + f(s) = 0$$
(4.1)

$$\dot{m}(s) + u(s) \times m(s) + v(s) \times n(s) + l(s) = 0$$
(4.2)

where m(s) and n(s) are the moment and stress vectors in the cross-section in terms of the length variable s. f(s) and l(s) are distributed force and torque along the rod, respectively. Herein, vector u(s) consists of bending and torsional curvatures, while v(s) includes shear deformation and elongation. Accordingly, the kinematics of an elastic rod can be completely defined by the vectors u and v expressed in the body frame $\{d_1(s), d_2(s), d_3(s)\}$ shown in Fig. 4.1(a).

Equations (4.1) and (4.2) can be extended to multiple elastic rods [2], and forwards kinematics referring to the mapping between joint space and Cartesian space variables can be represented by the following equations in which the inputs and outputs are both expressed in Cartesian space [10]. In order to improve computational efficiency, the kinematics is reformulated using Euler angles as shown below.

$$\dot{\theta}_1(s) = \frac{u_{ix}(s)\cos\theta_{i3}(s) - u_{iy}(s)\sin\theta_{i3}(s)}{\cos\theta_2(s)}$$

$$\tag{4.3}$$

$$\dot{\theta}_2(s) = u_{ix}(s)\sin\theta_{i3}(s) + u_{iy}(s)\cos\theta_{i3}(s) \tag{4.4}$$

$$\dot{\theta}_{i3}(s) = u_{iz}(s) - \dot{\theta}_1(s)sin\theta_2(s)$$
(4.5)

$$\dot{x}(s) = \sin\theta_2(s) \tag{4.6}$$

$$\dot{y}(s) = -\sin\theta_1(s)\cos\theta_2(s) \tag{4.7}$$

$$\dot{z}(s) = \cos\theta_1(s)\cos\theta_2(s) \tag{4.8}$$

$$\begin{bmatrix} u_{ix}(s) \\ u_{iy}(s) \end{bmatrix} = \left(\left(\sum_{j=1}^{n} K_{j} \right)^{-1} R_{Z}^{T}(\theta_{j3}(s) - \theta_{13}(s)) \right)$$

$$\times \sum_{j=1}^{n} R_{Z}^{T}(\theta_{j3}(s) - \theta_{13}(s)) K_{j} \begin{bmatrix} \hat{u}_{jx}(s) \\ \hat{u}_{jy}(s) \end{bmatrix} \right)$$

$$\dot{u}_{iz}(s) = \frac{k_{ix}(s)}{k_{iz}(s)} \left(u_{ix}(s) \hat{u}_{iy}(s) - u_{iy}(s) \hat{u}_{ix}(s) \right)$$

$$(4.10)$$

in which, the subscript *i* refers to the tube number. \hat{u}_i is also the initial curvature value while u_i represents its value after conformation. Here, $K_i = diag(k_{ix}, k_{iy}, k_{iz})$ denotes the stiffness matrix calculated from Young's modulus and moment of inertia, and θ_{i3} is the 3rd Euler angle of the ith tube. The transformation between the body frames of the 1st and the ith tubes is also represented by a pure rotation denoted by the matrix R_Z .

4.2.2 Jacobian Derivation for the Concentric-Tube Robots

Solving Eqs. (4.3)-(4.10), the robot's position and orientation are directly obtained with no need to perform extra calculation to convert local curvatures into Cartesian coordinates. However, the reformulated structure includes a nonlinear differential equation; so linearization is employed to derive the closed-form solution. To this end, let us rearrange the above kinematic model in a compact form in which $\Theta(s) = [\theta_1(s) \ \theta_2(s) \ \theta_{i3}(s)]^T$ and $X(s) = [x(s) \ y(s) \ z(s)]^T$. Applying the Taylor series expansion and keeping the firstorder terms, we have

$$\begin{bmatrix} \dot{u}_{iz}(s) \\ \dot{\Theta}(s) \\ \dot{X}(s) \end{bmatrix} = \begin{bmatrix} g_{11} & g_{12} \\ g_{21} & g_{22} \\ g_{31} & g_{32} \end{bmatrix} \begin{bmatrix} 1 \\ s \end{bmatrix}$$
(4.11)

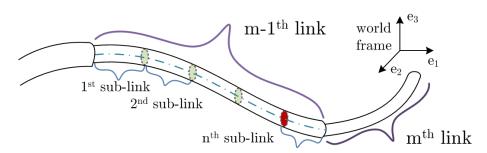


Figure 4.2: Links and sub-links of a concentric-tube robot.

in which, $g_{ij} = g_{ij}(u_{iz}(0), \Theta(0), X(0))$. Thus, the sought solution is produced by integration of Eq. (4.11) with respect to s.

$$F = \begin{bmatrix} u_{iz}(s) \\ \Theta(s) \\ X(s) \end{bmatrix} = \begin{bmatrix} g_{11} & g_{12} \\ g_{21} & g_{22} \\ g_{31} & g_{32} \end{bmatrix} \begin{bmatrix} s \\ \frac{1}{2}s^2 \end{bmatrix} + \begin{bmatrix} u_{iz}(0) \\ \Theta(0) \\ X(0) \end{bmatrix}$$
(4.12)

Due to linearization, the function approximation in Eq. (4.12) is accurate to within small intervals so this numerical technique can be considered as a piecewise closed-form solution. Hence, prior to its use, the entire robotic arm needs to be divided into links and small sub-links as shown in Fig. 4.2. Successive approximation for each sub-link is then performed. As a result, forward kinematics of the $(m-1)^{th}$ link is obtained as $\tilde{F}^{m-1} =$ $F^n(F^{n-1}(...F^1(u_{iz}^1(0), \Theta^1(0), X^1(0), l^1)..., l^{n-1}), l^n)$. Herein, for the jth sub-link $(1 \le j \le n)$, l^j is the corresponding length while the function F^j maps the vector $[u_{iz}^j(s) \Theta^j(s) X^j(s)]^T$ evaluated at its proximal end to the same vector evaluated at the sub-link's distal end using Eq. (4.12). Moreover, $l^j = H^j(p_1, p_2, ..., p_k)$ where k is the number of tubes in the entire robot, and p is the position of the proximal end. Finally, the forward kinematics of the entire robot is consecutively obtained in a similar manner, i.e., $\tilde{F} = \tilde{F}^m(\tilde{F}^{m-1}(...\tilde{F}^1()...))$.

In conjunction with the analytical solution introduced in subsection 4.2.1, the closed-form forward kinematics is differentiated to produce the Jacobian matrix for each sub-link. It

will be employed later on for control of concentric-tube robots. Using Eq. (4.12), the Jacobian is derived as

$$J_{G}^{j} = \begin{bmatrix} J_{g1}^{j} & J_{g2}^{j} \\ 0 & I_{k \times k} \end{bmatrix}$$
(4.13)

where

$$J_{g1}^{j} = \begin{bmatrix} \frac{\partial F^{j}}{\partial u_{iz}^{j}(0)} & \frac{\partial F^{j}}{\partial \Theta^{j}(0)} & \frac{\partial F^{j}}{\partial X^{j}(0)} \end{bmatrix}$$
(4.14)

$$J_{g2}^{j} = \begin{bmatrix} \frac{\partial F^{j}}{\partial H^{j}} \frac{\partial H^{j}}{\partial p_{1}} & \frac{\partial F^{j}}{\partial H^{j}} \frac{\partial H^{j}}{\partial p_{2}} & \dots & \frac{\partial F^{j}}{\partial H^{j}} \frac{\partial H^{j}}{\partial p_{k}} \end{bmatrix}$$
(4.15)

The last row in Eq. (4.13) was added to J_G^j so that consecutive Jacobian matrices of the sub-links can be multiplied together.

Except for the last sub-link, the lengths of the other sections do not change with respect to time. Only when the length of the last sub-link decreases to zero, the second sub-link towards the end starts to vary its length. Thus, except for the last sub-link, the Jacobian is not influenced by the linear motion of the concentric tube which results in $J_{g2}^{j} = 0$. This simplifies the corresponding Jacobian into

$$J_M^j = \begin{bmatrix} J_{g_1}^j & 0\\ 0 & I_{k \times k} \end{bmatrix}$$
(4.16)

For the last sub-link of the entire robot, the last row of the Jacobian matrix in Eq. (4.13) should be removed so that

$$J_L^j = \begin{bmatrix} J_{g1}^j & J_{g2}^j \end{bmatrix}$$
(4.17)

Using the chain rule, the Jacobian for the $(m-1)^{\text{th}}$ link \tilde{J}^{m-1} is obtained by multiplication of individual Jacobians in the following manner.

$$\tilde{J}^{m-1} = J^n J^{n-1} \dots J^2 J^1 \tag{4.18}$$

in which, J^j $(1 \le j \le n)$ is the Jocobian associated with the jth sub-link, and depending on the configuration, J^j is selected from the set $\{J_G^j, J_M^j, J_L^j\}$.

Thus, the relationship between the velocities of the distal and proximal ends is established as

$$[\dot{u}_{iz}(L) \dot{\Theta}(L) \dot{X}(L)]^T = \tilde{J}[\dot{u}_{iz}(0) \dot{\Theta}(0) \dot{X}(0)]^T$$
(4.19)

where $\tilde{J} = \tilde{J}^m \tilde{J}^{m-1} \dots \tilde{J}^1$, and L is the total length of the assembled robot. To control the tip's position, only $\Theta(L)$ and X(L) are required. However, based on the assumption of a torsionally compliant model outlined in subsection 4.2.1, $u_{iz}(L)$ equals zero in any position, which leads to $\dot{u}_{iz}(L) = 0$. This constraint has to be considered during position control. From this perspective, the Jacobian derived in this section is actually an augmented Jacobian with constraint on velocities in Cartesian space.

4.2.3 The Multi-Step Jacobian Method

In surgical robotics, maintaining smooth and safe motion is critical and must be guaranteed. When the inverse kinematics is implicit, such as in concentric tubes, the tracking accuracy can be improved by updating the inverse Jacobian at a high rate which in turn increases computational complexity. Thus, the following approximation is suggested to obtain an accurate approximation of the robot's inverse kinematics which can generate a smooth trajectory even at low control rates. Let us revisit the forward kinematics as following

$$\chi(L) = [u_{iz}(L) \ \Theta(L) \ X(L)]^T = \tilde{F}(\chi(0))$$
(4.20)

Performing a Taylor series expansion on Eq. (4.20), and keeping only the 1^{st} order term, Eq. (4.20) is converted to Eq. (4.22) which is employed in an inverse Jacobian-based control scheme.

$$\Delta\chi(L) = \overbrace{\begin{bmatrix}\frac{\partial\tilde{F}}{\partial\chi_1(0)} & \frac{\partial\tilde{F}}{\partial\chi_2(0)} & \dots & \frac{\partial\tilde{F}}{\partial\chi_i(0)}\end{bmatrix}}^{J} \cdot \Delta\chi(0) + H.O.T$$
(4.21)

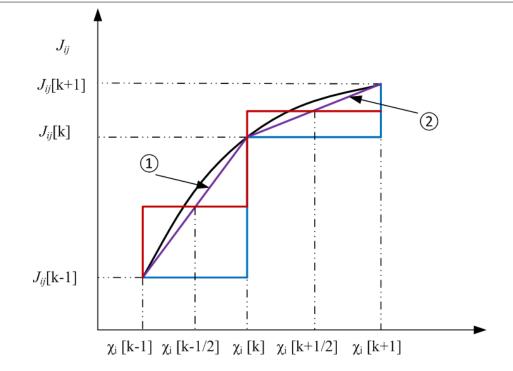


Figure 4.3: Function approximation using a multi-step approach.

$$\Delta \chi(L) \cong \tilde{J} \Delta \chi(0) \Rightarrow \Delta \chi(0) \cong J^{\dagger} \Delta \chi(L)$$
(4.22)

 J^{\dagger} is the inverse or pseudo-inverse of the Jacobian matrix that is used as a first order approximation of inverse kinematics. Inclusion of higher order terms (HOTs) is avoided in our implementation.

To have a fast approximation of the Jacobian while not sacrificing accuracy, the following procedure is exploited. Let us assume that the function shown in black in Fig. 4.3 is an arbitrary element of the Jacobian matrix, e.g., \tilde{J}_{ij} , whose value changes with respect to χ_i . During each control step, function \tilde{J}_{ij} can be estimated using a zero-order hold shown by the blue line. The area between the black and blue curves corresponds to the approximation error, and it decreases as a higher control rate is chosen. Using a first-order hold represented by the purple curve also provides a more accurate solution, but it is avoided here due to computational issues. Our suggested technique is to introduce a new zero-order hold function shown in red which covers almost the same area as the first-order hold does, but is easier to be evaluated in each control step. The value of the first-order hold evaluated at the middle point in each iteration is chosen as the value of this new hold function. Therefore,

$$\tilde{J}_{ij}[k+\frac{1}{2}] = \tilde{J}_{ij}[k] + \frac{\tilde{J}_{ij}[k+1] - \tilde{J}_{ij}[k]}{\chi_i[k+1] - \chi_i[k]} \times \frac{\chi_i[k+1] - \chi_i[k]}{2}$$
(4.23)

At each discrete control step denoted by k, $\tilde{J}_{ij}[k+1]$ is unknown; so to evaluate $\tilde{J}_{ij}[k+\frac{1}{2}]$ in Eq. (4.23), it is assumed that the changes in the Jacobian is almost the same during two successive iterations, i.e., $\tilde{J}_{ij}[k+1] - \tilde{J}_{ij}[k] \cong \tilde{J}_{ij}[k] - \tilde{J}_{ij}[k-1]$. Thus,

$$\tilde{J}_{ij}[k+\frac{1}{2}] \cong \frac{3}{2}\tilde{J}_{ij}[k] - \frac{1}{2}\tilde{J}_{ij}[k-1]$$
(4.24)

At each time instant, the following approximation holds for the elements of the Jacobian matrix which ultimately results in a multi-step Jacobian position control scheme. Due to the complexity of the \tilde{J} elements, all calculations were performed using Maple[®] software.

$$\Delta\chi(0) \cong \left(\frac{3}{2}\tilde{J}[k] - \frac{1}{2}\tilde{J}[k-1]\right)^{\dagger} \Delta\chi(L)$$
(4.25)

4.3 Simulation Study

Before the results are presented, it is worth noting that when updating the Jacobian, the boundary condition acts as an input signal, most of which is known except for $u_{iz}(0)$. One practical way to resolve this problem is to measure this value using a force/torque sensor mounted at the robot's base; however, this approach is not applicable for a simulation study. Fig. 4.4 illustrates the trend of $\beta = u_{iz}(L)$ with respect to $\eta = u_{iz}(0)$ for a given rotation angle α between the tubes in a two-tube robot. In six simulated configurations, the mapping turns out to be monotonic and roughly linear. Therefore, a piecewise linear approximation as in Eq. (4.26) is adopted to find the slope of this mapping. Using Eq. (4.27), $u_{iz}(0)$ can be obtained iteratively starting from an arbitrary value of $u_{iz}(L)$. Here, k represents the

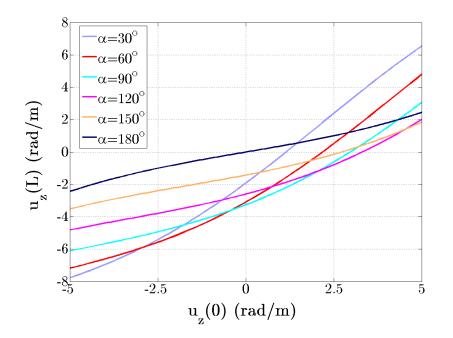


Figure 4.4: The relationship between boundary conditions: $u_{iz}(L)$ with respect to $u_{iz}(0)$ as a function of the rotation angle in a two-tube robot.

iteration number.

$$\begin{bmatrix} u_{iz}(s) \\ \alpha_i(s) \end{bmatrix} = G(u_{iz}(0), \alpha_i(0), s)$$

$$\Rightarrow \begin{bmatrix} \dot{u}_{iz}(L) \\ \dot{\alpha}_i(L) \end{bmatrix} = \begin{bmatrix} \frac{\partial G_{1..n}}{\partial u_{iz}} & \frac{\partial G_{1..n}}{\partial \alpha_i} \end{bmatrix} \cdot \begin{bmatrix} \dot{u}_{iz}(0) \\ \dot{\alpha}_i(0) \end{bmatrix}$$

$$\eta[k+1] = \eta[k] - \left(\frac{\partial G_{1..n}}{\partial u_{iz}}\right)^{-1} \cdot \left(\beta[k] - 0\right)$$
(4.27)

The diameters, lengths, curvatures, and mechanical properties of the three tubes used for the simulation of a three-tube robot are listed in Table 4.2 in which the lengths of straight and curved sections of the tubes are represented by l and L, respectively. The radius of curvature is also denoted by r. We also simulated a two-tube robot consisting of the middle and outer tubes defined in Table 4.2. These parameters are the actual parameters of our two-tube robot that is experimented in Section 4.4.

Tube pair	1 (inner)	2 (middle)	3 (outer)
l (mm)	250	155	12
L (mm)	150	152.6	152.6
r (mm)	100	250	250
Stiffness ratio	0.25	0.85	1
(compared to the 3^{rd} tube)			

Table 4.2: Parameters of the Tubes for Simulations

In the simulation study for the three-tube robot, $u_{iz}(0)$ converged successfully within three iterations while the calculation time was negligible. This method was initially developed for a two-tube robot, and it can be extended to any number of tubes. At the next step, the Jacobian-based control scheme was evaluated by running a trajectory tracking test whose results are shown in Fig. 4.5. The desired trajectory vector in this simulation was defined by $[u_{iz}(L) \equiv 0 \ \Theta_{tr}(L) \ X_{tr}(L)]^T$, and the two-tube and three-tube robots tracked the designed trajectory accurately. In the graphs each sub-link's length was set to be 10 mm.

We ran the tracking simulation 1000 times. It took total of 1.3 sec to calculate the Jacobian and the forward kinematics in the two-tube robot case using 10 mm sub-links. The same calculation for the three-tube robot took less than 3 sec on a desktop computer with a dual-core 2.4 GHz 32 Bit processor.

To compare the improvement in trajectory tracking using the introduced multi-step Jacobian technique, the two-tube robot was simulated to follow a straight line whose length was 80 mm. First, each Jacobian update size was set to 1mm. The modified Jacobian reduced the mean tip positioning error from 2.15×10^{-2} mm to 1.14×10^{-3} mm compared to the conventional Jacobian matrix. Setting the update step to be 8 mm which corresponds to a low update rate in a control system, the mean tracking error was reduced from approximately 1.5 mm to 0.6 mm. Corresponding results are shown in Fig. 4.6.

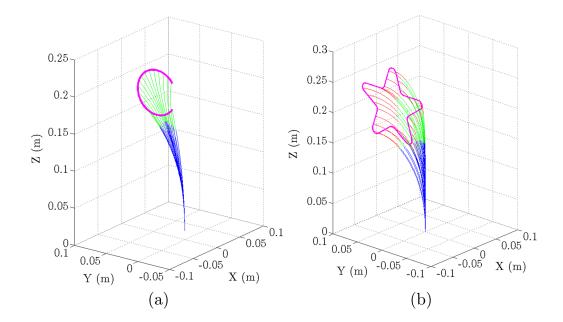


Figure 4.5: Trajectory tracking using (a) two-tube (blue:outer tube, green: inner tube) (b) three-tube concentric-tube robots (blue:outer tube, green: middle tube, red: inner tube).

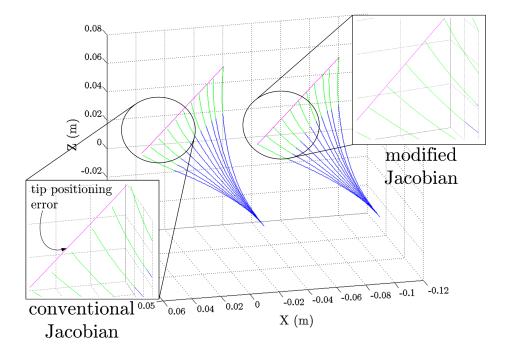


Figure 4.6: Trajectory tracking using conventional Jacobian and modified multi-step Jacobian approach in the two-tube robot.

4.4 Experimental Validation

4.4.1 Setup Description

The experimental evaluation of the proposed Jacobian-based control approach was carried out using the concentric-tube robot composed of two superelastic tubes (see Fig. 4.7). The inset drawing in Fig. 4.7 illustrates the Nitinol tubes each of which has a straight section at its proximal end followed by a distal section with a constant curvature.

The outer tube was rotated with a rotary T-RS60 stage while the inner tube was respectively inserted and rotated using a linear T-LSR300B stage and another rotary T-RS60 stage (Zaber Technologies, Canada). The robot was equipped with a Nano43 6-DOF force/torque sensor (ATI Industrial Automation, United States) located at the base of the inner tube. This sensor was used to align the tubes knowing the fact that the the torsion is minimized when the tubes are fully aligned. The angle difference between the two tubes was obtained in this way as 306.3°. In the setup, an EM (electromagnetic) tracking system (Aurora, Northern Digital Inc., Canada) was used for determining position during tracking; however, the control algorithm was updated using the tip's position provided by the forward kinematics. This strategy gave more stable results. A sensor coil of the EM tracker was attached to the tip of the inner tube by a light plastic adaptor. A multi-threaded application for realtime control was developed using Microsoft[®] C++, MATLAB[®] and the QuaRC[®] Toolbox (Quanser Consulting Inc., Canada).

We utilized the modified Jacobian approach with damped least-squares method as a classical approach to avoid singularities during trajectory tracking [11]. However, the main disadvantage of this singularity-avoidance technique is an increase in positioning error. A detailed analysis of the singularity and manipulability measures for concentric-tube robots is part of our ongoing research.

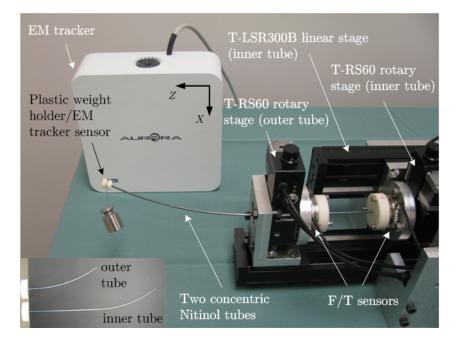


Figure 4.7: Our concentric-tube robot setup.

4.4.2 Experiments and Results

We now provide some experimental results using the scheme described above for our concentric-tube robot with two tubes. In our test-bed, three experiments were conducted to evaluate trajectory tracking. In these cases, the initial rotary angles are set at $[0 \ 60^{\circ}]$ which are very close to a singularity of the robot. This enabled us to test the singularity-avoidance scheme that was implemented since we encountered several singular configurations.

In the first experiment, a straight line in the XY plane of the setup's coordinate frame indicated in Fig. 4.7 was required to be followed by the robot's tip in 40 seconds. The tip is also expected to remain stationary in the XZ and YZ planes. Fig. 4.8 displays the results. Accordingly, the root mean squared error in the entire 3D plane and the final positioning error at the tip's location were 1.79mm and 3.86mm, respectively. As seen in Fig. 4.8, singularity avoidance was maintained which generated a small curved path in the vicinity of the origin in the XY plane subplot. As the next test, a sinusoidal motion profile in the XY plane was used as the reference trajectory. The desired and experimental paths followed

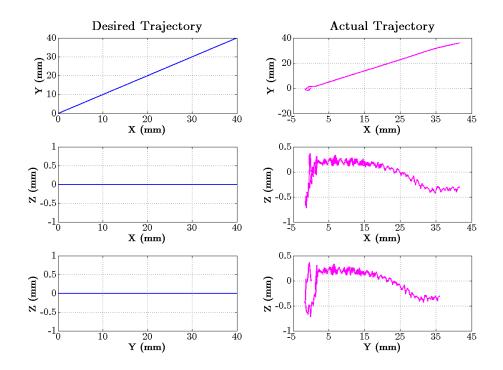


Figure 4.8: Desired and experimental trajectories in XY, XZ, and YZ planes (linear trajectory, final tip position = $[41.59 \ 37.51 \ -0.31]^T$ mm).

by the robot's tip are presented in Fig. 4.9. The error values in this case were 1.56mm and 1.67mm, respectively. In both cases, the length of the sub-links was chosen to be 10mm. In the final experiment, a combination of linear and sinusoidal trajectories was utilized to develop a desired 3D trajectory. The trajectory resulting from the experiment indicates good tracking performance (see Fig. 4.10).

The results obtained confirm the capability of the suggested scheme to enable the robots tip to track desired trajectories with an acceptable accuracy. However, there are deviations from the desired paths which can be attributed to (1) measurement error of the EM tracker which has been reported to be around 1mm, (2) the forward kinematics error which is estimated to have an average value of 1.5mm using similar mechanical parameters in a two-tube robot [10]; and (3) inclusion of the singularity-avoidance technique. Furthermore, ignoring unmodeled dynamics, such as frictional torques [12], as have done in this study, may also have contributed to the positioning and tracking inaccuracies.

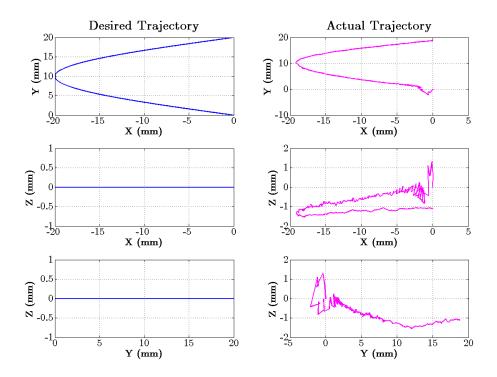


Figure 4.9: Desired and experimental trajectories in XY, XZ, and YZ planes (sinusoidal motion, final tip position = $[-0.02 \ 18.76 \ -1.12]^T$ mm).

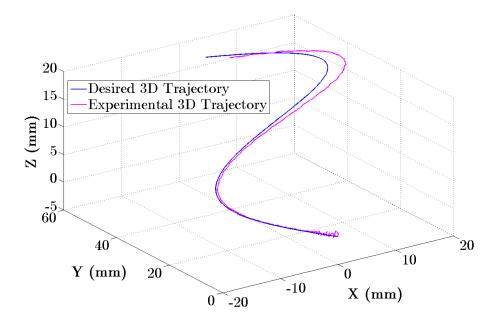


Figure 4.10: Desired and experimental trajectories in 3D (final tip position = $[2.329 \ 47.79 \ 19.65]^T$ mm, final desired position = $[0 \ 50 \ 20]^T$ mm).

4.5 Conclusion

A concentric-tube robot is well-suited for navigation along 3D complex curves since the robot's shape is sufficiently flexible. Using computer-assisted techniques, the shape of this device can be accurately controlled to guide it inside the natural orifices, lumens, and other anatomical areas in a variety of minimally invasive applications. From the control perspective, real-time positioning of this type of robots is challenging. However, addressing some of the computational issues makes it possible to develop a variety of closed-loop control strategies that can significantly increase the operational accuracy and performance of these robots.

The control approach presented in this chapter can be implemented efficiently. The proposed Jacobian-based controller was shown to provide reasonable performance without the need for excessive online or pre-computation. In our implementation, friction compensation was not considered. However, predicting frictional torques as described in [12] is expected to improve the overall tracking performance. That is left for future work. Another enhancement for a future study is to incorporate the effect of an external load.

Bibliography

- A. Asadian, M. R. Kermani, and R. V. Patel, "Robot-assisted needle steering using a control theoretic approach," *J. Intell. Robot. Syst.*, vol. 62, no. 3-4, pp. 397–418, 2011.
- [2] P. E. Dupont, J. Lock, B. Itkowitz, and E. Butler, "Design and control of concentrictube robots," *IEEE Trans. Robot.*, vol. 26, no. 2, pp. 209–225, 2010.
- [3] P. Sears and P. E. Dupont, "Inverse kinematics of concentric tube steerable needles," in *Proc. IEEE Int. Conf. Robot. Autom.* IEEE, 2007, pp. 1887–1892.
- [4] J. Lock, G. Laing, M. Mahvash, and P. E. Dupont, "Quasistatic modeling of concentric tube robots with external loads," in *Proc. IEEE/RSJ Int. Conf. Intell. Robots Syst.* IEEE, 2010, pp. 2325–2332.
- [5] R. J. Webster III, J. M. Romano, and N. J. Cowan, "Mechanics of precurved-tube continuum robots," *IEEE Trans. Robot.*, vol. 25, no. 1, pp. 67–78, 2009.
- [6] D. C. Rucker and R. J. Webster, "Mechanics-based modeling of bending and torsion in active cannulas," in *Proc. IEEE RAS/EMBS Int. Conf. on Biomed. Rob. Biomech.* IEEE, 2008, pp. 704–709.
- [7] R. J. Webster III, J. P. Swensen, J. M. Romano, and N. J. Cowan, "Closed-form differential kinematics for concentric-tube continuum robots with application to visual servoing," in *Experimental Robotics*. Springer, 2009, pp. 485–494.
- [8] D. C. Rucker, B. A. Jones, and R. J. Webster III, "A geometrically exact model for externally loaded concentric-tube continuum robots," *IEEE Trans. Robot.*, vol. 26, no. 5, pp. 769–780, 2010.
- [9] P. Sears and P. Dupont, "A steerable needle technology using curved concentric tubes," in *Proc. IEEE/RSJ Int. Conf. Intell. Robots Syst.*, 2006, pp. 2850–2856.

- [10] R. Xu and R. Patel, "A fast torsionally compliant kinematic model of concentrictube robots," in 2012 Annual International Conference of the IEEE Engineering in Medicine and Biology Society. IEEE, 2012, pp. 904–907.
- [11] G. Marani, J. Kim, J. Yuh, and W. K. Chung, "A real-time approach for singularity avoidance in resolved motion rate control of robotic manipulators," in *Proc. IEEE Int. Conf. Robot. Autom.*, vol. 2. IEEE, 2002, pp. 1973–1978.
- [12] J. Lock and P. E. Dupont, "Friction modeling in concentric tube robots," in *Proc. IEEE Int. Conf. Robot. Autom.* IEEE, 2011, pp. 1139–1146.

Chapter 5

Kinematic Instability in Concentric-Tube Robots: Modeling and Analysis

In this chapter, the issue of kinematic instability for concentric-tube robots is studied when the following two conditions are considered: (a) the robot consists of more than two concentric tubes, and (b) the tubes consist of straight sections followed by curved sections. In this chapter, we use the term "kinematic instability" when the tip position of the robot in the Cartesian domain jumps from one equilibrium point to another while having a constant joint-space configuration. This implies that in unstable configurations, the "forward kinematics" of the robot will have multiple solutions for one set of joint space variables. In the literature, a stability condition for two-tube robot without straight parts has been developed using a closed-form solution of the robot kinematics, which is a second-order nonlinear differential equation with boundary conditions. Considering the robot having more than two tubes and also with straight sections results in a set of complex high-order nonlinear ordinary differential equations with boundary conditions. This makes a closed-form solution almost impossible to obtain due to the mathematical complexity. In this chapter, a novel framework is proposed that can calculate the stability condition for robots consisting of multiple tubes with straight sections without solving the nonlinear ordinary differential equations. The resulting conditions restrict the pre-curvatures and length of the tube, as a design factor to guarantee kinematic stability within the whole workspace of the robot. Simulation results are presented in support of the developed theory.

5.1 Introduction

Concentric-tube robots have attracted a great deal of interest during the last five years due to the high dexterity and articulation that they can provide while having light weight, small diameter and hollow-shaft design. Since the robot is composed of pre-shaped hollow tubes, it can be used not only as an independent tool, but also as a host for other interventional devices. The aforementioned features make concentric-tube robots well-suited for delicate surgical procedures where dexterity is needed and the surgical environment is sensitive. In the literature, several surgical procedures have been proposed as applications that can take advantage of the unique physics of this robot, such as beating-heart tissue removal procedures [1], patent foramen ovale closure [2], and intracerebral hemorrhage evacuation [3].

The actuation of this robot is based on rotation and translation of a set of pre-curved tubes assembled concentrically. Depending on the mechanical interactions between consecutive tubes, the tip position and the robot shape are determined in the Cartesian domain. Because of the specific features of the kinematic chain and the different flow of motion/force/energy in concentric-tube robots, the conventional theory for classical robotics is not applicable. As a result, in the literature, several challenges in kinematic modeling for this type of robots, such as those resulting from bending, torsion [4, 5], friction [6], and external loading [7] have been considered. The complex physics of this robot that involves several mechanical couplings makes the computational cost high. Consequently, new quasi-analytical techniques are being developed to deal with such computational difficulties [8]. In addition to the modeling challenges, control and navigation of this robot has some unique features

S	Arc length	
m	Tube index	
$u_m(s) = [u_{mx}(s), u_{my}(s), u_{mz}(s)]^T$	Bending curvature and torsion of the m^{th} tube	
$\hat{u}_m(s) = [\hat{u}_{mx}(s), \hat{u}_{my}(s), \hat{u}_{mz}(s)]^T$	Pre-curvature of the m^{th} tube	
$\alpha_m(s)$	Twist angle difference between the m^{th}	
	and 1^{st} tube	
K_m	Stiffness matrix of the m^{th} tube	
k_{mx}, k_{my}, k_{mz}	Bending and torsional stiffness of the m^{th} tube	
L	Length of the curved section	
l	Length of the straight section	
p	Total number of tubes in a robot	
$q_m, m = 2, \dots, p$	Linearizion variables that the kinematic model	
	is linearized with respected to	
q_{mn}	Variable defined by $q_m - q_n$	
v	Poisson's ratio	
r_{mn}	Constant given by $(1+v) \ \hat{u}_m\ \ \hat{u}_n\ $	
c_1, c_2	Constants in the solution to a set of ODE	
ϵ	Trivial part of the solution to a set of ODE	
$ heta_m$	The angle difference between the m^{th} tube	
	and the 1^{st} tube at the proximal end	
E_{2}, E_{3}	Coefficient matrices defined in Eqs. (5.7) (5.24)	
<i>D</i> (*)	Determinant of matrix *	
N	Integer number	
i	Imaginary unit	
x	Vector of kinematic variables	
A	Coefficient matrix of the linearized kinematics	
В	Vector defined in Eq. (5.20)	
C	Constant vector in the solution to the	
	linearized kinematics	
λ_j	Eigenvalues of A	
$\lambda^{\dagger}, \lambda^{\dagger\dagger}$	Critical values of the eigenvalues that make	
	the kinematics unstable	
Λ	Diagonal matrix consisting of eigenvalues of A	
V	Matrix of eigenvectors of A	
$\sigma, \varsigma, \sigma_p$	Constants given by Eqs. (5.40) (5.47)	

that differ from conventional control techniques in classical robotics. Therefore, currently several research teams are working on addressing the fundamental control challenges for this robot namely: motion planning [9], inverse-kinematics-based and Jacobian-based position control [4, 10, 11], force disturbance rejection during targeting [12], compliance tuning in dealing with sensitive areas [13].

The focus of this chapter is a specific phenomenon, which exists in concentric-tube robots namely kinematic instability or the "snapping" problem. Based on the related literature [4, 5, 14], kinematic instability is when the forward kinematics solution of the concentric-tube robots loses the uniqueness; as a result the robot will jump quickly from one equilibrium position (with higher potential energy) to another equilibrium point (with lower potential energy). This fast and unexpected motion of the tip position cannot be controlled using joint variables; therefore, it can lead to unsafe interactions between the robot and the operational environment. Appropriately addressing the issue is vital for surgical applications (such as in neurosurgery). In [5], kinematic instability is explained from an energy perspective, when the potential energy function bifurcates to a new minimum. A stability condition is derived; however, the results only hold for tubes with small curvatures since the torsional effect in the curved section is ignored. In addition, kinematic instability is also discussed in [4], where an analytical kinematic model for a robot with two tubes was proposed, and the instability problem was studied via multiple solutions of the forward kinematics of the robot. Because this phenomenon does not exist in torsional-rigid models, but appears when the torsion effect is included in the robot kinematics, it can be concluded that the kinematic instability of concentric-tube robots is a result of accumulated torsional energy along the robot. This explains why snapping is more likely to happen when the robot has either high curvature or long body.

Two directions have been studied in the literature to prevent the occurrence of the mentioned instability: (a) modifying the path planned for the robot to avoid passing through the instability regions in joint-space while traveling within the Cartesian workspace [14]; and (b) tuning the design characteristics based on a stability condition that restricts the curvature/length of the tubes [4, 5]. The advantage of the first technique is that, extremelycurved tubes can be used to enlarge the workspace. However, a redundant number of tubes is needed because of the constraints in joint space for avoiding the instability region. Using the second technique kinematic stability will be guaranteed in the whole workspace, independent of the values of the joint variables. This feature is a crucial need for delicate applications.

It should be mentioned that in the literature the stability condition for a two-tube robot is derived while, to the best knowledge of the authors, extension to more complex cases (such as robots with more than two-tube interactions) have not been addressed yet. In this chapter the main focus is developing stability conditions for use in designing concentric-tube robots under the following two considerations: (a) the number of the tubes can be more than two, (b) the tubes can have straight parts before leading to the curvature. Using the technique proposed in this chapter, stability conditions for complex concentric-tube robots can be derived.

The rest of the chapter is organized as follows: Section 5.2 explains the basis for the proposed approach for deriving the stability condition for the two-tube case with and without straight sections. Section 5.3 modifies and generalizes this method to robots with three and more tubes. Simulation results are presented in Section 5.4 to demonstrate the application of the main results.

5.2 Kinematic Stability Condition for Two Concentric Tubes

In this section, a framework is implemented to find the kinematic stability conditions for two-tube robots with and without straight portions; the former result (without considering the straight parts) is compared to the results presented in the literature for two tubes. In the next section the conditions for more than two tubes are obtained.

5.2.1 Kinematic Model for Concentric-Tube Robots

In this chapter, a widely-used torsionally-complaint kinematics model, discussed in [4], is utilized for analysis of the instability problem. The model is shown in Eq. (5.1), in which, α_m represents the rotational angle difference between the first and m^{th} tube, and the total number of tubes in the robot is denoted as p. In addition, torsion (around z) and bending curvature (around x and y) are denoted by u_{mz} and $u_m|_{x,y}$, respectively. x, y and z are the axes of the tube's material coordinate frame [4]. Pre-curvatures of the tubes are denoted as \hat{u}_{mx} , \hat{u}_{my} and \hat{u}_{mz} (\hat{u}_{mz} is assumed to be zero [4]). K_n is a diagonal matrix consisting of the tubes' stiffnesses in different directions namely: k_{mx} for the x direction, k_{my} for the ydirection, and k_{mz} for the z direction. Note that, in the literature [4], it has been assumed that the stiffness of the tubes are isotropic in x and y directions ($k_{mx} = k_{my} = k_{mxy}$). In Eq. (5.1), s is the length variable. Note that the tube pre-curvatures, the tube stiffness, the angle differences, and the curvatures are functions of s which has been omitted in Eq. (5.1) for simplicity. More details of this kinematics model can be found in [4]. It has been shown that this model has good accuracy and is capable of mimicking the "snapping" phenomenon effectively for two-tube robots without straight portions [4].

$$u_{mz} = (-1/k_{1z})(k_{2z}u_{2z} + \dots + k_{pz}u_{pz})$$

$$\dot{u}_{mz} = \frac{du_{mz}}{ds} = (k_{mxy}/k_{mz})(u_{mx}\hat{u}_{my} - u_{my}\hat{u}_{mx})$$

$$u_{m}|_{x,y} = \left(\left(\sum_{n=1}^{p} K_{n}\right)^{-1}R_{z}^{T}(\alpha_{m})\left(\sum_{n=1}^{p} R_{z}(\alpha_{n})K_{n}\hat{u}_{n}\right)\right)\Big|_{x,y}$$

$$\dot{\alpha}_{m} = \frac{d\alpha_{m}}{ds} = u_{mz} - u_{1z}, \qquad m = 2, ..., p$$
(5.1)

Using the above-mentioned model, in order to analyze the instability phenomenon, the condition which ensures uniqueness of solutions of the forward kinematics should be calculated. The complex physics of interactions between the tubes makes the resulting equations a set of nonlinear ordinary differential equations (ODEs) with boundary conditions. The system consists of two equations for two-tube interactions and any addition of one tube to the system introduces two more equations to the model. As a result, in most cases, it is not straight forward to calculate a practical condition of uniqueness that can be analyzed to evaluate kinematic stability.

5.2.2 Kinematic Stability Condition for Two-Tube Robots without Straight Parts

To deal with the above-mentioned issue and to obtain the stability condition, in this part, a linearization framework (along the whole body of the robot) is proposed that calculates the linearized model of the system when the linearization point is considered as a new variable. The linearized behavior of the system is then analyzed using the standard techniques for dealing with a set of linear ODEs with boundary-conditions. Finally the uniqueness condition is determined, which guarantees kinematic stability.

It should be mentioned that the behavior of the linearized system can be a good approximation of the nonlinear system only in a very small neighborhood around the linearization point. Also considering the fact that in concentric-tube robots, the kinematics variables can change significantly along the tubes, the linearization can be inaccurate if it is performed with respect to only a few points along the robot. In order to address this problem, inspired by the concept of the Extended Kalman Filter (which is a linear observation technique for nonlinear systems), first the kinematics model is linearized with respect to the linearization variables ($q_m, m = 2, ..., q$) which corresponds to the angle differences between the tubes. The result of this linearization is a set of ODEs which can behave differently when different values for the linearization variables (q_m) are considered. Then, the behavior of the linearized system is analyzed, and finally the general uniqueness/stability condition is achieved, which is valid for all possible q_m . This means that if the stability condition is satisfied then the solution of the set of ODEs will be unique, regardless of the q_m value.

It can be seen in Eq. (5.1) that $\dot{\alpha}_m$ is already given by a linear equation. \dot{u}_{mz} is a nonlinear

function of α_m , which needs to be linearized around (q_m) . Assuming that all tubes have constant pre-curvatures and they are planar tubes (the assumptions are conventional as pointed out in [4]), the linearized set of ODEs can be achieved as follows:

$$\dot{u}_{mz}^{*} = \dot{u}_{mz} \Big|_{\alpha_{2}=q_{2},...,\alpha_{p}=q_{p}} + \sum_{m=2}^{p} \frac{d\dot{u}_{mz}}{d\alpha_{m}} \Big|_{\alpha_{2}=q_{2},...,\alpha_{p}=q_{p}} (\alpha_{m} - q_{m})$$

$$\dot{\alpha}_{m}^{*} = \dot{\alpha}_{m}, \quad m = 2,...,p$$

$$(5.2)$$

where, \dot{u}_{mz}^* and $\dot{\alpha}_m^*$ are linearized version of \dot{u}_{mz} and $\dot{\alpha}_m$ in Eq. (5.1). For two tubes, since there is only q_2 in the equations (which we set to q in this section), the explicit equations are:

$$\dot{u}_{2z}^{*} = \frac{(1+v)k_{1}\|\hat{u}_{1}\|\|\hat{u}_{2}\|(-\cos(q)q + \cos(q)\alpha_{2}^{*} + \sin(q))}{k_{1} + k_{2}}$$

$$\dot{\alpha}_{2}^{*} = \frac{(k_{1} + k_{2})u_{2z}^{*}}{k_{1}}, q \in \{0, 2\pi\}$$
(5.3)

In Eq. (5.3) $k_n = k_{nxy}$; $1 + v = k_{nxy}/k_{nz}$ (n = 1, 2). The general solutions to these equations are:

$$u_{2z}^{*}(s) = c_{1}e^{s\sqrt{\cos(q)r}} + c_{2}e^{-s\sqrt{\cos(q)r}}$$

$$\alpha_{2}^{*}(s) = \frac{(k_{1} + k_{2})(-c_{1}e^{s\sqrt{\cos(q)r}} + c_{2}e^{-s\sqrt{\cos(q)r}})}{k_{1}\sqrt{\cos(q)r}} + \epsilon$$
(5.4)

where,

$$r = (1+v) \|\hat{u}_1\| \|\hat{u}_2\| \tag{5.5}$$

In this chapter, $\|*\|$ denotes the Euclidean norm of a vector or the magnitude of a complex number. In Eq. (5.4), s is the length variable. ϵ is the trivial part of the solution, which will be discussed following equation (5.7). The constant values c_1 and c_2 are obtained by applying boundary conditions to the solutions, which are: $u_{2z}^*(L) = 0$, $\alpha_2^*(0) = \theta$, where L is the length of the curved section of the robot and θ is the angle difference between the two tubes at the proximal end [4]. After applying the boundary conditions, we have the following:

$$E_2 \begin{bmatrix} c_1 \\ c_2 \end{bmatrix} + \begin{bmatrix} 0 \\ \epsilon \end{bmatrix} = \begin{bmatrix} 0 \\ \theta \end{bmatrix}$$
(5.6)

where:

$$E_{2} = \begin{bmatrix} e^{L\sqrt{\cos(q)r}} & e^{-L\sqrt{\cos(q)r}} \\ \frac{k_{1}+k_{2}}{k_{1}(\sqrt{\cos(q)r)}} & -\frac{k_{1}+k_{2}}{k_{1}(\sqrt{\cos(q)r)}} \end{bmatrix}$$
(5.7)

Consequently, the uniqueness of the robot kinematics is equal to the uniqueness of the solution for c_1 and c_2 . This means that the coefficient matrix (E_2) should be non-singular to make the robot stable. It can be seen that ϵ is not multiplied by any constant variables (c_1, c_2) , so the value of ϵ cannot change any part of E_2 . In other words, ϵ has no effect on stability. In order to investigate the stability condition of the kinematics independently of q, the determinant of the coefficient matrix E_2 is needed as given below:

$$D(E_2) = \frac{(k_1 + k_2)(e^{L\sqrt{\cos(q)r}} + e^{-L\sqrt{\cos(q)r}})}{k_1(\sqrt{\cos(q)r})}$$
(5.8)

It can be seen that if $q \le \pi/2$ or $q \ge 3\pi/2$, then the determinant, $D(E_2)$, is non-negative and the kinematics has a unique solution. Therefore to find the stability condition, q should be considered as: $\pi/2 < q < 3\pi/2$, in which case, the determinant can be zero implying that the kinematics could be unstable. Consequently, considering $\pi/2 < q < 3\pi/2$, the determinant of E_2 can be simplified as follows:

$$D(E_2) = 2\frac{(k_1 + k_2)\cos(L\sqrt{-\cos(q)r})}{k_1(\sqrt{-\cos(q)r})}, q \in \{\pi/2, 3\pi/2\}$$
(5.9)

In order to guarantee kinematic stability, the determinant $D(E_2)$ should not be equal to

zero. Consequently, the stability condition can be satisfied as follows:

$$L\sqrt{r}\sqrt{-\cos(q)} \neq (1/2+N)\pi$$
 (5.10)

where N is an integer number. Since we have $\pi/2 < q < 3\pi/2$, it is true to say that $\sqrt{-\cos(q)}$ is a real scalar and is bounded by unity. Consequently, the stability condition for all possible q can be stated as follows:

$$L\sqrt{r} < \pi/2 \tag{5.11}$$

The achieved result is the same as the result that has been derived directly from the nonlinear equations [4]. This supports the effectiveness of the proposed technique. Since the method can be extended for more than two tubes, it can be modified to address the general problem.

5.2.3 Kinematic Stability Condition for Two-Tube Robots including Straight Parts

The stability condition developed in the previous section assumes that the two tubes have a non-zero curvature along the whole body. This assumption is not always valid since in many applications, the tubes have a straight part before the curvature starts. In fact the inner tube usually has a straight section, extending out of the outer tube for translational motion. The straight part changes the energy function of the system and can therefore change the stability condition for the kinematics. As the first step, in this section the formulations for two tubes (which is a simpler case) are derived and in the next section they will be extended for multiple tubes. As mentioned earlier, the kinematic instability in concentric-tube robots is caused by torsion energy stored along the robot. Extra solutions to the forward kinematics may appear because of the straight section since the maximum torsion happens within that part. To give an intuitive view of the straight part effect, the following example is designed. Considering Fig. 5.1, two tubes with pre-curvatures satisfying (5.11) are shown. Assuming that the outer (blue) tube is stationary while the inner tube (red) rotates through an angle $\alpha_2(0) < \pi$, the robot will only have one solution and it will be $\alpha_2(L) < \alpha_2(0)$. In the next step, imagine that a straight section is added to the inner tube, with the length $l = (\alpha_2(0) - \pi))/u_{1z}(0)$. This will result in the angle difference between the proximal ends to be $\alpha_2(0 - l) = \pi$. The kinematic relation will be: $\alpha_2(0 - l) = \pi$, $\alpha_2(L) < \pi$. In addition, it is known that there is always a trivial solution $\alpha_2(L) = \pi$ for the same initial condition $\alpha_2(0 - l) = \pi$, which is represented by the dashed lines in the figure. Consequently, two solutions are obtained for the same joint space value. This robot will have instability even if (5.11) is satisfied. This means that the stability condition will be different in presence of straight part.

In order to mathematically show the effect of the straight section on kinematic stability, the boundary condition of the system should be tuned as a result of the straight part as follows:

$$u_{2z}^{*}(L) = 0, \alpha_{2}^{*}(0) - l_{2}u_{2z}^{*}(0) + l_{1}u_{1z}^{*}(0) = \theta$$
(5.12)

where l_n (n = 1, 2) represents the length of the straight portion for the n^{th} tube. Consequently, the determinant of the coefficient matrix $(D(E_2^l))$ will be:

$$-(k_2l_1 + k_1l_2)\tanh(L\sqrt{\cos(q)r})\sqrt{\cos(q)r} - (k_1 + k_2)$$
(5.13)

As a result, the kinematics will have multiple solutions if Eq. (5.13) equals to zero. Knowing that tanh(*) = -i tan(i*), where i is $\sqrt{-1}$ and considering $D(E_2^l) = 0$, we will have:

$$Li\sqrt{\cos(q)r} = \arctan\left(\frac{k_1 + k_2}{(k_1l_2 + k_2l_1)i\sqrt{\cos(q)r}}\right)$$
(5.14)

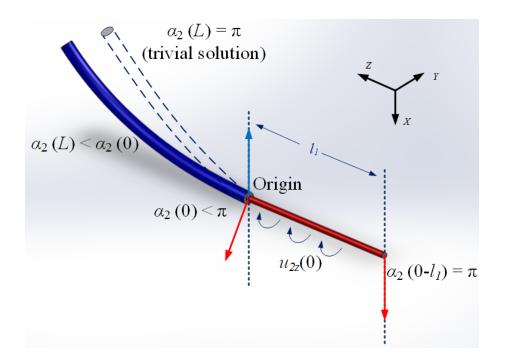


Figure 5.1: Demonstration of the possible multiple solutions for two tubes with a straight section. The blue and red arrows represent the rotational angles of the two tubes at that location.

Taking the Euclidean norm on both sides, the following is achieved:

$$\left\|Li\sqrt{\cos(q)r}\right\| = \left\|\arctan\left(\frac{k_1 + k_2}{(k_1l_2 + k_2l_1)i\sqrt{\cos(q)r}}\right)\right\|$$
(5.15)

Considering (7.15), and also $\|\arctan(*)\| \ge \arctan(\|*\|)$, the following can be developed:

$$L\left\|i\sqrt{\cos(q)r}\right\| \ge \arctan\left(\frac{k_1 + k_2}{(k_1l_2 + k_2l_1)\left\|i\sqrt{\cos(q)r}\right\|}\right)$$
(5.16)

As can be seen in Eq. (5.5), r is a positive real number; as a result we have: $\sqrt{r} \ge \left\|\sqrt{\cos(q)r}\right\| = \left\|i\sqrt{\cos(q)r}\right\|$. Accordingly, Eq. (5.16) will result in the following:

$$L\sqrt{r} \ge \arctan\left(\frac{k_1 + k_2}{(k_1 l_2 + k_2 l_1)\sqrt{r}}\right)$$
(5.17)

5.3. KINEMATIC STABILITY CONDITION FOR THREE OR MORE CONCENTRIC TUBES 94

Consequently, when the kinematics are unstable $(D(E_2^l) = 0)$, the tube parameters will satisfy the relation shown in Eq. (5.17). In other words, if the tube parameters are chosen such that Eq. (5.17) is never satisfied, then kinematic stability will be guaranteed. As a result, one stability condition for two-tube interaction considering the effects of the straight sections is as follows:

$$L\sqrt{r} < \arctan\left(\frac{k_1 + k_2}{(k_1 l_2 + k_2 l_1)\sqrt{r}}\right)$$
(5.18)

This stability condition exhibits the effect of the straight section. It can be seen that, for the robot having the same curved sections \sqrt{r} , the longer the straight part, the greater the chances of instability. When $l_1, l_2 \rightarrow 0$ the proposed condition reduces to the original condition given in Eq. (5.11) since $\arctan\left(\frac{k_1+k_2}{(k_1l_2+k_2l_1)\sqrt{r}}\right) \rightarrow \pi/2$.

5.3 Kinematic Stability Condition for Three or More Concentric Tubes

In the previous section, stability conditions for two-tube robots were calculated. In this section, the stability conditions are extended to three-tube robots and finally to multi-tube robots.

5.3.1 Kinematic Stability Condition for Three-Tube Robots without Straight Parts

It should be noted that because of significant mathematical complexity, it is neither efficient nor practical to calculate an explicit solution for the kinematics model when the robot has more than two tubes. Even if a solution can be obtained, the mathematical complexity makes it almost impossible to analyze the solution properly and have a stability condition that can be used in designing robots. Consequently, an indirect technique is proposed in the rest of this section, which can calculate a stability condition with no need for an explicit solution. For this purpose, the linearized model for the three-tube robot (calculated from Eq. (5.2) when q = 3) can be written as a set of linear first-order ODEs in the form:

$$\dot{x} = \frac{dx}{ds} = Ax + B \tag{5.19}$$

where $x = [u_{2z}^*, u_{3z}^*, \alpha_2^*, \alpha_3^*]$. Considering Eqs. (5.2) and (5.19), after some algebraic manipulations, it can be shown that for a three-tube robot, the matrix A is 4 by 4 in dimension and is always in the anti-diagonal block structure. A and B are shown as below:

$$A = \begin{bmatrix} 0 & 0 & a_{13} & a_{14} \\ 0 & 0 & a_{23} & a_{24} \\ a_{31} & a_{32} & 0 & 0 \\ a_{41} & a_{42} & 0 & 0 \end{bmatrix}, B = \begin{bmatrix} b_1 \\ b_2 \\ b_3 \\ b_4 \end{bmatrix}$$
(5.20)

In Eq. (5.20), the elements in A and B $(a_{ij}, b_j; i, j = 1, 2, 3, 4)$ are dependent on some of the tubes' parameters (\hat{u}, k, L) and linearization variables (q_m) . The general solution for this system has the following specific structure:

$$x(s) = V e^{\Lambda s} C + \int_0^s V e^{\Lambda(s-\tau)} V^{-1} B d\tau$$
(5.21)

where,

$$V = \begin{bmatrix} v_{11} & -v_{11} & v_{13} & -v_{13} \\ v_{21} & -v_{21} & v_{23} & -v_{23} \\ v_{31} & v_{31} & v_{33} & v_{33} \\ 1 & 1 & 1 & 1 \end{bmatrix}$$
(5.22)

In Eq. (5.22), Λ is a diagonal matrix consisting of the eigenvalues (λ_j ; j = 1, 2, 3, 4) of A, and V represents a matrix of its eigenvectors. It can be shown that because of its structure,

the matrix A always has four distinct eigenvalues which have the following relationship: $\lambda_2 = -\lambda_1, \lambda_4 = -\lambda_3$ (see Appendix II). $C = V^{-1}x(0)$ is a constant vector that is to be determined. To calculate C, the boundary conditions $(u_{2z}^*(L) = 0, u_{3z}^*(L) = 0, \alpha_2^*(0) = \theta_2, \alpha_3^*(0) = \theta_3)$ are applied to the general solution, which results in:

$$E_3 C + x_{\epsilon} = \begin{bmatrix} 0 & 0 & \theta_2 & \theta_3 \end{bmatrix}^T$$
(5.23)

where,

$$E_{3} = \begin{vmatrix} v_{11}e^{\lambda_{1}L} & -v_{11}e^{\lambda_{2}L} & v_{13}e^{\lambda_{3}L} & -v_{13}e^{\lambda_{4}L} \\ v_{21}e^{\lambda_{1}L} & -v_{21}e^{\lambda_{2}L} & v_{23}e^{\lambda_{3}L} & -v_{23}e^{\lambda_{4}L} \\ v_{31} & v_{31} & v_{33} & v_{33} \\ 1 & 1 & 1 & 1 \end{vmatrix}$$
(5.24)

and the vector x_{ϵ} is calculated from the integral term in Eq. (5.21). As discussed for Eq. (5.7), the uniqueness of these general solutions, only depends on whether the coefficient matrix E_3 is invertible or not. In other words, there is only one solution for the robot kinematics if the determinant of the coefficient matrix $(D(E_3))$ is not zero. Considering the relationship between the eigenvalues ($\lambda_2 = -\lambda_1$, $\lambda_4 = -\lambda_3$), $D(E_3)$ is calculated as follows:

$$D(E_3) = v_{\epsilon}(e^{-L\lambda_1} + e^{L\lambda_1})(e^{-L\lambda_3} + e^{L\lambda_3})$$
(5.25)

where $v_{\epsilon} = -(v_{31} - v_{33})(v_{11}v_{23} - v_{13}v_{21})$. Note that v_{ϵ} equal to zero will make at least two eigenvectors of A linearly dependent (see the structure of V in Eq. (5.22)), which cannot be true for a 4×4 matrix having four distinct eigenvalues. Consequently, since v_{ϵ} cannot be zero, the robot kinematics will be stable as long as the following holds:

$$D(E_3) \neq 0 \iff \lambda_j \neq \pm i\pi/2L$$
 (5.26)

We can define the critical value (λ^{\dagger}) for the eigenvalues which makes the kinematics unstable as:

$$\lambda^{\dagger} = \pm i\pi/2L \tag{5.27}$$

Up to this point, kinematic stability is established based on the definition of the critical value (λ^{\dagger}) for the eigenvalues of the matrix A. In order to guarantee kinematic stability, first the eigenvalues of A should be calculated as functions of tube parameters (\hat{u}, k, l, L) using the characteristic polynomial of A; then the stability condition should be calculated which provides acceptable bounds for the tube parameters that prevent the eigenvalues from being equal to the critical value (λ^{\dagger}) .

However, calculating the relation between λ_j and tube parameters by solving the characteristic equation of the system ($D(\lambda) = 0$) is not straightforward, because of the algebraic complexity (See Appendix B). The aforementioned issue will become more complicated when the number of tubes increases. In order to address this, an indirect technique is proposed in this section, which can provide a compact sufficient stability condition that can be used in selecting tube parameters for designing concentric-tube robots.

For the above-mentioned purpose, a novel inner product of the pre-curvatures of two tubes is defined:

$$[\hat{u}_m, \hat{u}_n] = r_{mn} \cos(q_{mn}) \tag{5.28}$$

where,

$$r_{mn} = (1+v) \|\hat{u}_m\| \|\hat{u}_n\|$$
(5.29)

and $q_{mn} = q_m - q_n$, $q_{m1} = q_m$. In Eqs. (5.28), (5.29) and the rest of this subsection, the subscripts m, n = 1, 2, 3; m > n. From the definition of the inner product in Eq. (5.28), the following two inequalities can be obtained:

$$\|[\hat{u}_m, \hat{u}_n]\| \le r_{mn} \tag{5.30}$$

5.3. KINEMATIC STABILITY CONDITION FOR THREE OR MORE CONCENTRIC TUBES 98

$$\left\|\sqrt{[\hat{u}_m, \hat{u}_n]}\right\| \le \sqrt{r_{mn}} \tag{5.31}$$

Substituting the proposed definition Eq. (5.28), into the characteristic polynomial $(D(\lambda))$ results in :

$$D(\lambda) = \frac{1}{\sum_{i=1}^{3} k_i} \Big(k_1([\hat{u}_2, \hat{u}_1] - \lambda^2)([\hat{u}_3, \hat{u}_1] - \lambda^2) + k_2([\hat{u}_2, \hat{u}_1] - \lambda^2)([\hat{u}_3, \hat{u}_2] - \lambda^2) + k_3([\hat{u}_3, \hat{u}_1] - \lambda^2)([\hat{u}_3, \hat{u}_2] - \lambda^2) \Big)$$
(5.32)

The resulting equation provides better insight into the relationships between the tube parameters and the eigenvalues. From $D(\lambda) = 0$, it can be shown that, λ^2 always has real values (See Appendix A). Consequently, the solutions for λ that satisfied $D(\lambda) = 0$ are either purely real or purely imaginary. Considering Eq. (5.32), the solution for λ^2 (that can make $D(\lambda) = 0$) will satisfy Eqs. (5.33), and (5.34):

$$\min([\hat{u}_m, \hat{u}_n]) \le \lambda_j^2 \le \max([\hat{u}_m, \hat{u}_n])$$
(5.33)

$$\|\lambda_j\| \le \max\left(\left\|\sqrt{[\hat{u}_m, \hat{u}_n]}\right\|\right)$$
(5.34)

From Eqs. (5.31) and (5.34), we have:

$$\|\lambda_j\| \le \max(\sqrt{r_{mn}}) \tag{5.35}$$

The inequality above shows the bound of the eigenvalues according to the tube parameters. As a result, the robot kinematics will be stable over the whole workspace if the $\|\lambda^{\dagger}\|$ is not in this bound:

$$\max(\sqrt{r_{mn}}) < \left\|\lambda^{\dagger}\right\| \tag{5.36}$$

which can be rewritten as follows by combining with Eq. (5.27):

$$\max(L\sqrt{r_{mn}}) < \pi/2 \tag{5.37}$$

It should be noted that, since the upper bound of $\|\lambda\|$ is utilized to establish the stability condition, instead of the exact solution for $\|\lambda\|$, the result is a sufficient condition. In other words, it is possible that the robot is stable, when using tube parameters outside the range defined in Eq. (5.37). The stability condition shown in Eq. (5.37) means that for a three-tube robot (without a straight section) if all of the tube pairs (i.e., tubes 1&2, tubes 2&3, and tubes 1&3) are stable, the kinematics of the whole robot will be stable.

5.3.2 Kinematic Stability Condition for Three-Tube Robots including Straight Parts

In this section, the goal is to define the stability condition for three-tube robots with straight parts, in which the boundary conditions have the following form: $u_{mz}(L) = 0$, $\alpha_m(0) - u_{mz}(0)l_m + u_{1z}(0)l_1 = \theta_m$. Consequently, the determinant of the coefficient matrix can be obtained following a similar approach as in Eq. (5.25):

$$D(E_3^l) = h_1 e^{L(\lambda_1 + \lambda_3)} + h_2 e^{L(\lambda_1 - \lambda_3)} + h_3 e^{-L(\lambda_1 + \lambda_3)} + h_4 e^{-L(\lambda_1 - \lambda_3)}$$
(5.38)

where, h_j (j = 1, 2, 3, 4) consist of the elements in the eigenvector matrix details of which are omitted due to the space limitations. Considering the definition of the eigenvector matrix $(AV = \Lambda V)$ and Eq. (5.38), it can be seen that $D(E_3^l)$ is a function of λ_j and tube parameters (\hat{u}, k, l, L) . In order to find the critical value $(\lambda^{\dagger\dagger})$ for the eigenvalues which makes $D(E_3^l) = 0$, the following nonlinear transformation is applied to Eq. (5.38).

$$Li\lambda_j = \arctan\left(\frac{\xi}{i\lambda_j}\right)$$
 (5.39)

5.3. KINEMATIC STABILITY CONDITION FOR THREE OR MORE CONCENTRIC TUBES 100

where ξ is the unknown parameter to be solved by substituting Eq. (5.39) into $D(E_3^l) = 0$. After solving ξ , the $\lambda^{\dagger\dagger}$ (that satisfies $D(E_3^l) = 0$) will be achieved in the following format:

$$Li\lambda^{\dagger\dagger} = \arctan\left(\frac{k_1 + k_2 + k_3}{\left(\frac{1}{2}\sigma + \frac{1}{2}\sqrt{\sigma^2 - \zeta}\right)i\lambda^{\dagger\dagger}}\right)$$

$$\sigma = l_1(k_2 + k_3) + l_2(k_1 + k_3) + l_3(k_1 + k_2)$$

$$\zeta = (k_1 + k_2 + k_3)(k_1l_2l_3 + k_2l_1l_3 + k_3l_1l_2)$$
(5.40)

Up to this point, the critical value $(\lambda^{\dagger\dagger})$ is achieved for a three-tube robot with straight parts. As discussed in Eqs. (5.14)-(5.16), the following inequality can be obtained from Eq. (5.40):

$$L\|i\lambda^{\dagger\dagger}\| \ge \arctan\left(\frac{k_1 + k_2 + k_3}{\left(\frac{1}{2}\sigma + \frac{1}{2}\sqrt{\sigma^2 - \zeta}\right)\|i\lambda^{\dagger\dagger}\|}\right)$$
(5.41)

Since ζ is a positive number, Eq. (5.41) results in:

$$L\|\lambda^{\dagger\dagger}\| \ge \arctan\left(\frac{k_1 + k_2 + k_3}{\sigma\|\lambda^{\dagger\dagger}\|}\right)$$
(5.42)

As mentioned before, adding straight parts to the robot design will change the boundary condition of the kinematics model while the characteristic equation remains the same. As a result, the conclusion achieved for λ_j in Eq. (5.35) is valid for a three-tube robot with straight parts.

This means that the kinematics of a three-tube robot with straight parts will be unstable if the $\lambda^{\dagger\dagger}$ is within the bounds of the possible solutions for λ . In other words, considering Eq. (5.35), if the following holds, then the kinematics will be unstable:

$$\max(\sqrt{r_{mn}}) \ge \left\|\lambda^{\dagger\dagger}\right\| \tag{5.43}$$

Combining Eqs. (5.42) and (5.43), it can be concluded that if the kinematics are unstable,

5.3. KINEMATIC STABILITY CONDITION FOR THREE OR MORE CONCENTRIC TUBES 101

we have:

$$L\max\left(\sqrt{r_{mn}}\right) \ge \arctan\left(\frac{k_1 + k_2 + k_3}{\sigma \max\left(\sqrt{r_{mn}}\right)}\right)$$
 (5.44)

As a result, kinematic stability can be guaranteed if the tube parameters are chosen to satisfy the following stability condition for a three-tube robot with straight parts:

$$L \max\left(\sqrt{r_{mn}}\right) < \arctan\left(\frac{k_1 + k_2 + k_3}{\sigma \max\left(\sqrt{r_{mn}}\right)}\right)$$
(5.45)

The obtained stability condition is different from that for the two-tube case Eq. (5.18) due to the effect of the third tube. In Eq. (5.45), if the third tube stiffness is set to zero, then the stability condition reduces to the two-tube condition in Eq. (5.18).

5.3.3 Extension to Multiple Tubes

The approach used in previous subsections can be used for robots with more than three tubes. It can be shown that the linearized model will always have a block anti-diagonal structure, which would result in a similar format for the characteristic polynomial corresponding to that in Eq. (5.32). So the conditions obtained in Eq. (5.37) can be extended for any number of tubes:

$$\max(L\sqrt{r_{mn}}) < \pi/2,\tag{5.46}$$

where m, n = 1, 2, ..., p; m > n, and p is the total number of tubes. For the robot with straight sections, when the kinematics are unstable, the critical values for the eigenvalues satisfy the relationship in Eq. (5.39), which would result in a similar inequality to that in Eq. (5.42). Following the technique developed in the previous subsection, it can be shown that the stability condition for the general case (multiple tubes with straight sections) is as

	L(m)	$\hat{u}(m^{-1})$	$k (Nm^2)$	v
tube 1	0.157	1/0.120	0.040	0.3
tube 2	0.157	1/0.150	0.050	0.3
tube 3	0.157	1/0.180	0.060	0.3

Table 5.2: Parameters of Concentric-Tube Robots

follows:

$$L \max(\sqrt{r_{mn}}) < \arctan\left(\frac{\sum_{m=1}^{p} (k_m)}{\sigma_p \max(\sqrt{r_{mn}})}\right)$$

$$\sigma_p = (k_2 + \dots + k_p)l_1 + (k_1 + k_3 + \dots + k_p)l_2$$

$$+ \dots + (k_1 + \dots + k_{p-1})l_p$$
(5.47)

5.4 Simulation Validation

In the previous sections, the stability conditions were developed for multi-tube robots with and without straight parts. In order to show that these conditions are able to predict kinematic stability of a concentric-tube robot in its entire workspace, both stability conditions and forward kinematics are calculated for a robot. By comparing these two results, it can be seen that when the stability conditions are satisfied, the robot is alway stable. The implementation of the kinematics is achieved using the technique proposed in [12], which has been shown to provide good accuracy.

In the first test, the stability of a two-tube robot with a straight portion is studied. For this robot, tube 1 (in Table 5.2) is the inner tube and tube 2 is the outer one. The parameters of these two tubes, such as the length of the curved sections (*L*), pre-curvatures (\hat{u}), the stiffnesses (*k*), and Poisson's ratio (*v*) are defined as shown in Table 5.2. The length of the straight part of tube 2 is equal to zero ($l_2 = 0$). In order to study the effect of l_1 (the straight part of tube 1) on kinematic stability, we need to determine at which value of l_1 the robot will be kinematically unstable. One way is to use the stability condition in Eq. (5.18).

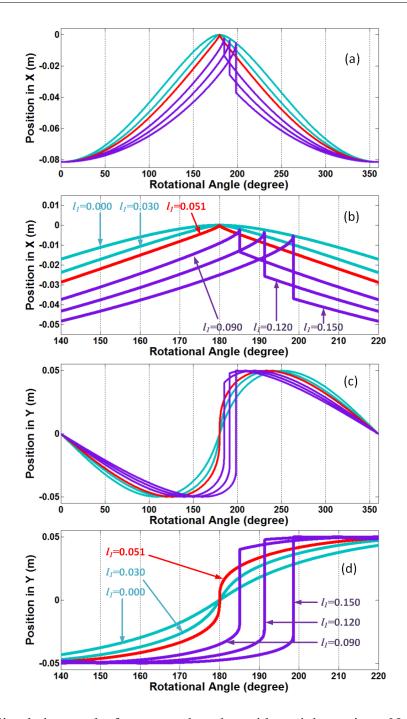


Figure 5.2: Simulation results for a two-tube robot with straight sections. Note that a large number of different l_1 were tested in the program, only a few of them were plotted here. (a) position of the robot tip in X direction; (b) magnified view of (a) around the snapping area; (c) position of the robot tip in Y direction; (d) magnified view of (c) around the snapping area. X and Y axes are defined in Fig. 5.1

After some calculations, it can be shown that the robot is stable when l_1 is smaller than 0.051m. Another way to achieve this result is to calculate the forward kinematics of the robot via simulation when different values of l_1 are considered. As shown in Fig. 5.2, the tip position of the robot is calculated, when the inner tube rotates a full revolution and the outer tube remains stationary. This calculation was repeated many times when l_1 varies from 0 to 0.150m. The simulation results shows that the robot is stable when $l_1 < 0.051m$ (blue curves), and critically stable when $l_1 = 0.051m$ (red curves). The purple curves have a discontinuous point in the tip Cartesian position during the continuous movement of the joint space values. This means that the tip of the robot suddenly jumps from one position to another in Cartesian domain. So the kinematics of the robot are unstable when $l_1 > 0.051m$. In conclusion, the simulation results are in an complete agreement with the derived stability condition.

For a three-tube robot without any straight section, the stability condition becomes conservative, because the maximum value of λ_j in Eq. (5.35) is used for developing the stability condition. But when the three tubes have the same value of pre-curvatures, i.e., $\max(\sqrt{r_{mn}}) = \min(\sqrt{r_{mn}})$ in Eq. (5.33), the exact value of λ_j will be obtained (since the radius of the bound around λ_j converges to zero). In this specific situation, the stability condition is not conservative any more. A three-tube robot without straight sections is studied to verify this result. We assume that the inner, middle, and outer tubes of this robot have the same pre-curvature \hat{u}_{123} . The other parameters such as L, k, v are from tube 2. Using the stability condition in Eq. (5.37), it can be concluded that the robot will be stable if $\hat{u}_{123} < 1/0.114(m^{-1})$. In the simulation tests, the tip position of the robot is calculated when the inner tube rotates a full revolution and the other two tubes remain stationary. This procedure is repeated when \hat{u}_{123} equals to a set of different values. As discussed earlier, the red line in Fig. 5.3. corresponds to the critically stable situation. So the kinematics are critically stable when $\hat{u}_{123} = 1/0.114(m^{-1})$, which agrees with the result in stability condition.

The last test is designed to validate the stability condition for a general three-tube robot which has three different pre-curvatures, stiffness and length for the straight parts. For this

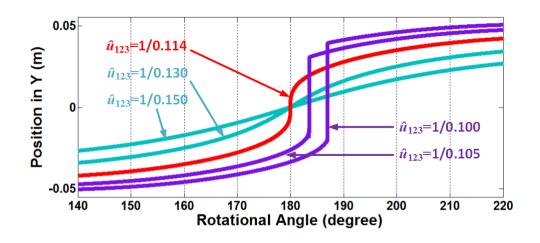


Figure 5.3: Tip position (in Y direction) of a three-tube robot without straight parts. Note that a large number of different \hat{u}_{123} were tested in program, only a few of them were plotted here.

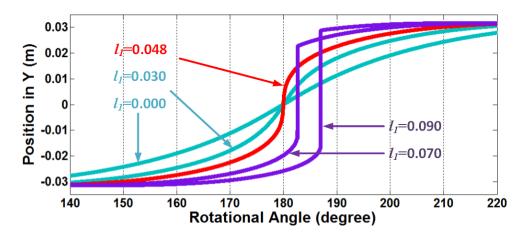


Figure 5.4: Tip position (in Y direction) of a three-tube robot with straight parts. Note that a large number of different l_1 were tested in the program, only a few of them were plotted here.

purpose, tube 1, tube 2 and tube 3 are chosen as the inner, middle and outer tubes of the robot, respectively. The straight parts of tube 2 and tube 3 were set to $l_2 = 0.010m$, $l_3 = 0$. Using the stability condition in Eq. (5.45), the robot is stable as long as $l_1 < 0.030m$. In simulation, the forward kinematics of the robot are calculated when tube 1 is rotated 360 degrees and the other two remain stationary. This calculation was repeated when l_1 equals a series of different values. As shown in Fig. 5.4, compared to previous simulations, the robot did not show critical stability at $l_1 = 0.030m$, but at a higher value $l_1 = 0.048m$.

This result shows that the stability condition is conservative.

5.5 Conclusions

In this chapter, a framework was proposed for analyzing the kinematic stability of concentrictube robots, in presence of (a) straight sections at the proximal ends and (b) multi-tube body architecture. It was mathematically shown that the proposed stability conditions are related to the tube parameters including pre-curvatures, stiffness, length of straight sections, and length of curved sections. Simulation results (for two-tube and three-tube robots) were given in support of the theory. In the simulations, it was shown that changing the length of the straight sections and/or increasing the number of tubes can directly affect the robot's kinematic stability. A good agreement was observed between the proposed theory and the simulated forward kinematics.

Bibliography

- A. H. Gosline, N. V. Vasilyev, A. Veeramani, M. Wu, G. Schmitz, R. Chen, V. Arabagi, J. Pedro, and P. E. Dupont, "Metal mems tools for beating-heart tissue removal," in *Proc. IEEE Int. Conf. Robot. Autom.* IEEE, 2012, pp. 1921–1926.
- [2] N. V. Vasilyev, A. H. Gosline, E. Butler, N. Lang, P. J. Codd, H. Yamauchi, E. N. Feins, C. R. Folk, A. L. Cohen, R. Chen *et al.*, "Percutaneous steerable robotic tool delivery platform and metal microelectromechanical systems device for tissue manipulation and approximation closure of patent foramen ovale in an animal model," *Circulation: Cardiovascular Interventions*, vol. 6, no. 4, pp. 468–475, 2013.
- [3] J. Burgner, P. J. Swaney, R. A. Lathrop, K. D. Weaver, and R. J. Webster, "Debulking from within: a robotic steerable cannula for intracerebral hemorrhage evacuation," *IEEE Trans. Biomed. Eng.*, vol. 60, no. 9, pp. 2567–2575, 2013.
- [4] P. E. Dupont, J. Lock, B. Itkowitz, and E. Butler, "Design and control of concentrictube robots," *IEEE Trans. Robot.*, vol. 26, no. 2, pp. 209–225, 2010.
- [5] R. J. Webster III, J. M. Romano, and N. J. Cowan, "Mechanics of precurved-tube continuum robots," *IEEE Trans. Robot.*, vol. 25, no. 1, pp. 67–78, 2009.
- [6] J. Lock and P. E. Dupont, "Friction modeling in concentric tube robots," in *Proc. IEEE Int. Conf. Robot. Autom.* IEEE, 2011, pp. 1139–1146.
- [7] D. C. Rucker, B. A. Jones, and R. J. Webster III, "A geometrically exact model for externally loaded concentric-tube continuum robots," *IEEE Trans. Robot.*, vol. 26, no. 5, pp. 769–780, 2010.
- [8] R. Xu and R. Patel, "A fast torsionally compliant kinematic model of concentrictube robots," in 2012 Annual International Conference of the IEEE Engineering in Medicine and Biology Society. IEEE, 2012, pp. 904–907.

- [9] L. G. Torres and R. Alterovitz, "Motion planning for concentric tube robots using mechanics-based models," in *Proc. IEEE/RSJ Int. Conf. Intell. Robots Syst.* IEEE, 2011, pp. 5153–5159.
- [10] J. Burgner, P. J. Swaney, D. C. Rucker, H. B. Gilbert, S. T. Nill, P. T. Russell, K. D. Weaver, and R. J. Webster, "A bimanual teleoperated system for endonasal skull base surgery," in *Proc. IEEE/RSJ Int. Conf. Intell. Robots Syst.* IEEE, 2011, pp. 2517–2523.
- [11] R. Xu, A. Asadian, A. S. Naidu, and R. V. Patel, "Position control of concentrictube continuum robots using a modified jacobian-based approach," in *Proc. IEEE Int. Conf. Robot. Autom.* IEEE, 2013, pp. 5813–5818.
- [12] R. Xu, A. Asadian, S. F. Atashzar, and R. V. Patel, "Real-time trajectory tracking for externally loaded concentric-tube robots," in *Proc. IEEE Int. Conf. Robot. Autom.*, 2014, pp. 4374–4379.
- [13] M. Mahvash and P. E. Dupont, "Stiffness control of surgical continuum manipulators," *IEEE Trans. Robot.*, vol. 27, no. 2, pp. 334–345, 2011.
- [14] C. Bergeles and P. E. Dupont, "Planning stable paths for concentric tube robots," in Proc. IEEE/RSJ Int. Conf. Intell. Robots Syst. IEEE, 2013, pp. 3077–3082.

Chapter 6

Real-time Trajectory Tracking for Externally-Loaded Concentric-Tube Robots

Concentric-Tube robots can offer a suitable compromise between force and curvature control. In a previous study by the authors, a real-time trajectory tracking scheme for an unloaded concentric-tube robot was developed. One of the practical barriers to the use of a concentric-tube robot in medical applications is compensation for the impact of environmental forces which can cause drastic deterioration in tracking performance. In this chapter, by modifying the robots forward kinematics and Jacobian, a new method is developed to facilitate tip tracking in real-time while accounting for an external load at the robots tip. By considering the tip deflection resulting from the external load, a novel duallayer control architecture is proposed to compensate for this deflection during trajectory tracking. In order to measure the force exerted on the tip position of the robot, a new technique is proposed that can move the sensing system from the distal tip to the proximal base. Experimental results are given to illustrate the effectiveness of the proposed method.

$\{e_1, e_2, e_3\}$	World frame	
8	Arc length	
i	Tube index	
$ \begin{array}{ c c c c c }\hline \{d_1(s), d_2(s), d_3(s)\} \\\hline n(s) = [n_x(s), n_y(s), n_z(s)]^T \\\hline m(s) = [m_x(s), m_y(s), m_z(s)]^T \end{array} $	Body frame of the cross-section located at s	
$n(s) = [n_x(s), n_y(s), n_z(s)]^T$	Stress vector represented in the body frame	
$m(s) = [m_x(s), m_y(s), m_z(s)]^T$	Bending moment vector represented	
	in the body frame	
$u_i(s) = [u_{ix}(s), u_{iy}(s), u_{iz}(s)]^T$	Bending curvature and torsion of the i^{th} tube	
	which are represented in the body frame	
	Pre-curvature of the i^{th} tube	
$v(s) = [v_x(s), v_y(s), v_z(s)]^T$	Shear strains and elongation represented	
	in the body frame	
f(s)	Distributed force vector represented	
	in the body frame	
l(s)	Distributed moment vector represented	
	in the body frame	
	Stiffness matrix of the i^{th} tube	
	Bending and torsional stiffness of the i^{th} tube	
	Length of the curved section	
$\Theta(s) = \theta_1(s), \theta_2(s), \theta_{i3}(s)$	Euler angles of the rotation matrix $R(s)$	
	of the i^{th} tube	
$r(s) = [x(s), y(s), z(s)]^T$	Position vector of the cross-section located at s	
	represented in the world frame	
M(s)	Bending moment vector represented	
	in the world frame	
$\alpha_i(s)$	Twist angle difference between the i^{th} tube and	
	the 1^{st} tube	
$R_Z(\alpha_i(s))$	Rotation matrix between the body frames of	
	the i^{th} and the 1^{st} tube	
F_{ext}	External point force at the tip of the robot	
	represented in the world frame	
P_i	Position of the proximal end of the i^{th} tube	
H	Mapping between P_i to each sub-link's length	
Ĩ	Jacobian matrix of a sub-link	

Table 6.1: Nomenclature I

6.1 Introduction

A concentric-tube robot as a subset of continuum robots is composed of a sequence of telescoping pre-curved elastic tubes inserted one inside the next. In this flexible robotic

X	Position of robot's tip in the Cartesian space
X_{meas}	Measured position of robot's tip in the Cartesian space
q	Joint variables of the robot
q_{des}	Desired trajectory in joint space
w	External point wrench at the tip of the robot
F(q,w)	Forward kinematics of the robot
J(q,w), C(q,w)	Jacobian and Compliance matrices of the robot
Δ	Deflection of the robot under loading
$\hat{\Delta}$	Estimated deflection of the robot under loading
U _{int}	Controller's input signal
S	Laplace variable

 Table 6.2: Nomenclature II

structure, axial rotation and translation of individual tubes with respect to each other can generate 3D curvatures. Thus, the shape of the robot can be controlled in order to guide it inside lumens, natural orifices, and other anatomical organs in a variety of medical applications specially involving unreachable or confined surgical sites.

Accurate position control of surgical instruments is a vital need in Robotics-Assisted Minimally Invasive Surgery (RAMIS); however the small size of the incision reduces the robot rigidity and, as a result, challenges positioning accuracy. As is known, flexible surgical tools (such as surgical needles [1]) have been widely used in percutaneous minimally invasive interventions. However, complex and inaccurate kinematics modeling of flexible/continuum mechanisms has imposed limitations on accurate control of the tip motion in RAMIS. This topic has been the subject of recent publications for concentric-tube robots [2, 3], and is explored further in this study.

Modeling the shape of concentric-tube robots has evolved over the last few years. Historically, a variety of mechanical phenomena, e.g., bending [4], torsion [2] [5], and friction between the tubes [6] have been gradually taken into account to improve modeling accuracy. It has been shown that the assumption of zero external load in kinematic modeling can cause considerable error in estimating the robot configuration [7]. To deal with this issue, in [7] and [8] the forward kinematics of the robot are modified to include the effects of external loading. However, most of the developed models are mathematically complex and computationally expensive. To achieve a good balance between computational efficacy and numerical accuracy, the authors proposed a fast torsionally-compliant model [9], which was later utilized to develop a feasible strategy for real-time tip tracking in free motion [3]. Human-in-the-loop architecture was developed in [2], and [10] respectively using an inverse kinematics scheme and an inverse Jacobian technique (with singularity avoid-ance) as local controllers. Implementation of Magnetic Resonance Imaging based position control (utilizing inverse kinematics) is given in [11]. In addition, more advanced control architectures such as stiffness control [12] have been recently studied in the literature.

In this chapter, the problem of real-time position control in the presence of undesirable robot deflection is studied. The deflection is caused by: (a) variations in external loading, and (b) alteration of kinematic behavior of the robot in the presence of external forces. The ultimate goal is to navigate the robot accurately regardless of external disturbances. This feature is important in medical applications, where the targeting accuracy strongly correlates with the performance of the administered therapy. For this goal, deflection of a concentric-tube robot in the presence of external disturbances is estimated; then, the desired trajectory is reshaped using the estimated robot deflection in order to compensate for the effect of varying loading. For this purpose, the interaction force between the robot tip position and environment should be used in the proposed control architecture. In this chapter a new scheme is proposed that uses force sensors at the proximal end (close to the driving unit) of the robot. This removes the need for measuring the force at the distal end (close to the robot's tip position) while compensating for the internal forces between the tubes. This feature is motivated by the fact that having a sensor close to the robot's tip is not very feasible in practical application.

6.2 Forward Kinematics and Jacobian in the Presence of an External Point Load

Modeling of a concentric-tube robot under an external load has been the subject of several research papers [7, 8]. Existing models include distributed wrench to mimic robotenvironment interaction, and apply lumped wrench as boundary conditions to the governing set of equations. However, due to the limitations of sensing technologies, it is not feasible to obtain accurate force and torque information along the robot's shaft, and update the equations. Computational complexity is also a barrier to real-time implementation in existing techniques. In the following section, fast forward kinematics and the resulting Jacobian [3] are introduced so as to incorporate the impact of the external load for real-time trajectory tracking.

6.2.1 Fast Torsionally Compliant Model for the Loaded Robot

According to Cosserat rod theory, a single elastic rod obeys the equations of equilibrium [8]:

$$\dot{n}(s) + f(s) = 0$$
 (6.1)

$$\dot{m}(s) + \dot{r}(s) \times n(s) + l(s) = 0$$
(6.2)

where m(s) and n(s) are the moment and stress vectors in the cross-section in terms of the length variable s; f(s) and l(s) are respectively the distributed force and torque along the rod; and $r(s) = [x(s) \ y(s) \ z(s)]^T$ is the position vector for a given cross-section represented in the world frame as shown in Fig. 6.1(a). For an assembly of q tubes, equations Eqs. (6.1) and (6.2) are extended as follows in which the subscript *i* denotes the tube number:

$$\sum_{i=1}^{q} \left(\dot{n}_i(s) + f_i(s) \right) = 0 \tag{6.3}$$

$$\sum_{i=1}^{q} \left(\dot{m}_i(s) + \dot{r}_i(s) \times n_i(s) + l_i(s) \right) = 0$$
(6.4)

Defining $\dot{M}(s) = \sum_{i=1}^{q} \dot{m}_i(s)$ as the derivative of the net moment, and knowing that in the absence of the external torque, we have $\sum_{i=1}^{q} l_i(s) = 0$, equation Eq. (6.4) is rewritten as:

$$\dot{M}(s) = -\dot{r}(s) \times F_{ext} \tag{6.5}$$

where $F_{ext} = \sum_{i=1}^{q} n_i(s)$ represents the external point force. Thus, the modified forward kinematics which accounts for the external point load is obtained by adding Eq. (6.5) to the unloaded structure introduced in [3]. The new model is formulated as shown below:

$$\dot{u}_{iz}(s) = \frac{k_{ix}(s)}{k_{iz}(s)} \left(u_{ix}(s)\hat{u}_{iy}(s) - u_{iy}(s)\hat{u}_{ix}(s) \right)$$
(6.6)

$$\dot{\theta}_1(s) = \frac{u_{ix}(s)cos\theta_{i3}(s) - u_{iy}(s)sin\theta_{i3}(s)}{cos\theta_2(s)}$$
(6.7)

$$\dot{\theta}_2(s) = u_{ix}(s)sin\theta_{i3}(s) + u_{iy}(s)cos\theta_{i3}(s)$$
(6.8)

$$\dot{\theta}_{i3}(s) = u_{iz}(s) - \dot{\theta}_1(s)sin\theta_2(s) \tag{6.9}$$

$$\dot{x}(s) = \sin\theta_2(s) \tag{6.10}$$

$$\dot{y}(s) = -\sin\theta_1(s)\cos\theta_2(s) \tag{6.11}$$

$$\dot{z}(s) = \cos\theta_1(s)\cos\theta_2(s) \tag{6.12}$$

$$M(s) = -\dot{r}(s) \times F_{ext} \tag{6.13}$$

in which, \hat{u}_i is the initial curvature value while u_i represents its value after conformation. θ_1 and θ_2 are the first and second Euler angles shared by all tubes; θ_{i3} stands for the 3rd Euler angle of the *i*th tube's cross-section.

For modeling the kinematics of unloaded concentric-tube robots [9], it was assumed that at any cross section, bending moment from all tubes were balanced, and so the net moment

6.2. FORWARD KINEMATICS AND JACOBIAN IN THE PRESENCE OF AN EXTERNAL POINT LOAD

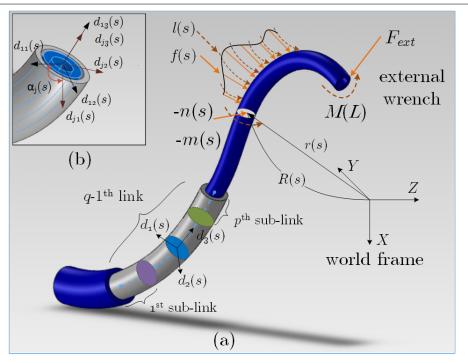


Figure 6.1: (a) A loaded concentric-tube robot consisting of q links or tubes each of which is composed of p sub-links [3]; (b) the robot's cross section showing coordinate frames associated with the 1st and the jth tubes [9].

was zero. To add the impact of the external load to the model, the curvatures in the X and Y directions are updated in the following manner:

$$\begin{bmatrix} u_{ix}(s) \\ u_{iy}(s) \end{bmatrix} = \left(\sum_{j=1}^{q} K_{j}\right)^{-1} \left(R_{Z}^{T} \left(\theta_{i3}(s) - \theta_{13}(s) \right) \\ \times \sum_{j=1}^{q} R_{Z}^{T} \left(\theta_{j3}(s) - \theta_{13}(s) \right) K_{j} \begin{bmatrix} \hat{u}_{jx}(s) \\ \hat{u}_{jy}(s) \end{bmatrix} + R_{i}^{T} M(s) \right)$$
(6.14)

in which, $K_j = diag(k_{jx}, k_{jy}, k_{jz})$ refers to the stiffness matrix calculated from Young's modulus and moment of inertia. The transformation between the body frames of the 1st and the jth tubes is also represented by a pure rotation denoted by the matrix $R_Z(\alpha_j(s))$ in Eq. (6.14). Herein, $\alpha_j(s) = \theta_{j3}(s) - \theta_{13}(s)$ in which $1 \le j \le q$. In addition, R_i is the rotation matrix between the body frame of the *i*th tube with respect to the world frame. For

more details, see Fig. 6.1(b).

Finally, equations Eqs. (6.6)-(6.14) describe the forward kinematics of the concentric-tube robot in the presence of an external point load on the shaft. Note that except for the curvature variables which are expressed in the body frame $\{d_1(s), d_2(s), d_3(s)\}$, other variables are represented in the world frame shown in Fig. 6.1. A linearization technique is employed at this point to derive a closed-form solution for the robot's forward kinematics. Applying a first-order Taylor series expansion to this nonlinear mapping, we have:

$$\begin{bmatrix} \dot{u}_{iz}(s) \\ \dot{\Theta}(s) \\ \dot{r}(s) \\ \dot{M}(s) \end{bmatrix} = \begin{bmatrix} g_{11} & g_{12} \\ g_{21} & g_{22} \\ g_{31} & g_{32} \\ g_{41} & g_{42} \end{bmatrix} \begin{bmatrix} 1 \\ s \end{bmatrix}$$
(6.15)

in which $\Theta(s) = [\theta_1(s) \ \theta_2(s) \ \theta_{i3}(s)]^T$. The sought piece-wise solution is therefore obtained by integration of Eq. (6.15) with respect to s.

$$\begin{bmatrix} u_{iz}(s) \\ \Theta(s) \\ r(s) \\ M(s) \end{bmatrix} = \begin{bmatrix} g_{11} & g_{12} \\ g_{21} & g_{22} \\ g_{31} & g_{32} \\ g_{41} & g_{42} \end{bmatrix} \begin{bmatrix} s \\ \frac{1}{2}s^2 \end{bmatrix} + \begin{bmatrix} u_{iz}(0) \\ \Theta(0) \\ r(0) \\ M(0) \end{bmatrix}$$
(6.16)

Subsequently, the robot's arm is divided into links and small sub-links (see Fig. 6.1(a)), and the kinematic equations for each segment are derived as described in this section. Successive approximation is eventually employed to find the forward kinematics of the full robot, namely, F. The entire procedure has been outlined in detail in [3].

6.2.2 A Modified Jacobian for the Loaded Robot

Once the closed-form solution of each sub-link is obtained, the forward kinematics \tilde{F} are differentiated to derive the associated Jacobian matrix \tilde{J} . Compared with the unloaded concentric-tube robot [3], in the presence of the external point load, one more vector variable, i.e., M, is introduced in the vector Θ . Let us define,

$$\tilde{J}_{g1} = \begin{bmatrix} \frac{\partial \tilde{F}}{\partial u_{iz}(0)} & \frac{\partial \tilde{F}}{\partial \Theta(0)} & \frac{\partial \tilde{F}}{\partial P(0)} & \frac{\partial \tilde{F}}{\partial M(0)} \end{bmatrix}$$
(6.17)

$$\tilde{J}_{g2} = \begin{bmatrix} \frac{\partial \tilde{F}}{\partial H} \frac{\partial H}{\partial P_1} & \frac{\partial \tilde{F}}{\partial H} \frac{\partial H}{\partial P_2} & \dots & \frac{\partial \tilde{F}}{\partial H} \frac{\partial H}{\partial P_q} \end{bmatrix}$$
(6.18)

where P_j represents the position of the proximal end of the j^{th} tube along the z-axis. Moreover, H is the mapping which projects the P_j elements to each sub-link's length. Except for the last sub-link in each link, we have:

$$\tilde{J} = \begin{bmatrix} \tilde{J}_{g1} & 0\\ 0 & I_{q \times q} \end{bmatrix} \text{ otherwise, } \begin{bmatrix} \tilde{J}_{g1} & \tilde{J}_{g2}\\ 0 & I_{q \times q} \end{bmatrix}$$
(6.19)

Finally, the relationship between the velocities of the robot's distal and proximal ends is established as shown below in which L is the length of the assembled robot:

$$[\dot{u}_{iz}(L) \dot{\Theta}(L) \dot{r}(L) \dot{M}(L)]^{T} = J [\dot{u}_{iz}(0) \dot{\Theta}(0) \dot{r}(0) \dot{M}(0)]^{T}$$
(6.20)

In Eq. (6.20), the robot's Jacobian J is obtained by multiplication of individual Jacobians \tilde{J} . This equation is part of an inverse Jacobian-based scheme for position/orientation control.

6.3. THE EFFECT OF EXTERNAL LOADING AND A DUAL-LAYER CONTROL APPROACH 6.3 The Effect of External Loading and a Dual-Layer Con-

6.3 The Effect of External Loading and a Dual-Layer Control Approach

In this section, the effect of external loading on the tip position is studied and a dual-layer control approach is proposed to minimize the impact of external disturbances on trajectory tracking. Needless to say, the forward kinematics of the robot are not only a function of the joint variables q but also of the external wrench w. The effect of external loading in the position domain is called "deflection" in this chapter. It should be noted that the analytical inverse kinematics in the presence of an external wrench has not yet been developed for concentric-tube robots, due to the computational complexity. As a result, it is not possible to utilize a conventional inverse-kinematic controller in order to eliminate the effect of external loading and minimize the associated deflection.

In this section, a dual-layer controller consisting of an inner loop and an outer loop is developed for trajectory tracking in Cartesian space. In brief, the objective of the inner control loop is to make a new inverse model of the robot in the differential domain and remove the effect of deflection on the tip velocity. Then, the outer controller transforms the tracking from the velocity domain to the position domain, and alleviates the impact of system uncertainties.

6.3.1 The Inner Control Loop

Let us consider the forward differential model of the robot as shown below [13]:

$$\dot{X} = J(q, w)\dot{q} + C(q, w)\dot{w}$$
(6.21)

Here, C is the compliance matrix which correlates the derivative of the external wrench to the robot's tip velocity. Thus, the tip motion in Cartesian space \dot{X} is expressed by Eq. (6.21) in which the dot denotes the time derivate and $C = \frac{\partial F}{\partial w}$. This shows that the

external wrench influences the tip motion through two different mechanisms, namely, the Jacobian and compliance terms. In order to design a proper control scheme for rejecting the total effect of the external loading and to have a better insight over the kinematics of the deflection, the total deflection Δ_{total} can be calculated as:

$$\Delta_{total} = \Delta_1 + \Delta_2$$

where, $\Delta_1 = \int C(q, w) \dot{w} dt$
 $\Delta_2 = \int (J(q, w) - J(q, 0)) \dot{q} dt$ (6.22)

Therefore, equation Eq. (6.21) is rewritten as Eq. (6.23) which is called the Standard Total Deflection (STD) model. This representation is close to the standard conventional definition of arm flexibility in flexible-link manipulators [14, 15].

$$\dot{X} = J(q,0)\dot{q} + \dot{\Delta}_{total} \tag{6.23}$$

In the next step, the STD model is employed to design an inverse model-based scheme for the inner loop controller. To this end, the following alternatives (Type-I and Type-II) are proposed:

1) Kinematics-based Deflection Estimation and Cancellation (Type-I): Considering the proposed STD representation, the Type-I control rule Eq. (6.24) can be used to reject the external load.

$$\dot{q}_{des} = J(q,0)^{-1} (U_{int} - \hat{\dot{\Delta}}_{total})$$
 (6.24)

where U_{int} represents the controller's input signal and $\dot{\Delta}_{total}$ is an estimation of the rate of change of the total deflection. $\dot{\Delta}_{total}$ is calculated through numerical derivation of the robot's forward kinematics considering the loaded and unloaded conditions using the following relationship:

$$\hat{\dot{\Delta}}_{total} = \frac{d}{dt} \left(F(q, w) - F(q, 0) \right)$$
(6.25)

6.3. THE EFFECT OF EXTERNAL LOADING AND A DUAL-LAYER CONTROL APPROACH 120

Applying the Type-I control scheme, the robot's tip velocity \dot{X} will converge to the input of the inner loop U_{int} which can be considered equal to the desired velocity in the velocity tracking mode. Consequently, the known nonlinear terms of the robot's model are eliminated, and the resulting dynamics will be an input-to-output linearized system, shown in Eq. (6.26).

$$\dot{X} = U_{int} \tag{6.26}$$

It is worth mentioning that due to several sources of uncertainty in the system, namely, those due to the erroneous forward kinematics model ΔF , force measurement errors $\Delta \omega$, and the robot's unmodeled dynamics, the actual tip velocity \dot{X} does not exactly match the modeled tip velocity \dot{X} . This mismatch is denoted by δ as shown below:

$$\tilde{X} = U_{int} + \delta \tag{6.27}$$

This relationship will be used to design the outer-loop controller which will be introduced later in this section. The proposed Type-I controller is considered as the inner-layer control scheme. Note that to benefit from this technique, a numerical derivation of the total deflection is required which might amplify the noise level. Thus, a Kalman filter is used to suppress the noise signal.

2) Tip Velocity Measurement for Deflection Cancellation (Type II): Revisiting Eq. (6.21), the deflection caused by the wrench derivative $\dot{\Delta}_1$ can be directly estimated without taking a numerical derivative and measuring the robot's tip velocity \dot{X}_{meas} as shown below:

$$C(q,w)\dot{w} = \dot{\Delta}_1 \cong \dot{X}_{meas} - J(q,w)\dot{q}$$
(6.28)

Consequently, taking Eqs. (6.28) and (6.21) into account, the Type-II inner-loop is realized by the following control law.

$$\dot{q}_{des} = J(q, w)^{-1} \Big(U_{int} - \left(\dot{X}_{meas} - J(q, w) \dot{q} \right) \Big)$$
(6.29)

6.3. THE EFFECT OF EXTERNAL LOADING AND A DUAL-LAYER CONTROL APPROACH 121

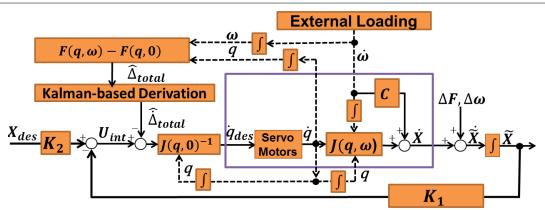


Figure 6.2: Control block diagram for the proposed tracking algorithm.

Using the Type-II controller, the tip velocity measurement is used to cancel out the known nonlinearity of the robot which yields the same dynamics as those represented by Eq. (6.27). However, to realize this controller and reject the impact of a varying external disturbance, it is required to have access to the tip velocity at a sufficiently high sampling rate. In medical interventions, it is not always feasible to accurately register the tip velocity at a high rate. Electromagnetic tracking [9, 12], MRI [11], and ultrasound [16] have been widely utilized for position sensing. However, in most cases, neither accuracy nor the sampling rate is adequate to estimate velocity for accurate force rejection that has fast dynamics.

6.3.2 The Outer Control Loop

Using the inner control loop, an inverse model-based approach in the velocity domain was presented to deal with the deflection caused by the external load. In order to a) take advantage of the proposed technique in position domain and b) alleviate the effect of existing uncertainties, an outer control loop was added to shape the desired trajectory so as to adjust U_{int} toward tip positioning. It should be noted that since the majority of the system's nonlinearity was eliminated through implementing the inner loop at a high update rate, the proposed outer loop could be run at a low control rate. Consequently, an electromagnetic tracker providing the position information at a relatively low rate was used in the outer

loop to reject the undesirable effects of uncertainties while controlling the robot in position domain. The proposed outer loop controller is designed as follows:

$$U_{int} = -K_1 \tilde{X} + K_2 X_{des} \tag{6.30}$$

where, K_1 and K_2 are the design factors for tuning the performance of the closed-loop system, and will be introduced later in this section. Combining Eqs. (6.27) and (6.30), the system dynamics are rewritten as:

$$\tilde{X} = \frac{K_2}{S + K_1} X_{des} + \frac{\delta}{S + K_1}$$
(6.31)

in which, S is the Laplace operator. Considering the achieved first-order linear dynamics between the desired input X_{des} and the robot's tip position X, the outer loop can be designed such that the closed-loop behaves as a fast and stable system. Setting $K_1 = K_2 = k$, the tip tracking system acts as a low-pass filter which has a tunable bandwidth using the parameter k as well as a unity gain in steady-state. Increasing the value of k makes the system faster but more susceptible to high-frequency uncertainties and unmodelled dynamics represented by δ in Eq. (6.31). However, it will in turn increase the magnitude of the applied input signal to the inner loop U_{int} , and adversely influence the tracking performance by saturating the actuators. In summary, Fig. 6.2 depicts the block diagram for the two-layer closed-loop control system for tip tracking while rejecting or minimizing the impact of the external force.

6.4 Simulation Study: Trajectory Tracking in the Presence of a Tip Load

We simulated a two-tube robot whose geometrical parameters and mechanical properties used for the study are listed in Table 6.3. The lengths of the straight and curved sections of

Tube pair	inner	outer
<i>l</i> (m)	0.150	0.012
<i>L</i> (m)	0.153	0.153
r (m)	0.250	0.250
Absolute stiffness	0.0413	0.048
value (Nm ²)		

Table 6.3: Parameters of the Two-Tube Robot

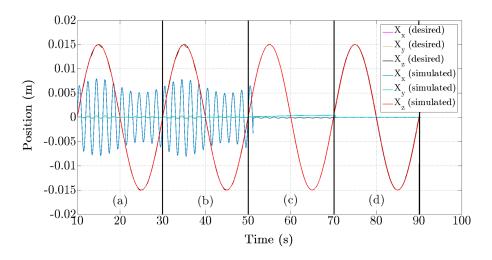


Figure 6.3: Simulation of the tip position $X = [X_x \ X_y \ X_z]^T$ tracking using four control strategies: (a) unloaded Jacobian, (b) loaded Jacobian J, (c) loaded Jacobian J plus $\dot{\Delta}_{total}$, and (d) the dual-layer approach.

the tubes are represented by l and L, respectively, and the radius of curvature is denoted by r. These listed values correspond to the actual parameters of the robotic setup that is used in the experiments discussed in Section 6.5. The length of each sub-link was also assumed to be 10 mm.

Fig. 6.3 illustrates the results of our simulation study in which a sinusoidal motion profile with an amplitude of 15 mm and a frequency of 0.05 Hz was applied as the desired trajectory to move the robot in the z direction. In this test, the robot remained stationary along other axes, and the tip load was also set to have the functional form $f_x = 0.2sin(2\pi \times 0.05t)$ N. Four different control strategies were examined here: (a) the

6.4. SIMULATION STUDY: TRAJECTORY TRACKING IN THE PRESENCE OF A TIP LOAD 124

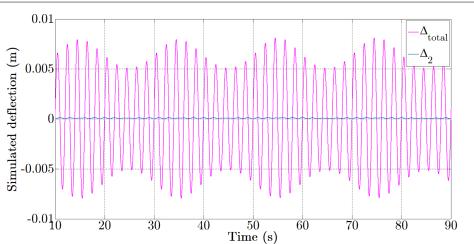


Figure 6.4: Simulation of the tip deflection: comparison between the total deflection and the Jacobian-related component.

inverse Jacobian approach with no load compensation [3] where $\dot{q}_{des} = J(q, 0)^{-1} \dot{X}_{des}$, (b) the inverse Jacobian approach with only load inclusion where $\dot{q}_{des} = J(q, w)^{-1} \dot{X}_{des}$. The compliance component, $C(q, w)\dot{\omega}$, is neglected in this architecture. (c) the inverse Jacobian approach using the inner loop controller defined in Eq. (6.24). The external load is fully considered and the total deflection is compensated for in velocity mode. (d) the dual-layer control approach realized by combining Eqs. (6.24) and (6.30). Here, the effects of loading, transformation from velocity mode to position mode, and uncertainties are taken into account.

As shown in Fig. 6.3, the pure Jacobian-based techniques, i.e., strategies (a) and (b), exhibited poor performance with a maximum tracking error of 7.9 mm along the x-axis. Inclusion of the inner loop in the controller (strategy (c)) reduced the tracking error to a great extent. However, there was still a small drifting error which could be a result of the numerical uncertainties in integration and quantization. Finally, adding the outer loop to the control structure improved the performance, and demonstrated accurate tip tracking in the presence of the tip load. Fig. 6.4 shows the total deflection Δ_{total} , and the deflection component associated with the Jacobian part, Δ_2 . As can be seen, Δ_1 dominates Δ_2 ; so most of the tip deflection in the case of loading is attributed to the compliance component,

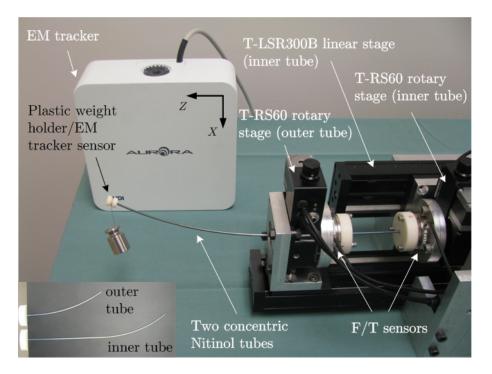


Figure 6.5: A view of our concentric-tube robotic system.

and that was why ignoring the term $C(q, w)\dot{\omega}$ in the force rejection algorithm led to poor tracking performance (see (a) and (b) in Fig. 6.3).

6.5 Experimental Study

6.5.1 Setup Description

The experimental evaluation was performed using a concentric-tube robot which consists of two superelastic Nitinol tubes (see Fig. 6.5). The inset plot in this figure shows the tubes each of which has a straight section at its proximal end followed by a distal section with a fixed curvature.

The outer tube was rotated with a rotary T-RS60 stage (Zaber Technologies, Canada) while the inner tube was respectively inserted and rotated using a linear T-LSR300B stage and another rotary T-RS60 stage. An Aurora EM (electromagnetic) tracker (Northern Digital Inc., Canada) was used for position sensing and validating the forward kinematics. For this purpose, a sensor coil of the EM tracker was attached to the robot's tip by a light plastic adaptor. Also, a metal weight (0.2-0.5 N) was hung from the adapter using a rubber band to represent the external load. By lifting and dropping the weight, a varying force can be exerted on the robot. A multi-threaded application was developed using Microsoft[®] C++, MATLAB[®] and the QuaRC[®] Toolbox (Quanser Inc., Canada). The inner control loop was updated at 500 Hz, while the outer loop was sampled at 40 Hz to measure tip position using EM tracking.

In order to update the force vector F_{ext} used in the model, a force sensing scheme is needed that provides inputs to the force rejection controller. Due to practical considerations and implementation issues (such as limited space on the tip of the robot, need for sensor sterilizability in an actual clinical application, etc.), it is not preferable to install conventional force sensors, such as strain gauges, directly on the distal end. In this chapter, it is proposed to fuse the measurements of two 6-DOF (degrees-of-freedom) sensors (a two-tube configuration) mounted at the base of the two tubes. As a result, each sensor measures the forces acting on the corresponding tube. By fusing these measurements, the friction and internal interaction forces will cancel each other out and the residual will be the tip force. In this project two Nano43 ATI sensors were utilized.

6.5.2 Experimental Results

In the first study, the forward kinematics model proposed for the loaded model was validated. For this purpose, the outer tube was rotated a full turn at 3 °/sec while the external tip load was set to be $f_x = 0.5$ N. The measured tip position as well as the predicted values using the loaded model and the unloaded scheme (i.e., based on not considering the external load) [3] are shown in Fig. 6.6. The mean-squared errors (MSEs) using the loaded and unloaded schemes were 1.4 mm and 9.5 mm, respectively.

At this stage, experimental results for pure force rejection (regulation) and trajectory track-

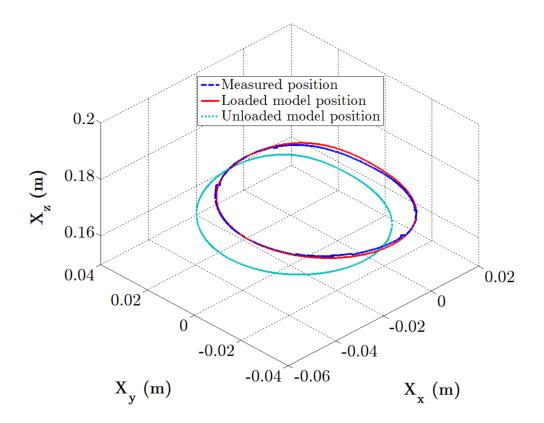


Figure 6.6: Model validation: comparison between measured and predicted tip positions using loaded and unloaded schemes.

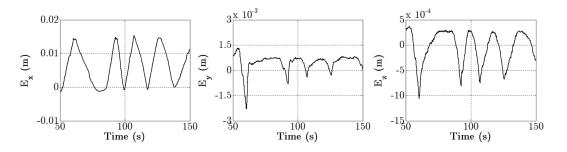


Figure 6.7: Regulation using the inverse unloaded Jacobian approach [3].

ing are presented. In the first experiment, a time-varying external tip force with an amplitude smaller than 0.5 N along the x-axis was applied. Our first objective was to regulate the robot so as to reject the external force while maintaining the same tip position. As observed in Fig. 6.7, the maximum positioning error was reported to be 15.5 mm along the x-axis while only the robot's Jacobian was incorporated [3] in the control loop. The maximum

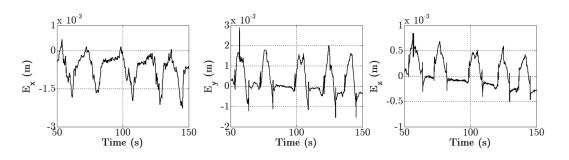


Figure 6.8: Regulation using the proposed dual-layer control approach.

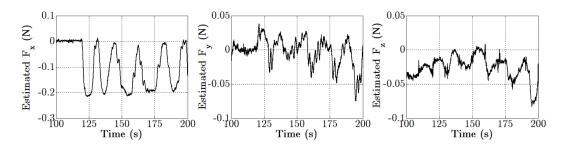


Figure 6.9: Estimated tip force components during trajectory tracking using the proposed dual-layer control approach $F_{ext} = [F_x \ F_y \ F_z]^T$.

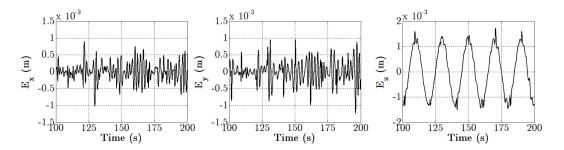


Figure 6.10: Tip tracking error using the proposed dual-layer control approach.

tracking errors along the y- and z- axes were obtained as 2.3 mm and 1.1 mm, respectively. Next, the proposed control scheme was examined under the same test conditions in terms of tip force characteristics. Fig. 6.8 clearly demonstrates the capability of the two-layer approach to regulate the robot while the tracking error E was limited to $[2.2 \ 2.8 \ 0.8]^T$ mm during the entire motion.

To perform trajectory tracking under a time-varying tip load, a sinusoidal reference signal with an amplitude of 10 mm and frequency of 0.05 Hz was applied to move the robot in

the z direction. The tuning parameter of the outer loop k was set to be 2.5. The estimated tip force components, F_{ext} , from 100 s to 200 s are shown in Fig. 6.9, and Fig. 6.10 plots the tracking errors along the three axes. In this experiment, the maximum tip positioning error in the z direction was approximately 1.7 mm. Since the external load had the largest magnitude along the x-axis, the robot was initially prone to considerable deflection in this direction; however, because of the proposed control scheme, perfect regulation limited E_x to $\pm 1 \text{ mm}$.

Bibliography

- A. Asadian, M. R. Kermani, and R. V. Patel, "A novel force modeling scheme for needle insertion using multiple kalman filters," *IEEE Trans. Instrum. Meas.*, vol. 61, no. 2, pp. 429–438, 2012.
- [2] P. E. Dupont, J. Lock, B. Itkowitz, and E. Butler, "Design and control of concentrictube robots," *IEEE Trans. Robot.*, vol. 26, no. 2, pp. 209–225, 2010.
- [3] R. Xu, A. Asadian, A. S. Naidu, and R. V. Patel, "Position control of concentrictube continuum robots using a modified jacobian-based approach," in *Proc. IEEE Int. Conf. Robot. Autom.* IEEE, 2013, pp. 5813–5818.
- [4] P. Sears and P. Dupont, "A steerable needle technology using curved concentric tubes," in *Proc. IEEE/RSJ Int. Conf. Intell. Robots Syst.*, 2006, pp. 2850–2856.
- [5] R. J. Webster III, J. M. Romano, and N. J. Cowan, "Mechanics of precurved-tube continuum robots," *IEEE Trans. Robot.*, vol. 25, no. 1, pp. 67–78, 2009.
- [6] J. Lock and P. E. Dupont, "Friction modeling in concentric tube robots," in *Proc. IEEE Int. Conf. Robot. Autom.* IEEE, 2011, pp. 1139–1146.
- [7] J. Lock, G. Laing, M. Mahvash, and P. E. Dupont, "Quasistatic modeling of concentric tube robots with external loads," in *Proc. IEEE/RSJ Int. Conf. Intell. Robots Syst.* IEEE, 2010, pp. 2325–2332.
- [8] D. C. Rucker, B. A. Jones, and R. J. Webster III, "A geometrically exact model for externally loaded concentric-tube continuum robots," *IEEE Trans. Robot.*, vol. 26, no. 5, pp. 769–780, 2010.
- [9] R. Xu and R. Patel, "A fast torsionally compliant kinematic model of concentrictube robots," in 2012 Annual International Conference of the IEEE Engineering in Medicine and Biology Society. IEEE, 2012, pp. 904–907.

- [10] J. Burgner, P. J. Swaney, D. C. Rucker, H. B. Gilbert, S. T. Nill, P. T. Russell, K. D. Weaver, and R. J. Webster, "A bimanual teleoperated system for endonasal skull base surgery," in *Proc. IEEE/RSJ Int. Conf. Intell. Robots Syst.* IEEE, 2011, pp. 2517–2523.
- [11] H. Su, D. C. Cardona, W. Shang, A. Camilo, G. A. Cole, D. C. Rucker, R. J. Webster, and G. S. Fischer, "A mri-guided concentric tube continuum robot with piezoelectric actuation: a feasibility study," in *Proc. IEEE Int. Conf. Robot. Autom.* IEEE, 2012, pp. 1939–1945.
- [12] M. Mahvash and P. E. Dupont, "Stiffness control of surgical continuum manipulators," *IEEE Trans. Robot.*, vol. 27, no. 2, pp. 334–345, 2011.
- [13] D. C. Rucker and R. J. Webster, "Computing jacobians and compliance matrices for externally loaded continuum robots," in *Proc. IEEE Int. Conf. Robot. Autom.* IEEE, 2011, pp. 945–950.
- [14] M. Moallem, R. V. Patel, and K. Khorasani, *Flexible-link robot manipulators: control techniques and structural design*. Springer-Verlag New York, Inc., 2000.
- [15] S. F. Atashzar, M. Shahbazi, H. A. Talebi, and F. Towhidkhah, "A force observation method for tracking control of flexible-link manipulators," *Robotica*, vol. 31, no. 04, pp. 669–677, 2013.
- [16] H. Ren, N. V. Vasilyev, and P. E. Dupont, "Detection of curved robots using 3d ultrasound," in *Proc. IEEE/RSJ Int. Conf. Intell. Robots Syst.* IEEE, 2011, pp. 2083–2089.

Chapter 7

FBG Sensing in Continuum Robots

Due to their small size and flexibility, fiber Bragg grating (FBG) sensors are very well suited for integration into needle-sized continuum robots for shape estimation and force measurement. Two main challenges in extending previous shape and force sensing technologies to pre-curved continuum robots, such as concentric-tube robots, are measuring torsion information for accurate shape estimation, and protecting FBG sensors from the surrounding environment. In this chapter, first, a novel helically-wrapped FBG sensor design and the corresponding force-curvature-strain model are developed to provide simultaneous curvature, torsion and force measurements. To validate this design and modeling technique, sensorized Nitinol tubes were fabricated and tested in an experimental setup. The results showed that accurate and sensitive curvature, torsion and force measurements can be obtained at a 100Hz sampling rate. Secondly, in order to protect the FBG sensors from the cutting force when used in concentric-tube robots, the manufacture and assembly techniques of a sensorized tube were further improved by putting a protective sleeve on top of the previous structure. Experimental results showed that the FBG sensor was well protected and can provide accurate measurements. Finally, the criterion for designing continuum robots with optimal 3D force sensing capability is studied using mathematical models and simulations.

Table 7.1: Nomenclature I

l	Length of a helical fiber	
$l_{arepsilon}$	Length of a strained helical fiber	
l_s	Length of the FBG in a helical fiber	
r	Radial offset from the fiber to the center of the tube	
h	Pitch of the helix	
$arepsilon_a,arepsilon_t,arepsilon_l$	Axial, shear and total strains in a helical fiber	
$\overline{\overline{\varepsilon}_a}$	Average axial strain along a helical fiber	
w_1, w_2	Weight of axial and shear strains in ε_l	
R_b	Bend radius of a curved tube	
au	Torsion in a curved tube	
κ_{xy}	Curvature vector with a magnitude of $1/R_b$	
α_b	Direction of the curvature vector κ_{xy}	
δΤ	Change in temperature	
β	Thermal sensitivity	
b	Bend radius of a helical fiber	
r_s, α_s	Position vector and orientation angle of the	
	middle point of the FBG sensor	
$r_u, r_l, \alpha_u, \alpha_l$	Position vectors and orientation angles of the	
	start and end points of the FBG sensor	
A	Matrix that represents the linear mapping between	
	curvatures and strains	
S	Arc length	
i	Tube index	
$u_i(s) = [u_{ix}(s), u_{iy}(s), u_{iz}(s)]^T$	Bending curvature and torsion of the i^{th} tube	
$\hat{u}_i(s) = [\hat{u}_{ix}(s), \hat{u}_{iy}(s), \hat{u}_{iz}(s)]^T$	Pre-curvature of the <i>i</i> th tube	
K_i	Stiffness matrix of the i^{th} tube	
k_{ix}, k_{iy}, k_{iz}	Bending and torsional stiffness of the i^{th} tube	
v	Poisson's ratio	
$\Theta(s) = \theta_1(s), \theta_2(s), \theta_{i3}(s)$	Euler angles of the rotation matrix $R(s)$	
	of the i^{th} tube	
$X(s) = [x(s), y(s), z(s)]^T$	Position vector of the cross-section located at s	
M(s)	Bending moment vector	
R_{Θ}	Rotation matrix between the body frames of	
	the i^{th} and 1^{st} tube	
F_{ext}	External point force at the tip of the robot	
	represented in the world frame	

L	Total length of the robot		
L _{tran}	Length of the straight section of the robot		
L_c	Length of the curved section of the robot		
L_s	Arc length from the proximal end of the robot to the location		
	of the FBG sensor		
J_M	Jacobian matrix of $M(L)$ with respect to $M(0)$		
J_C	Compliance matrix of $[u(L_s), M(L)]^T$ with respect to $[M(0), F_{ext}]^T$		
$J_{C\varepsilon}$	Compliance matrix of $[\varepsilon(L_s), M(L)]^T$ with respect to $[M(0), F_{ext}]^T$		
J_{CX}	Compliance matrix of $\varepsilon(L_s)$ with respect to F_{ext}		
d	Distance vector from the location of FBG sensor to the robot's tip		
D	Skew-symmetric matrix of vector d		
n	Normal vector of a plane		
$\tilde{\varepsilon}_l$	Measured strain in a helical FBG sensor		
В	Augmented matrix consisting of D and n		

Table 7.2:	Nomenc	lature II
------------	--------	-----------

7.1 Introduction

Continuum robots are suitable for surgical interventions because of their small size and flexibility, as well as high dexterity in comparison to conventional minimally invasive tools. By incorporating curvature and force sensing into the design of a continuum robot, the robot shape and tissue-robot interaction can be controlled to enhance the efficacy of the treatment administered and improve patient safety [1–5].

Fiber Bragg grating (FBG) sensors have a high strain sensitivity, signal-to-noise ratio and sampling rate, and are immune to electromagnetic interference. These sensors also meet the size constraints imposed by continuum robots in minimally-invasive surgery and for these reasons have been used in sensing applications for continuum robots.

The 3D shape of needle-based continuum robots is reconstructed from curvature measurements using FBG sensors embedded into the robot's shaft [6, 7], or a flexible sheath that can be inserted into the robot's hollow center [8]. Using this shape information, a flexible needle can be steered through soft tissue [9], and a cable-driven robot can be positioned accurately [10]. For applications that involve large deflections, shape sensing has also been studied [11]. These works assume that negligible torsion is applied to the flexible robot during the operation; however, during needle steering and tissue manipulation tasks, the applied torsion can affect the accuracy of 3D shape reconstruction and the orientation of the tool tip becomes unknown [12].

Pre-curved tools can enhance directional control and have been used in many applications, such as CT-guided aspiration biopsy, radiofrequency ablation (StarBurst[®], AngioDynamics), discography (Pakter[®]), vertebral body access and infusion during vertebroplasty (Osteo-Rx[®], Cook Medical). In addition, a special type of continuum robot, consisting of a set of concentrically assembled pre-curved needles, was proposed to provide surgeons with multiple DOFs in constrained environments [13–16]. The curved structure of these tools can experience considerable torsion under both force and torque loading. Twisting FBG sensors in a helical pattern provides both the amplitude and direction of torsion [17], but the multi-core design gives low sensitivity and is difficult to manufacture. This chapter proposes a novel technique to provide high sensitivity, accurate torsion measurement on straight and pre-curved surgical tools and continuum robots.

Force sensing in continuum robots has been studied in [18–20], where the applied force is estimated from tip deflection or joint-level force information. These works show that the sensing capabilities of continuum robots are highly dependent on the inherent compliance of the robot body. For robots that are laterally flexible and axially incompressible it is difficult to have high quality force measurements in all three dimensions. FBG-based 3D tip force sensors have been developed for catheter ablation [5] and vitreoretinal surgery [4] by modifying the axial stiffness of the sensing structures; however, these structures do not have a hollow center for passing micro-surgical instruments or delivering therapy. A lateral force sensing system based on FBG sensors was developed for a continuum robot with a hollow center [3], but the method proposed requires that the sensing structure be initially straight. Our system focuses on developing high accuracy lateral force measurement on pre-curved continuum robots, embedding FBG sensors into the robot body to provide dynamic force

measurement and protect the fibers.

To address the challenge of simultaneously measuring curvature, torsion and applied lateral force on straight and pre-curved continuum robots, the design and manufacture of a novel helically-wrapped FBG sensing technology is proposed (as shown in Fig. 7.1) and a force-curvature-strain model is developed. A high-precision custom engraving technique is designed, and used to create the desired helical grooves on a super-elastic cylindrical structure. To measure the curvature and torsion in the robot from the strain in the helicallywrapped fibers a curvature-strain model is developed. Further, a force-curvature-strain model is derived, incorporating a nonlinear mapping between the tip force and strain in the FBG sensors. The calculation of the inverse of this model is then proposed to obtain accurate force measurements from the FBG readings with minimal computational cost. The novel sensing technology and calculation techniques proposed are evaluated experimentally by embedding three FBG sensors into a pre-curved Nitinol tube at the same cross-section. The results demonstrate that this technology can provide accurate and sensitive curvature, torsion and force measurement for continuum robots.

7.2 Design of Helically-Wrapped FBG Sensor

In this section the design of a helically-wrapped FBG sensor is proposed and the criteria for determining proper FBG sensing elements and helical patterns are described. The model for accurately measuring curvature, torsion and force from FBG strain values, for precurved continuum robots that are flexible in bending and axially stiff to compression, is then obtained. In this chapter, torsion will be referred to as the twist angle per unit length (i.e. rad/m) as defined in differential geometry of curves.

7.2.1 Selection of FBG Sensors

There are many parameters to consider when selecting FBG sensors for an application and the most pertinent parameters to this helical pattern design are the sensor length, reflectivity, maximum strain and minimum bend radius. For flexible robots, the curvature and torsion continuously change along the robot body, especially when the robot is exposed to large bending. It is known that FBG sensors may output distorted or split-peak spectra under uneven strain distribution. For this reason, the FBG sensor should be short enough that it behaves as a point-strain sensor; however, the sensor's Full-Width-Half Maximum bandwidth increases as the sensor length shortens, causing a decrease in the signal-to-noise ratio. Generally speaking, optical fibers with FBG segments cannot survive a bending radius under 10 mm without signal loss. Draw Tower Gratings (DTG), which are formed by writing the FBGs during the fiber drawing process, are an exception as the fiber can support higher strain such that the bend radius can be approximately 3 mm without noticeable loss of signal strength. The drawback of this technology is that the reflectivity for short DTGs (1 mm) is only 0.5%. For this work, an FBG sensor (Technica S.A., China) with a 1 mm length, 50% reflectivity, 17 mm minimum bending radius, 125 um diameter, and 1%strain range was chosen, based on the requirements of the application and the analysis of the experimental results shown below.

7.2.2 Curvature-Strain Model for Helical FBG sensors

In a helical layout, the strain in the FBGs is not in the same direction as the axial or shear strain in the tube. As such, a new model must be derived that relates the bending curvatures and torsion in the tube to the strain in the FBG sensors. In this chapter this relationship is termed the curvature-strain model.

In Fig. 7.1(a), the helical fiber is flattened into a right triangle on a plane. The width equals the circumference at radius r, where r represents the radial offset from the fiber to the

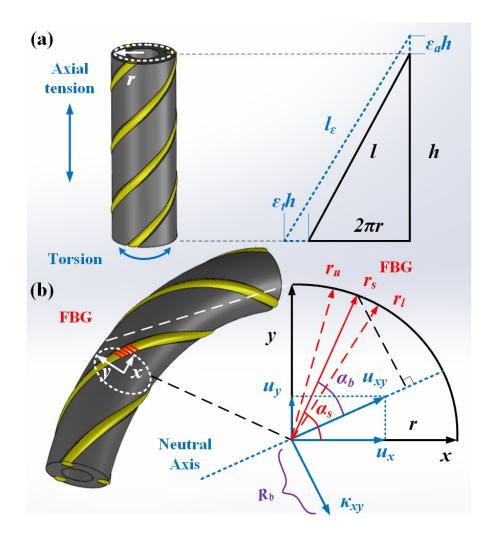


Figure 7.1: Demonstration of the curvature-strain model for helical-wrapped FBG sensors. κ_{xy} is the curvature vector commonly used for representing the bending radius and the direction of bending. u_{xy} is the curvature vector used for deriving the curvature-strain model presented in this work. Note that $||u_{xy}|| = ||\kappa_{xy}|| = R_b$.

center of the tube and h is the pitch of the helix.

The length of the helical fiber can be calculated as:

$$l = \sqrt{(2\pi r)^2 + h^2} \tag{7.1}$$

When the tube has an axial strain ε_a , and shear strain ε_t , the height and the width will become $(1 + \varepsilon_a)h$, $(2\pi r + \varepsilon_t h)$, respectively. The resulting strain in the fiber is shown in

Eq. (7.2), where the length of the strained fiber is denoted by l_{ε} .

$$\varepsilon_l = (l_{\varepsilon}/l) - 1 \tag{7.2}$$

$$l_{\varepsilon} = \sqrt{(2\pi r + \varepsilon_t h)^2 + (1 + \varepsilon_a)^2 h^2}$$
(7.3)

Eq. (7.2) reveals the nonlinear relationship between the strain in the tube and those in the FBG sensors, but this nonlinearity complicates the derivation of the curvature-strain model and makes the inverse calculation difficult. In practice, the effective strain measurement range of an FBG sensor is within 1%, which means both ε_a and ε_t are always small values (< 0.01). Therefore, Eq. (7.2) can be linearized with respect to (ε_a , ε_t) at the point (0, 0):

$$\varepsilon_l \approx w_1 \varepsilon_a + w_2 \varepsilon_t \tag{7.4}$$

$$w_1 = h^2/l^2, \quad w_2 = 2\pi r h/l^2$$
 (7.5)

 w_1 and w_2 can be interpreted as the weight of ε_a and ε_t in the resultant ε_l . The ratio between w_1 and w_2 represents the axial to shear sensitivity of the FBG sensor:

$$w_1/w_2 = h/(2\pi r) \tag{7.6}$$

It can be seen that when $h = 2\pi r$, the helical FBG sensor will be equally sensitive to axial and shear strain. By changing the pitch of the helix h for a given tube diameter, the sensitivity of the sensor in each direction can be tuned. Eq. (7.7) gives the bend radius of a helix, and h should be chosen to guarantee that the bending radius b is always larger than the minimum bending radius of the FBG sensor.

$$b = (r^2 + (h/2\pi)^2)/r$$
(7.7)

Eq. (7.4) relates strain in FBG sensors to the axial and shear strain in a tube. To complete the curvature-strain model, a mapping from the bending curvatures and torsion in the tube

to the axial and shear strain are needed:

$$\varepsilon_a = ||(u_{xy} - \hat{u}_{xy}) \times r_s|| \tag{7.8}$$

$$\varepsilon_t = (u_z - \hat{u}_z)r \tag{7.9}$$

where

$$u_{xy} = \begin{bmatrix} u_x \\ u_y \end{bmatrix}, \ \hat{u}_{xy} = \begin{bmatrix} \hat{u}_x \\ \hat{u}_y \end{bmatrix}, \ r_s = \begin{bmatrix} r\cos(\alpha_s) \\ r\sin(\alpha_s) \end{bmatrix}$$
(7.10)

 \hat{u}_x and \hat{u}_y are the bending pre-curvatures and \hat{u}_z is the pre-torsion within the tube. u_x , u_y and u_z are the curvatures and torsion under deformation. r_s and α_s are the position vector and orientation angle of the FBG sensor. These variables are defined in the body frame at a cross-section along the centerline, as shown in Fig. 7.1(b). A detailed explanation of u_x , u_y and u_z , as well as the coordinate system used can be found in [16].

In the curvature-strain model above, u_{xy} is defined using the bending curvature convention of the Cosserat rod theory. This is suitable for force estimation in large deflecting beams, but not convenient for use with current shape reconstruction algorithms. Fig. 7.1(b) shows the bend radius R_b , and direction of curvature α_b , which are the commonly used definitions for bending curvature in shape reconstruction. Following this convention, the axial and shear strain can be calculated as:

$$\varepsilon_a = r \left(\frac{\sin(\alpha_b)}{R_b} - \frac{\sin(\hat{\alpha}_b)}{\hat{R}_b} \right) = r \frac{\sin(\alpha_b)}{R_b} - \hat{\varepsilon}_a, \qquad \varepsilon_t = (\tau - \hat{\tau})r \tag{7.11}$$

where τ is the torsion with respect to the centerline, and $1/\hat{R}_b$ and $\hat{\tau}$ are the pre-curvature and pre-torsion. The relationship between the two sets of bending curvature and torsion conventions is:

$$\tau = u_z, \quad R_b = \frac{1}{\|u_{xy}\|}, \quad \alpha_b = \alpha_s - \arctan\left(\frac{u_y}{u_x}\right)$$
(7.12)

$$u_x = \cos(\alpha_s - \alpha_b)/R_b, \quad u_y = \sin(\alpha_s - \alpha_b)/R_b$$
 (7.13)

Combining Eqs. (7.4), (7.8) and (7.9) or Eqs. (7.4) and (7.11) results in the curvaturestrain model for each FBG sensor. A set of linear equations can be formed to give the relation between curvature and torsion, and the strain in the three helically-wrapped FBG sensors, as shown in Eq. (7.14):

$$\varepsilon_l^i = w_1 \varepsilon_a^i + w_2 \varepsilon_t^i, \quad i = 1, 2, 3 \tag{7.14}$$

where *i* represents the index number of each FBG sensor. By solving these equations, the curvature and torsion measurements are obtained. For example, if Eq. (7.11) is substituted into Eq. (7.14):

$$\varepsilon_{l}^{1} = w_{1}(r\sin(\alpha_{b}^{1})/R_{b} - \hat{\varepsilon}_{a}^{1}) + w_{2}(\tau - \hat{\tau})r$$

$$\varepsilon_{l}^{2} = w_{1}(r\sin(\alpha_{b}^{2})/R_{b} - \hat{\varepsilon}_{a}^{2}) + w_{2}(\tau - \hat{\tau})r, \quad \alpha_{b}^{2} = \alpha_{b}^{1} + 120^{\circ} + \epsilon_{21}$$
(7.15)
$$\varepsilon_{l}^{3} = w_{1}(r\sin(\alpha_{b}^{3})/R_{b} - \hat{\varepsilon}_{a}^{3}) + w_{2}(\tau - \hat{\tau})r, \quad \alpha_{b}^{3} = \alpha_{b}^{1} + 240^{\circ} + \epsilon_{31}$$

The equations above assume three helically-wrapped FBG sensors, spaced 120° apart, are used for measuring the bending curvatures and torsion. However, due to difficulties in placing each FBG at an exact orientation, error terms ϵ_{21} , and ϵ_{31} should be introduced, and estimated more accurately through calibration. Solving Eq. (7.15) gives an analytical expression for α_b^1 , Eqs. (7.16) and (7.17). R_b and τ can then be found through substitution into Eq. (7.14):

$$\alpha_b^1 = -\arctan\left(\frac{R_b\varepsilon_r(\hat{\varepsilon}_a^3 - \hat{\varepsilon}_a^1) + R_b(\hat{\varepsilon}_a^1 - \hat{\varepsilon}_a^2) - \sin(\alpha_b^3 - \alpha_b^1)\varepsilon_r + \sin(\alpha_b^2 - \alpha_b^1)}{-\cos(\alpha_b^3 - \alpha_b^1)\varepsilon_r + \cos(\alpha_b^2 - \alpha_b^1) + \varepsilon_r - 1}\right),$$
(7.16)
$$\varepsilon_r = \frac{\varepsilon_l^2 - \varepsilon_l^1}{\varepsilon_l^3 - \varepsilon_l^1}$$
(7.17)

Strain sensors are also influenced by temperature, and a temperature term can be added to Eq. (7.14) to provide a temperature-compensated curvature-strain model, as shown in Eq. (7.18):

$$\varepsilon_{l}^{i} = \delta T \beta + w_{1} \varepsilon_{a}^{i} + w_{2} \varepsilon_{t}^{i}, \quad i = 1, 2, 3, 4$$
(7.18)

where δT is the change in temperature and β represents the thermal sensitivity. It is proposed that a fourth fiber with a helical pitch different from the pitch of the other three fibers be added to measure temperature through coupled sensor calculations.

7.2.3 FBG Sensors under Uneven Strain Distribution

For applications that require high resolution measurements, the assumption that a helicallywrapped FBG experiences the same strain along the sensing segment will not hold any more. To deal with this situation, the effects of the strain variations in a FBG sensor is modeled in this subsection. $\bar{\varepsilon}_a$ is defined as the average strain along the hellically-wrapped FBG sensor, which can be formulated as follows:

$$\bar{\varepsilon}_a = \int_{\alpha_l}^{\alpha_u} \varepsilon_a(\alpha) d\alpha \middle/ (\alpha_u - \alpha_l)$$
(7.19)

In which,

$$\alpha_u - \alpha_l = \frac{2\pi l_s}{l} \tag{7.20}$$

where α_u and α_l are the orientation angles of the start and end points of the FBG sensing segment. l_s is the length of the FBG. By solving Eq. (7.19), the analytical expression of the bending strain is obtained:

$$\bar{\varepsilon}_a = \frac{(u_{xy} - \hat{u}_{xy}) \cdot (r_l - r_u)l}{2\pi l_s} \tag{7.21}$$

The torsion of the shaft remains almost the same along the FBG sensing segment, so the formulation for calculating torsional strain is still valid. Combing Eqs. (7.4), (7.9) and (7.21) results in the improved curvature-strain model. It can be seen that this model still presents a linear relationship between the curvature of the robot and strain of FBGs, thus can be

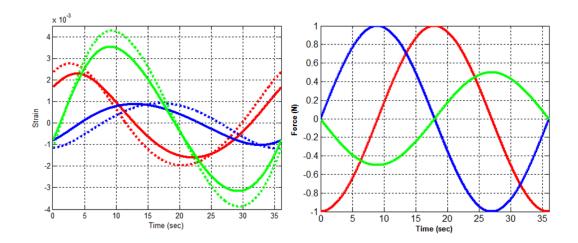


Figure 7.2: (a) The dashed lines are the strain values calculated from the previous model in subsection 7.2.2; the solid lines are from the new model; (b) the time-varing force that applied at the tip of the robot.

summarized as a simple algebraic equation:

$$\varepsilon_l = A(u - \hat{u}) \tag{7.22}$$

where $u = [u_x, u_y, u_z]$ is the vector that contains curvatures and torsion values and A is the matrix that converts them into strain values.

To visualize the differences between the previous and the improved models, simulations were performed using a planar tube with $1/0.15 \ m^{-1}$ bend radius, and $0.040 \ m^{-1}$ bending stiffness. A sinusoidal force $[F_x = \sin((t - \pi/2)\pi/18), F_y = \sin(t\pi/18), F_z = 0.5 \sin((t + \pi)\pi/18)]^T$ was applied at the tip of the robot and the strain outputs from the two proposed curvature-strain models were calculated and plotted in Fig. 7.2. The FBG sensor was at 0.020 m along the robot shaft, and the total length of the tube was 0.157 m. The dashed lines are the values from the previous model and the solid lines are from the new model. In this chapter, since all the experiments used FBG sensors with 1 mm sensing segment, the differences between these two models are negligible.

7.2.4 Force-Curvature Model of a Single Super-Elastic Tube

The curvature-strain model derived in subsection 7.2.2 relates the strain in the FBG sensors to the bending curvatures and torsions in the continuum robot. To model the relationship between the force at the tip of the robot and the strain in each FBG, it is necessary to develop a force-curvature model that can be used in conjunction with the curvaturestrain model. Kinematic models of concentric-tube robots have been proposed to calculate the positions, orientations, curvatures and torsion of any points along the super-elastic robot [13, 14, 16]. In the authors' previous work, a computationally efficient kinematic model was proposed [16], and presented as follows for a single tube:

$$\dot{\theta}_1(s) = \frac{u_x(s)\cos\theta_3(s) - u_y(s)\sin\theta_3(s)}{\cos\theta_2(s)}$$
(7.23)

$$\dot{\theta}_2(s) = u_x(s)\sin\theta_3(s) + u_y(s)\cos\theta_3(s) \tag{7.24}$$

$$\dot{\theta}_3(s) = u_z(s) - \dot{\theta}_1(s)\sin\theta_2(s)$$
 (7.25)

$$\dot{x}(s) = \sin \theta_2(s) \tag{7.26}$$

$$\dot{y}(s) = -\sin\theta_1(s)\cos\theta_2(s) \tag{7.27}$$

$$\dot{z}(s) = \cos\theta_1(s)\cos\theta_2(s) \tag{7.28}$$

$$\dot{M}(s) = -\dot{r}(s) \times F_{ext} \tag{7.29}$$

where X(s) = [x(s), y(s), z(s)] is the position and $\Theta(s) = [\theta_1(s), \theta_2(s), \theta_3(s)]$ is the orientation for a given cross-section along the centerline of the tube. M(s) consists of the bending and torsional moments attributed to the point force F_{ext} applied at the tip of the robot. The four above mentioned variables are defined with respect to the world frame. The space variable s represents the arc length measured from the proximal end of the tube. The

bending curvatures and torsion of the robot under loading can be calculated as follows:

$$u_{xy}(s) = \begin{bmatrix} u_x(s) \\ u_y(s) \end{bmatrix} = k_x^{-1} \left(k_x \begin{bmatrix} \hat{u}_x(s) \\ \hat{u}_y(s) \end{bmatrix} + R_{\Theta}^T M(s) \Big|_{xy} \right)$$
(7.30)

$$u_z(s) = k_z^{-1} [0 \ 0 \ 1]^T R_{\Theta}^T M(s) \Big|_z$$
(7.31)

where k_x and $k_z = k_x/(1 + v)$ are the bending and torsional stiffness defined in the body frame and their values are coupled through Poisson's ratio v. R_{Θ} is the rotation matrix of the body frame relative to the world frame. More details about this model can be found in [16]. A piece-wise linearization technique is applied and leads to a quasi-analytical solution for the robot's forward kinematics (denoted by *Kine*):

$$[\Theta(s) \ M(s)]^{T} = Kine(\Theta(0), M(0), F_{ext})$$
(7.32)

The two-point boundary conditions $\tilde{\Theta}(0)$ and $\tilde{M}(L) = 0$ (*L* is the total length of the robot body), and tip force F_{ext} are the inputs of this kinematic model. The solutions $[\Theta(s) M(s)]^T$ are iteratively solved using the shooting method. The updating strategy in each step is:

$$\Delta M(0) = J_M^{-1} \| \tilde{M}(L) - M(L) \|$$
(7.33)

$$J_M = \frac{\partial M(L)}{\partial M(0)} \tag{7.34}$$

 J_M is derived and evaluated in the same fashion as the Jacobian matrix discussed in the authors' previous paper [16]. Combining Eqs. (7.32), (7.33) and (7.34), the curvature and torsion at any point along the centerline of the robot can be calculated. By setting the arc length equal to the location of the FBG sensors L_s , the curvature and torsion at that position $u(L_s)$ is obtained. Connecting the force-curvature and curvature-strain models together results in a complete force-curvature-strain model.

7.2.5 Strain-Force Calculation

The force-curvature-strain model is a "forward" calculation. In other words, it provides the amount of strain in each FBG given the tip force. To calculate the tip force from the FBG strain readings, the "inverse" calculation needs to be developed. The inverse of the force-curvature model is found by altering the boundary conditions of Eq. (7.32) such that the input to the model consists of curvatures and the output is the force measurement. Specifically, the boundary conditions become $\tilde{\Theta}(0)$, $\tilde{M}(L) = 0$ and $\tilde{u}(L_s)$, and the outputs are $[\Theta(s), M(s)]$, u(s) and F_{ext} . In this way, solving Eq. (7.32) is a three-point boundary value problem, and the updating strategy becomes:

$$\begin{bmatrix} \Delta M(0) \\ \Delta F_{ext} \end{bmatrix} = J_C^{-1} \begin{bmatrix} \tilde{u}_{Ls} - u(L_s) \\ \tilde{M}(L) - M(L) \end{bmatrix}$$
(7.35)

where J_C is the Compliance matrix of $[u(L_s), M(L)]^T$ with respect to $[M(0), F_{ext}]^T$, which can be derived as follows:

$$J_C = [J_{Cu} \ J_{CM}]^T (7.36)$$

$$J_{Cu} = \begin{bmatrix} \frac{\partial u(L_s)}{\partial \Theta(L_s)} & \frac{\partial u(L_s)}{\partial M(L_s)} \end{bmatrix} \begin{bmatrix} \frac{\partial \Theta(L_s)}{\partial M(0)} & \frac{\partial \Theta(L_s)}{\partial F_{ext}} \\ \frac{\partial M(L_s)}{\partial M(0)} & \frac{\partial M(L_s)}{\partial F_{ext}} \end{bmatrix}$$
(7.37)

$$J_{CM} = \begin{bmatrix} \frac{\partial M(L)}{\partial M(0)} \frac{\partial M(L)}{\partial F_{ext}} \end{bmatrix}$$
(7.38)

It is also possible to merge the strain-curvature calculation into this procedure such that the strain-curvature-force relationship can be solved at once. Assuming that the measured strain values are $\tilde{\varepsilon}_l$, the updating strategy becomes:

$$\begin{bmatrix} \Delta M(0) \\ \Delta F_{ext} \end{bmatrix} = J_{C\varepsilon}^{-1} \begin{bmatrix} \tilde{\varepsilon}_l - \varepsilon(L_s) \\ \tilde{M}(L) - M(L) \end{bmatrix}$$
(7.39)

$$J_{C\varepsilon} = \left[\frac{\partial \varepsilon_l}{\partial u} J_{Cu} \ J_{CM}\right]^T \tag{7.40}$$

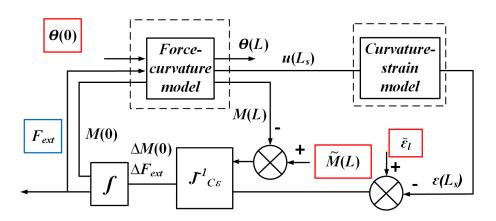


Figure 7.3: Signal flow digram for Strain-Force Calculation. The boundary conditions in red blocks are the inputs of the model chain. One of the outputs of this calculation is the tip force measurement (the blue block).

where $\partial \varepsilon_l / \partial u$ is derived from Eq. (7.4) and $J_{C\varepsilon}$ is the Compliance matrix of $[\varepsilon(L_s), M(L)]^T$ with respect to $[M(0), F_{ext}]^T$. The complete force-curvature-strain model and its inverse calculation are shown in a signal diagram in Fig. 7.3.

7.3 Engraving Helical Grooves on Super-elastic Nitinol Tubes

Embedding helically-wrapped strain sensing fibers into continuum robots is an effective solution for obtaining curvature, torsion and force measurement. However, there are many challenges in engraving precision grooves into the surface of flexible tubes including workpiece fixation, accurate depth of cut control, precision profiling and smooth surface finishing. Straight surface slots have been created using micro-milling, laser cutting and electrical-discharge machining (EDM) but each of these methods have deficiencies in helical and patterned slot formation for FBG fixation. Micro-milling requires the workpiece to be rigidly constrained as the forces required to remove material bend the tube and straightslot reinforcement techniques cannot be applied for helical cutting. Laser etching eliminates cutting force concerns and six-axis systems can be used to make various patterns, though the laser needs to be quite powerful to penetrate deep enough into Nitinol to make FBG slots, making the depth of cut difficult to control and the surface finish quite rough. These deficiencies create strain measurement inaccuracy, and safety concerns when installing the micron-scale fibers. Wire-EDM can meet the accuracy and surface finish specifications, and is also a low force machining method; however, the need to pass the wire from one end of the workpiece to the other restrains pattern design. The degrees of freedom offered by commercial systems further limits grooving to straight configurations.

The limitations of current machining techniques motivated the design of a novel three-axis engraving system for machining patterns on cylindrical structures, such as rods and tubes. To ensure repeatability, accuracy and quality surface finishing the main focus of this system was to constrain a flexible rotating and translating cylindrical workpiece while minimizing the force required in removing material. To meet these objectives a fixed block with a hollow bore was created to provide constant support to the workpiece and a machining system incorporating milling and turning techniques was designed for low-force material removal, as shown in Fig. 7.4. The system removes material by advancing the workpiece through the precision bore in the block and onto a depth-controlled spinning end mill, while rotating the workpiece along its longitudinal axis as desired for patterning. The end mill is inserted through a separate hole in the block with a wide-angle entry that is used for the application of pressurized air and lubricating coolant throughout the machining process. This reduces tool wear and workpiece torsion, improving cutting accuracy and surface finish. A conical extrusion was added to the block to observe the tool-workpiece interface in real-time through a microscope as shown in Fig. 7.4(b) and (c). The block was made from 3D-printed ABS to damp vibrations, create a low friction surface and ease manufacturing as a new block should be used when changing the tube diameter. Although the ABS block provided satisfactory support to bending, it was still important to reduce the cutting force required to prevent torsion, local tube deformation and vibration so a spinning end mill (944215-C6, Harvey Tool, United States) with ideal feed rate and RPM parameters was used. The machining apparatus itself was constructed from modular aluminum base plates from which two high accuracy, large workspace linear stages (T-LSR300B, Zaber

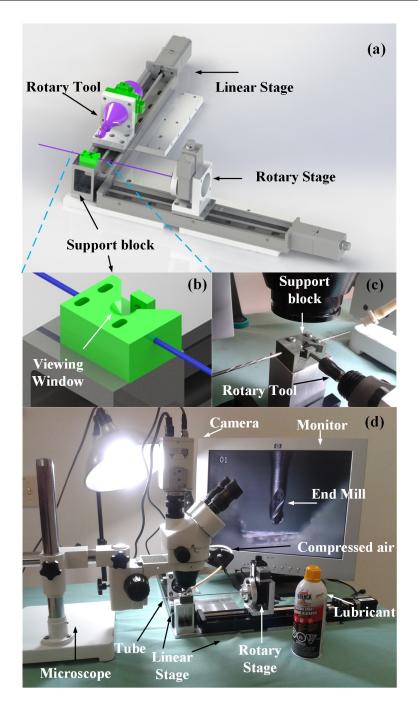


Figure 7.4: (a) The CAD model of the engraving system. (b) A magnified view of the support block. (c) The 3D-printed support block. (d) The actual customized engraving system.

Technologies, United States), and the workpiece support platform were mounted. A rotary stage (T-RS60A, Zaber Technologies, United States) and a rotary spindle (200 series rotary

tool, Dremel, United States) were then mounted to the linear stages to create a portable system. To ensure depth of cut accuracy equal to the linear stage resolution a multimeter continuity test was used to probe for contact between the end mill and workpiece. After machining the workpiece the surface finish was found to be smooth from visual and tactile inspection, and the pitch of the helical slots and the distance between the slots were accurate as validated using digital calipers. Fig. 7.4(b) and (d) show the results of the engraving process.

7.4 Experimental Validation on a Single Tube

To validate the proposed embedded sensing technology and modeling techniques described above, a series of experiments were performed on both straight and pre-curved Nitinol tubes with embedded FBG sensors.

Three helical slots are engraved on the surface of both Nitinol tubes using the customized engraving system. Both tubes have dimensions of 90 mm (length) x 2 mm (outer diameter) x 1 mm (inner diameter) to meet general size constraints for needle-based therapies. The wall thickness was chosen to safely embed the optical fibers into grooved slots. The optical fibers were bonded into each helical slot with Cyanoacrylate adhesive (10810, Elmers Products Inc., United States). The grooves are 0.35 mm deep, and 0.4 mm (1/64") wide for the straight tube and 0.8 mm (1/32") wide for the curved tube to accommodate enough space for the adhesive to secure the fiber. The liquid adhesive provides a thin film bond between the glass fiber and Nitinol tube to ensure the two materials of similar elastic modulus (or greater for Nitinol), strain by the same amount. The pitch of each helical slot is 23 mm, resulting in a bending radius of 21 mm for each optical fiber when the tube is not under deformation.

As shown in Fig. 7.5, the proximal end of each tube was fixed to a rotary stage to evaluate the resolution and accuracy of curvature, torsion and force measurements for the sensorized

robot at all possible orientations. A commercial FBG interrogator (SM130, Micron Optics, United States) was used to obtain the reflected wavelength of each FBG at a 100 Hz sampling rate.

7.4.1 Validation on Straight Tubes

The Nitinol tube in the first set of experiments is initially straight, and the tube is fitted with a 5 mm FBG segment bonded into one of the helical slots.

Measuring Torsion

To demonstrate the effectiveness of the helical design for torsion sensing, as shown in Fig. 7.5(a), the distal end is attached to a rigid fixture while the proximal end is rotated by the motorized stage at a constant speed. The strain values, calculated from the FBG sensor wavelengths, are plotted as the stage is rotated clockwise from its neutral position (Fig. 7.6(a)) and then counter-clockwise from its neutral position (Fig. 7.6(b)). A linear best-fit line is plotted on top of the strain-torsion measurements to show that the strain in the FBG sensor is proportional to the torsion as described in Eq. (7.9). The strain/torsion ratio is 0.0185 and 0.0196 for clockwise and counter-clockwise rotation and the small differences are due to the asymmetrical nature of the helical structure.

Spectrum Distortion under Large Bending

Helically-wound fibers with long FBG segments are prone to peak-distortion under large bending due to the uneven distribution of strain within the FBG segment. There is no accurate model, to date, that can relate this phenomenon with the parameters of the FBG sensor and helical pattern. Experiments were performed to conduct a qualitative analysis for choosing the appropriate FBG sensor length based on the resolution required and curvature experienced. The rigid fixture at the distal end of the tube was removed and several

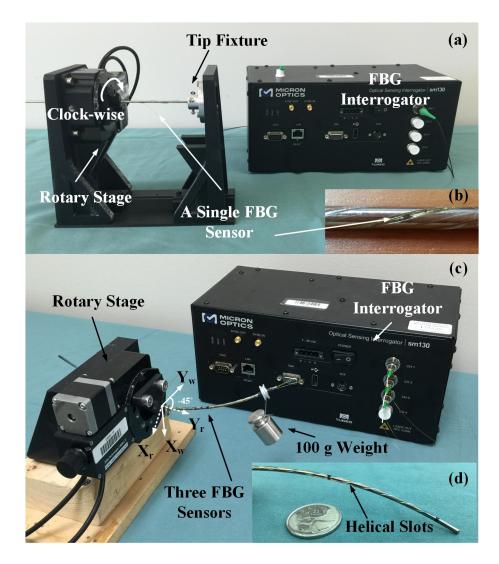


Figure 7.5: (a) Experimental setup for straight-tube torsion validation. (b) Magnified view of fiber embedded in grooved tube. (c) Experimental setup for pre-curved tube analyses. The robot base denoted (X_r, Y_r) , and is rotated -45° with respect to the world frame (X_w, Y_w) . (d) Magnified view of the pre-curved tube with helical grooves.

calibration weights were placed at the tube tip to generate various bending curvatures at the FBG sensor location. The tube was rotated through one full rotation and showed a smooth trigonometric signal for weights under 40g. At weights above 40g, the peak began to broaden causing signal distortion, as can be seen in Fig. 7.7(a) and (b). A short FBG sensor can be used to avoid this problem, but the signal-to-noise ratio decreases since the Full-Width-Half-Maximum bandwidth of the FBG sensor is related to the length of the

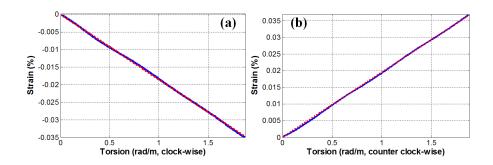


Figure 7.6: The torsion measurements (blue) when the motorized stage rotates in a clockwise direction (a) and a counter-clockwise direction (b). The red lines are the linear best-fit to the measurement data.

sensing segment. As shown in Fig. 7.7(c), when both sensors were bonded to a flat static structure, the noise from a 1mm FBG sensor (blue) is significantly larger than that of a 5mm sensor (red). From the discussions above, it can be concluded that long FBG sensors will provide better resolution, but short sensors will allow for larger curvature and force measurement.

7.4.2 Validation on Curved Continuum Robots

The Nitinol tube in the second set of experiments was heat-treated into a planar curved shape ($\hat{u}_x = 0$, $\hat{u}_y = 1/0.15$ rad/m, $\hat{u}_z = 0$). Three optical fibers, each with a 1mm FBG segment, were hand-laid into the machined slots at the same cross-section, 50 mm from the distal tip. The angular position α_s^i and radial offset r^i of each FBG sensor, as well as the Poisson's ratio of the manufactured tube, were identified using the calibration technique explained below.

Calibration Method

A 120 g calibration weight was placed on a 2.6 g pulley at the tip of the curved tube while the motorized stage rotated 360°, as shown in Fig. 7.5. The wavelength sampled from the FBG sensors was compared with the wavelength calculated by the force-curvature-strain

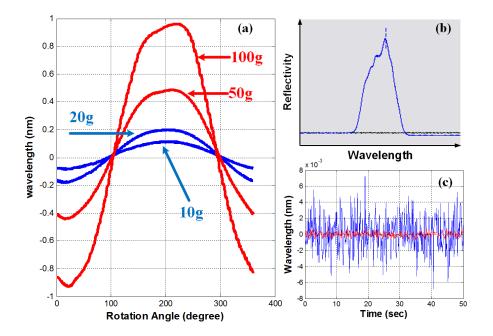


Figure 7.7: (a) Demonstration of the effects of increased bending on the distortion of the FBG sensor output signal. (b) An example of a reflected spectrum with peak distortion. (c) Comparison between the noise from a 1 mm FBG (blue line) and a 5 mm FBG (red line).

Table 7.3: Parameters of the Helically-Wrapped FBG Sensors

<i>h</i> (mm)	$r^{i}, i = 1, 2, 3 \text{ (mm)}$	$\alpha_{s}^{i}, i = 1, 2, 3 (^{\circ})$	v
23	0.75, 0.75, 0.72	115, 235, 347	0.6

model to account for inaccuracies in the FBG sensor hand lay-up. The desired FBG sensor angular positions (120° apart) and radial offset (0.73 mm) were reasonably well met after tuning between the sampled data to calculated data. After tuning, the overall Poisson's ratio was higher than that of Nitinol, and can be attributed to the machined helical grooves. The resulting parameter values are presented in Table 7.3, and the sampled and calculated wavelengths for each sensor are displayed in Fig. 7.8.

It can be seen that the maximum and minimum values for the blue curve, as well as the green curve, do not have the same amplitude, the peak-to-peak amplitude varies between fibers, and the phase difference between the fibers does not fully correlate with the specified

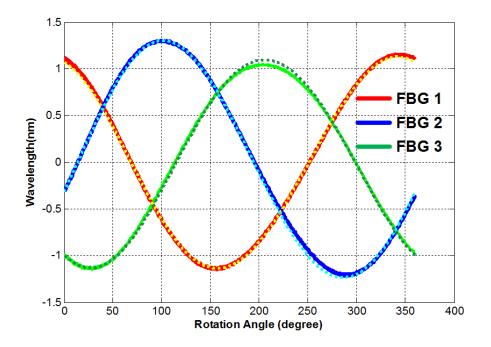


Figure 7.8: The solid lines are the wavelengths reflected from three FBG sensors that are helically-embedded in a curved tube. The wavelength output of each FBG was biased at the beginning of the test. The dashed lines are the corresponding values from the force-curvature-strain model using the calibrated parameters listed in Table 7.3.

angular position values. This anisotropic behavior is caused by pre-curvature and torsional loading, which motivated the development of our nonlinear force-curvature-strain model for accurate measurements.

Measuring Curvature and Torsion

To generate continuously-varying bending curvatures and torsions in the shaft of the Nitinol tube, a series of weights were placed on the pulley on the distal end of the tube, while the proximal end rotated one full revolution. Finite element analysis showed the proximal end of the tube could yield at 200 g, so a maximum weight of 150 g was used. The curvature-strain model was then used to obtain curvature and torsion measurements from the FBG sensor strain data sampled at 100 Hz.

There was not a straightforward way to directly validate the torsion and bending measure-

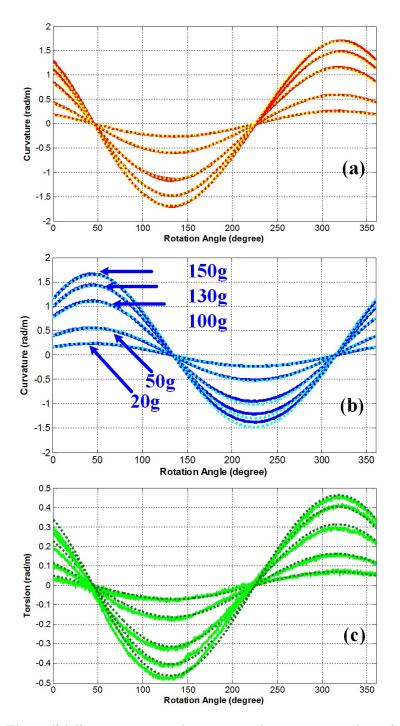


Figure 7.9: The solid lines represent the measured curvature and torsion values using helically-wrapped FBG sensors. The dashed lines are the theoretical values calculated from the model described in subsection 7.2.4. (a) plots the measured and theoretical values of $(u_x - \hat{u}_x)$ under a series of loading; (b) and (c) display $(u_y - \hat{u}_y)$ and $(u_z - \hat{u}_z)$, respectively.

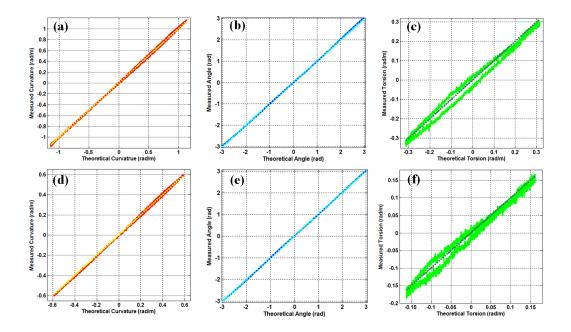


Figure 7.10: Demonstration of the accuracy and repeatability in bending curvature and torsion measurement. A weight of 100 g was used at the distal tip of the pre-curved Nitinol tube for (a), (b) and (c). A weight of 50 g was used for (d), (e), and (f). The red, blue, and green solid lines are the measurements of u_x , α_b^1 , and τ , divided by the theoretical value. A ratio of 1 between the measured and theoretical value is denoted by a dashed line.

ments at arbitrary cross sections of the pre-curved tube, so an evaluation method similar to [7] was used to calculate these values. The Cosserat modeled curvature and torsion values were compared with the measured values provided by the FBG sensors and the results are shown in Fig. 7.8. The errors for curvature and torsion measurement (e_u^x, e_u^y, e_u^z) under each weight are summarized in Table 7.4. It can be seen that the RMS errors of curvature measurements are 2% - 4% of the total range measured. The bending curvature measurements show less noise than the torsional measurements because of the pitch chosen, which is limited by the sensor minimum bend radius.

To assess the hysteresis of bending curvatures and torsion measurement in the pre-curved Nitinol tube, the proximal end was rotated through a full revolution, with a 100 g weight, then a 50 g weight, suspended by the pulley at the distal end. The measurements of u_x , u_y , u_z , α_b , R_b and τ were collected. These curvature and torsion values were compared with

Weights (g)	Max e_u^x, e_u^y, e_u^z (rad/m)	RMS e_u^x, e_u^y, e_u^z (rad/m)
20 + 2.6	0.0170, 0.0183, 0.0457	0.0057, 0.0084, 0.0104
50 + 2.6	0.0252, 0.0321, 0.0386	0.0096, 0.0140, 0.0131
100 + 2.6	0.0485, 0.0788, 0.0575	0.0178, 0.0324, 0.0230
130 + 2.6	0.0647, 0.0921, 0.0555	0.0288, 0.0398, 0.0227
150 + 2.6	0.0753, 0.1115, 0.0616	0.0326, 0.0470, 0.0278

Table 7.4: Errors in Curvature and Torsion Measurements

the theoretical values from the mechanics-based model discussed in subsection 7.2.4. The ideal ratio of experimental to theoretical values is 1. This procedure generated large variations in u_x , u_y , τ (u_z), and α_b , and minimal variation in R_b . The resulting measurements are plotted in Fig. 7.10 for u_x (a, d), α_b^1 (b, e), and τ (c, f). The measurements for u_x and u_y are quite similar, and the performance of R_b will be evaluated in the next experimental set. The bending curvature measurements show high accuracy and repeatability using both curvature-strain models, and torsion measurements show reasonable accuracy and repeatability and are affected mostly by hysteresis and noise. Based on the specific application of this technology, the helical pitch, sensor location, and pre-curvature can be modified to improve torsion accuracy, and resolution. The hysteresis may be due to nonlinearities in the shear moduli of this Nitinol tube caused by in-house heat treatment, which was not included in the mechanics-based model.

The resolution of this sensing technology was evaluated by suspending a series of weights incrementally at the distal tip of the Nitinol tube and observing the smallest distinguishable measurements for curvature and torsion. The base of the tube was orientated at 45° from the direction of gravity such that tip loading would cause both bending and torsion at the sensing location. The Nitinol tube was kept stationary during this experiment to avoid vibrations from the motor or weights. First, a set of weights with small increments (120 g, 130 g, 135 g, 137 g, and 138 g) were used for testing the resolution of bending curvatures, shown in Fig. 7.11(a, b), and torsion, shown in Fig. 7.11(c). The smallest distinguishable bending curvature measurements are 0.012 rad/m for u_x , and 0.016 rad/m for $1/R_b$. A

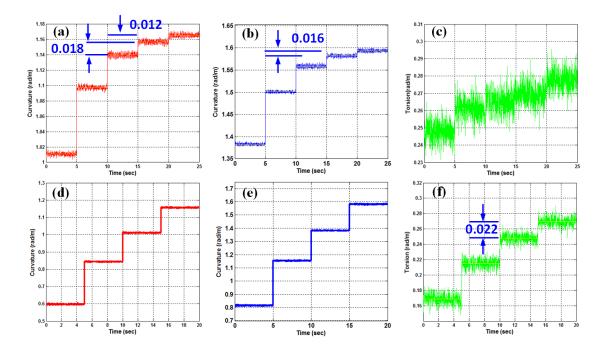


Figure 7.11: Demonstration of the resolution in bending curvature and torsion measurements. The pre-curved Nitinol tube was positioned at 45° relative to gravity and weights of 120 g, 130 g, 135 g, 137 g, and 138 g were suspended at the tip in (a), (b) and (c). Weights of 70 g, 100 g, 120 g, and 137 g were used for (d), (e), and (f). The red and blue lines show the measured bending curvatures, u_x , $1/R_b$. The green lines show the measured torsion, τ . The yellow line denotes the mean value at each incremental load over 5 seconds.

second set of weights with larger increments (70 g, 100 g, 120 g, and 137 g) was used to increase the torsion signal, since the resolution of torsion could not be clearly seen with the first weight set. The bending curvatures are plotted in Fig. 7.11(d, e), and the torsion is plotted in Fig. 7.11(f). The smallest distinguishable torsion measurement, τ , is 0.022 rad/m.

Measuring Lateral Forces

In addition to obtaining curvature and torsion measurements during the above experiments, the lateral tip force was calculated based on the force-curvature-strain model. Force measurement is accurate to within 5% of the total range measured throughout all configurations of the pre-curved Nitinol tube, as shown in Fig. 7.12. The small errors, especially near 220° ,

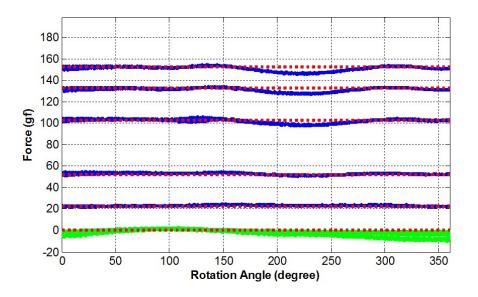


Figure 7.12: The red lines represent the amount of gravity force applied at the tube tip while the motorized stage rotates a full revolution. The blue lines are the force measurements in the direction of gravity (F_x) while the green lines are the force measurements in the other direction (F_y) .

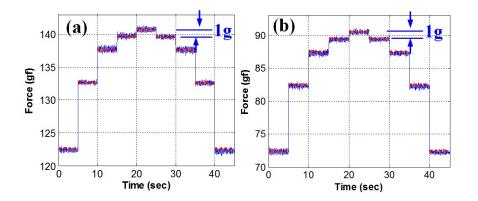


Figure 7.13: Two set of weights were put on the tube tip to test the resolution of the proposed force sensing technolgoy. In (a), the weights are 120g, 130g, 135g, 137g, 138g. In (b), the weights are 70g, 80g, 85g, 87g, 88g. The blue lines are the measured forces using FBG sensors and the red lines are the theoretical gravity values.

can be attributed to unmodeled nonlinearites and inaccuracies in calibrated parameters and tool fabrication. Similar error amplitudes are found in both lateral directions (e_F^x, e_F^y) and the weights used and the errors e_F^x are presented in Table 7.5.

To demonstrate the resolution of this sensing technology, a series of weights was incre-

Weights (g)	22.6	52.6	102.6	132.6	152.6
Max e_F^x (gf)	2.12	2.23	5.13	5.47	7.07
RMS e_F^x (gf)	0.87	0.92	1.97	2.07	2.62

Table 7.5: Errors in Force Measurements

mentally added to the pulley at the distal tip of the robot, with the robot at a fixed angle of 45° . It can be seen from Fig. 7.13(a) that the resolution is better than 0.01N as the system clearly distinguish between 1g weights. A separate series of weights was then used for this experiment and Fig. 7.13(b) shows the consistency in performance.

7.5 Design of a Sensorized Concentric-Tube Robot

In the previous sections, a single tube continuum robot was sensorized to measure force and torque by embedding FBG sensors in a helical slot on the outer surface of the shaft. This section presents an enhanced design that extends this technique to Concentric-Tube Robots (CTR) with multiple tubes. The proposed design fully protects the fiber from being severed by cutting forces (the force present at the edge of the outer tube as it moves across the surface of the inner tube). Experimental results are presented that demonstrate the sensitivity and accuracy of force measurements of a sensorized CTR.

7.5.1 Design and Fabrication of a Sensorized Tube Assembly

The general design concept of a sensorized CTR is shown in Fig. 7.14. FBG sensors are sandwiched in a sensorized tube assembly, to provide shape and force measurements during the robot motion without getting damaged. The sensorized tube assembly has five components: FBG sensor, sensor carrier, protective sleeve, protective housing, and mount-ing plate. These components and their assembly are shown in Fig. 7.15. The sensor carrier

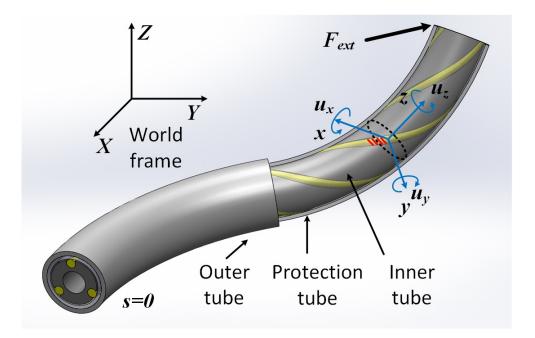


Figure 7.14: Demonstration of the design concept of a sensorized concentric-tube robot.

is a pre-curved Nitinol tube with engraved helical slots. The protective sleeve is a thinwalled Nitinol tube that protects the FBGs from cutting forces and pressure points without significantly increasing the robot diameter as compared to alternatives such as plastic tubes or polytetrafluoroethylene (PTFE) heat shrinks. In addition, using the same material as the other tubes simplifies the mechanics-based strain-force model. To avoid discontinuities in the sensing signal and minimize pretension, the protective sleeve is made with the same precurvature as the sensor carrier. The sleeve diameter is also slightly larger than the carrier diameter to avoid damaging the fibers during assembly. Based on previous experiments, we chose a clearance of 0.15 mm (diameter) between these tubes. A draw tower grating FBG sensor (FBGS Technologies, Germany) with a 3 mm sensing segment and 125 m diameter is bonded into the helical slots of the sensor carrier with cyanoacrylate adhesive (10810, Elmers Products Inc., United States). The protective housing is rapid prototyped from ABS plastic and is used to hold the protective sleeve and to protect the exposed section of the fiber. The mounting plate uses set screws to holds the sensor carrier in the desired orientation and connects the assembly to the drive unit. The CTR used in the experiments consists

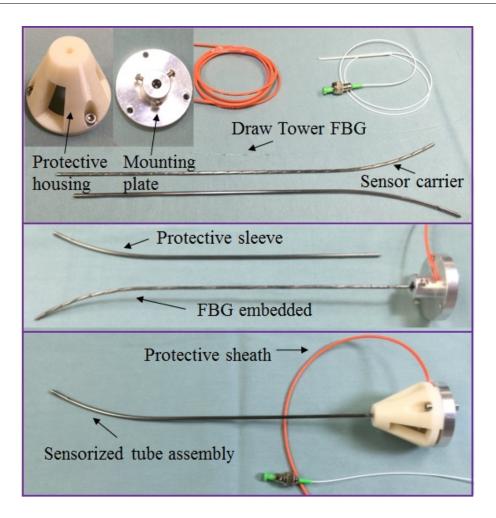


Figure 7.15: The sensorized tube assembly and components.

of the sensorized tube assembly shown in Fig. 7.15 and a straight outer tube, as shown in Fig. 7.17(a). The drive unit uses commercial linear stages (MXE, Tolomatic, United States) and rotary stages (FHA-mini, Harmonic Drive, United States). As presented in [5], the location of the FBG sensor, the stiffness of the outer tube and sensorized tube, and the overall Poisson's ratio were calibrated by attaching a 50g weight to the robots tip, and rotating the sensorized tube over a full 360 revolution as shown in Fig. 7.17(b).

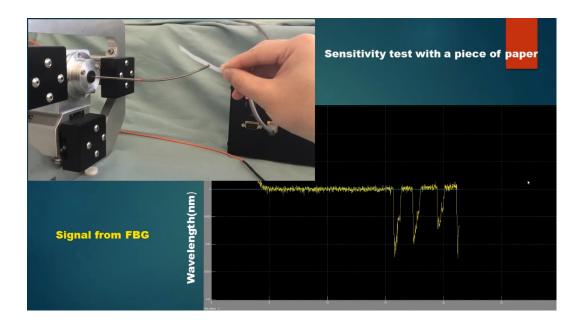


Figure 7.16: Illustration of the sensitivity of the sensorized CTR in force sensing

7.5.2 Experimental Validation on a Concentric-Tube Robot

To demonstrate the sensitivity of the developed sensorized CTR, a piece of printing paper was used to gently press the robot's tip several times. From the signals shown in Fig. 7.16, it can be seen that the reflective wavelength response strongly to the paper touching force. To assess the effect of the cutting force on the FBG sensor, the sensorized tube was moved in and out by a linear stage at a speed of 3 mm/s, while the outer tube was held stationary. The reflected wavelength of the FBG sensor was recorded during this time for further analysis. To assess the performance of the proposed sensing technology, vertical and horizontal loads were applied at the tip of the robot in two consecutive tests as shown in Figs. 7.17(b) and (c). In the vertical loading tests, a series of weights (30g, 40g, 45g, 47g, 48g) were applied incrementally at the robots tip. The reflected wavelength from the FBG sensor was recorded and converted to force values. The strain-force calculation used in this work is an extension of the algorithm presented in [5], so as to make applicable to CTR with more than a single tube. The accuracy in the horizontal direction was evaluated by manually pulling the tip of the robot using a string attached to a commercial force/torque sensor

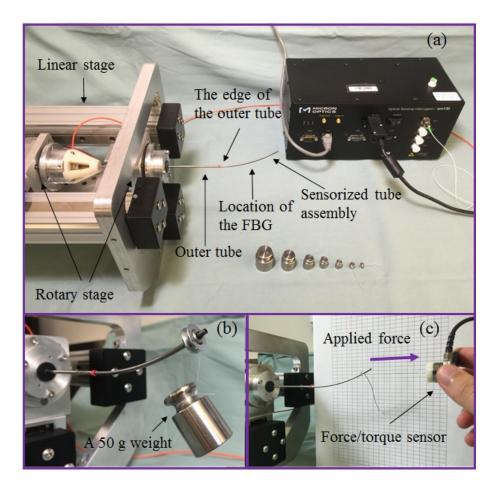


Figure 7.17: (a) The experimental setup for force sensing calibration and validation; (b) vertical loading senario; (c) horizontal loading scenario.

(Nano17, ATI Industrial Automation, United States). The force measurements from the sensorized robot and commercial sensor were recorded simultaneously. For both tests, the robot was stationary (with the orientation shown in Figs. 7.17(b), (c)) and the FBG sensor was sampled at a rate of 100 Hz.

7.5.3 Results and Discussion

Fig. 7.18 shows the FBG sensor response when the sensorized tube was moved in and out of the outer tube. During the movement, the FBG response is continuous and smooth, indicating that the cutting force and pressure from the tube interactions are well distributed

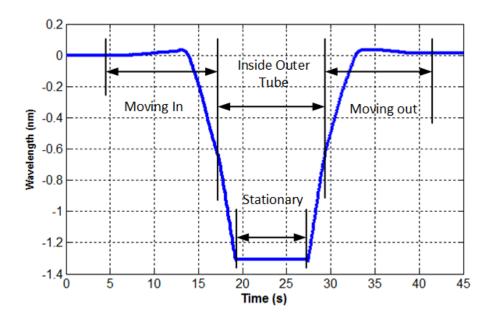


Figure 7.18: The wavelength output when the inner tube translates relative to the outer tube (biased at the beginning).

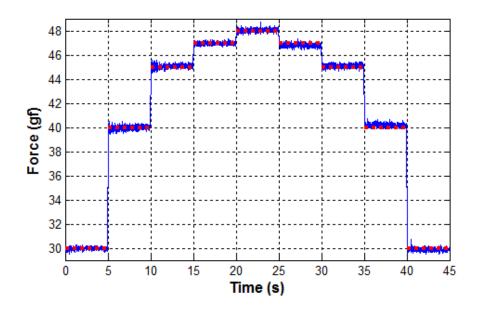


Figure 7.19: Comparision of the theoretical force values (red) and the measured force values from the sensorized CTR (blue).

by the protection sleeve. It is important to note, that the reflected wavelength shows large changes before the FBG is fully inside the outer tube. This behavior seems to contradict the usual assumption that a CTR will have a discontinuous change in curvature at the distal

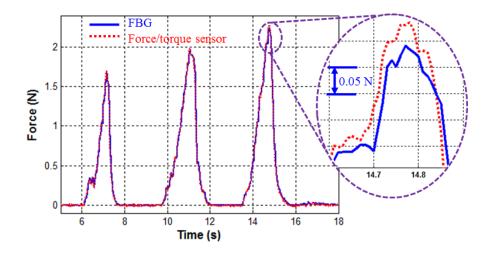


Figure 7.20: Comparision of the force values measured using Nano17 (red) and the sensorized CTR (blue).

edge of the outer tube. This finding suggests the need for a further investigation in modeling CTR. Fig. 7.19 shows the performance of the proposed sensing technology when the robot is under vertical loading. It can be seen that the force resolution is better than 1 gf. The maximum and RMS error were 0.05 N and 0.03 N, respectively. Under horizontal loading, the force measurements calculated from the FBG signal match the force/torque sensor readings accurately, as shown in Fig. 7.20. The maximum errors occurred at the peak force values (Fig. 7.20, detail view), where some high frequency disturbances were introduced by hand tremor during manual manipulation of the force/torque sensor. The magnitude of these errors does not jeopardize the application of this technology for medical interventions. The maximum and RMS errors in this test were 0.06 N and 0.02 N, respectively. This technology is currently being used in our lab for haptics enabled CTR.

7.6 3D Force Sensing in Pre-curved Continuum Robots

For axially stiff robotic tools, such as da Vinci instruments and interventional needles, 3D force sensing has remained a big challenge, since the deformations in the axial direction

under loading are mostly below the measurement range of strain sensors. On the other hand, in pre-curved robots, the axial forces (defined in the tip frame) can generate bending effects on the robot shaft in the same way as lateral forces. This feature makes it possible to obtain 3D force sensing in this particular type of robot. In this section, the problem of 3D force sensing in pre-curved continuum robots is modeled mathematically and studied using numerical simulations. The results of the study consists of a design criterion for choosing the locations where strain sensors need to be placed in order to achieve optimal sensing performance.

7.6.1 An Alternative Method for Strain-Force Calculation

An alternative strain-force calculation approach is developed, which decomposes the threepoint boundary value problem into two two-point boundary value problems. This new method is compatible with the majority of the forward kinematic models proposed for continuum robots in the literature and not only limited to the author's previous models. More importantly, this method provides an explicit force-curvature-strain relationship, which is the key knowledge in analyzing 2D and 3D force sensing problems discussed in the following subsections.

The alternative method is built on the assumption that the robot is quasi-static at any moment during the deflection caused by an external force. Since the force-curvature model proposed in subsection 7.2.4 does not consider any dynamic effects of the continuum robot either, this assumption will not decrease the accuracy of the results compared to the previous method. Following this assumption, the bending moment at a certain sensorized crosssection should be equal to the torque generated by the tip force, which can be described as follows:

$$R_{\Theta}^{T}(L_{s})K(u-\hat{u}) = d \times F_{ext} = DF_{ext}$$
(7.41)

$$d = X(L) - X(L_s)$$
(7.42)

$$D = \begin{bmatrix} 0 & -d_z & d_y \\ d_z & 0 & -d_x \\ -d_y & d_x & 0 \end{bmatrix}$$
(7.43)

in which u and \hat{u} are the curvature and pre-curvature vectors. $R_{\Theta}^{T}(L_{s})$ is the rotation matrix between the body frame at the sensorized cross-section and the world frame. d is the distance vector starting at the location of the FBGs and ending at the robot tip.

Eq. (7.41) presents an explicit expression of the relationship between the tip force and the curvatures and torsion of the robot at the sensorized cross-section, which can be used for curvature-force calculation when combined with the forward kinematics of continuum robots as shown in Fig 7.21(a). Due to the cross product on the right side of Eq. (7.41), the curvature-force calculation has infinite number of solutions. Hence, the curvature and torsion values from a single cross-section are not enough to calculate 3D forces. This conclusion could not be obtained directly from the previous strain-force model presented in subsection 7.2.5, since all the formulas are implicit; however, simulation and experimental results based on that method strongly support this conclusion.

Given $F_z = 0$, F_x and F_y are solvable, which results in the following updating strategy for solving F_{ext} in each iteration:

$$\Delta F_{ext}\Big|_{xy} = D_{1,2}^{\dagger} R_{\Theta}^T(L_s) K(\tilde{u}_{Ls} - u(L_s))$$
(7.44)

where $D_{1,2}$ denotes the first and second rows of *D*. The updating strategy for strain-force calculation becomes:

$$\Delta F_{ext}\Big|_{xy} = J_{CX}^{\dagger}(\tilde{\varepsilon}_l - \varepsilon(L_s))$$
(7.45)

$$J_{CX} = A^{-1} K^{-1} R_{\Theta}(L_s) D_{1,2}$$
(7.46)

It should be noted that D is calculated from the forward kinematics as shown in Eqs. (7.42) and (7.43). The signal flow of the two strain-force calculation methods are presented

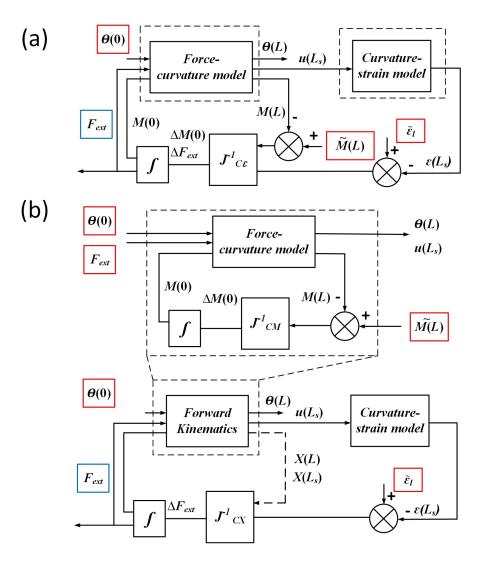


Figure 7.21: Signal flow diagram for two strain-force calculation methods. (a) Previous strain-force calculation method. (b) Alternative Strain-force calculation method. The red blocks represent the inputs of these calculations and the blue ones are outputs.

in Fig. 7.21. It can be seen that the first method has only one step, where three boundary conditions are used together to solve F_{ext} . On the other hand, the second method consists of two steps, boundary conditions $\theta(0)$ and $\tilde{M}(L)$ are used to obtain the intermediate variables X(L) and $X(L_s)$, then the boundary conditions $\theta(0)$ and $\tilde{\varepsilon}_l$ are brought into the calculation to finally solve F_{ext} . The computational cost of the latter method will be higher because of the two-step architecture.

Simulations were designed to assess the performances of the two proposed strain-force calculation methods. The signal flow of these simulations are shown in Fig. 7.22(a). At first, sinusoid forces were applied on a continuum robot, causing strains in two FBG sensors installed on a single cross-section. These strain values of the FBGs were calculated from the forward force-strain model in subsection 7.2.4 and are plotted in Fig 7.22(b). The parameters of this continuum robot and the locations of the FBG sensors are listed in Table 7.6 (tube 1). Then based on the FBG strain values, force measurements were obtained by using the two proposed strain-force calculation methods, as presented in Fig 7.22(c). White noise was added to the strain signals (after 18 seconds in Fig. 7.22(b, c)), to evaluate the performance of strain-force calculations under disturbances. The sinusoid forces used for testing the first and second strain-force calculation methods were $F_{ext} = [\sin((t + t)))$ $(2\pi/3)\pi/18$, $\sin(t\pi/18)$] and $[0.5\sin((t+2\pi/3)\pi/18), 0.5\sin(t\pi/18)]$, respectively. From Fig. 7.22(c), it can be seen that both methods can obtain accurate force measurements. It also shows that the signal-to-noise ratio of these force measurements was similar to that of the FBG signals. In other words, the noise of FBG sensors was not amplified in force measurements.

7.6.2 Multi-Plane 2D Force Sensing

The definitions of lateral and axial forces are clear for a straight robotic tool as shown in Fig. 7.23(a). In this case, forces in the axial direction do not generate enough strains for the current sensing technology to detect. However, for a pre-curved robotic tool, the direction of its axis continuously changes, making the definitions of lateral and axial forces to be dependent on the particular cross-section. Furthermore, forces in all three directions F_x , F_y and F_z can generate enough strain signals on FBG sensors. Hence, FBG sensors installed on a single cross-section of a pre-curved robotic tool can measure 2D forces that are not contained in the (x, y) plane.

To address the problems of measuring arbitrary 2D forces (out of the (x, y) plane) for pre-

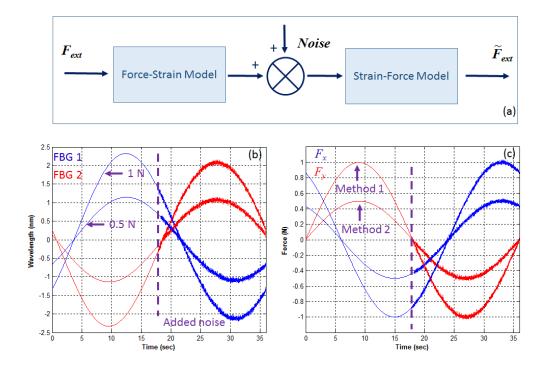


Figure 7.22: Demonstration of the performances of the two proposed strain-force calculation methods with and without added noise. (a) The signal flow of the simulations. (b) The strain values of the FBG sensors when the robot is under load. (c) Force measurements using these strain-force calculation methods developed.

	L_{tran}	L_s^1 (mm)	L_s^2 (mm)	R_b	$L_c \text{ (mm)}$	k (1/m)
Tube 1	0	20	N/A	150	150*pi/4	0.040
Tube 2	0	20	80	150	150 * pi/4	0.020
Tube 3	100	0	100	50	50 * pi/2	10
Tube 4	100	0	100	50	50*pi	10

Table 7.6: Parameters of the Tubes for Simulation Studies

 L_{tran} is the length of the straight section of the tube; L_c is the length of the curved section of the tube; L_s^i is the location of the i^{th} FBG sensor on the tube.

curved robotic tools, the strain-force calculation proposed in subsection 7.6.1 is further generalized. A force vector in a plane that is defined by a normal vector n is presented as:

$$\langle n, F_{ext} \rangle = 0 \tag{7.47}$$

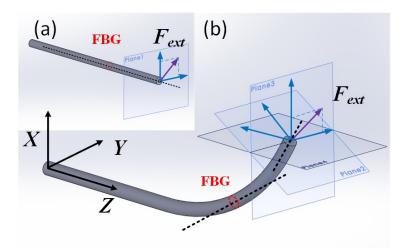


Figure 7.23: Lateral and axial forces for straight robotic tools (a) and pre-curved robotic tools (b).

where $\langle \rangle$ represents the inner product of two vectors. F_{ext} is a 3D vector but we use it to represent a 2D force since its elements are constrained by Eq. (7.47). By adding this equation into Eq. (7.41), it is possible to solve for all three components of F_{ext} . Based on this modification, the updating strategy for the strain-force calculation becomes:

$$\Delta F_{ext} = J_{CX}^{\dagger}(\tilde{\varepsilon}_l - \varepsilon(L_s)) \tag{7.48}$$

$$J_{CX} = A^{-1} K^{-1} R_{\Theta}(L_s) B \tag{7.49}$$

where,

$$B = \begin{bmatrix} 0 & -d_z & d_y \\ d_z & 0 & -d_x \\ -d_y & d_x & 0 \\ n_x & n_y & n_z \end{bmatrix}$$
(7.50)

In order to have an unique solution of ΔF_{ext} , the rank of the matrix *B* should be three, which requires that there is at least one set of three linearly independent rows. Considering rows 1, 2 and 4 as an example of a set of linearly independent rows, the determinant of the

matrix:

$$B_{1,2,4} = \begin{bmatrix} 0 & -d_z & d_y \\ d_z & 0 & -d_x \\ n_x & n_y & n_z \end{bmatrix}$$
(7.51)

is:

$$d_z(d_x n_x + d_y n_y + d_z n_z) (7.52)$$

In order for the determinant to be non-zero, the following relationship should hold:

$$\langle d, n \rangle \neq 0 \tag{7.53}$$

If a different set of three rows is used such as 1, 3 and 4 or 2, 3 and 4, the same result as in (7.53) is obtained. Note that rows 1, 2 and 3 are linearly dependent - they form a 3×3 skew-symmetric matrix of rank 2. The inequality (7.53) indicates the observability conditions of force sensing, when a single sensorized cross-section is used. Specifically, when the force vector is in a plane parallel to the distance vector *d*, the force cannot be decoupled, or observed. In the rest of this chapter, we define the term "unobservable planes" to denote the planes containing or being parallel to the plane containing the vector *d*. There is an infinite number of unobservable planes for each *d*.

A graphical representation of unobservable forces is shown in Fig. 7.24. In all three figures, both force components F_x and F_y can generate exactly the same bending and torsional effects on the sensor cross-section. It is impossible to uniquely decouple the force vector into two directions.

7.6.3 Robot Design for Optimal 3D Force Sensing

In order to solve the 3D force sensing problem in a pre-curved continuum robot, a method for decoupling the unobservable 2D forces must be developed, because a 3D force vector always has a projection on at least one of the unobservable planes. In this subsection, we

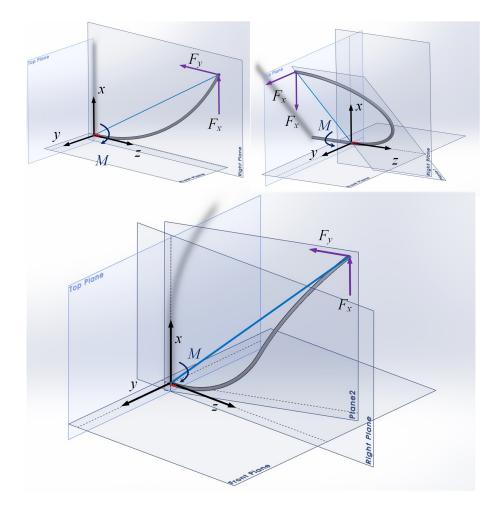


Figure 7.24: Three examples of unobservable forces. In these cases, the force vector cannot be decoupled into two elements by using strain sensors on a single cross-section.

will discuss the technique of using FBG sensors on multiple cross-sections to decouple unobservable forces, and achieve 3D force sensing.

Inequality (7.53) demonstrates that the observability of force sensing is purely determined by the position vector between the sensorized cross-section and robot's tip (d). This vector exists in the force-curvature relationship but not in the curvature-strain model. Hence, in the following derivations for 3D force sensing, only the force-curvature model is used, omitting the curvature-strain model for simplicity.

The feasibility of calculating 3D force from the curvature information of two sensorized

cross-sections was studied in simulations, as shown in Fig.7.25, where a periodic 3D force (F_{ext}) was applied on a flexible robot (tube 2 in Table 7.6). The signal flow of this simulation is illustrated in Fig. 7.25(a). Firstly, the curvatures at two cross-sections of this robot were calculated by using the force-curvature model presented in subsection 7.2.4 (Fig. 7.25(b, e)). Then these curvatures were mixed with a certain amount of noise and converted back to the force measurements (\tilde{F}_{ext}) using the proposed curvature-force calculation methods discussed in subsections 7.2.4 and 7.6.1. Since these two methods gave similar results, only the outputs of the second method were plotted (Fig. 7.25(c, f)). It can be seen that when the magnitude of noise is zero (Fig. 7.25(b, c, d)), the inverse calculation can achieve accurate force measurements. This indicates that it is possible to use sensors on two cross-sections to obtain 3D tip forces. However, when a small amount of noise (compared to the magnitude of the curvature signals) is added on top of the curvature signals (shown in Fig. 7.25(e)), the force measurements contains a large amount of noise which significantly reduces their resolution and accuracy. Furthermore, as shown in Fig. 7.25(f, g), the noise level was correlated to the condition number of J_{CX} in Eq. (7.46). The relationship between the noise amplification and condition number will be modeled and analyzed in detail in the following paragraphs.

A pre-curved tube with sensors installed on two cross-sections is used to analyze the above mentioned noise amplification, as shown in Fig. 7.26(a). The curvatures of the robot at the sensorized cross-sections have the following relationship with the tip force:

$$\begin{bmatrix} u_1 - \hat{u}_1 \\ u_2 - \hat{u}_2 \end{bmatrix} = J_{CX} F_{ext}$$
(7.54)

$$J_{CX} = K^{-1} \begin{bmatrix} -d_{y1} & d_{x1} \\ -d_{y2} & d_{x2} \end{bmatrix}$$
(7.55)

In this example, u_i is a scalar that represents the bending curvature; \hat{u}_i indicates the corresponding pre-curvature; F_{ext} and d are 2D vectors that represent the tip force and the

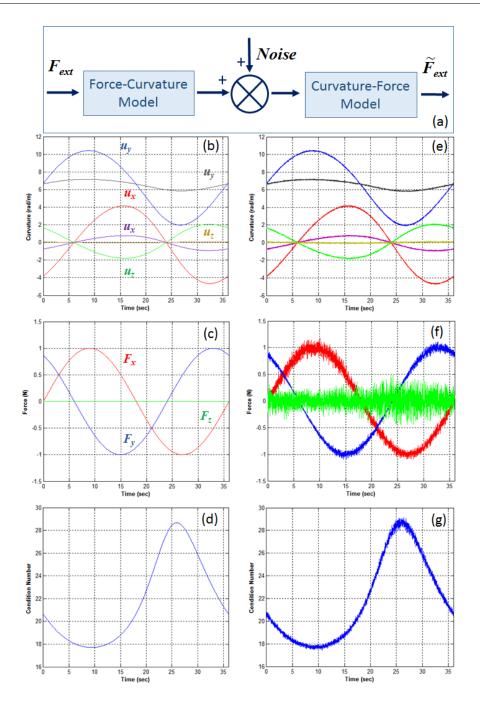


Figure 7.25: Simulation studies for 3D force sensing, using curvature measurements of two sensorized cross-sections. (a) Simulation signal flow. (b, c, d) Simulation results when the noise level is zero. (e, f, g) Simulation results when the noise level is around 2% of the curvature signals. (d, g) Condition numbers of J_{CX} in Eq. (7.46), which is the update strategy for the strain-force calculation.

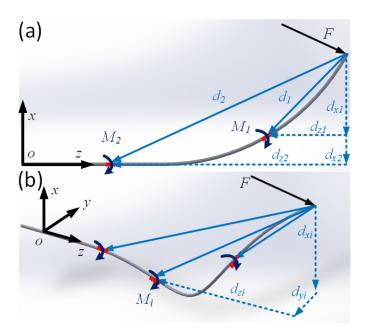


Figure 7.26: Pre-curved continuum robots with multiple sensorized cross-sections for 2D or 3D force sensing. The red marks represent the sensorized cross-sections.

tip-sensor distance, respectively. The subscript i is the index of the cross-section. All the variables are defined with respect to the world frame.

The condition number of J_{CX} is the dominant factor in determining the noise amplification of the curvature-force calculation. Two simulation studies were performed to demonstrate the relation between the condition number of J_{CX} and the noise level in force measurements. The signal flow of these simulations is shown in Fig. 7.25(a). A time-varying force is applied to tube 2 and tube 3 (Table 7.6), which share the same stiffness and sensor locations, but with different condition numbers of the matrix J_{CX} . It can be seen that in both cases noise signals are amplified compared to the noise level of the curvature signals, but the one with the higher condition number (5.8) amplifies the noise signal much more than the one with the lower condition number (2.6).

To reduce noise amplification, the relative distance between robot's tip and the sensorized cross-sections (represented by vector d_i) should be designed carefully, such that the condi-

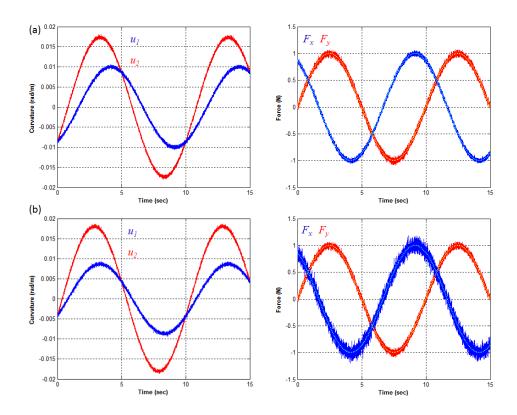


Figure 7.27: Demonstration of the relation between condition number and noise amplification in curvature-force calculations. (a) The condition number is 2.6; (b) the condition number is 5.8.

tion number of J_{CX} is close to one. When J_{CX} is an orthogonal matrix, i.e.,

$$J_{CX}^T J_{CX} = I \tag{7.56}$$

then the condition number of J_{CX} is one. Substituting Eq. (7.55) in Eq. (7.56), results in the following condition for the optimal tip-sensor configuration:

$$||d_1|| = ||d_2||, \quad \langle d_1, d_2 \rangle = 0 \tag{7.57}$$

The equation above shows that if the locations of the robot's tip and the two sensor crosssections can form an isosceles right triangle with the robot's tip as the apex, then the noise amplification can be eliminated. Eq. (7.57) can be used as a design criterion for sensorized

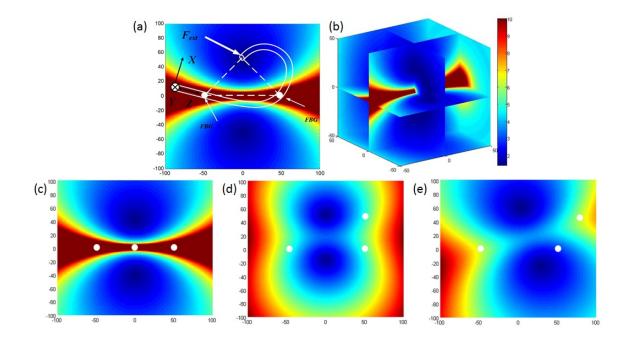


Figure 7.28: Condition number map for designing the shape of a sensorized continuum robot; (a) two sensorized cross-sections for measuring 2D unobservable forces; (b) two sensorized cross-sections for 3D force sensing; (c, d, e) three sensorized cross-sections for measuring 2D unobservable forces.

pre-curved continuum robots if 3D forces sensing is necessary for the targeted application. This criterion is obtained from 2D force measurements, but can be generalized into the condition for 3D force, in which d_i is a 3D vector.

Eq. (7.57) gives the optimal tip-sensor configuration for 3D sensing, but in many applications, a certain amount of noise amplification is acceptable, depending on the required resolution. Hence, a map of condition numbers was numerically calculated and plotted as a reference tool for designing the shape of a sensorized robot, based on the condition number. As shown in Fig. 7.28, the white dots are the positions of sensorized cross-sections, and the color at each point in space represents the condition number of J_{CX} when the tip of the robot is at that location. The colors in this map vary from dark blue to red, corresponding to the condition numbers varying from 1 to 10.

From Fig. 7.28(a, b), it can be seen that the 3D map is the result of the rotation of a 2D

map with respect to the centerline connecting two sensorized cross-sections. In order to measure 3D forces (or unobservable 2D forces) without high noise amplification, the shape of the continuum robot needs to be curved more than 180 degrees. Continuum robots such as needles or concentric-tube robots usually do not have a bending curvature as big as the one shown in Fig. 7.28(a), but for many cardiac ablation catheters this is quite common.

Fig. 7.28(c, d, e) show that adding more sensing points along the body of the robot does not necessarily improve the condition number or reduce the noise level. In the sensor layouts presented in Fig. 7.28(c, d, e), the third sensorized cross-section actually makes the dark blue region become smaller, which means that the robot's body has to bend more to obtain reasonable signal-noise ratio.

7.7 Conclusions

In this work a sensing technology was proposed for simultaneous curvature, torsion, and force measurement of continuum robots for surgical applications. The sensing structure designed is composed of FBG sensors embedded into helical grooves in the robot shaft. A novel engraving system was developed, which provided high accuracy for a wide range of helical patterns. A nonlinear relationship (termed the force-curvature-strain model) was derived to obtain measurements from FBG strain readings. The sensing technology was validated using experimental setups for straight and pre-curved tubes under torque and lateral loading conditions that resulted in large bending and torsion. The results obtained showed that this novel sensing technology provides real-time, simultaneous curvature, torsion and force information with high precision, resolution and sampling rate throughout all robot configurations.

This technology is generalized to a concentric-tube robot by adding a protective layer between the inner and outer tubes, such that the cutting forces generated from robot's movements cannot damage the FBG sensors. Experimental results showed that the sensorized concentric-tube robot is able to provide high speed and resolution force measurements. The problem of 3D force sensing in pre-curved continuum robots was studied via mathematical modeling and simulations. The results showed that when the body of the robot has a significant amount of bending, it is possible to decouple force measurements in all three dimensions. A design criterion and a condition number map were obtained, which are essential tools in designing continuum robots with high quality 3D force sensing abilities.

Bibliography

- M. Khoshnam, A. Yurkewich, and R. V. Patel, "Model-based force control of a steerable ablation catheter with a custom-designed strain sensor," in *Proc. IEEE Int. Conf. Robot. Autom.*, 2013, pp. 4479–4484.
- [2] W. Wei and N. Simaan, "Modeling, force sensing, and control of flexible cannulas for microstent delivery," *Journal of Dynamic Systems, Measurement, and Control*, vol. 134, no. 4, pp. 1–12, 2012.
- [3] I. Iordachita, Z. Sun, M. Balicki, J. U. Kang, S. J. Phee, J. Handa, P. Gehlbach, and R. Taylor, "A sub-millimetric, 0.25 mn resolution fully integrated fiber-optic forcesensing tool for retinal microsurgery," *Int. J. Comput. Assist. Radiol. Surg.*, vol. 4, no. 4, pp. 383–390, 2009.
- [4] X. He, J. Handa, P. Gehlbach, R. Taylor, and I. Iordachita, "A submillimetric 3-dof force sensing instrument with integrated fiber bragg grating for retinal microsurgery," *IEEE Trans. Biomed. Eng.*, vol. 61, no. 2, pp. 522–534, 2014.
- [5] K. Yokoyama, H. Nakagawa, D. C. Shah, H. Lambert, G. Leo, N. Aeby, A. Ikeda, J. V. Pitha, T. Sharma, R. Lazzara *et al.*, "Novel contact force sensor incorporated in irrigated radiofrequency ablation catheter predicts lesion size and incidence of steam pop and thrombus," *Circulation: Arrhythmia and Electrophysiology*, vol. 1, no. 5, pp. 354–362, 2008.
- [6] Y.-L. Park, S. Elayaperumal, B. Daniel, S. C. Ryu, M. Shin, J. Savall, R. J. Black, B. Moslehi, and M. R. Cutkosky, "Real-time estimation of 3-d needle shape and deflection for mri-guided interventions," *IEEE/ASME Trans. Mechatronics*, vol. 15, no. 6, pp. 906–915, 2010.
- [7] R. J. Roesthuis, M. Kemp, J. J. van den Dobbelsteen, and S. Misra, "Threedimensional needle shape reconstruction using an array of fiber bragg grating sensors," *IEEE/ASME Trans. Mechatronics*, vol. 19, no. 4, pp. 1115–1126, 2014.

- [8] S. C. Ryu and P. E. Dupont, "Fbg-based shape sensing tubes for continuum robots," in *Proc. IEEE Int. Conf. Robot. Autom.*, 2014, pp. 3531–3537.
- [9] M. Abayazid, M. Kemp, and S. Misra, "3d flexible needle steering in soft-tissue phantoms using fiber bragg grating sensors," in *Proc. IEEE Int. Conf. Robot. Autom.*, 2013, pp. 5843–5849.
- [10] R. J. Roesthuis, S. Janssen, and S. Misra, "On using an array of fiber bragg grating sensors for closed-loop control of flexible minimally invasive surgical instruments," in *Proc. IEEE/RSJ Int. Conf. Intell. Robots Syst.*, 2013, pp. 2545–2551.
- [11] H. Liu, A. Farvardin, R. Grupp, R. J. Murphy, R. H. Taylor, I. Iordachita, and M. Armand, "Shape tracking of a dexterous continuum manipulator utilizing two large deflection shape sensors," *IEEE Sensors*, vol. 15, no. 10, pp. 5494–5503, 2015.
- [12] K. B. Reed, A. M. Okamura, and N. J. Cowan, "Modeling and control of needles with torsional friction," *IEEE Trans. Biomed. Eng.*, vol. 56, no. 12, pp. 2905–2916, 2009.
- [13] P. E. Dupont, J. Lock, B. Itkowitz, and E. Butler, "Design and control of concentrictube robots," *IEEE Trans. Robot.*, vol. 26, no. 2, pp. 209–225, 2010.
- [14] R. J. Webster III, J. M. Romano, and N. J. Cowan, "Mechanics of precurved-tube continuum robots," *IEEE Trans. Robot.*, vol. 25, no. 1, pp. 67–78, 2009.
- [15] R. Xu, A. Asadian, A. S. Naidu, and R. V. Patel, "Position control of concentrictube continuum robots using a modified jacobian-based approach," in *Proc. IEEE Int. Conf. Robot. Autom.* IEEE, 2013, pp. 5813–5818.
- [16] R. Xu, A. Asadian, S. F. Atashzar, and R. V. Patel, "Real-time trajectory tracking for externally loaded concentric-tube robots," in *Proc. IEEE Int. Conf. Robot. Autom.*, 2014, pp. 4374–4379.
- [17] C. G. Askins, G. A. Miller, and E. J. Friebele, "Bend and twist sensing in a multiplecore optical fiber," in *Optical Fiber Communication Conference*. Optical Society of America, 2008, p. OMT3.
- [18] D. C. Rucker and R. J. Webster III, "Deflection-based force sensing for continuum robots: A probabilistic approach," in *Proc. IEEE/RSJ Int. Conf. Intell. Robots Syst.*, 2011, pp. 3764–3769.
- [19] K. Xu and N. Simaan, "An investigation of the intrinsic force sensing capabilities of continuum robots," *IEEE Trans. Robot.*, vol. 24, no. 3, pp. 576–587, 2008.

[20] M. Mahvash and P. E. Dupont, "Stiffness control of surgical continuum manipulators," *IEEE Trans. Robot.*, vol. 27, no. 2, pp. 334–345, 2011.

Chapter 8

Conclusion and Future Work

8.1 Concluding Remarks

This thesis started with a review of the state of art in the field of concentric-tube robots, with a focus on modeling, control and sensorization problems. It was noted that many fundamental theoretical problems for CTRs such as, kinematic modeling, position control and intrinsic sensing had not been sufficiently well addressed in the literature on CTRs. This has prevented CTRs from being used effectively in practical medical applications. Therefore, in the author's opinion, solving the problem of kinematic modeling should have top priority since the development of various control and sensing algorithms depend on it. In this thesis, first, a computationally efficient kinematic model of CTRs was proposed. This then enabled us to make theoretical contributions in a number of research topics on CTRs, including position control, kinematic instability analysis and strain-force modeling for intrinsic force sensing. In addition, this thesis presented our contributions in technological advancements in CTRs, including shape setting, engraving, sensorization of Nitinol tubes and drive unit prototyping. These novel technologies could play an important role in the future design of CTRs for practical applications. The following paragraphs summarize the contributions and provide concluding remarks for each chapter:

- Chapter 2 presented the design and fabrication of CTRs and its drive units. It was shown that for shaping Nitinol tubes in a laboratory environment, a 1/2 inch thick low-carbon steel plate can be used as the mold material. The design of a desktop micro-engraver capable of making helical patterns on thin-walled Nitinol tubes with high precision was also presented. Three robotic prototypies were designed for driving CTRs in different applications. The third design achieved a good combination of cost efficiency, compactness, and functionality.
- Chapter 3 showed that piecewise linearization was an effective method in solving the kinematics of CTRs. Using this method, our proposed kinematic model can be implemented at 1 kHz using MATLAB and the QuaRC tool box [1, 2]. A higher computation speed can be achieved by programing this model in C++. In general, the loss of accuracy lost for our model was less than 0.1 mm compared to the most accurate models in the literature [3, 4]. The high accuracy and computational efficiency of our model is especially useful in real-time applications, such as teleoperation, online motion planning, and interactive robot design for CTRs.
- Chapter 4 described the Jacobian matrix derived from the forward kinematic model proposed in the Chapter 3. This Jacobian inherits the computational efficiency of the kinematic model. As a result, the proposed Jacobian-based position controller can be implemented at a high servo rate as well. A robot prototype with four motorized stages was used to test the position control algorithm in experiments. The results showed that the robot can follow pre-defined trajectory accurately in 3D space while also avoiding singularity regions. The fast forward kinematics and the corresponding Jacobian matrix will be particularly useful in future developments of complex control algorithms for CTRs, such as impedance control, force control and redundancy resolution.
- Chapter 5 modeled and analyzed the property of kinematic instability in CTRs. By analyzing the uniqueness of the solutions to the forward kinematics of CTRs, a set of

close-formed stability conditions were obtained. A few CTRs with different parameters (curvature, length, stiffness, etc.) were used in simulation studies to evaluate the effectiveness of the proposed conditions. The results showed that when the robot did not satisfy the stability conditions, the tip of the robot could jump from one position to another with very little motion of the motors. These conditions have explicit expressions which provide an intuitive interpretation of stability in relation to the robot parameters. Using these conditions as inequality constraints, an optimization algorithm can be developed for designing CTRs with optimal stability for a given workspace.

- Chapter 6 proposed a loaded kinematic model of CTRs and a force-rejection controller for position tracking under a time varing force disturbance. Two sets of control experiments were performed to assess the proposed model and controller. The first one was tip position regulation and the second one was trajectory tracking. In both tasks, the errors were less than ±1 mm. The disturbance forces were generated by moving a weight up and down, which was attached at the tip of the robot. The frequency of the external forces was still quite low, less than 0.5 Hz, limited by the speed of the drive unit and the accuracy of the force sensors. Further evaluation of this method is needed for medical applications with high frequency disturbances, such as thoracic and beating heart surgeries.
- Chapter 7 presented the design of a sensorized CTR using helically-wrapped FBG sensors. This special sensor layout can provide simultaneous curvature, torsion, and force measurements for CTRs. This design was first implemented on a single pre-curved tube robot to evaluate its feasibility. Three helically slots were engraved on the surface of a Nitinol tube for embedding FBG sensors. A series of bending and torsional loading tests were performed in experiments. The results showed that the curvature and torsion of this tube can be measured accurately. These curvature and torsion values can be related to the tip force through the kinematic model developed

in Chapter 6. This curvature-force calculation was formulated as solving a threepoint boundary-value problem for the loaded kinematic model. Experimental results demonstrated that this force sensing technique provided a resolution of 0.1 N at 100 Hz sampling rate on a single-tube robot. The proposed sensorization technique was generalized to CTRs with multiple tubes. In order to protect the FBG sensors from the "cutting forces" resulting from other tubes, a protection sleeve was slid on top of the FBG sensors. Experiment showed that a sensorized CTR consisting of two tubes had similar sensing performance as the above mentioned single-tube robot. 3D force sensing for continuum robots was discussed in the last part of this chapter. It was shown that 3D force sensing is feasible, but often results in poor accuracy due to noise amplification in the strain-force calculation. A design criterion was developed for designing robots with an optimal force sensing capability. The simulation results showed that 3D force sensing can be achieved with high accuracy for robots designed using this criterion.

With regard to the research topics covered in this thesis, the following are the main contributions:

- Kinematic modeling of CTRs: We developed a computationally efficient torsionally compliant kinematic model and its associated Jacobian matrix for CTRs. This approach enables researchers to adapt control algorithms from rigid-link robotics to CTRs without worrying about the computational cost.
- Stability analysis for CTRs: A general design criterion was developed that can guarantee stability of a CTR in its entire workspace. This stability condition is valid for CTRs having an arbitrary number of tubes, with or without transmission segments.
- Position control under time-varying loading: A force-rejection control scheme based on a loaded kinematic model was developed. Using this approach, CTRs can be used in applications involving tool-tissue interactions.

- 4. Micro-machining of thin-walled Nitinol tubes: A specialized Swiss-type desktop micro-engraver was developed, which can generate helical patterns on flexible thin tubes. Creating complex 2D/3D patterns is also possible using this machine.
- 5. FBG-based shape and force sensing for continuum robots: Helically-wrapped FBG sensors were embedded into the walls of continuum robots in order to obtain simultaneous curvature, torsion, and force information.
- 6. A sensorized concentric-tube robot: FBG sensors were integrated into a multiple tube CTR for force sensing. These sensors were well protected from the cutting forces between the moving tubes in a CTR. 2D and 3D force sensing problems of continuum robots were addressed.
- 7. Drive Unit designs for CTRs: three prototypes were built for different applications of CTRs. The most recent prototype is one of the most cost effective and compact CTR designs in the literature. This portable device is low-cost (less than \$1200) and can be easily integrated with other robotic platforms.

8.2 Suggested Future Work

Since CTRs are at an early stage of development, there are many directions that future research can take to improve the technology. A brief overview of several interesting topics is as follows:

8.2.1 Modeling and Control

• Nonlinear elasticity modeling: Current torsionally compliant kinematics present poor accuracy when the tubes have high curvatures. This is mainly because one of the most important mechanical effects is missing in the model, which is nonlinear elasticity.

By including this feature into our previously developed fast model, we will be able to substantially improve the accuracy of the kinematics, while still ensuring the realtime performance.

- Shape control of CTR: In several CTR applications, not only the tip position of the robot is important, but also the entire shape. For this situation, a control algorithm that can command the positions of multiple points along the shaft of the robot will be required. This has not been reported in literature so far. A large number of tubes may be used in a CTR for shape control, depending on the complexity of the desired shape for the specific application.
- Distributed force control: For some surgical tasks, the effectiveness of the treatment is directly influenced by the amount of force applied over time, for example, cardiac ablation. This requires the tip force to be well regulated to a constant value. At the same time, the force along the robot body should be as small as possible to avoid tissue damage. A control scheme that can regulate the contact force at the tip and along the robot body should be developed.
- Needle insertion: Previous studies have ignored the interaction forces between tubes and tissue when inserting a CTR as a steerable needle. This is not valid when the tubes are very flexible or the tissue is relatively stiff. Since the mechanical behavior of biological tissues is time-varying and highly nonlinear, advanced control algorithms should be developed for proper deployment of the robot.

8.2.2 Technological Improvements

• An electric tube shaping setup: To date, there are no conclusive results on the optimal design of a CTR for a given clinical application. This means that several iterations of building a CTR may still be needed to find a reliable design rule. Until then, the demand for shaping Nitinol tubes will increase with time. Therefore, a reliable device

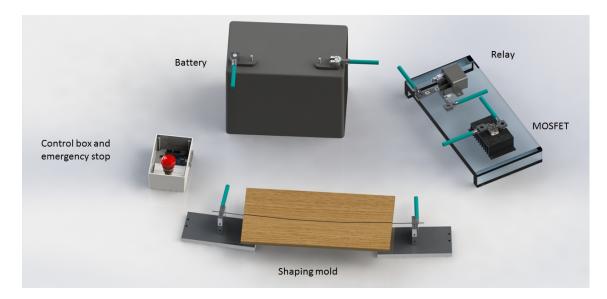


Figure 8.1: Conceptual design of an electric tube shaping setup.

that quickly and repeatedly shapes Nitinol tubes will be important for a research lab to succeed in CTR research. An electric shaping method will be a better choice than traditional methods such as air ovens and sand baths, in terms of the cost and flexibility. A conceptual design of an electric tube-shaping setup is shown in Fig. 8.1.

- 3D printed tubes: 3D printing would be an ideal option for making patient-specific CTRs. It also gives the possibility to add complex geometric features on the surfaces of the tubes to enhance their functionality. However, commercially available printers cannot build thin tubes with the strength required for CTRs. With the current developing speed of 3D printing technologies, it can be foreseen that 3D printed CTRs will be developed in the near future.
- Patterned concentric tubes: Cutting well designed patterns on the surface of Nitinol tubes will give the robot many extra features. It would have the potential to reduce friction between the tubes, increase flexibility in certain directions to avoid damage, and change the overall stiffness by matching or mismatching the patterns on different tubes.

- Further development of the CTR drive unit: As mentioned in Chapter 2, very few designs of the CTR drive unit have considered the sterilization problem. But it is one of the most important features for a medical device designed for clinical use. Designing a drive unit that can detach the tubes and associated mechanisms for the sterilization process will be a necessary step for bringing CTRs into the operating room.
- Shape and force sensing for CTR with complex curvatures: In this thesis, only one cross-section of the CTR was sensorized for curvature, torsion and force sensing. For CTRs with complex shapes, to obtain accurate shape information or distributed force measurements, FBG sensors have to be embedded into three or four different cross-sections. The performance of a sensorized CTR with numerous FBG sensors will need further evaluation.
- Interventional OCT imaging probe: OCT (Optical Coherence Tomography) provides
 high quality images with resolution similar to histology. But interventional applications are still limited to vascular systems because the probe is often designed as a
 catheter. OCT technology combined with CTRs could give clinicians access to deep
 lesions inside organs, thereby helping in diagnostic procedures. Surgeons may not
 need to perform traditional biopsies in some cases. Instead, visual biopsies could be
 done through OCT imaging since the image quality is good enough for diagnosis.
- Virtual Operating Room (VOR): A virtual environment could be useful as a visualization tool for demonstrating the potentials of CTRs in medical applications. Using a VOR, surgeons can be included in the initial phase of the robot design, to ensure that the robot can be seamlessly integrated into the workflow of the operating room. An example of a VOR is shown in Fig. 8.2. This VOR was developed in Unity, which is becoming the main platform for Virtual Reality (VR) or Augmented Reality (AR). A CAD model of our CTR prototype was added in this environment, as shown in Fig. 8.2(b). This VOR can be projected onto VR or AR glasses to give an immersive

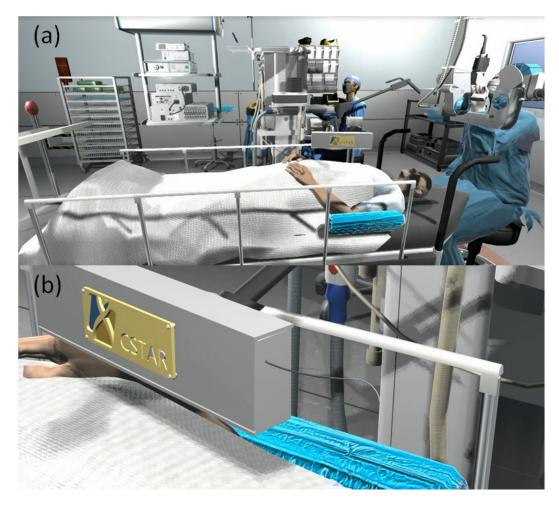


Figure 8.2: (a) Full size virtual operating room developed in Unity (purchased from Unity Asset Store). (b) Magnified view of the virtual CTR developed by our group.

experience to the user, which could be helpful for both robotic research and surgical training purpose.

8.2.3 Clinical Applications

• Bronchoscopic biopsy and Radio Frequency (RF) ablation: RF ablation is a suitable treatment for lung cancer because of its ability to neutralize the tumor inside the lung, eliminating the need for lobectomy. Bronchoscopic RF ablation is less invasive than inserting the needle from the chest, such that the procedure does not require an



Figure 8.3: Needle-tipped catheter for intramyocardial injection

operating room. By incorporating CTRs in conventional bronchoscopes, even the peripheral tumors can be reached under video/CT guidance. In addition, umbrellashaped RF needles can be carried by CTRs and inserted into the tumor to enlarge the ablation region.

Intramyocardial injection (for treating reversible myocardial ischemia): percutaneous cardiac catheterization methods and devices are being actively investigated as a means to deliver cellular products. Current research in this area is focused primarily on the development of cardiac catheters and methods that can provide targeted delivery of high concentrations of cell suspensions to specific regions of the myocardium. One example of needle-tipped catheters for intramyocardial injections is shown in Fig. 8.3. CTRs will performance much better than catheters for repeated multiple injections.

Bibliography

- R. Xu and R. Patel, "A fast torsionally compliant kinematic model of concentric-tube robots," in 2012 Annual International Conference of the IEEE Engineering in Medicine and Biology Society. IEEE, 2012, pp. 904–907.
- [2] R. Xu, A. Asadian, A. S. Naidu, and R. V. Patel, "Position control of concentric-tube continuum robots using a modified jacobian-based approach," in *Proc. IEEE Int. Conf. Robot. Autom.* IEEE, 2013, pp. 5813–5818.
- [3] P. E. Dupont, J. Lock, B. Itkowitz, and E. Butler, "Design and control of concentric-tube robots," *IEEE Trans. Robot.*, vol. 26, no. 2, pp. 209–225, 2010.
- [4] D. C. Rucker, B. A. Jones, and R. J. Webster III, "A geometrically exact model for externally loaded concentric-tube continuum robots," *IEEE Trans. Robot.*, vol. 26, no. 5, pp. 769–780, 2010.

Appendix A

Sensorization of a Surgical Robotic Instrument for Force Sensing

A surgical robotic system could substantially benefits from force sensing technologies, especially for applications that require high performance position and force control. In Chapter 7, it can be seen that Fiber Bragg Grating (FBG) sensors have many advantages over commercial force/torque sensors (Nano43, ATI Industrial Automation, United States) for sensorizing concentric-tube robots. In this appendix, as an extension of Chapter 7, we present the development and application of FBG sensors for a general purpose robotic instrument (Large Needle Driver, Intuitive Surgical, United States). This sensorized instrument showed a resolution of 0.05 N at 1 kHz sampling rate. It is compatible with the da Vinci Surgical System and can be used for skills assessment and force control in specific surgical tasks on phantom tissue, using the da Vinci Research Kit (dVRK): tissue palpation, knot tightening during suturing and Hem-O-Lok tightening during knotless suturing. The tasks were designed to demonstrate the robustness of the sensorized force measurement approach. The results of further evaluation by a group of expert and novice surgeons performing the three tasks mentioned above are also presented in this appendix.

A.1 Introduction

Over the past 25 years, hospitals worldwide have shifted from open surgery to minimally invasive surgery (MIS) for many procedures. MIS has been shown to reduce mortality, decrease blood loss, decrease pain, and shorten the length of hospital stays [1–7]. Although MIS has had improved results when compared to open surgery, many studies have shown that MIS procedures take significantly more time [1–7]. This is mainly a result of the high level of psychomotor skills needed to perform MIS safely [8], which has resulted in a longer learning curve in MIS training [9]. Robotic-assisted minimally invasive surgery (RAMIS) has reduced some of the difficulties present in conventional MIS, leading to improved surgical outcomes and shorter operating times and training periods [10–12]. Currently, the most widely used surgical robot is the da Vinci Surgical System by Intuitive Surgical, which is used daily in RAMIS procedures worldwide. These improved outcomes are mainly a result of enhanced vision of the surgical site, innovations in tool design to increase dexterity, and increased precision through automatic movement transformations [13, 14]. On the other hand, current RAMIS takes away the force sensation that surgeons need to manipulate tissue accurately and safely. Further, force information is useful for assessing the skill of novice surgeons and can reduce training times. In literature, multiple designs of sensorized robotic systems have been proposed to provide force feedback in RAMIS. A tele-operated robotic system consisting of two PHANTOM haptic devices and customized laparoscopic tools was proposed to provide haptic sensation to the surgeon during RAMIS [15]. A pair of sensorized da Vinci instruments were integrated with a pair of 7-DOF industrial robots within a RAMIS testbed [16–18], and has shown improved surgical performance in suture tightening with visual force feedback (VFF) and direct force feedback (haptics). Using a modified da Vinci system with a sensorized instrument tip, researchers were able to validate the performance of surgeons with the help of lateral force feedback in a realistic scenario [19]. The designs referenced above made use of strain gauges, which can be difficult to miniaturize, sterilize and integrate into surgical tools with high measurement accuracy.

FBG sensors are an effective alternative for force sensing in medical applications due to their high sensitivity, low signal-to-noise ratio, minimal size, biocompatibility, sterilizability and EM isolation. These sensors have been successfully incorporated into hand-held tools [20–22] and various surgical robotic systems [23–27]. These custom-designed instruments have demonstrated the capabilities of FBGs in surgical force sensing, and work that focusses on integrating this sensing technology into commercially available surgical robots will allow for more immediate use. This appendix proposes a novel lateral 2-DOF force sensing instrument that incorporates FBG sensors onto the tool shaft of the commercially available da Vinci Large Needle Grasper for use in RAMIS. The sensing system demonstrated high accuracy and resolution throughout the experiments was independent of the wrist orientation, and disturbances due to axial force and force coupling. The instrument was assessed by comparing the calculated force reading from the sensors with those from a commercial force and torque (F/T) sensor. The sensorized RAMIS instrument was then used in specific simulated surgical tasks on a da Vinci Surgical Robot by a group of four novices and two expert surgeons. The subjects' performance with and without visual force feedback is discussed, as well as the instrument's potential capabilities in skills assessment.

A.2 Design of the Sensorized Surgical Instrument

This section introduces the design and modeling of a novel 2-DOF lateral force sensing technology for commercially available surgical instruments. The proposed sensor layout and model provides force information from strain sensors attached along a cylindrical shaft, which is common in commercial surgical tools, without modification to the tool itself. Since FBG sensors have a small diameter and provide high resolution and high sensitivity strain measurements, these sensors can be placed near the tool tip to measure tool-tissue interaction forces without interference from the surgical trocar commonly used in RAMIS.

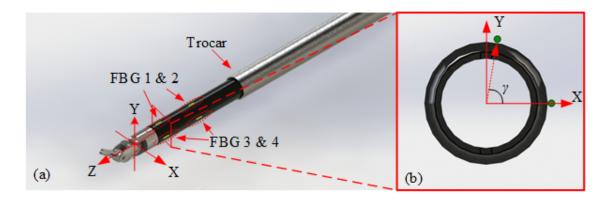


Figure A.1: (a) A 3D view of the sensorized da Vinci instrument (b) A cross-sectional view of the sensorized tool with two FBG sensors located with an angular difference of γ .

A.2.1 Two Cross-Section Design

In previous lateral force sensing designs, strain gauges were placed at a single cross-section along the tool shaft to measure the lateral forces at the tip [24, 28, 29]. This configuration assumes the contact force is at the same location throughout the surgical task, although this is not the case in complex tissue-tool manipulation tasks where wristed tools are employed. Placing sensors further from the tool tip could reduce errors due to unknown force locations; however, the surgical trocar would compromise the ability to measure tool-tissue forces accurately. A further issue with the single cross-section design is that secondary bending moments will be generated when the orientation of the grasper is not in line with the tool axis. The proposed design, shown in Fig. A.1(a) with the da Vinci Large Needle Driver, uses four strain sensors placed at two cross-sections to measure the true contact force irrespective of the location of the force along the tool body and the grasper orientation. The design also compensates for axial and torsional disturbances caused by tool-tissue interaction and cable tension. Incorporating FBG strain sensors allows for a minimized distance between the two cross-sections and the distance from the sensors to the tool tip. Trade-offs between the force sensing resolution and proximity of the sensors to the tool tip can be optimized by properly choosing the sensor locations of the two cross-sections. A detailed force-strain model of this sensing method is discussed in the following subsection.

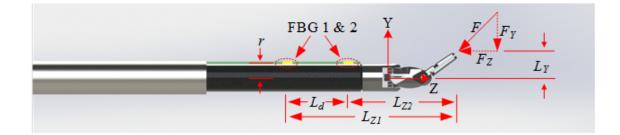


Figure A.2: A side view of the sensorized da Vinci Instrument.

A.2.2 Force-Strain Model

A force-strain model is proposed to calculate the 2-DOF lateral force in a surgical tool from the four FBG sensors in a two cross-section layout. A formula is then derived to calculate the resolution of this sensing technology, based on the sensor locations and noise characteristics.

As shown in Fig. A.2, FBG 1 and 2 form a line parallel to the axis of the tool, and these two FBGs are used to calculate the 1-DOF lateral force F_Y . FBG 3 and 4 are offset 90° from FBG 1 and 2, and are used to calculate the orthogonal 1-DOF lateral force F_X . Assuming the da Vinci instrument behaves as a linear cantilever beam, the stress and strain in the RAMIS instrument at FBG 1 & 2 can be obtained from Eq. A.1:

$$\sigma = \frac{F_Z}{A} - \frac{r(F_Z L_Y + F_Y L_Z)}{I}, \quad \varepsilon = \frac{\sigma}{E}$$
(A.1)

where $F = [F_X, F_Y, F_Z]$ is the force applied to the tip of the instrument, $L = [L_X, L_Y, L_Z]$ is the translation vector between of the tip of the robot and the FBG sensor location; r is the radial offset between the centers of the instrument crosssection and a FBG sensor. A and I are the area and area moment of inertia and E represents the Youngs modulus. All the variables are defined in the frame shown in Fig. A.2, of which the Y-axis is the central axis of the first pin in the instruments wrist and the Z-axis is the central axis of the instrument shaft. The relationship between the strain in the FBG sensor, and the shift in the reflected wavelength is given in Eq. (A.2) where λ , $\hat{\lambda}$, ε and ΔT represent the shifted wavelength, original wavelength under zero-loading, strain, and temperature change, respectively. The sensitivity coefficients of the strain and temperature variables are noted as k_{ε} and $k_{\Delta T}$, respectively. Substituting ε from Eq. (A.1) into Eq. (A.2), the wavelength of an FBG sensor under force loading (*F*) can be obtained, as shown in Eq. (A.3).

$$\lambda - \hat{\lambda} = k_{\varepsilon}\varepsilon + k_{\Delta T}\Delta T \tag{A.2}$$

$$\lambda = k_{\varepsilon} \left(\frac{F_z}{AE} - \frac{r(F_z L_Y + F_Y L_Z)}{EI} \right) + k_{\Delta T} \Delta T + \hat{\lambda}$$
(A.3)

The lateral force, F_Y , is a function of the reflected wavelength from FBG 1 and FBG 2, as shown in Eq. (A.4). L_d is the distance in between FBG 1 and FBG 2 in z direction. k_{12} is the force-wavelength coefficient of FBG 1 and 2. By solving Eq. (A.4), F_Y is obtained as shown in Eq. (A.5).

$$\lambda_1 - \lambda_2 = k_{\varepsilon} \left(\frac{rL_d}{EI} \right) F_Y - (\hat{\lambda}_2 - \hat{\lambda}_1) = k_{12} F_Y - (\hat{\lambda}_2 - \hat{\lambda}_1)$$
(A.4)

$$F_Y = k_{12}^{-1} \left((\lambda_1 - \lambda_2) + (\hat{\lambda}_2 - \hat{\lambda}_1) \right)$$
 (A.5)

The formula for calculating F_X can be derived in the same way as F_Y . Combining these two formulas results in Eq. (A.6), which gives the 2-DOF lateral force.

$$\vec{F}_{Theo} = \begin{bmatrix} F_X \\ F_Y \end{bmatrix} = \begin{bmatrix} k_{12}^{-1} \left((\lambda_1 - \lambda_2) + (\hat{\lambda}_2 - \hat{\lambda}_1) \right) \\ k_{34}^{-1} \left((\lambda_3 - \lambda_4) + (\hat{\lambda}_4 - \hat{\lambda}_3) \right) \end{bmatrix}$$
(A.6)

The resolution of the sensorized RAMIS instrument is dictated by the noise, wavelength stability, and layout of the FBGs. The strain sensitivity of the FBG is very high so will not be the limiting factor. By orienting the two FBG pairs perpendicular to each other,

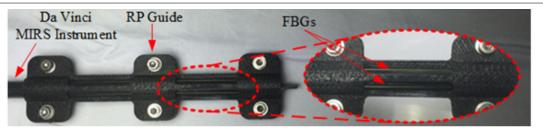


Figure A.3: Illustration of the 3D printed installation guide for FBG alignment.

the 2-DOF force readings are decoupled. This gives a condition number of one for the strain to force calculation matrix, which eliminates noise amplification. Assuming the FBG noise is normally distributed, Eq. (A.7) defines the theoretical resolution of the sensorized instrument, where λ_{noise} is the FBGs noise.

$$resolution = \sqrt{2}k_{12}^{-1}\lambda_{noise} \tag{A.7}$$

Eq. (A.6) assumes the two pairs of FBGs are 90° apart, which cannot be guaranteed due to manufacturing inaccuracies. As a result, the theoretical FBG force needs to be transformed to obtain the actual lateral 2-DOF force, \vec{F}_{Lat} , as shown in Eq. (A.8). γ is the angle between FBGs 3 and 4 and FBGs 1 and 2. γ is illustrated in Fig. A.1(b).

$$\vec{F}_{Lat} = \begin{bmatrix} 1 & 0\\ -\cot\gamma & \csc\gamma \end{bmatrix} \vec{F}_{Theo}$$
(A.8)

A.3 Experimental Validation of the Sensorized Surgical Instrument

To assess the accuracy and precision of the proposed sensing technology in lateral force sensing during surgical tasks, a sensorized RAMIS instrument was constructed and evaluated under various loading conditions.

A.3. EXPERIMENTAL VALIDATION OF THE SENSORIZED SURGICAL INSTRUMENT

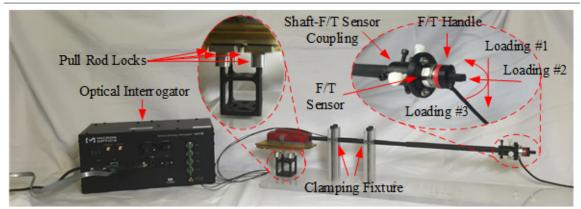


Figure A.4: The experimental setup for calibrating and evaluating the sensorized instrument.

A.3.1 Experimental Setup

The sensing technology is mounted on to a da Vinci Large Needle Driver for use in many RAMIS procedures. The FBGs selected are 125 m in diameter and 10 mm in length (os1100, Micron Optics, US). The minimum distance between the FBG cross-sections to attain 0.05 N resolution was determined to be 90 mm using Eq. (A.7), where k_{12}^{-1} is 17 N/nm and λ_{noise} was empirically obtained as ± 2 pm.

A.3.2 Calibration

A 3D printed rapid prototyped (RP) guide was used to facilitate accurate positioning and orientation of the FBGs on the tool shaft during the hand lay-up process using cyanoacrylate adhesive. As shown in Fig. A.3, two optical fibers were passed through the inner channels of the RP guide and placed onto the tool shaft, parallel to the tool axis and 90 degrees apart from each other. Since the fibers used only have one FBG on each, another two fibers were again laid onto the shaft in the same fashion. The end-points of the 10 mm FBGs along the fiber were difficult to locate precisely and the fiber laying process could not guarantee a specific separation distance, therefore, the FBGs were laid at two cross-sections 100 mm apart. The experimental setup, shown in Fig. A.4, was used to calibrate

A.3. EXPERIMENTAL VALIDATION OF THE SENSORIZED SURGICAL INSTRUMENT

for uncertainties in the mechanical structure and sensor integration, and evaluate the performance of the force-sensing instrument. The setup includes a mounting apparatus to fix the base of the da Vinci instrument and lock the internal cables, and a second mounting apparatus to fix a commercial force sensor (Nano17 F/T, ATI Industrial Automation, United States) to the shaft and lock the wrist joint. A RP handle was attached to the other side of the ATI sensor, from which various force and torque loadings could be applied by hand. The data from both the F/T sensor and the FBG interrogator (SM130, Micron Optics, US) were recorded simultaneously in a C++ program running on a Windows 7 laptop computer.

To accurately measure lateral forces in the manufactured instrument, various torque and force loads were exerted on the RP handle and the force readings from the FBG sensing technology (\vec{F}_{Lat}) and the commercial force sensor (\vec{F}_{nano}) were compared to determine empirical constants. Eq. A.8 was rewritten in the form of Eq. A.9 to isolate the empirical constants a, b, c, d and e which relate to the mechanical properties of the RAMIS instrument and the structural layout of the FBG sensors. Eq. A.10 was used to align the coordinate frame \vec{F}_{nano} with \vec{F}_{Lat} , where θ is the angle between the X-axis of the sensorized instrument and the commercial sensor. The constants a, b, c, d and e were then determined using the Levenberg-Marquardt algorithm, and are presented in Table A.1.

$$\vec{F}_{Lat} = \begin{bmatrix} a & 0 \\ c & d \end{bmatrix} \begin{bmatrix} \lambda_1 - \lambda_2 \\ \lambda_3 - \lambda_4 \end{bmatrix} + \begin{bmatrix} b \\ e \end{bmatrix}$$
(A.9)

$$\vec{F}_{Nano} = \begin{bmatrix} F_{NanoX} \\ F_{NanoY} \end{bmatrix} = \begin{bmatrix} \cos(\theta) & -\sin(\theta) \\ \sin(\theta) & \cos(\theta) \end{bmatrix}^{-1} \vec{F}_{Lat}$$
(A.10)

A.3.3 Evaluation

To evaluate the accuracy and resolution of the proposed sensing technology, the sensorized RAMIS instrument was loaded along the *X*-axis with a series of weights (0g, 100g, 150g,

A.3. EXPERIMENTAL VALIDATION OF THE SENSORIZED SURGICAL INSTRUMENT

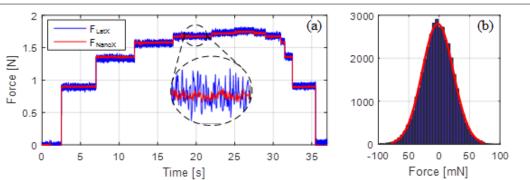


Figure A.5: (a) Force values measured from the FBG and Nano17 sensors in response to a series of weights applied to the sensorized instrument (b) Error histogram of the FBG force measurement.

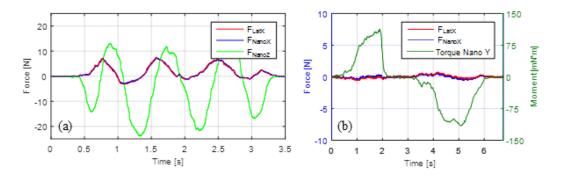


Figure A.6: Demonstration of the performance of the two cross-section FBG sensing under different loading disturbances. (a) F_X values measured from FBG and Nano17 sensors under a varying axial loading (b) F_X values measured from FBG and Nano17 sensors under varying force coupling about the Y axis.

Table A.1: Calibrated Parameters

a	b	с	d	e	θ
-20.52	11.54	-5.41	28.95	20.11	193.1°

170g, 180g, 185g, 187g, 188g) at the F/T handle (Fig. A.4) and then unloaded. The sensing technology shows high measurement accuracy and rapid response throughout the trial, as shown in Fig. A.5(a), with F_{LatX} (blue) and F_{NanoX} (red) sampled at 1 kHz. To attain accuracy specifications, the error (blue bars) between F_{LatX} and F_{NanoX} throughout this 35 second period is shown in Fig. A.5(b). From this data, the sensorized RAMIS instru-

ment is determined to have accuracy to ± 0.05 N within a 95% confidence interval in each of its 1-DOF sensing directions. To investigate the performance of the sensorized RAMIS instrument in the presence of axial loading disturbances, varying lateral forces (F_{LatX} in blue, F_{NanoX} in red), and axial forces (F_{NanoZ}) were applied to the F/T handle. As can be seen in Fig. A.6(a), the sensorized instrument maintains its high level of performance independent of any axial disturbance (F_Z). The rejection of force coupling disturbances was also assessed, by twisting the RP handle, as a wristed instrument may do while manipulating tissue. Force coupling causes the same increase in the bending moment in the two sensorized cross-sections, which is compensated for in Eq. (A.4). The force measurements (F_{LatX} in red, F_{NanoX} in blue) maintain close correlation when this force coupling (*Torque NanoY* in green) is applied as displayed in Fig. A.6(b).

A.4 Experimental Evaluation in Surgical Tasks

To assess the ability of the sensorized instruments in various surgical tasks, a group of four novice and two expert surgeons performed three surgical tasks: suture knot tightening, Hem-O-Lok tightening and tumor localization by palpation using a commercial surgical robot.

A.4.1 Surgical Task Setup

The surgical task setup consists of the lateral force-sensing surgical instrument, the da Vinci surgical robot and surgeon console, and three surgical test-beds for: knot tightening, Hem-O-Lok tightening and palpation. The surgical robot was integrated with the da Vinci Research Kit (dVRK), and the force information from the sensorized Large Needle Driver was overlaid on the right eye viewer of the surgeons console using a frame grabber (Epiphan DVI2USB3.0, Canada). This VFF was provided as a changing color bar with the numeric force information. Custom-made interchangeable surgical test-beds, shown in Fig. A.7, were mounted on a commercial F/T sensor (Gamma, ATI Industrial Automation, United States), and the force readings were logged simultaneously with the sensorized instrument force readings. The suture knot tightening task required subjects to tighten pretied square suture knots with one-hand. The one-handed suturing setup made for shorter training periods, and allowed the F/T sensor to read suture tension values. The Hem-O-Lok tightening task required subjects to slide Hem-O-Lok clips across a suture thread and into the phantom tissue wall using one hand. The tumor localization by palpation task used a soft phantom tissue with a 15 mm diameter phantom tumor made from a stiffer material embedded in it. This testbed was then covered with an opaque phantom skin.

A.4.2 Evaluation

Task 1: Suture Knot Tightening

The subjects were instructed to tighten knots to a desired force, and to try to consistently apply this force throughout the tests. The subjects were given six practice knots with VFF to adjust to the system. Following the training period, subjects completed four sets of the task, each time tightening three knots. Two sets were completed with VFF and two were completed without VFF, in a randomized, alternating order. The force information from the sensorized tool was used for VFF. Because only one hand is used in the suturing knot tightening, the tension in the suture thread can be measured and recorded using the commercial force torque sensor, as showing in Fig. A.7. An example of the suture tension applied over time is shown in Fig. A.8(a), with a mean peak force illustrated by the dotted line. For a sample size of 72 knot tightening tasks (6 subjects, 12 knots each, half with VFF), the mean peak forces were recorded of the subjects' force, with and without VFF, and the error of the applied force from the target force is shown in Fig. A.8(b). It can be seen that the error of the forces applied within the suturing task are more consistent with VFF.

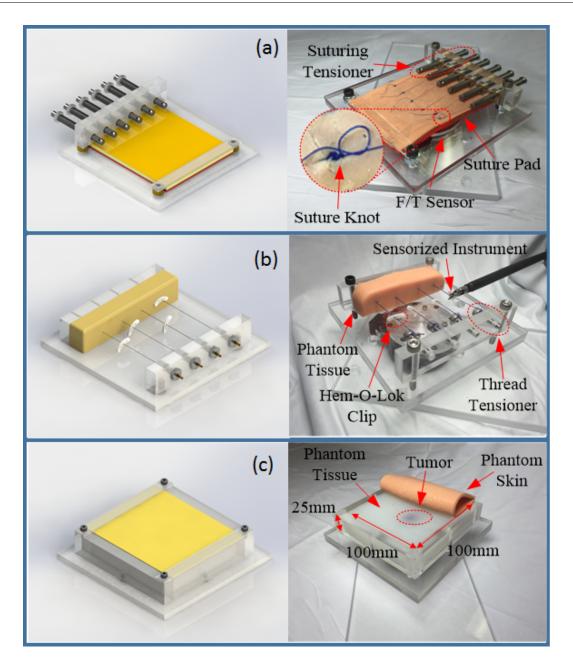


Figure A.7: Demonstration of custom made testbeds for three surgical tasks. (a) Onehanded suture knot tightening testbed (b) Hem-O-Lok tightening testbed (c) Tumor localization by palpation testbed.

Task 2: Hem-O-Lok Tightening

It was hypothesized that the skill level of a surgeon could be differentiated in Hem-O-Lok by assessing the force profile provided by the sensorized RAMIS instrument. Hem-O-Loks

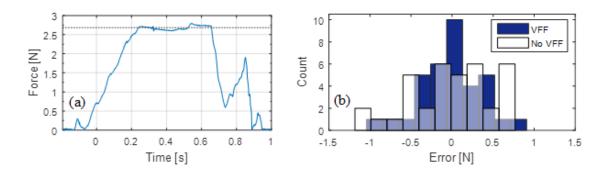


Figure A.8: Illustration of the definition of the mean peak force, representing the applied tension to the suture. (b) Histogram of the force error measured from a group of six subjects performing one-handed suturing tasks with and without VFF.

are plastic clips used in a range of surgeries for knotless suturing. This process saves surgeons significant amounts of time which is particularly critical in partial nephrectomies. Subjects were not given VFF, and were asked to perform two sets of four Hem-O-Lok tightening exercises using the Hem-O-Lok testbed, with one set performed first as practice. Two data sets were generated, differentiated according to expertise, with experts having formal training using the da Vinci Surgical robot, and novices having little to no experience in surgery or in using the da Vinci robot The difference in the force profiles of surgeons and novices is mainly characterized by novices gradually increasing the force they applied throughout their movement, as is evident in Fig. A.9(a), and experts applying a steadier force and completing the task quicker, as shown in Fig. A.9(b). The force information, although not quantitatively analyzed, shows that novice and surgeon subjects can be differentiate through Hem-O-Lok tightening force profiles.

Task 3: Tumor Localization by Palpation

Tumor localization by palpation is the process of pressing on tissue with the objective of finding a tumor. Subjects practiced the palpation task with and without VFF on tissue with visible, and then covered, tumors. Once familiar with the tissue behavior the subjects were tasked with finding a tumor with and without VFF. The testbed used for the VFF and

A.5. A METHOD FOR INSTALLING FBG SENSORS INSIDE SURGICAL ROBOTIC INSTRUMENTS 211

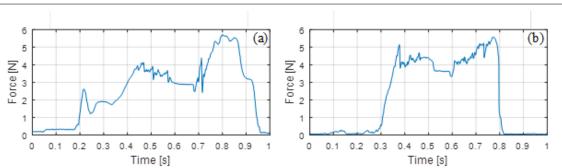


Figure A.9: The force profiles of one novice (a) and one expert surgeon (b) when performing Hem-O-Lock tightening, measured by the FBG sensors.

without VFF task was randomized, as was the order in which the VFF or without VFF task was performed. From the data for the six subjects, only one tumor was successfully located with VFF and no tumors were located correctly without VFF. The system is still under development, with an emphasis on improving performance in this task.

A.5 A Method for Installing FBG Sensors inside Surgical Robotic Instruments

Metallic foil strain gauges are widely used in sensorizing robotic surgical instruments for research applications, due to their small size with respect to commercially available force/torque sensors [1], [2]. However, these gauges offer poor signal-to-noise ratio, require constant calibration and cannot survive sterilization procedures without specialized protective coating. Fiber Bragg Grating (FBG) sensors overcome these problems and have become a good alternative to metallic foil strain gauges in surgical robotic applications [3], [4]. The authors have previously sensorized a da Vinci surgical instrument with FBG sensors [30] that provides force measurements at a rate of 1 kHz with high resolution. A drawback of this design is that the sensors are prone to damage as they are mounted on the outer surface of the instrument. In [31], it is suggested to embed the FBG sensors into engraved slots on the instrument shaft. This method provides better protection to the sensors;

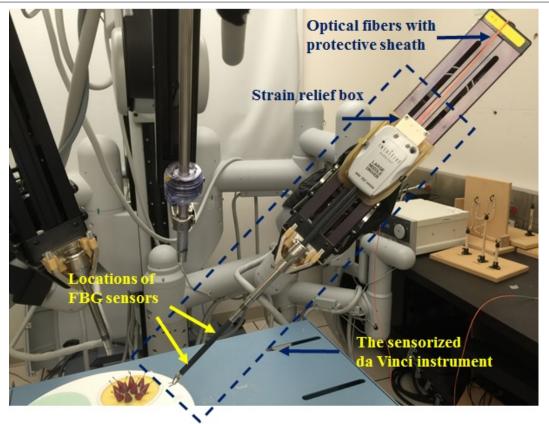


Figure A.10: Sensorized instrument mounted on a da Vinci robot

however, it modifies the mechanical design of the instrument, reduces its structural rigidity, and adds machining costs. Furthermore, the interaction between the trocar and the instrument shaft may scrape off the adhesive or protective coating used in installing the FBG sensors. In this section, a novel method for installing FBG sensors on the interior of a da Vinci surgical instrument (Intuitive Surgical, United States) is proposed and validated. Four FBG sensors (Technica S.A, China) were installed on the inner surface of the instrument using a custom template. These sensors are well protected, capable of providing accurate force sensing and do not interfere with the functioning of the instrument. Fig. A.10 illustrates the sensorized instrument mounted on the da Vinci surgical system. The proposed technique does not require expensive components or special manufacturing facilities, and it therefore ideal for use in research labs in order to sensorize existing instruments for projects related to robot control, surgical training and skills assessment.

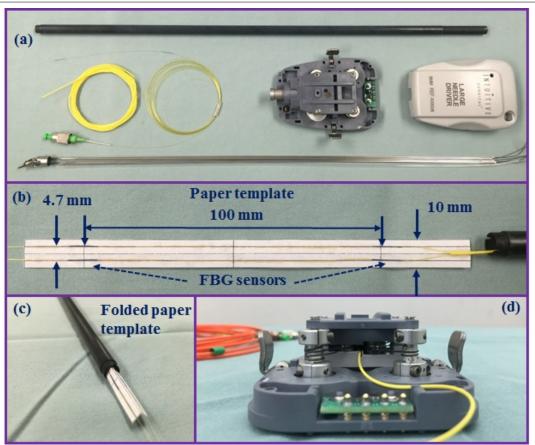


Figure A.11: (a) Disassembled da Vinci instrument; (b) paper template; (c) folded paper template (d) rear view of the sensorized instrument after reassembly.

A.5.1 Materials and Methods

This section describes the method for sensorizing a da Vinci instrument without major modifications to the tool. A Large Needle Driver da Vinci instrument was disassembled as shown in Fig. A.11(a). The grasper and the pull rods were removed from the tool shaft to allow the installation of the sensors. Two cross-sections of the tool shaft were sensorized with optical fibers that both contained two FBGs. Previous work demonstrated the use of this sensor layout for accurate measurement of lateral forces applied on an instrument, independent of the location of the forces and orientations of the instrument tip [7]. A template was designed as a key component to facilitate the installation process (Fig. A.11(b)). This template has three main functionalities: 1) A sensor alignment guide: to measure forces

in orthogonal directions, the optical fibers should be installed 90 apart around the instrument shaft. This template aligns the FBGs and separates the fibers for a certain distance in order to place the sensors could be placed at the desired locations on the inner surface (Fig. A.11(b)); 2) An adhesive carrier: to ensure proper bonding of the fibers to the inner surface, an adequate amount of adhesive (10810, Elmers Products Inc., United States) needs to be applied. The template provides a flat and wide area allowing for insertion of the fibers in the shaft while keeping the adhesive in place (Fig. A.11(c)). Once the fibers are in the desired location, a rigid rod is used to push the paper against the inner surface, ensuring the fibers are in full contact with the shaft. 3) Protective layer: the template permanently covers the FBG sensors inside the tool shaft, preventing damage from the pullrods during instrument reassembly and robotic manipulation. Calibration of the parameters for force sensing uses the same procedure as that described in [7]. Two experiments were conducted to assess the performance of the sensorized instrument. The first experiment assessed the effectiveness of the sensors to measure force. A force/torque sensor (Nano17, ATI Industrial Automation, United States) was mounted on the tip of the instrument (Fig. A.12). Time varying forces were manually applied on the handle and the readings from both sensing modalities were recorded. The second experiment determined the resolution of the sensor. A set of weights were hung at the tip of the instrument to determine the smallest distinguishable increment that can be measured.

A.5.2 Results

Fig. A.13 shows the force measurements from the force/torque sensor and the FBG sensors. For the x and y directions (in the frame of the force/torque sensor), both sensing modalities presented very similar measurements at low and high frequencies. The RMS errors were 0.09 N in the x direction and 0.08 N in the y direction. The resolution of this sensing technology is shown in Fig. A.14. The minimal distinguishable increment is 10 gf (0.098 N) at 1 kHz sampling rate (Fig. A.14(a)). This resolution can be improved to 5 gf (0.049



Figure A.12: Experimental setup for evaluating the performane of force sensing.

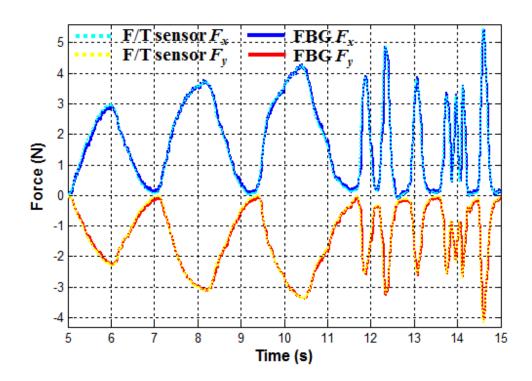


Figure A.13: Comparision of the force measurements from the force/torque sensor (dot) and the sensorized instrument (solid).

N) using the built-in averaging filter (10 times) of the interrogator (SM130, Micron Optics, Atlanta, GA, USA) as shown in Fig. A.14(b).

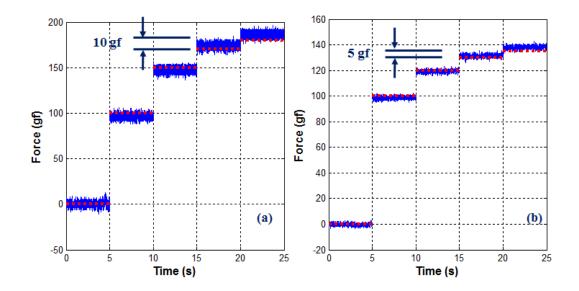


Figure A.14: Comparision of the theoretical force values (red) and the measured values from the sensorized instrument (blue).

A.6 Conclusion

In this appendix, first, a sensorized robotic instrument was proposed for 2-DOF lateral force sensing. The force-strain model and sensing capabilities of this technology were validated by the construction and testing of a sensorized da Vinci Large Needle Driver. Experimental results demonstrated the instruments high resolution and accuracy, and compensation for disturbances such as axial force and force coupling. The sensorized instrument was further evaluated in three surgical tasks using the dVRK operated by a group of novice and expert surgeons. The tasks consisted of suture knot tightening, Hem-O-Lok tightening and tumor localization via tissue palpation. The performance of the subjects in the suture knot tightening task was improved with the help of VFF. In the Hem-O-Lok tightening task, the subjects level of expertise was distinguishable from their recorded force profiles. In the palpation task, VFF added minimal improvement and requires further investigation.

Secondly, a novel technique for integrating FBG sensors on the interior of robotic surgical instruments was presented. A custom template allows accurate placement of the FBG sensors and protects them from damage during re-assembly of the instrument and also

during normal instrument use. The proposed technique was demonstrated on a standard da Vinci instrument, showing that only minor modifications are necessary that do not affect how the instrument is interfaced with and controlled by a da Vinci robot. Furthermore, validation experiments with this instrument show that accurate force measurements can be achieved at a sampling rate of 1 kHz. Our ongoing research focuses on using this force sensing technology for hybrid position and force control, impedance control, haptics-enabled tele-operation and approaches for surgical skills assessment.

Bibliography

- [1] A. Iribarne, R. Easterwood, E. Y. Chan, J. Yang, L. Soni, M. J. Russo, C. R. Smith, and M. Argenziano, "The golden age of minimally invasive cardiothoracic surgery: current and future perspectives," *Future cardiology*, vol. 7, no. 3, pp. 333–346, 2011.
- [2] C. C. L. or Open Resection Study Group *et al.*, "Laparoscopic surgery versus open surgery for colon cancer: short-term outcomes of a randomised trial," *The lancet oncology*, vol. 6, no. 7, pp. 477–484, 2005.
- [3] M. G. Patti, C. A. Pellegrini, S. Horgan, M. Arcerito, P. Omelanczuk, A. Tamburini, U. Diener, T. R. Eubanks, and L. W. Way, "Minimally invasive surgery for achalasia: an 8-year experience with 168 patients," *Annals of surgery*, vol. 230, no. 4, p. 587, 1999.
- [4] T. Walther, V. Falk, S. Metz, A. Diegeler, R. Battellini, R. Autschbach, and F. W. Mohr, "Pain and quality of life after minimally invasive versus conventional cardiac surgery," *The Annals of thoracic surgery*, vol. 67, no. 6, pp. 1643–1647, 1999.
- [5] W. R. Chitwood, J. R. Elbeery, J. F. Moran, and M. I. S. Workgroup, "Minimally invasive mitral valve repair using transthoracic aortic occlusion," *The Annals of thoracic surgery*, vol. 63, no. 5, pp. 1477–1479, 1997.
- [6] K. Nagpal, K. Ahmed, A. Vats, D. Yakoub, D. James, H. Ashrafian, A. Darzi, K. Moorthy, and T. Athanasiou, "Is minimally invasive surgery beneficial in the management of esophageal cancer? a meta-analysis," *Surgical endoscopy*, vol. 24, no. 7, pp. 1621–1629, 2010.
- [7] J. Rassweiler, O. Seemann, M. Schulze, D. Teber, M. Hatzinger, and T. Frede, "Laparoscopic versus open radical prostatectomy: a comparative study at a single institution," *The Journal of urology*, vol. 169, no. 5, pp. 1689–1693, 2003.

- [8] A. Gallagher, N. McClure, J. McGuigan, K. Ritchie, and N. Sheehy, "An ergonomic analysis of the fulcrum effect in the acquisition of endoscopic skills," *Endoscopy*, vol. 30, no. 07, pp. 617–620, 1998.
- [9] D. Lau, J. G. Lee, S. J. Han, D. C. Lu, and D. Chou, "Complications and perioperative factors associated with learning the technique of minimally invasive transforaminal lumbar interbody fusion (tlif)," *Journal of Clinical Neuroscience*, vol. 18, no. 5, pp. 624–627, 2011.
- [10] S. H. Baik, H. Y. Kwon, J. S. Kim, H. Hur, S. K. Sohn, C. H. Cho, and H. Kim, "Robotic versus laparoscopic low anterior resection of rectal cancer: short-term outcome of a prospective comparative study," *Annals of surgical oncology*, vol. 16, no. 6, pp. 1480–1487, 2009.
- [11] B. M. Benway, S. B. Bhayani, C. G. Rogers, L. M. Dulabon, M. N. Patel, M. Lipkin, A. J. Wang, and M. D. Stifelman, "Robot assisted partial nephrectomy versus laparoscopic partial nephrectomy for renal tumors: a multi-institutional analysis of perioperative outcomes," *The Journal of urology*, vol. 182, no. 3, pp. 866–873, 2009.
- [12] K. Narazaki, D. Oleynikov, and N. Stergiou, "Robotic surgery training and performance," *Surgical Endoscopy and Other Interventional Techniques*, vol. 20, no. 1, pp. 96–103, 2006.
- [13] K. Moorthy, Y. Munz, A. Dosis, J. Hernandez, S. Martin, F. Bello, T. Rockall, and A. Darzi, "Dexterity enhancement with robotic surgery," *Surgical Endoscopy and Other Interventional Techniques*, vol. 18, no. 5, pp. 790–795, 2004.
- [14] J. C. Byrn, S. Schluender, C. M. Divino, J. Conrad, B. Gurland, E. Shlasko, and A. Szold, "Three-dimensional imaging improves surgical performance for both novice and experienced operators using the da vinci robot system," *The American Journal of Surgery*, vol. 193, no. 4, pp. 519–522, 2007.
- [15] M. Tavakoli, R. Patel, and M. Moallem, "Haptic interaction in robot-assisted endoscopic surgery: a sensorized end-effector," *The International Journal of Medical Robotics and Computer Assisted Surgery*, vol. 1, no. 2, pp. 53–63, 2005.
- [16] A. Talasaz, A. L. Trejos, and R. V. Patel, "Effect of force feedback on performance of robotics-assisted suturing," in *Proc. IEEE RAS/EMBS Int. Conf. on Biomed. Rob. Biomech.* IEEE, 2012, pp. 823–828.

- [17] A. Talasaz and R. V. Patel, "Integration of force reflection with tactile sensing for minimally invasive robotics-assisted tumor localization," *IEEE transactions on haptics*, vol. 6, no. 2, pp. 217–228, 2013.
- [18] A. Talasaz, A. L. Trejos, S. Perreault, H. Bassan, and R. V. Patel, "A dual-arm 7-degrees-of-freedom haptics-enabled teleoperation test bed for minimally invasive surgery," *Journal of Medical Devices*, vol. 8, no. 4, p. 041004, 2014.
- [19] C. E. Reiley, T. Akinbiyi, D. Burschka, D. C. Chang, A. M. Okamura, and D. D. Yuh, "Effects of visual force feedback on robot-assisted surgical task performance," *The Journal of thoracic and cardiovascular surgery*, vol. 135, no. 1, pp. 196–202, 2008.
- [20] D. S. Yurkewich, A. Escoto, A. L. Trejos, M.-E. LeBel, R. V. Patel, and M. D. Naish, "Low-cost force-sensing arthroscopic tool using threaded fiber bragg grating sensors," in *Proc. IEEE RAS/EMBS Int. Conf. on Biomed. Rob. Biomech.* IEEE, 2014, pp. 28– 33.
- [21] B. Gonenc, M. A. Balicki, J. Handa, P. Gehlbach, C. N. Riviere, R. H. Taylor, and I. Iordachita, "Preliminary evaluation of a micro-force sensing handheld robot for vitreoretinal surgery," in *Proc. IEEE/RSJ Int. Conf. Intell. Robots Syst.* IEEE, 2012, pp. 4125–4130.
- [22] X. He, J. Handa, P. Gehlbach, R. Taylor, and I. Iordachita, "A submillimetric 3-dof force sensing instrument with integrated fiber bragg grating for retinal microsurgery," *IEEE Trans. Biomed. Eng.*, vol. 61, no. 2, pp. 522–534, 2014.
- [23] J. Peirs, J. Clijnen, D. Reynaerts, H. Van Brussel, P. Herijgers, B. Corteville, and S. Boone, "A micro optical force sensor for force feedback during minimally invasive robotic surgery," *Sensors and Actuators A: Physical*, vol. 115, no. 2, pp. 447–455, 2004.
- [24] X. He, M. A. Balicki, J. U. Kang, P. L. Gehlbach, J. T. Handa, R. H. Taylor, and I. I. Iordachita, "Force sensing micro-forceps with integrated fiber bragg grating for vitreoretinal surgery," in *SPIE BiOS*. International Society for Optics and Photonics, 2012, pp. 82 180W–82 180W.
- [25] A. Üneri, M. A. Balicki, J. Handa, P. Gehlbach, R. H. Taylor, and I. Iordachita, "New steady-hand eye robot with micro-force sensing for vitreoretinal surgery," in *Proc. IEEE RAS/EMBS Int. Conf. on Biomed. Rob. Biomech.* IEEE, 2010, pp. 814–819.

- [26] R. Xu, A. Yurkewich, and R. V. Patel, "Curvature, torsion, and force sensing in continuum robots using helically wrapped fbg sensors," *IEEE Robotics and Automation Letters*, vol. 1, no. 2, pp. 1052–1059, 2016.
- [27] R. J. Roesthuis, S. Janssen, and S. Misra, "On using an array of fiber bragg grating sensors for closed-loop control of flexible minimally invasive surgical instruments," in *Proc. IEEE/RSJ Int. Conf. Intell. Robots Syst.*, 2013, pp. 2545–2551.
- [28] A. L. Trejos, R. V. Patel, M. D. Naish, and C. M. Schlachta, "Design of a sensorized instrument for skills assessment and training in minimally invasive surgery," in *Proc. IEEE RAS/EMBS Int. Conf. on Biomed. Rob. Biomech.* IEEE, 2008, pp. 965–970.
- [29] A. Trejos, R. Patel, M. Naish, A. Lyle, and C. Schlachta, "A sensorized instrument for skills assessment and training in minimally invasive surgery," *Journal of Medical Devices*, vol. 3, no. 4, p. 041002, 2009.
- [30] K. S. Shahzada, A. Yurkewich, R. Xu, and R. V. Patel, "Sensorization of a surgical robotic instrument for force sensing," in *SPIE BiOS*. International Society for Optics and Photonics, 2016, pp. 97 020U–97 020U.
- [31] S. J. Blumenkranz and D. Q. Larkin, "Force and torque sensing for surgical instruments," Feb. 3 2015, uS Patent 8,945,095.

Appendix B

Mathematical Derivations for Chapter 5

In this part, the eigenvalues of the linearized three-tube kinematic model are discussed. From (5.20), the characteristic equation for A is:

$$\lambda^{4} + w_{2}\lambda^{2} + w_{0} = 0$$

$$\Rightarrow \lambda^{2} = \frac{1}{2}(-w_{2} \pm \sqrt{w_{2}^{2} - 4w_{0}})$$
(B.1)

where, w_0 and w_2 are calculated from the elements in the matrix A (see the linearized model of the robot):

$$w_{2} = \frac{(1+v)}{\sum_{j=1}^{3} k_{j}} (k_{1}(\|\hat{u}_{1}\|\|\hat{u}_{2}\|\cos(q_{2}) + \|\hat{u}_{1}\|\|\hat{u}_{3}\|\cos(q_{3}))$$

$$+ k_{2}(\|\hat{u}_{1}\|\|\hat{u}_{2}\|\cos(q_{2}) + \|\hat{u}_{2}\|\|\hat{u}_{3}\|\cos(q_{3})$$

$$+ k_{3}(\|\hat{u}_{1}\|\|\hat{u}_{3}\|\cos(q_{2}) + \|\hat{u}_{2}\|\|\hat{u}_{3}\|\cos(q_{3}))$$

$$w_{0} = \frac{(1+v)^{2}\|\hat{u}_{1}\|\|\hat{u}_{2}\|\|\hat{u}_{3}\|}{\sum_{j=1}^{3} k_{j}} (k_{1}\|\hat{u}_{1}\|\cos(q_{2})\cos(q_{3}))$$

$$+ k_{2}\|\hat{u}_{2}\|\cos(q_{2})\cos(q_{3}) + k_{3}\|\hat{u}_{3}\|\cos(q_{3})\cos(q_{3}2))$$
(B.2)

From (B.1), it can be seen that there are four distinct solutions for the eigenvalues of the linearized robot kinematics which have the following relationships: $\lambda_2 = -\lambda_1$, $\lambda_4 = -\lambda_3$.

We now show that λ_j^2 is a real number, which results in having purely real or purely imaginary values for λ_j . This is true when $w_2^2 - 4w_0 \ge 0$. Using (B.2) we can write $w_2^2 - 4w_0$ as follows:

$$W/(k_1 + k_2 + k_3)^2 \tag{B.3}$$

where,

$$W = W_0 + W_1 + W_2 + W_3 \tag{B.4}$$

with

$$W_{0} = (1+v)^{2} (k_{1}^{2}(||\hat{u}_{1}|| ||\hat{u}_{2}|| \cos(q_{2}) - ||\hat{u}_{1}|| ||\hat{u}_{3}|| \cos(q_{3}))^{2} +k_{2}^{2} (||\hat{u}_{1}|| ||\hat{u}_{2}|| \cos(q_{2}) - ||\hat{u}_{2}|| ||\hat{u}_{3}|| \cos(q_{32}))^{2} +k_{3}^{2} (||\hat{u}_{1}|| ||\hat{u}_{3}|| \cos(q_{3}) - ||\hat{u}_{2}|| ||\hat{u}_{3}|| \cos(q_{32}))^{2} W_{1} = (1+v)^{2} (k_{2} ||\hat{u}_{1}|| ||\hat{u}_{2}|| \cos(q_{2}) + k_{3} ||\hat{u}_{1}|| ||\hat{u}_{3}|| \cos(q_{3}) -k_{2} ||\hat{u}_{2}|| ||\hat{u}_{3}|| \cos(q_{32}) - k_{3} ||\hat{u}_{2}|| ||\hat{u}_{3}|| \cos(q_{32}))^{2} W_{2} = (1+v)^{2} (k_{1} ||\hat{u}_{1}|| ||\hat{u}_{2}|| \cos(q_{2}) - k_{1} ||\hat{u}_{1}|| ||\hat{u}_{3}|| \cos(q_{3}) -k_{3} ||\hat{u}_{1}|| ||\hat{u}_{3}|| \cos(q_{3}) + k_{3} ||\hat{u}_{2}|| ||\hat{u}_{3}|| \cos(q_{32}))^{2} W_{3} = (1+v)^{2} (k_{1} ||\hat{u}_{1}|| ||\hat{u}_{2}|| \cos(q_{2}) + k_{2} ||\hat{u}_{1}|| ||\hat{u}_{2}|| \cos(q_{2}) -k_{1} ||\hat{u}_{1}|| ||\hat{u}_{3}|| \cos(q_{3}) - k_{2} ||\hat{u}_{2}|| ||\hat{u}_{3}|| \cos(q_{32}))^{2}$$

Noting that W is a summation of four non-negative terms, which ensures $W \ge 0$. As a result, λ_j^2 is a real number, and λ_j is either real or purely imaginary.

Curriculum Vitae

Name:	Ran Xu	
Post-secondary Education and Degrees:	B.Sc, Harbin Engineering University (HEU) Harbin, Heilongjiang, People's Republic of China	2004-2008
	M.Sc-Ph.D. Candidate, Shandong University (SDU) Jinan, Shandong, People's Republic of China	2008-2010
	Ph.D., Western University (UWO) London, Ontario, Canada	2010-2016
Selected Honors	NSERC CREATE CAMI Program stipend Scholarship	2012-2014
and Awards:	Western Graduate Research Scholarship	2010-2014
	China Scholarship Council Study Abroad Scholarship	2010-2014
	WeiChai Outstanding Graduate Scholarship	2009
	Outstanding Undergraduate Thesis of HEU (Top 1%)	2008
	Second Prize, National Electronic Design Contest	2007
	First Prize, Provincial Electronic Design Contest	2006
	First Prize, Mechanical Design Contest of HEU	2006
	Haitai Scholarship	2006
	Excellent All-Around Student	2006
	First-Class Excellent Academic Scholarship	2005-2006
Related Work	Research Assistant	2010-2016
Experience:	Canadian Surgical Technologies	
	and Advanced Robotics (CSTAR)	
	Teaching Assistant University of Western Ontario	2011-2014
	Research Assistant Shandong University	2008-2010

Related Work	Lecturer
Experience:	LecturerShandong Medical College

Publications:

– P. S. Zarrin, A. Escoto, **R. Xu**, R. V. Patel, M. D. Naish, A. Trejos, Development of an optical fibre-based sensor for grasping and axial force sensing, IEEE Int. Conf. Robot. Autom., ICRA, 2017 (submitted).

- R. Xu, A. Yurkewich, and R. V. Patel, Curvature, torsion, and force sensing in continuum robots using helically wrapped fbg sensors, IEEE Robotics and Automation Letters, vol. 1, no. 2, pp. 1052-1059, 2016.

- R. Xu, A. Yurkewich, and R. V. Patel, Shape sensing for torsionally compliant concentrictube robots, in SPIE BiOS. International Society for Optics and Photonics, 2016, pp. 97020V.

- R. Xu, A. Escoto, K. S. Shahzada, C. Ward, R. V. Patel, "A Method for Installing FBG Sensors inside Surgical Robotic Instruments," Hamlyn Symposium on Medical Robotics, 2016.

– A. Srivastava, R. Xu, A. Escoto, C. Ward and R. V. Patel, Design of an Ultra-Thin Strain Sensor Using Superelastic Nitinol for Applications in Minimally Invasive Surgery, in Proc. IEEE Int. Conf. on Advanced Intelligent Mechatronics, 2016, pp. 794-799.

– K. S. Shahzada, A. Yurkewich, **R. Xu** and R. V. Patel, "Sensorization of a surgical robotic instrument for force sensing," in Proc. SPIE BiOS. 2016, pp. 97020U.

- R. Xu, S. F. Atashzar, and R. V. Patel, Kinematic instability in concentric-tube robots: modeling and analysis, in Proc. IEEE RAS/EMBS Int. Conf. on Biomed. Rob. Biomech. 2014, pp. 163-168.

- R. Xu, A. Asadian, S. F. Atashzar, and R. V. Patel, Real-time trajectory tracking for externally loaded concentric-tube robots, in Proc. IEEE Int. Conf. Robot. Autom., 2014, pp. 4374-4379.

- R. Xu, A. Asadian, A. S. Naidu, and R. V. Patel, Position control of concentric-tube continuum robots using a modified jacobian-based approach, in Proc. IEEE Int. Conf. Robot. Autom. 2013, pp. 5813-5818.

- R. Xu and R. Patel, A fast torsionally compliant kinematic model of concentric-tube robots, in 2012 Annual International Conference of the IEEE Engineering in Medicine and Biology Society. 2012, pp. 904-907.

2009-2010

– F. X. Guan, **R. Xu**, and W. Yang, The Design of Security Defensive and Alarm System Based on WinCE and GPRS, Experimental Technology and Management, 2009, vol. 26, no. 11, pp. 45-48.

Professional Service:

Reviewer of IEEE Transactions on Robotics Reviewer of IEEE Transactions on Biomedical Engineering Reviewer of Annals of Biomedical Engineering Reviewer of Journal of Medical Robotics Research Reviewer of IEEE Robotics and Automation Letters Reviewer of IEEE International Conference on Robotics and Automation (ICRA), 2013present Reviewer of IEEE/RSJ International Conference on Intelligent Robots and Systems (IROS), 2015-present Reviewer of IEEE RAS/EMBS International Conference on Biomedical Robotics and Biomechatronics (BioRob), 2016